Star clusters

Cover illustration:
Hubble Space Telescope image (edited) of the globular cluster M80 (NGC 6093)
Credit: The Hubble Heritage Team (STScI/AURA)
Acknowledgment: M. Shara and D. Zurek (AMNH), and F. Ferraro (ESO)

Images on the bottom of the odd pages:
Snapshots from an N-body simulation of an encounter between a star cluster and a giant molecular cloud (from Chapter 8).

ISBN-10: 90-393-4374-8
ISBN-13: 978-90-393-4374-6

Star clusters

Sterrenhopen
(met een samenvatting in het Nederlands)

Proefschrift

ter verkrijging van de graad van doctor
aan de Universiteit Utrecht
op gezag van de rector magnificus, prof. dr. W.H. Gispen,
ingevolge het besluit van het college voor promoties
in het openbaar te verdedigen op

vrijdag 20 oktober 2006 des middags te 12.45 uur

door

Mark Gieles

geboren op 10 mei 1977 te Dordrecht

Promotor: Prof. dr Henny Lamers

Copromotor: Dr Simon Portegies Zwart

This research has been supported by the Netherlands Research School for Astronomy (NOVA).

Contents

Contents v

1. Introduction and summary 1
1.1. Star clusters: setting the stage 1
1.2. Formation, evolution and properties of star clusters 2
1.3. Summary of this thesis 8

I Observations of the formation and disruption of clusters 13

2. Hierarchical star formation in M51: Star/cluster complexes 15
2.1. Introduction 16
2.2. Observations 17
2.3. Properties of the complexes 22
2.4. Comparison between the properties of cluster complexes and GMCs . 29
2.5. Discussion 32
2.6. Summary and conclusions 34

3. The star cluster population of M51: Age distribution and relations among the derived parameters 39
3.1. Introduction 40
3.2. Observations, reduction and photometry 42
3.3. The selection of the clusters and the photometry master list. 48
3.4. Determination of the cluster parameters from their energy distribution 51
3.5. Extinction 59
3.6. The age distribution of the clusters 60
3.7. A population of short-lived clusters 67

3.8. Cluster sizes . . . 69
3.9. Correlations with the cluster radius . . . 71
3.10. Conclusions . . . 74

4. The star cluster population of M51: Cluster disruption and formation history 79
4.1. Introduction . . . 79
4.2. The observations . . . 81
4.3. Exploration of the parameters which determine the disruption time . . 87
4.4. Input parameters for modelling the cluster population of M51 . . . 91
4.5. Analytical model for generating a cluster population . . . 92
4.6. Fitting observed age-mass distribution to predictions . . . 93
4.7. Implication of the derived disruption time . . . 99
4.8. Conclusions . . . 100

5. Disruption time scales of star clusters in different galaxies 103
5.1. Introduction . . . 104
5.2. The predicted dependence of the disruption time on cluster parameters and environment . . . 104
5.3. The empirically determined disruption times . . . 109
5.4. The dependence of the disruption time on the conditions in the host galaxy . . . 110
5.5. Conclusions . . . 114

II N-body simulations of the disruption of star clusters 115

6. Theory of gravitational shocks 117
6.1. Introduction . . . 117
6.2. Tidal shocks . . . 118
6.3. Compressive gravitational shocks . . . 121

7. The effect of spiral arm passages on the evolution of stellar clusters 123
7.1. Introduction . . . 124
7.2. Spiral arm parameters . . . 126
7.3. Simple analytical estimates for one-dimensional tidal perturbations . . 130
7.4. N-body simulations . . . 133
7.5. Cluster mass loss and disruption by spiral arm perturbations . . . 138
7.6. Discussion and conclusions . . . 142

8. Star cluster disruption by giant molecular clouds 145
8.1. Introduction . . . 146
8.2. Initial conditions . . . 147
8.3. Cluster energy gain and mass loss due to an encounter with a GMC . 150
8.4. Validation with N-body simulations . . . 153

8.5. Cluster disruption time due to GMC encounters . . . 163
8.6. Conclusions and discussion . . . 168

9. Clusters in the solar neighbourhood: how are they destroyed? 171
9.1. Introduction . . . 171
9.2. The decreasing mass of star clusters . . . 172
9.3. Comparison with observed age distribution of clusters in the solar neighbourhood . . . 176
9.4. Discussion and summary . . . 177

III A maximum to the masses of regular star clusters 179

10. The luminosity function of star clusters: implications for the maximum mass and luminosity 181
10.1. Introduction . . . 182
10.2. Data . . . 184
10.3. Masses and luminosities at different ages . . . 184
10.4. The luminosity functions of five galaxies . . . 193
10.5. A cluster population model . . . 199
10.6. The maximum cluster luminosity . . . 208
10.7. Discussion . . . 210
10.8. Conclusion . . . 212

11. Observational evidence for a truncation of the star cluster initial mass function at the high mass end 213
11.1. Introduction . . . 214
11.2. Source selection and photometry . . . 215
11.3. The luminosity function . . . 216
11.4. Comparison with a cluster population model . . . 218
11.5. Discussion and conclusions . . . 219

12. Samenvatting in het Nederlands 221
12.1. Sterrenhopen: algemene introductie . . . 221
12.2. Samenvatting van dit Proefschrift . . . 224

13. Resumen en Castellano 227
13.1. Cúmulos de estrellas: Introducción general . . . 227
13.2. Resumen de esta Tesis . . . 229

List of publications 233

Dankwoord 237

References 239

CHAPTER 1

Introduction and summary

1.1. Star clusters: setting the stage

Star clusters are observed in galaxies of almost all type and are considered the fundamental building blocks of galaxies. The member stars of a cluster are approximately of the same age and this makes star clusters unique laboratories for studies of stellar evolution. The stars in the clusters are bound by mutual gravitational attraction and, due to relatively high stellar densities, interesting dynamical events, such as stellar collisions and binary formation and disruption, take place in a cluster.

The Milky Way has long been the main playground for studies of star clusters. A classic distinction was made between the open clusters, which are young (< few Gyr) members of the disc with low masses ($\sim 10^{2-4}\,M_{\odot}$), and the globular clusters, which are part of the Galactic halo/bulge, are massive ($\sim 10^{4-6}\,M_{\odot}$), very dense and have almost the age of the universe. Typical radii of star clusters are in a very narrow range ($2-4$ pc), yielding a huge spread in central densities ($10^{1-6}\,M_{\odot}\,\mathrm{pc}^{-3}$).

In the early 90's (extra-galactic) star clusters in the mass range of globular clusters and with ages of open clusters were discovered. This made the earlier mentioned distinction less obvious and led to the belief that star clusters form in a continuous mass distribution. Recent observations have shown that these so-called young massive clusters (YMCs) are generally formed with a power-law initial mass function, similar to that of the open clusters, but distinctly different than the peaked mass function of globular clusters. In galaxies with high star formation rates more star clusters are formed, pushing the high-mass tail of the mass function to higher masses.

YMCs have drawn a lot of attention in recent years, since they might reveal the formation of old globular clusters in the early universe. Due to the high light-to-mass

ratio of stellar populations at young ages, YMCs are observable up to large distances ($\lesssim 100\,\mathrm{Mpc}$) and they are considered as good tracers of the star formation history of their host galaxy. Although all stars are probably formed in a clustered environment, less than 1% of the stars in our Milky Way are members of a star cluster. Internal dynamical effects and external tidal effects limit the life-time of clusters. This raises a fundamental problem in interpreting the observed age distribution of clusters as their formation history. More precisely, it will underestimate the cluster formation rate at old ages. In addition, many embedded star clusters will not survive the very early evolution in which the gas, which is left-over from the star formation process, is blown away by stellar winds and supernovae. This "infant mortality" makes a relation between cluster formation rate and star formation rate non-trivial.

In this introduction a general outline is given of our current understanding of the formation, the evolution and the fundamental properties of star clusters and standing problems (§ 1.2). A summary of the contributions presented in this thesis is given in§ 1.3.

1.2. Formation, evolution and properties of star clusters

1.2.1. The formation from giant molecular clouds

Stars and star clusters are formed from cold ($\lesssim 10\,\mathrm{K}$) molecular gas, which, in our Milky Way, constitutes approximately 10% of the total gas content of the interstellar medium (ISM). This molecular component is concentrated in clouds, of which the number of clouds as a function of their mass is well described by a power-law distribution (e.g. Solomon et al. 1987). The index of the distribution is around -1.5, which makes most mass residing in massive clouds ($> 5 \times 10^4\,M_\odot$), the so-called giant molecular clouds (GMCs). Internally, there is an equilibrium between gravitational forces working inwards and internal pressure working outwards.

When the GMC is disturbed by external pressure perturbations, e.g. by spiral density waves or Galactic scale interactions or mergers, parts of the cloud can collapse forming stars in the highest density regions of the clouds. After a short embedded phase (see § 1.2.2), these star forming regions will show up in the optical wavelengths as HII regions, with strong Hα emission coming from gas that is ionised by the ultraviolet (UV) radiation from young (hot) stars. The luminosity function of these HII regions is also characterised by a power-law distribution, but with a slightly smaller index (-2) than for the GMC mass function (Kennicutt et al. 1989). The smallest HII regions, the (ultra) compact HII regions, can be as small as 0.1-1 pc (Habing & Israel 1979), e.g. where ionisation is caused by individual stars or small, very compact, clusters. If the GMC has formed stars over a large range of densities, multiple HII regions can form from a single GMC. These star forming complexes still bear the imprints of the progenitor GMC, such as the characteristic mass-radius relation: $M \propto R^2$ (e.g. Elmegreen et al. 2001; Chapter 2). Because of this mass-

radius relation, the most massive complexes can have radii much larger ($\sim 100\,\mathrm{pc}$) than the radii of individual star clusters ($\sim 2-4\,\mathrm{pc}$, e.g. Larsen 2004).

It is unclear if these complexes of young stars and clusters are expanding, stable or merging entities. Simulations of complexes show evidence that these complexes will merge due to dynamical friction (Fellhauer & Kroupa 2005), implying that a large fraction of the stars formed out of the GMC can end up in a single cluster. However, this will be highly dependent on external shear and tidal field effects and could, therefore, be strongly dependent on galactic environment. Low density complexes are more likely to be dispersed by tidal shear and therefore result in multiple clusters and individual stars.

1.2.2. Early evolution: expelling the gas

In Fig. 1.1 (left) the star forming region NGC 7129 in the Milky Way is shown. The image is taken with the recently launched *Spitzer* infra-red (IR) space telescope. The IR-radiation comes from dust located in parts of the GMC that were not used for star formation and that absorbs UV light from young, hot stars and re-radiates it in the IR. The bright points in the image are the regions around the massive stars and it is clear that there are many of them. In the optical wavelengths this embedded cluster would not be visible, because of the dust extinction. The stars inside the cluster also form with a power-law mass function with index ~ -2.35, e.g. Salpeter (1955) or Kroupa (2001), implying that there are many low mass stars that we can not see in this image.

In the middle panel of Fig. 1.1 we show a *Hubble Space Telescope (HST)* image of the young star clusters NGC 346 in the Small Magellanic Cloud (SMC). Here the nebular light is from gas that is ionised by hot stars and more of the low mass stars can be seen. When this cluster would have been at a larger distance, it would probably have been picked up by an Hα survey and referred to as HII region. Since at the distance of the SMC the individual stars can be resolved, it is called a cluster. The dust has been destroyed by the intense UV radiation and this would be a later stage in the formation of the cluster than that of NGC 7129. The remaining gas will not stay there, but will be blown away by the combined effect of strong stellar winds from O and B stars and supernovae ejecta (Castor et al. 1975). The result of this can be seen in the right side of Fig. 1.1, which shows the clusters NGC 3603 in our Milky Way, which is half-way this gas expulsion phase.

The cluster NGC 346 (Fig. 1.1, middle) is in the crucial phase between embedded in left-over gas of the GMC and having expelled this gas. Many clusters do not survive this short lasting phase. The reason is the star formation efficiency (ϵ). Assume a GMC with mass $M_{\rm n}$ that forms stars with efficiency ϵ, typically a few per cent, then a fraction (1-ϵ) of the GMC mass is not converted into stars. Stellar winds and supernovae expel this left-over gas from the clusters on short time-scales ($\lesssim 1\,\mathrm{Myr}$, see Elson et al. 1989 for a discussion). With the mass, also binding energy is removed from the system. If the stars are initially virialised, the velocities of stars are too high

once the gas is removed. This causes the cluster to expand and loose stars, or even completely dissolve (Goodwin 1997; Geyer & Burkert 2001; Boily & Kroupa 2003).

This infant mortality scenario of embedded clusters is supported by observations that show that the formation rate of embedded star clusters in the solar neighbourhood is about an order of magnitude higher than the formation rate of star clusters, suggesting an infant mortality rate of $\sim 90\%$ (Lada & Lada 2003). Similar estimates ($\sim 50-90\%$) have been reported for clusters in the "Antennae" and M51 by Fall et al. (2005) and Chapter 3 of this thesis, respectively. However, a direct comparison between these latter values and the solar neighbourhood is hard, since the extra-galactic estimates are not based on a comparison to embedded clusters, but on a comparison to young ($\lesssim 10\,\mathrm{Myr}$) clusters that are already detected in the optical. Therefore, the true infant mortality rates of embedded clusters are probably higher than inferred in these studies.

How this gas removal phase affects the cluster initial mass function (CIMF) is still largely unknown. Lada & Lada (2003) report a power-law distribution for the mass distribution of embedded star clusters with an index of -1.7, which is in between the index for GMCs (-1.5) and the one observed for the luminosity function of HII regions (-2). Theoretical arguments suggest that the amount of mass lost in the gas expulsion phase must depend on the mass of the embedded cluster, hence causing a difference between the embedded and initial mass function (Kroupa & Boily 2002). However, observational uncertainties on the determination of the different mass functions are still too large to give an univocal solution to this problem.

Figure 1.1: Left: *Spitzer/IRAC* image of the young embedded cluster NGC 7129 (courtesy of R. Hurt). Middle: *HST/ACS* image of the young cluster NGC 346 in the Small Magellanic Clouds (courtesy of A. Nota). Right: Young star cluster NGC 3603 in the Milky Way, taken with *HST/WFPC2* (courtesy of W. Brandner).

1.2.3. The cluster initial mass function

Recent observations have revealed that the dichotomy between the Galactic open and globular clusters is less clear in other galaxies. This was probably first noted due to the existence of "blue globular cluster" in the Large Magellanic Cloud (LMC), which can have masses up to $10^5\,M_\odot$ and ages much younger ($<1\,$Gyr) than the globular clusters. Also in M31, clusters much younger than the mean age of globular clusters ($\sim 13\,$Gyr) and more massive than the average open clusters have been reported (e.g. van den Bergh 1969). Going to more vigorous star formation environments, such as interacting galaxies like M51 (Larsen 2000; Chapters 2, 3 &11; Fig. 1.3) and IC 2163/NGC 2207 (Elmegreen et al. 2006), starburst galaxies (Meurer et al. 1995) and merging galaxies like the "Antennae" galaxies (NGC 4038/4039, Whitmore et al. 1999b) show that YMCs cover the full mass range from about $10^{2-3}\,M_\odot$ up to several times $10^6\,M_\odot$. These observations suggest a more continues cluster formation mechanism, where the YMCs are simply the high mass tail of the distribution. Recent theoretical work (Elmegreen & Efremov 1997) supports this scenario by suggesting that the CIMF results naturally from the turbulent properties of the ISM, where more massive clusters can form in high pressure environments. In this scenario the high pressure environments needed to form YMCs occur in galaxy wide disturbances in interacting and merging galaxies.

The interacting galaxy M51 is a nice example of a disturbed galaxy where many young star clusters are found (Fig. 1.3, Chapters 3 & 11). Another prediction of this theory is the cluster initial mass function (CIMF), which should have a power-law distribution with index -2, e.g. very close to what is observed for the luminosity function of individual HII regions (see § 1.2.1). This is also observed for the mass distribution of young clusters in the "Antennae" galaxies (Zhang & Fall 1999). In Fig. 1.2 we show the mass distribution of the clusters in the "Antennae" galaxies (top panel) and compare this to the mass distribution of globular clusters in the Milky Way (bottom panel). The high mass ends look very similar. However, there are many more low mass clusters observed in the "Antennae" galaxies as compared to the globular clusters. Similar power-law mass functions have been observed for young clusters in M51 (Bik et al. 2003) and for the LMC and SMC (Hunter et al. 2003). The power-law description of the CIMF suggests that the high mass end can be explained by the total number clusters that are formed. For a power-law mass function with index -2, the most massive cluster depends on the total number of clusters (N) above some minimum cluster mass ($M_{\rm min}$) as $M_{\rm max} = N \times M_{\rm min}$. This assumes, however, a power-law nature of the mass function with a chance of finding a cluster with mass M scaling as $P \propto 1/M^2$, i.e. without a physical upper limit to the masses of clusters from environmental effects (but see Chapters 10 & 11).

1.2.4. Dynamical evolution of clusters

The difference in mass distribution between YMCs and globular clusters (Fig. 1.2) is often explained by preferential disruption of the low mass clusters, causing a power-

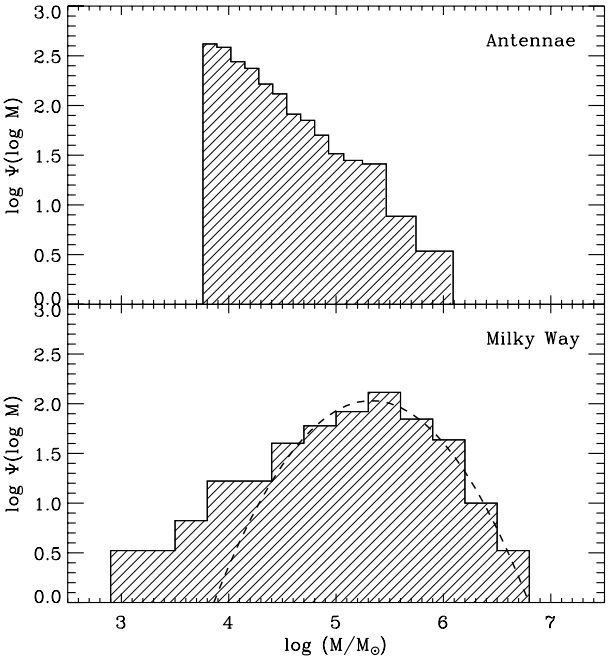

Figure 1.2: Top: initial mass distribution of star clusters in the "Antennae" galaxies. This distribution can be well described by a power-law function with index -2. Bottom: the mass distribution of the Galactic globular clusters, with a peak around $2 \times 10^5\, M_\odot$. (From Fall & Zhang 2001)

law mass function to "turn-over" bell-shaped function in logarithmic mass space.

The life times of globular clusters are limited by internal two and three body encounters between stars, in which stars can gain velocity and reach the escape velocity and leave the cluster. The tidal field of the galaxy lowers this escape velocity in a cluster, thereby speeding up this process of evaporation (Spitzer 1987). In addition, the galactic disc and bulge are an extra source of "heating", since stars gain energy after crossing the disc or bulge (also Spitzer 1987 and Chapter 6 for an explanation of the physics).

Several attempts have been made to evolve a power-law initial mass distribution into a log-normal distribution by dynamical evolution (Vesperini 1998; Fall & Zhang 2001; Vesperini & Zepf 2003). However, certain strong constraints on the initial conditions, like a strong increase in the velocity anisotropy with galactocentric radius (Fall & Zhang 2001) or a relation between cluster concentration and cluster mass (Vesperini & Zepf 2003), have to be made, to force an agreement with the observed lack of radial dependence of the turn-over mass. Alternative scenarios have been proposed, in which the observed turn-over in the globular cluster mass distribution is

Figure 1.3: *HST/ACS* image of the interacting galaxy pair NGC 5194/5195, taken as part of the Hubble Heritage program (Mutchler et al. 2005, http://archive.stsci.edu/prepds/m51/). The clumpy regions are mostly due to Hα emission from young star clusters. The light from $B/V/I$ + Hα (F435W/F555W/F814W+F658N) filters is shown.

a remnant of the formation process (Harris & Pudritz 1994).

For the open clusters in the solar neighbourhood it is also clear that disruption must have affected the age distribution, since there are hardly any open cluster with ages above a few Gyr. This was already noted by Oort (1958). Spitzer (1958) already held encounters with massive molecular clouds responsible for this. From the age distribution of open clusters, Wielen (1971) derived a mean dissolution time of 200 Myr. Hodge (1987) and Hodge (1988) compared this to the clusters in the SMC and LMC, respectively, and noted that the life times of clusters in the Magellanic Clouds are around a factor of ten longer compared to the Milky Way (solar neighbourhood). The disruption of clusters and comparisons to theoretical models are dealt with in more detail in Part I and II of this thesis.

1.3. Summary of this thesis

In this thesis several aspects of cluster formation, evolution and disruption are covered. The various chapters are grouped in three Parts, which are summarised in § 1.3.1-1.3.3.

1.3.1. Part I: Observations of the formation and disruption of clusters

The first part covers Chapters 2-5 of the thesis, and introduces observations of young (massive) clusters in the interacting spiral galaxy pair NGC 5194/5195 (M51, see Fig. 1.3). In **Chapter 2** *HST/WFPC2* observations of star and star cluster forming regions are presented. These so-called complexes are located on, or close to, the spiral arms of the galaxy. We derived ages and masses of these complexes by assuming that all stars in the complexes are formed at the same time and then comparing the integrated colours and the Hα equivalent widths to simple stellar population (SSP) models. We found that they are generally young ($\sim 10\,$Myr) and from the age dependent mass-to-light ratios of the SSP models we derived masses of $3-30\times10^4\,M_\odot$ and the measured radii are comparable to those of GMCs ($\sim 10-100$ pc). Since an individual complex consists of many ($\gtrsim 100$) stars and star clusters, the scenario that a single GMC forms a single star cluster when it becomes gravitationally unstable is probably too simplified. However, these complexes and GMCs share some fundamental properties, such as the mass-radius relation ($M \propto R^2$) and the surface brightness profile. This suggests we are seeing the stage where the GMC has just formed its stars, over a large range of densities, but the individual stars and clusters have not yet been dispersed by shear effects or merged due to dynamical friction.

A study of the individual clusters in the inner part ($\sim 5\times5\,$kpc) of the disc of M51 is presented in **Chapter 3**. Analogous to what was done in Chapter 2, we compared the colours in seven filters from the UV to the near-infrared (NIR) of thousands of point-like sources that were found in the *HST* images. By comparing the colours to SSP models and stellar models of different ages and taking into account extinction, we found that 1052 sources were better fit to a cluster model than a stellar model. From the ages and the mass-to-light ratios we derived the masses of the clusters. A fraction ($\sim 30\%$) of the sources is slightly resolved. We compared the light profile to different modeled cluster profiles convolved with the *WFPC2* point spread function (PSF). The majority of clusters are found in a small range of radii ($2-4\,$pc) and the number distribution of radii can be well approximated by a power-law distribution, with index -2.2 ± 0.2. No relation is found between the radii and masses of clusters, implying that young clusters are not formed in tidal equilibrium with the galaxy.

In **Chapter 4** we compare the ages and masses of the clusters found in Chapter 3 to detailed cluster population models. By assuming an initial power-law CIMF with index -2, which is observed for various galaxies, including M51 (§ 1.2.3), we analytically generate cluster populations with different cluster formation histories (CFHs) and disruption scenarios. The cluster disruption time depends on its mass as $t_{\rm dis} \propto$

$M_{\rm c}{}^{\gamma}$, with $\gamma \simeq 0.6$ (Boutloukos & Lamers 2003, Chapters 5, 7, 8 & 9) and, therefore, we can disentangle variations in the CFH from disruption. We found that the clusters in M51 are short lived, with an average life expectancy of $t_4 = 1.0^{+0.6}_{-0.5} \times 10^8$ yr, with t_4 the disruption time of a cluster with $M_{\rm c} = 10^4\,M_{\odot}$. N-body simulations of the galaxy interaction by Salo & Laurikainen (2000) suggest that two crossings of NGC 5195 are necessary to explain the observed extend of the HI-arm of M51. Since these tidal disturbances might have enhanced the cluster formation rate (e.g. Bergvall et al. 2003) we also created models with bursts in the formation history at the moments the companion galaxy NGC 5195 crossed the disc of M51. These models gave better fits compared to the constant formation rate and resulted in a slightly longer disruption time of $t_4 = 2.0^{+2.3}_{-1.1} \times 10^8$ yr. This disruption time is about an order of magnitude shorter than in other galaxies which have been studied.

In **Chapter 5** we show that the value found for the disruption time of clusters in M51 is an order of magnitude lower compared to the value for the clusters in the solar neighbourhood and M33 and even two orders of magnitude lower compared to the value for the SMC. The power-law dependence of the disruption time with cluster mass, e.g. the index $\gamma \simeq 0.6$, as found from observed age and mass distributions by Boutloukos & Lamers (2003) and in Chapters 4 and 9, is explained in this chapter. We use the results of Baumgardt & Makino (2003) of N-body simulations of clusters dissolving in a tidal field. These simulations consider a realistic stellar mass function, stellar evolution and a realistic tidal field for the Galaxy. The resulting disruption time depends on the number of stars (N) as $t_{\rm dis} \propto \beta[N/\ln(0.02\,N)]^x$. For the different cluster profiles considered, different values of β and x are found. We showed that $t_{\rm dis}$ can be approximated with high accuracy by $t_{\rm dis} \propto N^{0.62} = t_4\,(M_{\rm c}/10^4\,M_{\odot})^{0.6}$. The scaling factor t_4, can be related to the tidal field strength, which for a flat rotation curve scales linear with $R_{\rm G}$, the position in the Galaxy. Good agreement between the observationally determined value of t_4 and the one following from the N-body simulations is only found for the SMC. For the clusters in the solar neighbourhood and M33 the observationally determined value is a factor of five shorter than expected from tidal field effects only. For M51 (Chapter 4) the discrepancy is a factor of ten. We argue in this chapter that this could be caused by additional disturbances such as spiral arm and GMC passages, which are not included in the N-body models of Baumgardt & Makino (2003). This is topic of the next part of the thesis.

1.3.2. Part II: N-body simulations of the disruption of star clusters

The disruption of star clusters has been the subject of many theoretical studies, dating back to the pioneering studies of Bok (1934), Chandrasekhar (1942) and Spitzer (1940). Systematic and quantitative studies were probably triggered by the study of Spitzer (1958), who analytically estimated the disruptive effect of external perturbations on star clusters.

In **Chapter 6** I first give a short introduction to the dynamical aspects of external perturbations on star clusters: what happens to a globular cluster when it crosses the

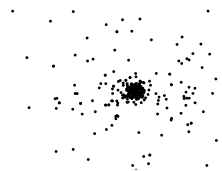

disc of the galaxy and what happens to an open cluster when a GMC passes? No new results are presented, just a simple explanation of the forces and time-scales at work during such events. The widely used "impulse approximation" is introduced here. Using the impulse approximation, first order estimates of the energy gain of a cluster after a tidal disturbance are derived.

The theory is applied and verified by means of detailed N-body simulations in **Chapter 7**, where we estimate the effect of spiral arms on star clusters. It is commonly accepted that spiral arms are the birthplaces of stars and star clusters, since the spiral density wave moves with a constant angular velocity through the disc, thereby sweeping up molecular gas on its way, since that is rotating with a nearly constant orbital velocity. This is beautifully illustrated in Fig. 1.3, where the dust lanes, which are dark in this optical image due to absorption by dust are slightly offset from the bright and young stars and clusters. However, clusters formed in the spiral arms will, depending on their location with respect to the corotation radius, sooner or later meet the spiral density wave again. This disturbance acts as a disc shock (Chapter 6) and can unbind stars from the clusters. We show that this effect is highly dependent on the relative velocity ($V_{\rm drift}$) between the cluster and the spiral arm, since the energy gain of the cluster scales with $V_{\rm drift}$ as $\Delta E \propto {V_{\rm drift}}^{-2}$ (Chapter 6). Therefore, the disruptive effect is largest close to the corotation radius, $R_{\rm CR}$, of the galaxy, i.e. the point where the orbital velocity of the cluster is equal to the angular velocity of the spiral arms. Since the solar neighbourhood is close to $R_{\rm CR}$ of our Galaxy, and there are four spiral arms in the Milky Way disc, the spiral arms make a relatively important contribute to the disruption of open clusters.

The short disruption times observed for M51 (Chapter 4), however, can not be explained by spiral arm passages. This is because the clusters studied in Chapters 3 & 4 are concentrated to the centre of the galaxy, where $V_{\rm drift}$ is large and the density contrast of the arm is low. However, the centre of M51 contains a large amount of molecular gas, in the form of GMCs (e.g. Garcia-Burillo et al. 1993), where the surface density of molecular gas in the disc is an order of magnitude higher than in the solar neighbourhood.

In **Chapter 8** we simulate encounters between GMCs and star clusters with N-body calculations. We verified existing expressions for the energy gain of a cluster due to an encounter with a GMC. These analytical expressions assumed a point-mass GMC, which we compared to simulations of more realistic GMC profiles. We show that the point-mass approximation is accurate when the encounters distance (p) is larger than a few GMC radii. However, the energy gain of the cluster scales with p as $\Delta E \propto p^{-4}$ (Chapter 6), making these distant encounters unimportant contributers to the disruption of clusters. This holds even when taking into account that there are far more distant encounters, since the number of encounters as a function of distance scales as $n(p) \propto p^2$. This results in an overall energy gain for clusters in a spatially homogeneous distribution of GMCs that scales as $\Delta E \propto p^{-2}$. Based on the simulations we introduce a description for the energy gain that is accurate for all encounters distances and takes into account extended GMCs.

The energy gain is compared to the mass loss of the cluster, which is a result

from the simulations, and we find that the fractional mass loss is about 25% of the fractional energy. This makes previous estimates, which estimate the time to bring the cluster energy to zero, a factor of four too short. We use the results of the simulations to estimate the disruption time of clusters. The $t_{\rm dis}$ due to GMC encounters scales linearly with the cluster density ($\rho_{\rm cl}$). Because of the observed very shallow relation between the radius and mass of clusters, $r_{\rm h} \propto {M_{\rm c}}^{\sim 0.1}$, the disruption time depends on the cluster mass as $t_{\rm dis} \propto {M_{\rm c}}^{\sim 0.7}$. The index is similar to the value of $\gamma \simeq 0.6$ derived from observations (Chapters 4, 5 & 9). This implies that GMCs can significantly shorten the life-time of clusters and preserve the value of γ. Based on the GMC density in the centre of M51, we estimate that there $t_4 \simeq 140\,{\rm Myr}$, which is very similar to the value of $t_4 \simeq 100 - 200\,{\rm Myr}$ derived from observations in Chapter 3.

In **Chapter 9** we predict the life-time of clusters in the solar neighbourhood. The cluster mass loss due to stellar evolution, the galactic tidal field (Chapter 5), the spiral arms (Chapter 7) and the GMCs (Chapter 8) are combined and used to predict a disruption time of $t_4 = 1.7 \times (M_{\rm c}/10^4\,M_{\odot})^{0.67}\,{\rm Gyr}$, close to the empirically derived value of $t_4 = 1.3 \times (M_{\rm c}/10^4\,M_{\odot})^{0.62}\,{\rm Gyr}$ (Lamers et al. 2005a). We predict the age distribution of open clusters, assuming a constant rate of formation during the last few Gyrs and find very good agreement with the observed one. Based on this disruption time and its dependence on cluster mass, we derive a formation rate of clusters in the solar neighbourhood of $3.5 \times 10^{-10}\,M_{\odot}{\rm yr}^{-1}{\rm pc}^{-2}$. This is a factor of 2 or 3 smaller than the star formation rate in the solar neighbourhood, based on studies of the embedded star clusters (Lada & Lada 2003), implying an infant mortality rate of 50-67% in the solar neighbourhood.

1.3.3. Part III: A maximum to the masses of star clusters

In this part we focus on the high mass end of the CIMF, in particular the maximum mass of star clusters.

In **Chapter 10** we introduce a method to reproduce the cluster luminosity function (CLF), based on an adopted CIMF, a cluster formation history and adopted disruption time. A similar model was used in Chapter 4 to reproduce the age and mass distribution of clusters in M51. The CLF is often related or even directly compared to the CIMF. The CLF, however, is a combination of CIMFs of different ages, in which the oldest are more evolved (disruption) and faded due to stellar evolution. It is, therefore, not trivial to derive the CIMF from the CLF. However, assuming that the high mass end of the CIMF is not affected by disruption too much, since $t_{\rm dis} \propto {M_{\rm c}}^{0.6}$, we can study the CLF of this part by modelling a multi-age population and taking into account the fading of clusters based on SSP models.

In this chapter we were interested in the high mass tail of the CIMF. More precisely, we want to know if the CIMF is truncated at some physical maximum mass, or is determined by size-of-sample effects (§ 1.2.3). If the latter is the case, then for all ages the CIMF would be power-law, and if we fade clusters according to their age, the CLF would still be a power-law. However, when the CIMF is truncated at some maximum mass ($M_{\rm max}$), and is sampled up to this maximum mass, then the CLF

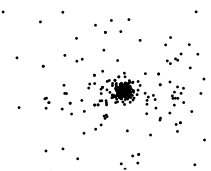

would be steeper on the bright side. This is because clusters with $M_{\rm max}$ have different luminosities for different ages. In fact, based on the SSP models, we can predict the slope on the bright side in different filters based on the fading of clusters taken from SSP models. We found tentative evidence for a steepening of the bright side of the CLF in M51 and NGC 6946, two spiral galaxies with a high cluster formation rate. Comparing the models with the observed CLFs, we derive a value for $M_{\rm max}$ in these galaxies of $M_{\rm max} \simeq 5 \times 10^5\,M_\odot$. If there was no physical upper limit, we predict that, based on a mass function index -2 and on the observed number of clusters above the detection limit, many clusters more massive than $5 \times 10^5\,M_\odot$ are expected, but not observed.

In **Chapter 11** we use *HST/ACS* data of M51, taken as part of the Hubble Heritage project, covering the entire disc of M51 with six pointings (Fig. 1.3). We exploited the superb resolution of the *ACS* camera (1 pixel=0.05"), to fit cluster light profiles to all sources ($\sim 75\,000$) that were found in the three different filters. If sources were fit with radii larger than the limiting spatial resolution, we assumed they were star clusters in M51. The advantage of this method is that we do not have to rely on a fit of SSP models to the broad band colours, as we did in Chapter 3. The CLF of these ~ 6000 clusters show a very clear double power-law distribution, confirming the theory introduced in Chapter 10. The CLF of M51 looks very similar to the CLF that was observed for clusters in the "Antennae" galaxies (Whitmore et al. 1999b), though the break point between the two power-laws occurs 1.6 mag brighter in the "Antennae". This implies that the maximum mass in the "Antennae" galaxies is a factor of four higher ($M_{\rm max} \simeq 2 \times 10^6\,M_\odot$) than in M51 ($M_{\rm max} \simeq 5 \times 10^5\,M_\odot$).

Part I

Observations of the formation and disruption of clusters

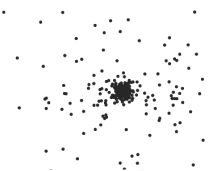

CHAPTER 2

Hierarchical star formation in M51: Star/cluster complexes

N. Bastian, M. Gieles, Yu. Efremov and H.J.G.L.M. Lamers

Astronomy and Astrophysics, v.443, p.79–90 (2005)

Abstract We report on a study of young star cluster complexes in the spiral galaxy M51. Recent studies have confirmed that star clusters do not form in isolation, but instead tend to form in larger groupings or complexes. We use *HST* broad and narrow band images (from both *WFPC2* and *ACS*), along with *BIMA*-CO observations to study the properties and investigate the origin of these complexes. We find that the complexes are all young ($<$ 10 Myr), have sizes between $\sim$85 and $\sim$240 pc, and have masses between 3-30 $\times 10^4 M_\odot$. Unlike that found for isolated young star clusters, we find a strong correlation between the complex mass and radius, namely $M \propto R^{2.33\pm0.19}$. This is similar to that found for giant molecular clouds (GMCs). By comparing the mass-radius relation of GMCs in M51 to that of the complexes we can estimate the star formation efficiency within the complexes, although this value is heavily dependent on the assumed CO-to-H_2 conversion factor. The complexes studied here have the same surface density distribution as individual young star clusters and GMCs. If star formation within the complexes is proportional to the gas density at that point, then the shared mass-radius relation of GMCs and complexes is a natural consequence of their shared density profiles. We briefly discuss possibilities for the lack of a mass-radius relation for young star clusters. We note that many of the complexes show evidence of merging of star clusters in their centres, suggesting that larger star clusters can be produced through the build up of smaller clusters.

2.1. Introduction

Recent studies of star cluster populations have shown that young star clusters do not form in isolation, but tend to be clustered themselves (Zhang et al. 2001; Larsen 2004). Despite the relatively large amount of attention that young star clusters have received in recent years, these complexes have been largely ignored, leaving many of their basic properties unknown. What triggers the formation of these complexes? What are their masses and sizes? Do their properties resemble those of giant molecular clouds (GMCs) from which they are formed or are they more akin to single young massive star clusters? It is this last question that may shed light on their formation mechanism.

Star/cluster complexes are the largest and oldest objects in the hierarchy of embedded groupings, which starts with multiple stars and finishes on galactic scales. The younger and smaller complexes are always within the older and the larger ones. This hierarchy is similar to the fractal distribution observed in the interstellar gas and in fact is the result of the latter (Elmegreen & Efremov 1997; Efremov & Elmegreen 1998)

Large star forming complexes associated with the spiral arms of disc galaxies are well known. Analytic considerations by Elmegreen (1994) showed that strong spiral arms will trigger GMC formation within them, which in turn may lead to the formation of star/cluster complexes. The range in age of objects within these star/cluster complexes is usually quite small (< 20 Myr) suggesting a coherent formation mechanism, which separates them from other large star forming regions within disc galaxies (such as the local Gould Belt in the Galaxy) which have a much larger intrinsic spread in age within them (Efremov 1995). Elmegreen & Elmegreen (1983) that complexes associated with spiral arms form from large HI/CO clouds due to gravitational instabilities along the spiral arm. If the complexes formed directly from large gas clouds we may expect them to retain some of the properties of their progenitor clouds. Additionally, the high pressures associated with spiral arms are conducive to the formation of massive star clusters instead of loose associations (Elson et al. 1987). Thus we may expect complexes associated with spiral arms to contain a rich population of compact stellar clusters.

Galactic giant molecular clouds (GMCs) have a clear relation between their mass and radius, namely $M_{\rm GMC} \propto {R_{\rm GMC}}^2$ (Solomon et al. 1987). This relation holds down to the scale of cloud clumps, which are only a few parsecs in radius (Williams et al. 1995). Young massive star clusters (YMCs), on the other hand, show a weak relation between cluster mass and radius, namely $M_{\rm YMC} \propto {R_{\rm YMC}}^{0.1}$, with a large scatter (Zepf et al. 1999; Larsen 2004; Bastian et al. 2005b) [1]. Assuming that virialised GMCs are the progenitors of young massive clusters, this result is quite surprising because it implies that this imprint from the parent GMC (i.e. the mass-radius relation) must be erased on timescales similar to the formation timescale of the clusters. Thus, a mechanism which destroys any initial mass-radius relation must be a key ingredient

[1] The data of Bastian et al. (2005b), of young star clusters in M51, are consistent with no relation between the mass and radius.

in star cluster formation models (Ashman & Zepf 2001). In this paper, we look at one scale larger than the individual star clusters, namely that of clusters of clusters, or cluster complexes.

An important question about these complexes concerns their future evolution. N-body simulations (Kroupa 1998) have shown that in complexes of high cluster densities, significant merging of clusters is likely. This may provide a mechanism for the formation of extremely massive clusters (Fellhauer & Kroupa 2002, 2005). On the other hand, Bastian et al. (2006) have shown that gas is being expelled from complexes in the Antennae galaxies ($\sim 10 - 40$ km/s). This will result in a rapid decrease in binding energy of the systems, and will tend to destroy the complexes. We will address this point by studying the properties of clusters within the complexes.

This paper is organised in the following way. In § 2.2 we present both the optical and CO observations and introduce the complexes in M51. § 2.3 is dedicated to the derivation of the properties of each complex (e.g. their size, age, mass and star formation rates), as well as an analysis of the cluster population within each complex. In § 2.4 we discuss the formation and evolution of the cluster complexes in light of their relation to young massive clusters and giant molecular clouds. Finally, in § 2.5 we discuss the complexes in terms of the general hierarchy of star formation within galaxies and in § 2.6 we summarize the main results.

2.2. Observations

2.2.1. *HST/WFPC2* and *ACS* observations

The observations used in this study were taken from the *HST* archive, and are presented in detail in Bastian et al. (2005b). The data set consists of two pointings, shown in Fig. 1 in Bastian et al. (2005b), each consisting of broadband F439W ($\approx$ B), F555W ($\approx$ V), F675W ($\approx$ R), F814W ($\approx$ I), and F656N (Hα) filters. In addition, Field 2 also has F336W ($\approx$ U) filter observations, which are crucial for age dating young star clusters. Thus, we will concentrate the detailed analysis on those complexes which have F336W observations, while using the others to corroborate the results.

We have also used the *Hubble Heritage ACS* images which cover the entire optical galaxy in F435W (B), F555W (V), F658N (Hα), and F814W (I) filters. For a full review of the exposure and reduction information, see Mutchler et al. (2005). Due to the large coverage and high spatial resolution, this data will mainly be exploited to obtain size estimates of the individual sources within the complexes.

The complexes were found using flux contour cuts on the F439W, F555W and F675W images. In the regions away from the centre of the galaxy, this resulted in a fairly unambiguous selection. Complexes in the inner spiral regions were discarded from our sample, as background variations made the identification of the complexes non-trivial. The one exception to this is a large complex in the north-eastern section of the inner spiral arms, as this complex was noted in the study of Scoville et al. (2001). These authors also noted the existence of Complex G2 in their study. The complexes are identified in Fig. 2.1. The numbering system (1 or 2) corresponds to

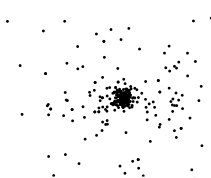

the two different spiral arms. Complexes with F336W observations are B1, C2, D2, E2, F2, and G2.

The magnitude of each complex was measured with a circular aperture with a size set equal to that of the complex (see § 2.3.1). The background was determined and subtracted using a ring with inner radius 6 pixels more than the radius of the complex, and with a width of 10 pixels. The magnitudes of the individual sources within the complexes were measured using the PSF fitting package `HSTphot` (Dolphin 2000). This is different from the technique used in Bastian et al. (2005b), who used aperture photometry. The change is due to the increased crowding within the complexes relative to the field.

The positions of the complexes are shown in Fig. 2.1, while Figs. 2.2 & 2.3 show enlarged images of the complexes without and with F336W($\sim U$)-band data respectively. Additionally, we show an *HST/ACS* colour composite image of the largest complex in our sample (Complex G2) along with an image of the complex containing the largest super-star cluster (Complex A1) in Fig. 2.4.

Throughout this paper, we assume the same distance to M51 as was used in Bastian et al. (2005b), namely 8.4 Mpc.

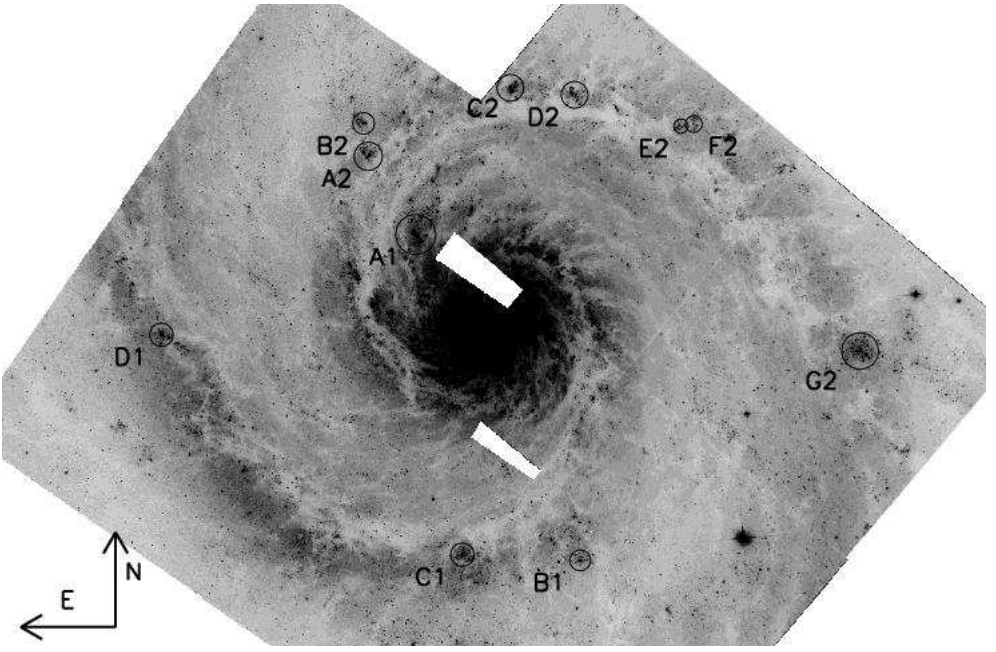

Figure 2.1: Positions of the cluster complexes overlayed on the F555W (V) band image. The complexes are identified with circles representing their measured radii as determined in § 2.3.1. The image is 260 × 170 arc-seconds^2

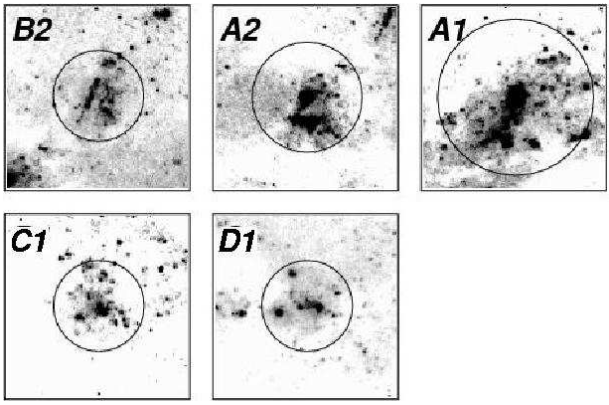

Figure 2.2: F555W images of the complexes without F336W data. The images are 120 × 120 pixels^2 (12 by 12 arc-seconds) which corresponds to $\sim 550 \times 550$pc^2. The circles on the images correspond to the radius derived for each complex.

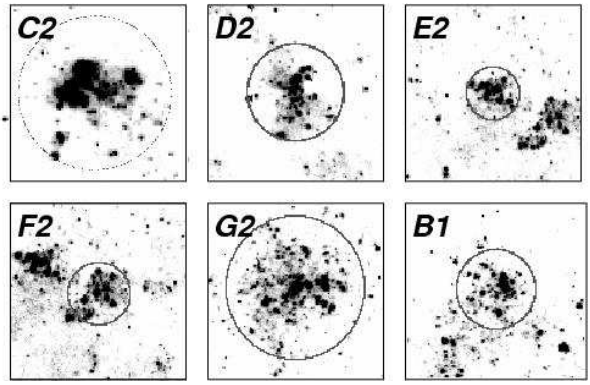

Figure 2.3: F555W images of complexes with F336W data. The image of Complex C2 is 70 × 70 pixels^2 which is approximately 300 by 300 pc^2. The rest of the images are 120 × 120 pixels^2 (12 by 12 arc-seconds) which corresponds to $\sim 550 \times 550$pc^2. The circles on the images correspond to the radius derived for each complex.

2.2.2. *BIMA CO* observations

We obtained CO (J=1-0) observations of M51 from the *BIMA SONG* (Survey of Nearby Galaxies) survey[2]. The data are presented in detail in Helfer et al. (2003). As described in Henry et al. (2003), we used an image of M51 which was obtained by

[2]The data were taken from the *NASA Extra-galactic Database*, which can be found at http://nedwww.ipac.caltech.edu/

Figure 2.4: Composite *HST/ACS* images of complex G2 (top) and A1 (bottom). The top panel is $\sim$ 475 pc on a side, while the bottom panel is $\sim$ 800 pc on a side. The circles in the bottom panel outline the outer and inner dust arcs, and shows that neither of them are centred on the young central star cluster (the centre of the arcs is marked by a cross).

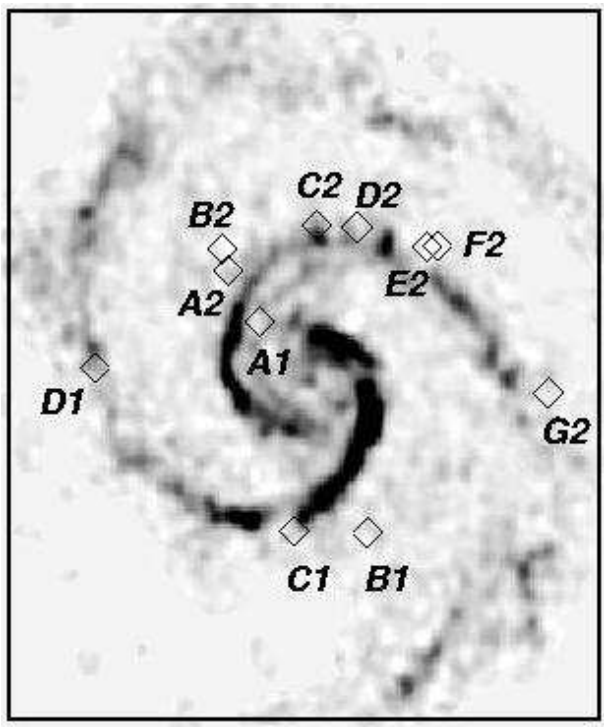

Figure 2.5: *BIMA* CO intensity map, dark indicates regions of high intensity. North is up, and east is to the left. The positions of the cluster complexes are shown as diamonds. Note that most of the complexes fall on the outer edges of the spiral arm pattern. The lack of spatial correspondence between the complexes and high CO intensity regions indicates that the complexes have already destroyed their parent GMCs.

integrating the intensity over all velocity channels. The details of the observations and reduction of the data are given in detail in the preceding references, and thus will not be repeated here. The CO data were converted to physical units, namely solar masses per square parsec, using the same procedure as Henry et al. (2003) who adopted a CO-to-H_2 conversion factor (from antenna temperature to mass) of $2 \cdot 10^{20}$ H_2 cm^{-2} (K km s^{-1})$^{-1}$ (Strong & Mattox 1996). Cloud sizes were determined by measuring the major and minor axes of each cloud and calculating the average. Fig. 2.5 shows the positions of the cluster complexes on top of the *BIMA* intensity map.

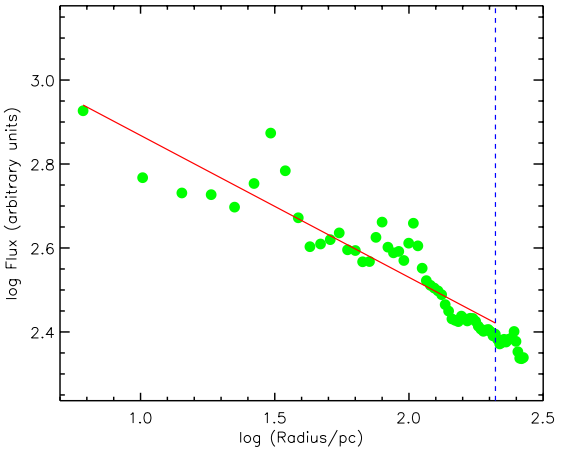

Figure 2.6: The flux in concentric circles of Complex G2. The solid red line represents a profile where flux $\propto r^{0.34}$, while the vertical dashed line marks the adopted size of the complex. The two bumps in the profile are bright sources within the complex. All complexes studied here have similar power-law flux profiles (see text).

2.3. Properties of the complexes

2.3.1. Sizes of the complexes

The size of the complexes were measured on the *HST/WFPC2* images and determined through the method used for star clusters, defined by Maíz-Apellániz (2001). The method defines the edge of the complex at the point where the colour, as a function of radius, becomes constant. To determine this point, we assumed that the complexes are circular, and measured the surface brightness in concentric rings. This provides us with surface brightness and colour profiles for each complex. An example of the flux distribution of one complex, Complex G2, is shown in Fig. 2.6. The vertical dashed line in the panel shows the radius adopted for this complex. The sizes of the complexes with U-band data (F336W) are shown in Table 2.1.

It is important to note however, that the individual sources within a complex do not show any colour dependence on their position. The trend seen in Fig. 2.6 is based on the *integrated* light within each radius, which includes the background. As one looks along the radius away from the centre, the background light begins to dominate until the measured colour is equal to that of the background, which we take as the radius of the complex.

Table 2.1: Properties of the complexes in M51 with F336W and Hα imaging.

ID	M_V [a] (mag)	$M_{V,\mathrm{cluster}}$ [b] (mag)	Mass[c] ($10^5 M_\odot$)	Radius (pc)	Tidal Radius (pc)	SFR/area ($M_\odot$ yr^{-1} kpc^{-2})
C2	-12.6	-10.2	1.4	160	37	2.59
D2	-12.4	-9.8[d]	1.1	160	35	0.07
E2	-11.2	-9.0	0.4	85	27	0.06
F2	-11.1	-9.0	0.3	100	26	0.06
G2	-13.3	-10.1	2.6	220	62	0.07
B1	-12.0	-10.4	0.7	125	36	0.06

[a] The magnitude of the complex within the defined radius. Uncorrected for extinction.
[b] The magnitude of the brightest source within each complex. Uncorrected for extinction.
[c] Total mass of the complex assuming an age of 7 Myr.
[d] Not shown in Fig. 2.9 because it appears to be a blend of sources, hence the colours are highly uncertain.

2.3.2. Intensity profile of the complexes

In Fig. 2.6 we show the flux in concentric circles in complex G2. We have overplotted (solid line) a function of the form, Flux $\propto r^{-0.34}$. A power-law of this form follows the data quite well (the two peaks at log radius of 1.5 and 2.0 in this distribution are due to two clusters). This corresponds to the projected density profile of a clump with $\rho(r) \propto r^{-\alpha}$, where α is 1.34 and ρ is in units of $M_\odot$ pc^{-3}. The flux profiles of the other complexes in our sample are also well fit by power-laws of this form, with the average index, $<\alpha> = 1.74 \pm 0.34$. We will discuss the physical implications of this in § 2.4.1.

2.3.3. Ages of the complexes

Ages determined by Hα measurements

The presence of Hα emission within the complexes indicate that they are quite young, and as such suffer from the degeneracy between age and extinction (e.g. Bastian et al. 2006). We therefore first determine the ages of the complexes (with F336W data) using the Hα emission line width, which is independent of extinction.

To estimate the equivalent widths of Hα we use the F656N narrow band filter. The F675W filter was used to estimate the continuum contribution. Photometry was performed using apertures set to be as large as the estimated radius of each the complex. The monochromatic flux in the F656N and F675W band can then be found as follows: $F_\lambda = SUM_\lambda * PHOTFLAM_\lambda / EXPTIME_\lambda$, where λ refers to the central wavelength of the filter, SUM_λ is the sum of the counts within the aperture (i.e. without background subtraction) and $PHOTFLAM_\lambda$ and $EXPTIME_\lambda$ were taken from the image headers.

The equivalent width of Hα can now be found by

$$EW(H\alpha) = 28.33 * \frac{F_{H\alpha} - F_R}{F_R} \tag{2.1}$$

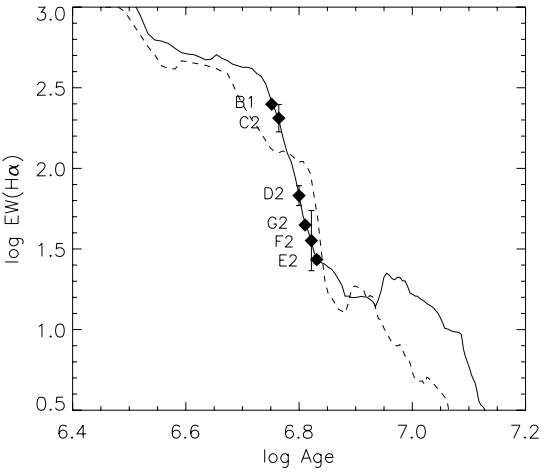

Figure 2.7: Determining the ages of the complexes from the observed equivalent width of Hα (EW(Hα)) combined with the Starburst99 models (Salpeter IMF). The solid line is for solar metallicity while the dashed line is for twice solar metallicity. The EW of each complex was put on the line, and the corresponding age is read off. The errors were calculated by varying the apertures used for the photometry by 5 pixels (plus and minus) around the measured radius. Note that the derived ages are largely independent of the assumed metallicity.

where 28.33 is the rectangular width of the Hα filter in Å.

The errors in EW(Hα) were estimated by calculating the EW values with apertures of plus and minus 5 pixels, which is approximately the uncertainty in the radius estimates.

We can then compare the derived EW for each complex, with *Starburst99* simple stellar population (SSP) models for solar metallicity and Salpeter IMF Leitherer et al. (1999), in order to derive the age of each complex. The results are shown in Fig. 2.7. We note that the assumed metallicity ($Z_\odot$ or $2Z_\odot$) does not significantly affect the derived ages. We see that the complexes are indeed very young, with ages between 5 and 8 Myr. In § 2.3.3 we will show that the measured cluster colours are well matched by cluster models of solar and twice solar metallicity.

This method assumes that each complex formed in an instantaneous burst, hence it puts a lower limit on the age of the complexes, as any additional formation of massive stars will tend to increase the equivalent width of Hα. This means that a combination of an older burst plus new star formation can mimic the observed strength of the equivalent width.

Along similar lines, we can also look for the presence of young O and B stars at the location of the complexes. For this we compare the location of the complexes (found in the optical) to far-*UV* images taken by the *GALEX* observatory. Fig. 2.8 shows the

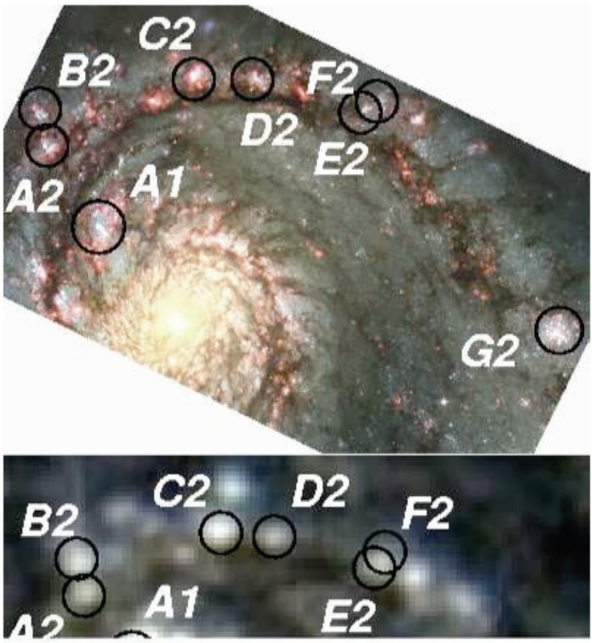

Figure 2.8: **Top:** *Hubble Heritage* image of the north western inner spiral arm of M51. **Bottom:** *GALEX* composite far-*UV* (blue) and near-*UV* (red) image of the same region. Bright regions indicate strong *UV* flux, indicating the presence of hot O and B stars. Note the semi-regular spacing of the complexes along the spiral arm in both images. North is up and east is to the left in this image.

composite *HST Heritage* image (top) as well as the composite far-*UV* (1530Å, blue) and near-*UV* (2310Å, red) *GALEX* image (bottom, taken from Bianchi et al. (2005) of the north western inner spiral arm. We find strong far-*UV* flux at the location of most of the complexes which is a further indication of the presence of young stars within the complexes. Also note the semi-regular spacing of star-forming regions along the spiral arm, the so-called "beads on a string" morphology. It appears that the largest isolated star-forming regions are outside the *HST* field of view, being located in the south-west and north-east of the galaxy. These complexes will be the subject of a future study which will exploit the full coverage of M51 with the *HST/ACS* mosaic.

A comparison of Fig. 2.5 and Fig 2.8 reveals the different stages of evolution of gas/star complexes in the NW arm, from A2 to G2. The HII complexes to the south-east of Complex C2 are seen in the *UV* but are not present in the CO data. Contrarily, the H II complex to the west of complex D2 is unseen in the *UV* but is bright in CO. Presumably, we are witnessing complexes in different stages of their evolution from CO complexes, to large H II regions, and finally to star/cluster complexes.

Finally, we note that complex G2 is located at a break of a strong CO/dust lane

and at the beginning of a large spur. Both of these observations may be hints into its formation. The position of G2 near the outer edge of the stellar arm might be explained by its age; however, we do not find any strong correlation between the distance from the arm edge and the age for the other complexes.

Ages from the individual clusters

We can also determine the ages of the complexes by looking at the ages of the individual star clusters within the complexes. Fig. 2.9 shows (F336W - F439W) *vs.* (F555W - F814W) for the sources within the six complexes for which we have F336W observations, which are essential for the age dating of young star clusters (e.g. Anders et al. 2004). We also show the solar (dashed-dotted line) and twice solar metallicity (solid line) `GALEV` SSP model tracks for a Salpeter IMF. The filled data points are clusters with $M_{\rm F555W} < -8.6$, which are highly likely to be star clusters. The open points are the fainter sources within each complex, which may be faint clusters or individual bright stars. Assuming, for the moment, that the sources within the complex are star clusters, we see that the majority of the clusters have ages of $\sim 4 - 10$ Myr. The exact age is difficult to determine due to age, extinction, and metallicity degeneracies for young clusters (e.g. Bastian et al. 2006). However, we conclude that the ages derived from the Hα equivalent widths of the complexes are consistent with the ages derived from the colours of the individual clusters.

In Fig. 2.9 we see that complexes C2, D2, and B1 have a relatively small amount of scatter of their points around the extinction vector, implying similar ages between all the clusters. The other complexes (E2, F2, and G2), however, contain some sources that appear much older (> 100 Myr) in the colour-colour diagram. These sources may in fact be young clusters which are heavily extincted or individual massive stars. In particular the sources in G2, show a significant amount of scatter perpendicular to the extinction vector. Taken at face value this suggests that this complex has been forming clusters for at least the last ~ 100 Myr.

Some of the sources which appear quite old in complexes E2, F2, and G2, however, may be individual bright stars. In order to test this, in Fig. 2.10 we plot the absolute magnitude of each source within complex G2 (uncorrected for extinction) *vs.* the colour (F555W - F814W, roughly V-I). The solid lines are `GALEV` SSP model tracks for a $500 M_\odot$ (lower) and $10^4 M_\odot$ (upper) cluster. The dashed lines are stellar isochrones (with solar metallicity) of 3, 5, and 10 Myr (from left to right respectively, Lejeune & Schaerer (2001). Open triangles show sources which appear extended, filled stars are sources which are not resolved (≤ 1 pc), open circles denote sources with strong Hα associated with them, and filled points are sources with no size information (either because of possible crowding or low signal-to-noise). We see that many of the objects in complex G2 are consistent with both the stellar isochrones and the cluster model tracks. We note however that there is a significant grouping of sources that would be consistent with star clusters of a few $\times 10^2 M_\odot$ to $\sim 10^4 M_\odot$ and ages between 4 and 10 Myr (between -0.3 and 0.5 in F555W-F814W).

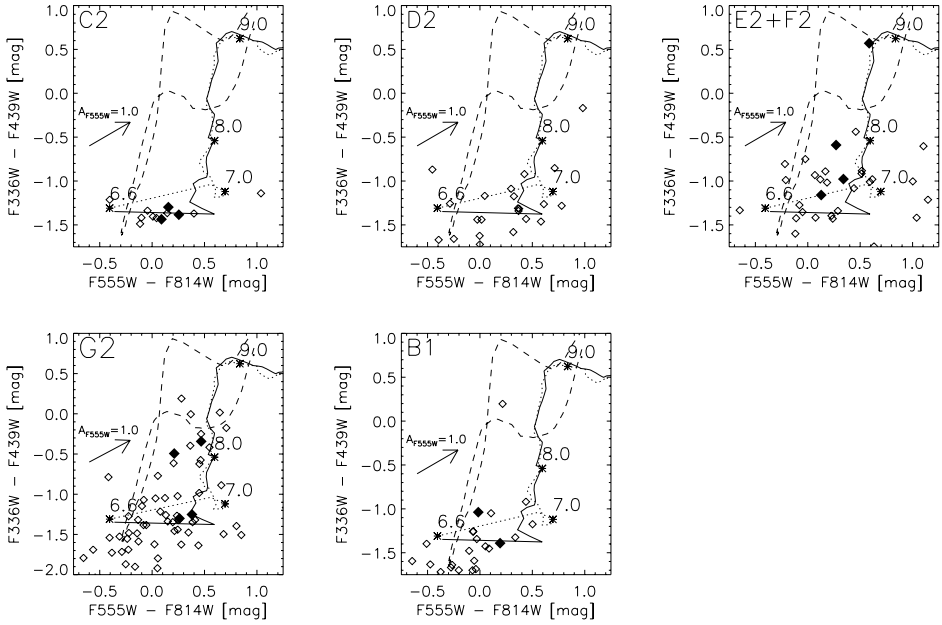

Figure 2.9: Colour-Colour diagrams for sources in the six cluster complexes with F336W observations. The names of the complexes are given in each panel. Filled points are for sources with $M_V < -8.6$ (uncorrected for extinction), while open points are fainter than this (somewhat arbitrary) limit. The solid line represents the `GALEV` SSP models for twice solar metallicity while the dotted line represents the same models but for solar metallicity. The asterisks mark age points on the evolutionary curves, labelled as the logarithm of the age in years. The long dashed line is a stellar isochrone for a solar metallicity, 10 Myr old, population (however the isochrone for twice solar metallicity is extremely similar in this region of colour space). The arrow in each panel represents the extinction correction of $A_{\rm F555W}$=1.0.

Stochastic sampling of the underlying stellar IMF can cause significant deviations from standard SSP model colours (e.g. Dolphin & Kennicutt 2002), therefore it is not completely unexpected that sources do not lie directly on the SSP model tracks. We also note that due to the large crowding in these complexes, accurate photometry is difficult and will tend to increase the scatter in diagrams such as Fig. 2.10. Without higher resolution imaging or spectroscopy of individual sources, the degeneracy between stars and star clusters is extremely difficult to break.

Based on the brightness criterion of $M_V < -8.6$, we conclude that there are clusters within the complexes and that their ages are between 4 and ∼10 Myr, although complexes G2, E2, and F2 seem to also contain older clusters.

It is interesting to note the existence of spatially resolved massive star clusters

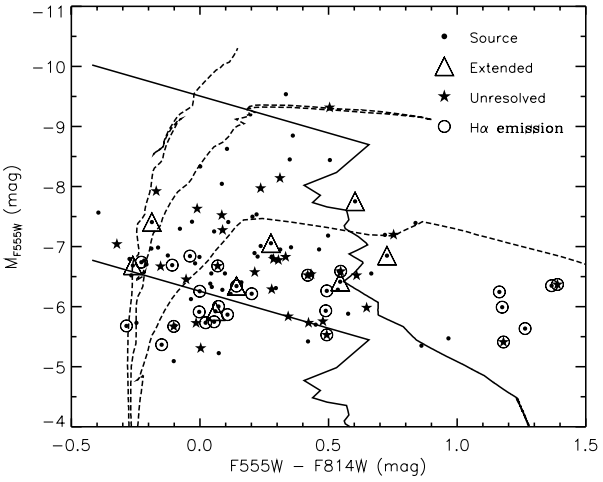

Figure 2.10: Colour-magnitude diagram of the sources within complex G2 (from the *ACS* images). The dotted lines are solar metallicity stellar isochrones for 3, 5, and 10 Myr from left to right (the twice solar metallicity isochrones occupy the same region in this figure). The solid lines are `GALEV` SSP (cluster) model tracks (Salpeter IMF and twice solar metallicity) for a $10^4 M_\odot$ (upper) and $500 M_\odot$ (lower) cluster. The open triangles denote sources which appear extended, the stars are sources which are not resolved ($\leq$ 1 pc), open circles are sources which have strong Hα emission associated with them, and filled dots are detected sources which have no size information (due to possible crowding or low S/N).

within the complexes, the most massive of which is located at the centre of complex A1. Using the available *HST/ACS* images, we find that this cluster has a magnitude of $m(F555W)_{ACS}$=18.3, and a colour m(F435W) - m(F555W) = *0.32*. This, together with the strong Hα emission, is consistent with the cluster being quite young and extincted. Using the same model and distance assumptions used throughout this work, and an assumed age of the cluster of 7 Myr, we find that this cluster has a mass of $\sim 10^5 M_\odot$, which is a lower limit as we have not corrected for extinction. Using the *ISHAPE* routine of Larsen (1999), we find this cluster to be well resolved, although significantly flattened. Using a Moffat profile with index 1.5, we find the FWHM along the major axis of the cluster to be 2.6±0.5 pc, and a major to minor axis ratio of 0.6. In a future work, we will present an in depth analysis of the cluster and stellar populations within each complex. Another interesting feature of this complex, are two dust arcs which appear to have the same centre, which is displaced from the young central massive star cluster (shown in the bottom panel of Fig. 2.4). The origin of these arcs remains unclear.

2.3.4. Masses of cluster complexes

The masses of the complexes were estimated by combining the complex luminosities and the age dependent mass-to-light (M/L) ratios of the `GALEV` SSP models. We assign all complexes the same age, ~ 7 Myr, and interpolate the SSP models between 4 and 8 Myr to determine M/L for this age. We have used the F555W magnitudes to derive the masses of the complexes, but we note that the other broad-band magnitudes give similar results. The masses of these complexes range from $0.3 \cdot 10^5 M_\odot$ (F2) to $3.0 \cdot 10^5 M_\odot$ (G2) and are given in Table 2.1. The errors on the determined masses (as seen in Fig. 2.12) are based on errors in the age estimate, from 4 to 12 Myr.

2.3.5. Star formation rates within the complexes

Using the continuum subtracted Hα images, we can estimate the star formation rates, $\Sigma_{\rm SFR}$, within the complexes. For this, we adopt the conversion factor of Hα luminosity to star formation rate of Kennicutt (1998b), namely

$$\Sigma_{\rm SFR}(M_\odot \ {\rm yr}^{-1}) = 7.9 \cdot 10^{-42} L(H\alpha)({\rm ergs \ s}^{-1}).$$

The values derived are shown in Table 2.1. The star formation rates per unit area of the complexes are comparable to the definition of a starburst galaxy (0.1 $M_\odot$ yr^{-1} kpc^{-2}, (Kennicutt et al. 2005), justifying complex C2 as a *localised starburst* (terminology from Efremov 2004). Other complexes from Table 2.1 have lower SFRs.

Star cluster complexes in the Antennae galaxies have area normalised star formation rates which are approximately 10 times higher than the ones studied here, despite having similar sizes (Bastian et al. 2006). This difference can be understood by comparing the GMCs properties in the two galaxies. The resolved GMCs in the Antennae (Wilson et al. 2003) have roughly 10 times the mass, and hence 10 times the density, as those in M51 for a given spatial size. Therefore, the differences in the SFR/area can be well explained through the Schmidt law (Schmidt 1959) where the rate of star formation is proportional to the gas density to the power N. Kennicutt (1998a) has shown that $N \sim 1.4 \pm 0.15$ for normal disc galaxies.

2.4. Comparison between the properties of cluster complexes and GMCs

2.4.1. The density profiles

In § 2.3.2 we found that the surface brightness of complex G2 is well fit by a power-law of the form Flux $\propto r^{-0.34}$. Assuming sphericity, this corresponds to a three dimensional density profile of $\rho \propto r^{-\alpha}$, with $\alpha = 1.34$. The other complexes were also shown to be well fit with profiles of this type, with $<\alpha> \ = 1.74 \pm 0.34$. This power-law profile is similar to that observed for GMCs ($\alpha = 1 - 2$, Ashman & Zepf 2001)[3] and much shallower than King profiles which fit old globular clusters

[3]Recent studies have shown that Galactic GMCs have $\alpha = 1.7 \pm 0.2$, Joao Alves priv. comm.

quite well. The similarity between the profiles of GMCs and the cluster complexes studied here suggests that the amount of luminous material formed is proportional to the gas density at that point within the GMC. We shall return to this point in § 2.5.1. Throughout the present work we assume that the complexes are spherical, which in the z-axis would make the complexes larger than the thickness of typical galactic discs. This is also true for the GMCs. If both the GMCs and the complexes are truncated in the vertical direction (i.e. flattened) our main conclusions would still remain valid.

2.4.2. Size and radius relation of GMCs and cluster complexes

By combining the study of the cluster complexes and GMCs in M51 we can gain insight into the hierarchical nature of structure formation within spiral galaxies. Solomon et al. (1987) showed that there is a clear relationship between size and mass for GMCs in the Galaxy, namely $M_{\rm Cloud} \propto R^2_{\rm Cloud}$, a consequence of virial equilibrium. This relation has also been found for GMCs outside the Galaxy (see summary in Ashman & Zepf 2001).

However, as shown here, a single massive GMC does not produce a single star cluster, but a complex of star clusters. Therefore it is interesting to see how these complexes fit into the hierarchy of star formation. We begin by searching for a relation between mass and radius for GMCs in M51. Fig. 2.11 shows the radius *vs.* mass for the detected GMCs within M51. The dashed vertical line shows the spatial resolution of the *BIMA* survey. We have fit a function of the form $\log M = \kappa \cdot \log R + c$ (i.e. $M \propto R^{\kappa}$). We find that $\kappa = 2.16 \pm 0.20$. The filled area corresponds to the best fit to the data above the resolution limit including the 1σ error (this area also includes the error on the zero point of the function).

Fig. 2.12 shows the result of the same analysis applied to the cluster complexes. Here we find that $\kappa = 2.33 \pm 0.19$. The filled area with the horizontal hash marks represents the best fit plus the corresponding 1σ errors. The filled area with the vertical hash marks is the fit (plus errors) of the GMCs extrapolated into the size range of the complexes. We see that the relations for the GMCs and the cluster complexes have almost the same slope, but are offset by ~ 0.3 dex in the vertical (mass) direction. This offset is related to the star formation efficiency which will be discussed in § 2.4.3.

We conclude that the cluster complexes follow a similar mass-radius relation as GMCs. On the contrary, young star clusters do not follow this mass-radius relation (e.g. Bastian et al. 2005b). This implies that the mass-radius relation must be broken below the scale of the complexes. If binding energy is the factor that determines the star formation efficiency (assuming that the star formation efficiency causes the lack of a mass-radius relation in young star clusters) then it is not the binding energy of the cloud which is important but the binding energy of the clumps within the cloud which is the dominant factor.

Additionally we note that the mass-radius relation holds for clumps within GMCs, down to the resolution limit (~ 0.5 pc and ~ 13 $M_{\odot}$ in the Rosette molecular cloud

(Williams et al. 1995). This suggests that the mass-radius relation is broken during (or after) the star formation process.

2.4.3. Star formation efficiency within the complexes

We have shown that the GMCs and the star cluster complexes in M51 share a very similar mass *vs.* radius relation. This offers a unique opportunity to investigate the star formation efficiency, $\epsilon = M_{\rm complex}/M_{\rm GMC}$, for each complex. Although we cannot measure the mass of the GMC that formed the present complexes, if we assume that the parent GMCs had the same size as the complexes, we can estimate the progenitor mass. Thus it remains to be shown that the radius of the clouds do not change significantly during the formation of the complexes.

We can estimate the timescale on which the GMCs will shrink by calculating their free fall time. The free fall timescale is $t_{\rm FF} \approx (\rho \cdot {\rm G})^{-\frac{1}{2}}$. Using the relation between the mass and radius of the clouds derived above, we see that the free fall timescale of GMCs, as a whole, is between 80 and 200 Myr. The ages (e.g. the upper limit of the formation timescale) of the complexes are between 5 and 10 Myr, much shorter than the collapse time of the GMCs. This means that the complexes formed from the GMCs on a timescale much shorter than the collapse time of the GMC. Thus the size of the complexes should be about the same as that of the GMC from which they formed.

In Fig. 2.12 we show the mass-radius relation for the complexes (the data points along with the best fitting power-law relation with the associated 1σ errors) and overplot the relation for the GMCs, extrapolated to the size scale of the complexes. The vertical offset between the best fit line of the complexes and the best fit line of the the GMCs is the star formation efficiency, ϵ. In the case of M51, we measure ϵ of the complexes to be 50 ± 20 %. The convergence of the two relations at higher masses suggests that there is a trend for ϵ to increase for larger complexes, but the trend is well within the observational errors.

An additional caveat to this approach is that we have assumed the mean Galactic CO-to-H_2 conversion factor. However, studies of M51 have shown that the conversion factor in M51 is roughly half that of the Galaxy (Boselli et al. 2002). Using this value would make GMCs half as massive as that estimated here, and therefore the star formation efficiency would be close to 100%. A final caveat to this estimate is the assumed stellar initial mass function for the complexes. We have assumed a Salpeter IMF from 0.1 to 50 $M_\odot$, however if we would assume a Kroupa-type stellar IMF, the masses of the complexes would be lowered by a factor of ~ 2, giving $\epsilon \simeq 25\%$. Therefore we are left to conclude that while this method to estimate the star formation efficiency is intriguing, it is limited at the present time by the assumptions that are required.

However, it should be noted that the assumed CO-to-H_2 factor will not effect the index of the mass-radius relation of the GMCs presented here. The GMCs in M51 used in this study are all located within the inner 5 kpc of the galaxy, and therefore we

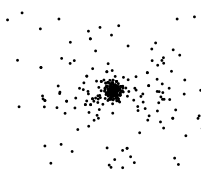

do not expect much cloud to cloud variation in the conversion factor, as the metallicity is not expected to change significantly over this area.

2.5. Discussion

2.5.1. Formation of the complexes

We can compare the properties of the complexes in M51 with those of complexes and young/old star clusters in the Antennae galaxies which have been measured by Whitmore et al. (1999b). Knot S[4] in the Antennae galaxies has an extremely similar power-law profile (Flux $\propto r^{-1/2}$) over $\sim$ 300 pc from the centre as complex G2. Additionally, the very young ($<$ 10 Myr) massive star cluster #430 in the Antennae follows the same power-law density distribution. However, the older cluster #225 ($\sim$ 500 Myr old) does not follow a clear power-law relation but instead has a sharp cut-off at $\sim$ 50 pc. Presumably cluster #225 was formed with a power-law density profile which has been eroded due to dynamical evolution. Additional support for this scenario comes from star clusters in the LMC, where young star clusters show a power-law density profile (with no distinct cut-off radius)(Elson et al. 1987) while older clusters have King-type profiles with a distinct tidal truncation.

The similarity between the profiles of GMCs and the complexes studied here suggests that the amount of luminous material formed at a certain radius within a GMCs is proportional to the density of the cloud at that radius. This naturally explains why the complexes share the same mass-radius relation as GMCs (see § 2.4.2), as any relation inherent to the progenitor cloud will be imprinted onto the complexes as they form. Additionally, the similarity between the projected profiles of the complexes, and young clusters implies a common formation mechanism (i.e. star formation proportional to the gas density).

However, young cluster systems, such as those of NGC 3256 (Zepf et al. 1999), M51 Bastian et al. (2005b), and various spiral galaxies (Larsen 2004) have a weak relation between their mass and radius (with a large scatter). The similarity between the density profiles of the complexes and young star clusters makes the lack of a mass-radius relation in star clusters all the more surprising. This is because we would also expect them to bear the imprint from the cloud of which they formed.

Ashman & Zepf (2001) have suggested that a star formation efficiency which depends on the binding energy (predicted by Elmegreen & Efremov 1997) of the progenitor GMC could destroy such a relation during the formation of young clusters. But this theory does not explain the shallower size distribution of star clusters relative to GMCs.

Another possible explanation for this lack of a mass-radius relation in young clusters is that dynamical encounters between young clusters (and gas clouds) add energy into the forming clusters, thereby increasing their radii. Some support for this sce-

[4]The large amount of substructure within this knot, particularly in the F555W ($\approx$V) and Hα bands, suggests that this knot is a cluster complex, and not just a single large star cluster.

nario is given by differences in the size distributions of clusters and GMCs. GMCs (e.g. Elmegreen & Falgarone 1996) and cloud clumps (e.g. Williams et al. 1995) follow the size distributions of $N(r)\mathrm{d} \propto r^{-\eta}\mathrm{d}$ where $\eta \approx 3.2$. Star clusters (both young and old), however, follow a shallower relation, namely a power-law with $\eta \approx 2.2$ (Bastian et al. 2005b). If the proto-clusters follow the same mass-radius relation as GMCs and clumps, then their density will be $\rho \propto M/R^3 \propto R^{-1}$, showing that the larger proto-clusters are less dense. Due to their lower density, we expect larger proto-clusters to be more affected by encounters, i.e. making large clusters even larger. This would tend to make the size distribution shallower, as observed.

2.5.2. Truncation of the size of the complexes

The complexes most closely associated with spiral arms (e.g. excluding complexes C1 and G2) have diameters similar to the minor axes of GMCs within the arms. We have shown that the size of a complex does not change significantly from the progenitor GMC. This suggests that the maximum size (and hence mass due to the mass-radius relation) of the complexes is determined by the size of the GMCs within the galaxy. Due to sheer effects, caused by the flat rotation curve of the disc, GMCs have a maximum size (hence mass). This in turn will determine the maximum sized complex which can form. If the star clusters within the complex are formed with an initial mass function, then the most massive cluster formed will be dependent on the size of the parent complex. There does seem to be a relation between the most massive GMC and the most massive star cluster within a galaxy (e.g. Wilson et al. 2003).

However, there are two exceptions where the size of a complex is larger than the typical semi-minor axis of a GMC. These two complexes (A1 and G2) do not seem to be directly related with a spiral arm, in fact A1 is on the inside of the spiral arm. G2 is located at the starting point of a large spur, which is a sign of instabilities in the arm. Instabilities, such as large spurs, may allow larger GMCs to exist for short periods, and hence explain the existence of these larger than expected complexes.

2.5.3. The evolution of the cluster complexes

As shown in § 3.2, the complexes studied here are all quite young. However, if the complexes are a long lived phenomenon, then we would expect to see complexes throughout the disc and not just associated with the spiral arms. Elmegreen (1994) predicted that the remnants left over from 'superclouds' within the spiral arms, (i.e. what we call complexes) should be observable as loosely bound stellar complexes in the inter-arm region of the galaxy. Do such inter-arm complexes exist? The present data set is not adequate to conclusively answer this question. As shown in Bastian et al. (2005b) the detection limit imposed by the data severely limits which clusters (e.g. how bright and hence how massive) we can observe. At an age of ~ 100 Myr, we can only detect clusters (with no extinction) which have masses above $10^4 M_\odot$. Therefore, we would miss smaller clusters belonging to the same complex, if they

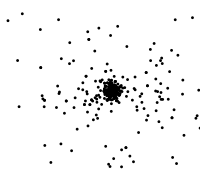

exist. We have found 3 candidate complexes with ages between 40 and 80 Myr as determined by the colours of the detected clusters. Deeper images are necessary to resolve this question.

In order to estimate whether or not the complexes studied here are gravitationally stable, we can compare their present radii with their estimated tidal radii. In a rotating disc, this can be estimated by

$$r_t = \left(\frac{G M_{\rm complex}}{2\,V_{\rm G}^2} \right)^{1/3} R_{\rm G}^{2/3}$$

where $M_{\rm complex}$, V_G, and R_G are the mass of the complex, the circular velocity of the galaxy at that point, and the distance to the galactic centre. If we assume a disc rotation velocity of 200 km/s (e.g. Rand 1993 for galactocentric distances greater than 1 kpc) and distances to the galactic centre between 2 and 4 kpc, then we see that complexes with masses between $10^4 M_\odot$ and $10^{5.5} M_\odot$ have tidal radii of 50 to 100 pc. In Table 2.1 we compare the measured sizes of the complexes with their derived tidal radii. We see that the tidal radii are much smaller than the measured radii, indicating that the outer material of the complexes are not bound to the complex. Because of the steep density profile of the complexes (see Fig. 2.6) the inner region may be bound and survive for extended periods. If this is the case, then the inner clusters are expected to merge within a few $\times 10^7$ years (e.g. Kroupa 1998; Fellhauer & Kroupa 2002), forming a single massive star cluster like object.

Elmegreen et al. (2000) and Larsen (2002) have speculated that the most massive cluster within the giant stellar complex in NGC 6946 may have formed by the merging of other members of the complex. This cluster is located in the centre of the complex and its measured age (through photometry and spectroscopy) appears to be the average of the surrounding clusters, which is exactly as the merger theory predicts. We note that the centres of many of the complexes presented here, show the presence of massive and elongated objects, in particular complexes A1, E2, F2, and G2. We take the presence of such objects as evidence for merging in the centre of the complexes. Higher resolution imaging should offer more definitive evidence of on-going merging in the centres of these complexes.

2.6. Summary and conclusions

1. **Cluster complexes in M51:** From archival *HST* imaging we identified 9 cluster complexes in the inner $\sim$ 5 kpc of M51. We derived their ages by comparing their equivalent widths of Hα to that of *Starburst99* SSP models. We checked the validity of these age measurements by comparing the colours of the star clusters within each complex to the `GALEV` SSP models. We find reasonable agreement between the two methods.

2. **GMCs in M51:** We have also measured the sizes and masses of a sample of giant molecular clouds in M51 from existing CO data. This was done in order to enable a comparison between the complexes and the gas content of the galaxy.

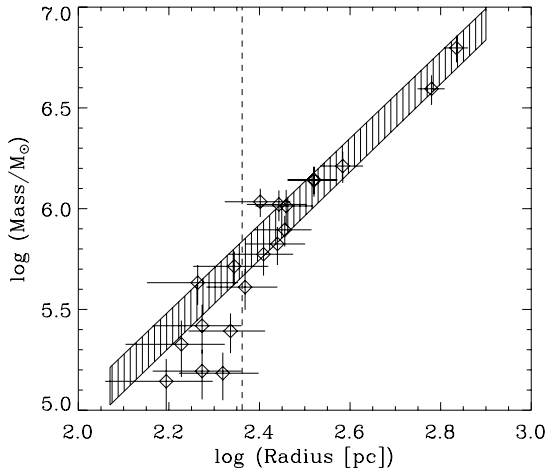

Figure 2.11: The mass *vs.* radius relation for GMCs in M51. The vertical dashed line indicates the spatial resolution of the *BIMA* survey. The filled area is a power-law fit to the data above the resolution limit, with index 2.16, and the corresponding 1σ error bars on the index (± 0.20) and the zero point.

3. **The star formation rate within the complexes:** We have measured the star formation rates within the complexes from the (continuum subtracted) Hα flux using the relation between the Hα flux and the star formation rate given by Kennicutt (1998b). The area normalised star formation rates are as high as starburst galaxies, thereby justifying their designation as *localized starbursts*, a label first coined by Efremov (2004). We found that the star formation rates (for a given size) within the complexes studied here are about a factor of 10 lower than complexes (of the same size) in the merging Antennae galaxies. We trace this difference to the molecular cloud populations within the two galaxies, as the GMCs in the Antennae galaxies are roughly 10 times more dense than the GMCs in M51. Thus, if star formation is proportional to gas density, as is the case in the commonly used Schmidt law of star formation, then the difference in the star formation rates between the two galaxies is readily understandable.

4. **The surface density distribution:** The cluster complexes follow the same surface density distribution as that of GMCs and young star clusters, namely a power law with exponent -0.74 ± 0.34. This corresponds to a spatial density $\rho \propto r^{-1.74}$. This provides a natural explanation for the similarity between the observed mass-radius distribution of GMCs and cluster complexes. Presumably older clusters follow a steeper density distribution with a distinct tidal truncation due to dynamical evolution.

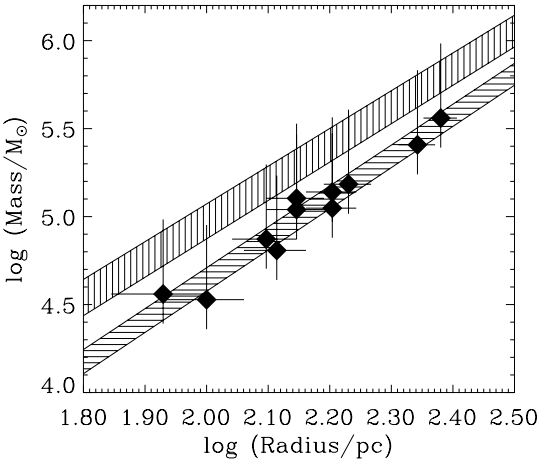

Figure 2.12: The mass *vs.* radius relation for cluster complexes in M51. The solid line is a power-law fit to the data with index, 2.3. The filled area with vertical hashes is the fit to the GMCs from Fig 2.11, extended into the size regime of the complexes. The filled area with the horizontal hash marks is the power-law fit to the complexes, with index 2.33, and the corresponding 1σ error bars on the index (± 0.19) and the zero point.

5. **The mass-radius relation:** The complexes in M51 follow the same mass-radius relation observed for GMCs. We conclude that this similarity is due to the imprint of the progenitor GMC onto the complex forming within it. The shared mass-radius relation is a natural consequence of the shared density distributions. Contrary to the complexes however, young star clusters do not share the same mass-radius relation (they follow a much weaker relation with a large scatter). We suggest that this may be due to interactions between the young star clusters and gas clouds. This scenario is supported by the observation that the size distribution is significantly shallower for star clusters (young and old) than for GMCs (Bastian et al. 2005b).

6. **Star formation efficiency:** We have argued that the size of the progenitor GMC and that of the each complex are the same, due to the short formation timescale relative to the free-fall timescale of the GMC. We estimate the star formation efficiency within each complex, by extending the observed mass-radius relation of GMCs to that of the scale of the complexes. In this way, we estimate that the star formation efficiency in the complexes is 50%. However, due to the required assumptions (CO-to-H_2 conversion factor and stellar IMF of the complex) the errors using this method are quite substantial, and hence this method is not viable at the present time.

7. **Evolution of the complexes:** The complexes studied here are quite similar to those modelled by Fellhauer & Kroupa (2002, 2005). Their models show that a significant amount of merging of the individual clusters is expected to happen within the complexes, which may lead to the formation of a much larger star cluster than would be expected from statistical sampling of a cluster initial mass function. This may explain why clusters with masses up to $5 \times 10^5 M_\odot$ are found in M51 (Bastian et al. 2005b), which is about the mass of the largest complex analysed here. Many of the complexes studied here show evidence of merging in their centres.

acknowledgements This research has benefited from the NASA Database. We thank Søren Larsen and Pavel Kroupa for useful and stimulating conversations. We would like to thank Alice Quillen for help in analysing the *BIMA* data. Yu.N. E. acknowledges support from grants RFFI 03-02-16288 and NSh 389-2003-2.

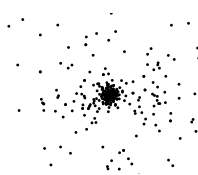

CHAPTER 3

The star cluster population of M51: Age distribution and relations among the derived parameters

N. Bastian, M. Gieles, H.J.G.L.M. Lamers, R. Scheepmaker and R. de Grijs

Astronomy and Astrophysics, v.431, p.905–924 (2005)

Abstract We use archival *Hubble Space Telescope* observations of broad-band images from the ultraviolet (F255W-filter) through the near infrared (*NICMOS* F160W-filter) to study the star cluster population of the interacting spiral galaxy M51. We obtain age, mass, extinction, and effective radius estimates for 1152 star clusters in a region of $\sim 7.3 \times 8.1$ kpc centred on the nucleus and extending into the outer spiral arms. In this paper we present the data set and exploit it to determine the age distribution and relationships among the fundamental parameters (i.e. age, mass, effective radius). We show the critical dependence of the age distribution on the sample selection, and confirm that using a constant mass cut-off, above which the sample is complete for the entire age range of interest, is essential. In particular, in this sample we are complete only for masses above $5{\times}10^4$ $M_\odot$ for the last 1 Gyr. Using this dataset we find: *i)* that the cluster formation rate seems to have had a large increase $\sim$ 50-70 Myr ago, which is coincident with the suggested *second passage* of its companion, NGC 5195, *ii)* a large number of extremely young ($<$ 10 Myr) star clusters, which we interpret as a population of unbound clusters of which a large majority will disrupt within the next $\sim$10 Myr, and *iii)* that the distribution of cluster sizes can be well approximated by a power-law with exponent, $-\eta = -2.2 \pm 0.2$, which is very similar to that of Galactic globular clusters, indicating that cluster disruption is largely independent of cluster radius. In addition, we have used this dataset to search for correlations among the derived parameters. In particular, we do not find any strong trends between the age and mass, mass and effective radius, nor between

the galactocentric distance and effective radius. There is, however, a strong correlation between the age of a cluster and its extinction, with younger clusters being more heavily reddened than older clusters.

3.1. Introduction

This study aims at understanding the formation history of star clusters, their properties and spatial distribution in the interacting spiral galaxy M51. To study such a system, one needs the superb spatial resolution of the *Hubble Space Telescope* (*HST*) in order to avoid crowding effects and to differentiate between individual stars, associations, and compact star clusters.

Although much work has already been done on extra-galactic star clusters using the *HST*, most studies have concentrated on specific components of the full cluster populations (e.g. star clusters in the centre of spiral galaxies, Böker et al. 2001) or star cluster systems in extreme environments such as galactic mergers (e.g. Miller et al. 1997, Whitmore et al. 1999b). In order to form a baseline to study the effects of environment on cluster formation, evolution and general cluster properties, one must study the properties of clusters in normal (i.e. more common) environments. It is only then that we are able to see which properties are truly unique for a given environment and which properties remain fixed across all environments.

One such property of star cluster systems that has a well-established baseline is that of the luminosity function. Larsen (2002) has shown that the cluster populations of spiral galaxies follow a luminosity distribution that is well represented by a power-law, $N(L) \propto L^{-\alpha}$, with α=2.0. This is remarkably similar to that found in all other environments (de Grijs et al. 2003a), and hence can be regarded as a general property of young star cluster systems. Recent work by Larsen (2004) shows that young clusters in spiral galaxies have typical sizes of $r_{\rm eff} \sim$ 3-10 pc, with the youngest clusters having extended halos. It remains to be seen how other properties, such as mass, age and spatial distributions depend on the environment in which the clusters form.

M51 provides an almost ideal astrophysical laboratory to study extra-galactic star clusters. This is due to its relatively close distance of $\sim$ 8.4 Mpc (Feldmeier et al. 1997) and its almost face-on orientation. Physically it is an interesting case study because it seems to have had a strong interaction with its companion, NGC 5195 an S0 peculiar galaxy, during the last few hundred Myr, which presumably caused its grand design spiral appearance as well as its high star formation rate. The M51/NGC 5195 encounter(s) have been modelled in great detail by many authors; this will allow us to compare the derived age distribution of the star clusters with the orbital parameters of the system, which are robustly established. The system has been modelled relatively successfully by a single early passage $\sim$300 $\pm$ 100 Myr ago (Toomre & Toomre 1972; Salo & Laurikainen 2000, hereafter SL00). Additionally, SL00 propose a model of a double passage, the first happening $\sim$400-500 Myr ago and the second, or last encounter, happening $\sim$50-100 Myr ago. This latter model seems to fit many observed

details that the single passage models fail to reproduce, such as the observed counter-rotation of the southern HI tail.

Much work has already been done on the star cluster system of M51. A full literature review is beyond the scope of this paper, but we refer the reader to the following work: (Bik et al. 2003, hereafter Paper I) have studied the star cluster population in a relatively small area to the north east of the nucleus that included inner sections of one of the spiral arms. They find that the mass function is reasonably well fit by a power-law of the form $N(M) \propto M^{-\alpha}$ where $\alpha \sim 2.0$. They also show that there is weak evidence for a possible increase in the cluster formation rate in the inner spiral arms at ~ 400 Myr ago, the proposed time of an interaction between M51 and NGC 5195, but that the evidence is only at the 2 σ level. Boutloukos & Lamers (2003) used the data from Paper I to determine the characteristic disruption timescale of clusters in this region, which is ~ 40 Myr for a $10^4 M_\odot$ cluster. Larsen & Richtler (2000) has studied a few of the "young massive clusters" which form the high end of the luminosity function, using combined *HST* and ground-based observations. He finds that although M51 has a relatively high star-formation rate, it fits the specific U-band luminosity (T_L^U) *vs.* star formation rate relation of non-starburst galaxies. This has been interpreted as showing that high-mass star clusters will form whenever the star formation rate is high enough. Scoville et al. (2001) have used many of the same *HST* images used in this study, to look at OB star formation in M51. They find that the mass function of OB star clusters is well represented by a power law of the form $N(M_{\rm cl})/{\rm d}M_{\rm cl} \propto M_{\rm cl}^{-2.01}$, in agreement with the results presented in Paper I. They also show that although the spiral arms only make up $\sim 25\%$ of the disc surface area they contain a much higher fraction of the catalogued HII regions.

This study is the second in a series of three, which aim at understanding the properties of the star cluster system of M51 as a whole. This paper introduces the data and techniques used to determine the cluster properties, analyses the age distribution as well as the correlations among the cluster parameters, namely their age, mass, extinction, size, galactocentric distance, and position in the galaxy. In the third paper (Gieles et al. 2005, hereafter Paper III) we determine the luminosity and mass distributions and derive the disruption timescale for clusters in M51.

The study is setup in the following way: in § 3.2 we present the observations used in this study, including the reduction and photometry. In § 3.3 the methods of finding the clusters and the selections applied to the data are elucidated. In § 3.4 we present our method of determining the ages, extinctions, and masses of each of the detected clusters, and discuss how contaminating sources are detected and removed. In §§ 3.5 and 3.6 the general properties of the cluster system are presented and discussed, while § 3.7 presents evidence for a young, short lived cluster population. In §§ 3.8 and 3.9 the size distribution and relations between size and the other cluster parameters are presented, followed by § 3.10 in which we summarize our main results.

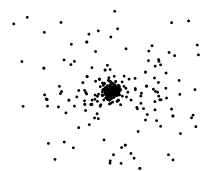

3.2. Observations, reduction and photometry

Our analysis of stellar clusters in M51 is based on observations done with the *Wide Field Planetary Camera-2* (*WFPC2*) and the *Near-Infrared Camera and Multi-Object Spectrometer* (*NICMOS*) on board the *HST*.

3.2.1. *WFPC2* Observations

Observations in 8 different passbands of the inner region of M51 were obtained from the *HST* data archive: F255W ($\approx$ UV), F336W ($\approx U$), F439W ($\approx B$), F502N ($\approx$ OIII), F555W ($\approx V$), F656N ($\approx$ Hα), F675W ($\approx R$) and F814W ($\approx I$). We emphasise that we have not transformed the *HST* filters into the standard Cousins-Johnson filter system.

An overview of the filters and exposure times is given in Table 1. Proposal ID 5777 and 7375 contain the F555W band images and will be referred to as Orientation 1 and Orientation 2, respectively. All the other orientations are rotated/shifted to these 2 base orientations. An overview of the orientation of the data sets is shown in Figures 3.1 and 3.2. The combined data sets span a region of about $180'' \times 200''$ (i.e. 7.3×8.1 kpc) containing the complete inner spiral arms of the galaxy.

The raw images were flat fielded using the automatic standard pipeline reduction at the Space Telescope Science Institute (STScI). Warm pixels were removed using the `warmpix` task which is part of the `IRAF/STSDAS`[1] package. Bad pixels where fixed with the `wfixup` task which interpolates over bad pixels in the x-direction.

Cosmic rays where treated differently for the three datasets. For the images consisting of multiple exposures of the same field per filter the task `crrej` was used. This combines exposures of the same field by rejecting very high counts on an individual pixel basis. Three iterations were done with rejection levels set to 8, 6 and 4σ.

In single exposure images the cosmic rays were removed using the `Lacos_im` package of van Dokkum (2001). This algorithm identifies cosmic rays of arbitrary shapes and sizes by the sharpness of their edges and reliably discriminates between poorly sampled point sources and cosmic rays. The parameter setting used was a `sigclip` of 6.5, a `sigfrac` of 0.5 and an `objlim` of 4. Four iterations were done to give the best result, because the result of the cosmic ray rejection is very sensitive to the settings. Careful tests were done to make sure no real sources were removed by the cosmic ray removal task. This resulted in almost cosmic ray free images. The few remaining cosmic rays will be rejected later when the photometry coordinates from the source detection in the different filters will be cross correlated.

[1] The Image Reduction and Analysis Package (`IRAF`) is distributed by the National Optical Astronomy Observatories, which is operated by the Association of Universities for Research in Astronomy, Inc., under cooperative agreement with the National Science Foundation. STSDAS, the Space Telescope Science Data Analysis System, contains tasks complementary to the existing `IRAF` tasks. In this study Version 2.1.1 (December 1999) was used.

Table 3.1: Overview of the datasets used.[†]Equivalent to the V3 Position Angle of the *WFPC2*.

ID	Filters	Exp. time	Observation Date	Orientation angle[†]
7375	F336W	2 x 600 s.	21 July 1999	275.9
(*WFPC2*)	F439W	500 + 600 s.		
	F555W	2 x 600 s.		
	F656N	1300 + 700 s.		
	F675W	500 s.		
	F814W	700 + 300 s.		
5777	F439W	2 x 700 s.	15 Jan 1995	101.5
(*WFPC2*)	F555W	600 s.		
	F675W	600 s.		
	F814W	600 s.		
5123	F502N	400 + 1400 s.	24 January 1995	93.2
(*WFPC2*)	F656N	500 + 1200 s.		
5652	F255W	4 x 500 s.	12 May 1994	333.0
(*WFPC2*)	F336W	2 x 400 s.		
7237	F110W	128 s.	28 June 1998	-113.2
(*NICMOS3*)	F160W	128 s.		

3.2.2. *NICMOS* Observations

NICMOS images were obtained with the *NIC3* camera, which has a field of view (FoV) of about $52'' \times 52''$. A mosaic of nine overlapping pointings of the *NIC3* camera of M51 was available in the archive, yielding a total FoV of $186'' \times 188''$ (i.e. 7.6 × 7.7 kpc) of the central region in the near-infrared F110W and F160W filters (see Fig. 3.2). Each of the nine mosaic positions was observed using a square dither in each filter setting.

Flat-fielding, dark frame correction and bias subtraction were all performed in the pipeline image reduction and calibration by the `calnica` task. Bad pixels were repaired with the `fixpix` task which uses static bad pixel mask images. All individual images in the dither pattern were shifted to the same orientation with `imshift`. The dither pattern constituted of shifts of an integer number of pixels, the images were perfectly aligned on subpixel level. The individual images in the same orientation were added with `imcombine` using the `crrej` method for cosmic ray rejection. Finally, the nine co-added images were mosaiced by matching sources in the overlap region and comparing histograms of the sky values. This results in a large square FoV overlapping a large area of the optical data set. Since the mosaic routine does not scale the count rates values when matching the individual chips, the mosaic images can be used for source selection and photometry.

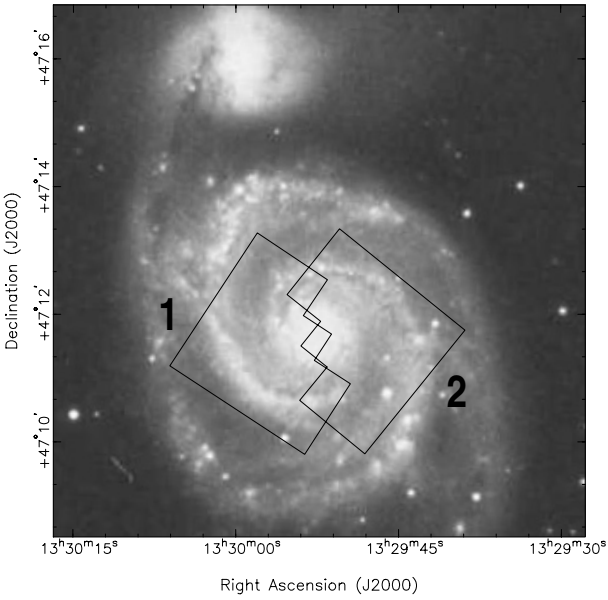

Figure 3.1: The orientation of the two *HST* pointings for the F336W, F439W, F555W, F675W, F814W, and F656N filters overlaid on a *Digital Sky Survey* image of M51. North is up, and east is to the left. The left orientation/pointing is referred to as field 1, while the right is referred to as field 2.

3.2.3. Source selection

Point-like sources were identified in the individual *WFPC2* chip images and the *NIC3* mosaic images with the `daofind` task from the DAOPHOT package (Stetson 1987). For the optical filters a threshold of 5σ was used, where σ is the sky noise. In order not to be biased towards certain areas on the chips, the value of σ was determined on a low background region on each of the chips. For the F255W filter the threshold was 4σ and for the near-infrared *NIC3* images the threshold was set to 8σ. The threshold was chosen such that in each filter and chip the resulting source density was more or less the same. No limitation was set on sharpness or roundness, to include as many sources as possible, including unrelaxed young clusters.

3.2.4. Photometry

WFPC2

The coordinates from the source lists, obtained from the `daofind` output, were used as an initial guess of the centers for the `phot` aperture photometry routine. For the WF chips we used an aperture, annulus (inner boundary of background annulus) and dannulus (width of the background annulus) of 3, 7 and 3 pixels respectively. For

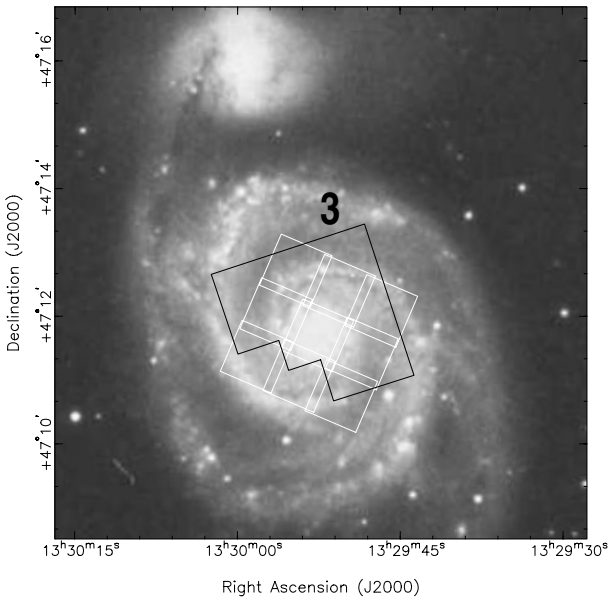

Figure 3.2: The orientation of the F255W FoV (black) and the *NIC3* mosaic (white).

the PC chip we used slightly larger values, namely 4, 10, 3 for the aperture, annulus and dannulus respectively. The chosen values for the apertures are ~ 3 times larger than the FWHM of the PSF in order to account for the fact that at the distance of M51, clusters appear slightly extended (i.e. are not point sources). Photometric calibration was done by applying zero-point offsets from Table 28.2 of Mobasher (2002) in the VEGAMAG system.

Total magnitudes were determined by correcting for flux outside the measurement aperture. Ideally aperture corrections are determined from real sources on the image. In the case of our data there were not enough isolated bright sources located in regions of low background to obtain a meaningful correction. Thus aperture corrections from the measurement aperture radius to a $0.5''$ radius were determined from analytically generated clusters by convolving a PSF (generated using `Tiny Tim`, Krist 1995) with King profiles using the `BAOlab` package (Larsen 1999). King profiles of concentration factor, c, of 30 ($c = r_t/r_c$ where r_t is the tidal radius and r_c is the core radius), and effective radius, $r_{\rm eff}$, of 3 pc (see § 3.8) were used for the analytic cluster profiles. The values for the three WF chips are averages. For the PC and WF chip in each filter the values are listed in Table 3. A final -0.1 mag. correction was applied to all sources to correct for the light missed in the $0.5''$ aperture. After applying the aperture corrections, the magnitudes where corrected for CTE loss according to the equations of Whitmore et al. (1999a).

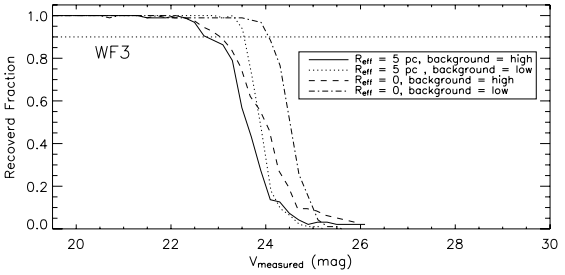

Figure 3.3: Recovered fraction of sources added to the F555W science images on the WF3 chip. Four examples are shown, combinations of low and high background and PSFs and extended clusters ($r_{\rm eff} = 5$ pc).

NICMOS

The photometry procedure for the *NIC3* images is essentially the same as for the *WFPC2* images. An aperture, annulus and dannulus of 2, 5 and 3 pixels were used, respectively. The flux was converted to magnitudes in the VEGAMAG system using the PHOTFNU values from the headers. Aperture corrections from the measurement aperture radius to a $1.0''$ radius were determined using the same technique as for the *WFPC2* images. Values are listed in Table 2. A final correction to a nominal infinite aperture correction of -0.08 mag (i.e., multiplying the flux with 1.075) was applied.

3.2.5. Incompleteness due to detection limits

In order to quantify at what magnitude our sample starts to be incomplete due to detection limitations, the 90% completeness limit was determined for each band for each pointing. To this end, artificial sources were added to the *HST* images and were recovered with exactly the same routines as used to find the real sources. A very important criterion is that objects should be 5 times above the standard deviation of the background. The value for σ should be the same as when real sources are found. The magnitude of the added sources were determined and an error criterion of Δmag < 0.2 was applied (see § 3.3), the same criterion as for the real sources to enter the photometry list. The tests were done for the PC1 and WF3 chips of both pointings separately.

Extended sources with different $r_{\rm eff}$ are simulated by convolving *WFPC2* PSFs, produced by `Tiny Tim`, with King profiles. The King profiles are produced by the `BAOlab` package (Larsen 1999). King profiles with a concentration index, c, of 30 with different $r_{\rm eff}$ were tried. In § 3.8 it is shown that the average size for *resolved* clusters in M51 is ~ 3 pc. Thus, we take a more conservative estimate of the completeness survey by assuming $r_{\rm eff} = 5$ pc (the more extended the cluster is the more diffuse it becomes, for a given brightness, making it more difficult to detect). On each chip,

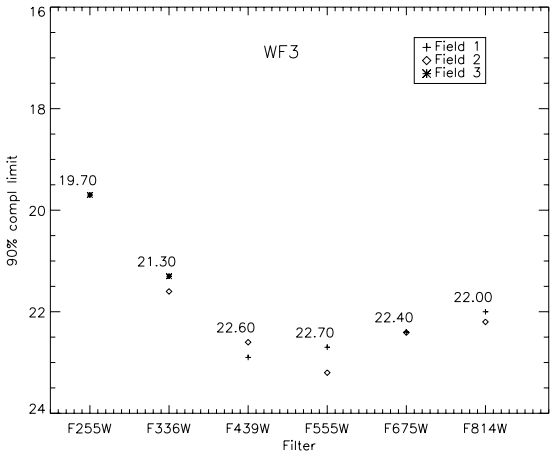

Figure 3.4: Worst case (high background, $r_{\rm eff} = 5$ pc clusters) 90% completeness limits for PC1 and WF3 for all filters and the three available *HST* pointings.

two regions were studied, one with low and one with high background levels. Since the aperture corrections were derived for average extended sources ($r_{\rm eff} = 3$ pc), the magnitudes of the artificial 5 pc sources are too faint and the magnitudes of the pure PSFs are too bright. In both cases the maximum offset is about 0.15 mag.

The recovered fraction as a function of magnitude in the F555W filter is plotted in Fig. 3.3 for the WF3 chip. Each plot shows the effects of background and source size. The plots show that for an individual chip the 90% completeness limit varies by more than a magnitude, depending on the location on the chip and the size of the source. We therefore do not have a clear detection limit but a region where incompleteness sets in. Details of this effect and its influence on the luminosity function are given in Paper III. The worst case 90% completeness limits are shown in Fig. 3.4 for all bands and for the 3 available *HST* pointings. When more than one pointing is available for a filter, the brightest (i.e. most conservative) 90% completeness limit of that filter is chosen.

For the remainder of this study the worst case 90% completeness limit was applied to the data. Since the PC chip has been shown to have many single bright stars (Lamers et al. 2002) and since its completeness limit is about 1 magnitude brighter than for the WF3 chip, we will only use the WF data for the remainder of this study.

Table 3.2: 90% completeness limits for the WF3 in the 3 different available pointings. Most conservative values are printed bold.

	PC1			WF3		
Filter	1	2	3	1	2	3
F255W	-	-	**18.80**	-	-	**19.70**
F336W	-	20.8	**20.45**	-	21.60	**21.30**
F439W	22.10	**21.80**	-	22.90	**22.60**	-
F555W	**21.80**	21.90	-	**22.70**	23.20	-
F675W	**21.20**	21.90	-	**22.40**	22.45	-
F814W	21.20	**21.00**	-	**22.20**	22.20	-

3.3. The selection of the clusters and the photometry master list.

The coordinate lists for the individual *WFPC2* chips were transformed to one system using the `metric` task. This task corrects for geometric distortion and yields coordinates with respect to one frame (WF3). Transformation matrices to convert the mosaic coordinates of field id #5652 (F255W and F336W) (see Table 1) to Orientation 1 and Orientation 2 coordinates, were determined by finding sources in common to both frames in the F336W filter. Since the #5777 program does not contain an F336W exposure, the F439W exposure was used instead. The sources used to find the transformations were selected to be isolated and spread over the images by as much as possible to make the transformation as accurate as possible. The spatial transformation functions were calculated based on the coordinates of the sources in the two frames using the `geomap` task in `IRAF`. The accuracy of the transformation is approximately 0.1-0.2 pixels. The same was done for the near-infrared filters (F110W and F160W). For these transformations identical sources were found in the F110W and F814W bands. In this case the accuracy was somewhat lower since the *NIC3* pixel size ($\approx 0.2''$) is larger then the WF pixel size ($\approx 0.1''$). The accuracy of the transformation function is still 0.2-0.3 WF pixels.

The final source list was made by cross correlating sources found in the various filters. First, a cross correlation between the F439W, F555W and F675W was done. If a coordinate was found in all 3 filters, allowing a mismatch of 1.4 pixels, it was defined as a genuine source. Then the other filters were compared with the source list, again allowing a mismatch of 1.4 pixels. The transformed coordinates of the F255W and F336W frame were allowed to have a 1.6 pixel mismatch. The F110W and F160W frames were allowed to have a 1.8 pixel mismatch. This was adopted because of the uncertainty in the transformation.

The resulting initial source list contains 3504 objects that are observed in at least the F439W, F555W, and F675W bands above the 5σ detection limit. Most of

Table 3.3: Aperture correction values for all filters (mag).

Filter	PC	WF3 (mean)	*NIC3*
F225W	−0.32	−0.14	
F336W	−0.31	−0.13	
F439W	−0.31	−0.13	
F555W	−0.32	−0.13	
F675W	−0.32	−0.13	
F814W	−0.33	−0.14	
F110W			-0.22 ± 0.01
F160W			-0.22 ± 0.01

† This value is applied to our sample. For clusters with $r_{\rm eff} = 5$ pc, these values decrease by ~ 0.15 mag. (e.g. to -0.28 for F555W in the WF3 chip).

these will be eliminated later in the study of their energy distributions because the photometry is uncertain or the energy distribution does not match that of cluster models (see § 3.4.5).

3.3.1. Contamination of the sample by stars

We estimate the possible number of massive stars that may contaminate our source sample by scaling the star population of the LMC, measured by Massey (2002) to the conditions in M51. This sample, which is complete down to $V \simeq 15.7$ mag or $M_V \simeq -3.2$ mag covers a total area of 10.9 kpc^2 and includes most of the bar, the 30 Doradus region and several other well populated fields. This area contains more than half of the mass of the LMC. We have calculated the intrinsic visual magnitudes, by adopting only foreground extinction of $A_V = 0.40$ mag and $E(B-V) = 0.13$ mag (Massey et al. 1995) and a distance modulus of 18.48 mag (Westerlund 1997) The total number of stars brighter than $M_V < -7.0$ mag (which corresponds to $V < 22.60$ at the distance of M51, for no extinction) is less than 100, and the number with $M_V < -8.0$ mag is 6. By far the majority of these stars are found in clusters. We can get an estimate of the fraction of the luminous *field* stars compared to the total fraction from the data in Table 12 of Massey (2002) which gives the number of massive stars outside clusters. (This is the only large and homogeneous extragalactic stellar sample deep enough to determine the relation between the populations of field stars and the total populations.) He found 186 field stars (i.e. outside known OB associations) more massive than 40 $M_\odot$, which corresponds to $M_{\rm bol} \leq -9$ mag. More than 90 per cent of these are on or near the main sequence, where $T_{\rm eff} > 25\,000$ K and hence the bolometric correction is so large that $M_V > -7.0$ mag. At most 10% of these stars, i.e. less than 18, are optically bright at $M_V < -7.0$ mag in the LMC.

With a total mass of the observed area of about 4×10^9 $M_\odot$ (Meatheringham 1991), this implies about 4 to 5 field stars more massive than 40 $M_\odot$ per 10^9 $M_\odot$.

(This number could be slightly higher if the dark matter content of the LMC within the region used here is considerable). This small number is due to the very steep IMF of the massive field stars. Massey (2002) showed that the stellar IMF of massive field stars can be approximated with $\Gamma \simeq -4$, compared to $\Gamma \simeq -1.3$ for cluster stars, where $\Gamma = \mathrm{d}(\log N(M))/\mathrm{d}(\log(M))$.

The total luminous mass of M51 within a radius of 5 kpc is $2.1 \times 10^{10} M_{\odot}$ (SL00). Scaling the number of field stars per unit mass in the LMC to that of M51, we estimate that at most 170 to 210 field stars with $M_V < -7.0$ will be in our field, and less than 15 to 20 with $M_V < -8.0$, *if there were no extinction in M51.* Even a moderate extinction will remove these stars from our sample.

Another estimate of contaminating stellar sources in our sample can be obtained by comparing the number of field stars to that of observed clusters. This comparison relies on the assumption that the ratio of field stars to clusters is the same in different galaxies. This assumption will not be valid for low or intermediate mass stars between galaxies with widely different cluster disruption timescales, as galaxies with shorter disruption timescales will have a higher field star to cluster ratio. However, for young massive stars (lifetimes less than 10 Myr), disruption is not expected to significantly influence this ratio. Using the catalogue of Bica et al. (1996) we see that there are ~ 180 clusters and associations brighter than $M_V = -6.94$ in the LMC (assuming a distance modulus to the LMC of 18.48 and an imposed completeness of $m_V = 22.70$ at the distance of M51). Using the arguments given above, there are < 18 young massive stars that are brighter than $M_V = -7.0$ in the LMC. Thus there are less than one field star for every ten clusters in the LMC. Therefore, using this approximation, we expect less than 10% of our M51 sample to be bright young stars.

A third alternative method to estimate the contamination by massive isolated field stars is to scale the number of isolated field stars in the LMC to that of M51 using the mass normalized star formation rates. In the studies summarized by Grimm et al. (2003), M51 has about half the star formation rate per unit galaxy mass as the LMC. So, using this assumption we expect half as many bright field stars in M51 as in the LMC per unit mass, which results (using the mass ratios above) in ~ 47 bright field stars.

We conclude that the number of contaminating stars in our sample is small[2]. Moreover, we will show in § 3.4.5 that most of these will be removed from the sample because they do not pass the criterion that their energy distribution can be fitted with a cluster model.

[2]In Paper I we found that massive young clusters in the inner NE-spiral arm of M51 have a surprisingly small flux in the O[III] λ5007 line. They interpret this as evidence that there is a lack of massive stars of $M > 30 M_{\odot}$ in the clusters. If this is also valid for the field stars, the number of contaminating field stars in our sample will be even smaller than estimated here.

3.4. Determination of the cluster parameters from their energy distribution

The age, mass and extinction of star clusters can be derived by comparing their spectral energy distributions to those of cluster evolution models (e.g. Paper I, de Grijs et al. 2003a,b,c). This method can also be used to eliminate contaminating sources (e.g. stars and background galaxies).

3.4.1. Adopted cluster models

We have adopted the updated `GALEV` simple stellar population (SSP) models (Schulz et al. 2002; Anders & Fritze-v. Alvensleben 2003) as our templates to derive ages, extinction values, and masses for each of the observed clusters in M51. These models use the isochrones from the Padova group, which seem to fit the data better than the Geneva tracks (Whitmore & Zhang 2002). The set of models that we use assumes a Salpeter stellar IMF from 0.15 - 50 $M_{\odot}$. We have used models with metallicities of 0.4, 1, and 2.5 $Z_{\odot}$, and a comparison between the different metallicities will be made in § 3.4.6.

There were two major reasons for selecting the updated `GALEV` tracks. The first is the inclusion of gaseous emission lines as well as continuum emission, which can severely affect the broad-band colours for young star clusters (see Anders & Fritze-v. Alvensleben 2003). The second is that they have been published in the *HST/WFPC2-NICMOS* filter system, which eliminates possible inaccuracies in converting the *HST* observations to the standard Cousins-Johnson system.

3.4.2. The fitting of the spectral energy distributions

We used the three-dimensional maximum likelihood fitting method (*3DEF*) developed in Paper I. The method has been described in detail there, and hence we will only give a brief summary of it here. In passing we note that this method has been tested against colour-colour methods of age fitting, and has shown itself to be superior (e.g., de Grijs et al. 2003b *vs.* Parmentier et al. 2003).

The method works as follows: we use a grid of SSP models, i.e. the `GALEV` models (see previous section) that give the broad-band colours of a single age stellar population as a function of age. For each model age, we apply 50 different extinctions in steps of 0.02 in $E(B-V)$. We adopted the Galactic extinction law of Savage & Mathis (1979), which was found to agree with the extinction law derived for M51 by Lamers et al. (2002). We then compare the model grid with the observed spectral energy distribution of the clusters using a minimum χ^2 test, with each observation weighted with its uncertainty. The model (age and extinction) with the lowest χ^2 is selected, and the range (i.e. maximum and minimum age) of accepted values is calculated by taking the most extreme model that satisfies $\chi^2_{\nu} < \chi^2_{\nu,\min} + 1$. Once the age and extinction have been calculated, the mass is found by comparing each observed filter magnitude to each model magnitude (iteratively with respect to age

Table 3.4: Empirical parameters for the uncertainty of the magnitudes: $\Delta(m) = 10^{d_1+d_2\times m}$

Filter	d_1	d_2
F255W	−8.540	+0.390
F336W	−7.850	+0.325
F439W	−8.320	+0.328
F555W	−7.800	+0.300
F675W	−7.600	+0.300
F814W	−8.230	+0.328

and extinction). Since we have first scaled the `GALEV` models to a *present mass* of $10^6 M_\odot$ the difference between the observed and the predicted magnitude (taking into account the distance modulus and extinction) can be converted to the present mass of the observed cluster[3].

3.4.3. Test of the accuracy of the method

We have tested the accuracy of the method used for the determination of the age and mass of clusters. To this purpose we created a grid of synthetic clusters, distributed evenly in logarithmic age, in the range of $7.0 < \log(t/\mathrm{yr}) < 10.0$ in 31 steps, and evenly in logarithmic mass in the range of $3.0 < \log(M/\mathrm{M}_\odot) < 6.0$ in 21 steps. This results in 651 synthetic clusters. The clusters have a distance modulus of $m - M = 29.64$, as for M51, and were assigned a random extinction of $0 < E(B-V) < 1.0$ mag with a Gaussian probability function that peaks at $E(B-V) = 0$ mag and has a $\sigma = 0.20$ mag. For each of these clusters we calculated the expected energy distribution in the same *HST/WFPC2* filters as used for this study of M51, using the `GALEV` cluster models with a metallicity of $Z = 0.02$, and a Salpeter IMF. The photometry of each synthetic cluster was given an uncertainty that depends on magnitude. The uncertainty was derived from the observations, which show that $\Delta(m)$ can be approximated quite well by $\Delta(m) = 10^{d_1+d_2\times m}$, where m is the magnitude and the values of d_1 and d_2 are empirically determined for each *HST* filter. These values are listed in Table 3.4. We then added a random correction to the magnitude of each cluster in each filter, within the interval $(-\Delta(m), +\Delta(m))$. This resulted in a list of 651 synthetic clusters with photometry and photometric errors similar to those of the observed clusters in M51.

We then ran these synthetic clusters through our cluster fitting program to determine the age, mass and extinction in exactly the same way as done for the observed

[3]All masses derived in this paper refer to the *present mass* of the clusters, not to their *initial mass.* If stellar evolution is the only mass loss mechanism of the cluster, the initial mass of the clusters can be retrieved by correcting the present mass for the fraction lost by stellar evolution, given by the `GALEV` models.

clusters. We adopted the same conservative magnitude limits as for the observed sample, as given in Table 3.2. The comparison between the input mass, age and extinction of the synthetic clusters and the result of the fitting gives an indication of the accuracy and reliability of the results. The result is shown in Figure 3.5.

The panels show the difference between input and output values of $\log(t)$, $\log(M)$ and $E(B-V)$ as a function of the V magnitude of the synthetic cluster. This parameter was adopted because the accuracy of the fitting is expected to depend on the accuracy of the input photometry, for which V is a good indicator. We have divided the results into four age bins (with parameters indicated in the figure), because the accuracy of the fit may be different in different age intervals, as the spectral energy distribution depends on age.

Figure 3.5a shows that the age determination is quite accurate, to within about 0.20 dex, for relatively bright clusters with $V < 21.0$ mag. For fainter clusters with $V > 21.0$ mag the uncertainty increases up to a maximum of about 1 dex for clusters with $V > 22.0$ mag. The scatter is approximately symmetric around the zero-line with two exceptions.
(i) For the youngest faint clusters with $t < 30$ Myr and $V > 21.5$ mag the age is more likely to be overestimated than underestimated. This is the consequence of the simple fact that the two youngest `GALEV` cluster models have ages of 4 and 8 Myr. So a cluster cannot be fitted to a model younger than 4 Myr, which limits the possible negative values of $\log(t_{\rm out}/t_{\rm in})$.
(ii) Faint clusters with ages of $\log(t/{\rm yr}) > 7.5$ have a higher probability to be fitted with a younger cluster model than with an older cluster model. This might reduce the number of old clusters derived from the fitting of the SEDs of observed clusters. This effect will be taken into account in the analysis of the observed mass and age distributions of the M51 clusters.

Figure 3.5b shows that the mass determination is quite accurate for relatively bright clusters with $V < 21.0$ mag. For fainter clusters with $V > 21.0$ mag the uncertainty decreases up to a maximum of about -0.5 dex to $+1.0$ dex for the faintest clusters. The scatter is approximately symmetric around the zero-line, except for the tendency to overestimate the mass of the faint old clusters. This is a direct result of the underestimate of the age.

Figure 3.5c shows that the extinction can be derived quite accurately for young clusters with $\log(t/{\rm yr}) < 8.5$ and $V < 21.5$ mag. For fainter clusters there is a symmetric scatter up to about $\Delta E(B-V) \simeq 0.1$ mag. For clusters older than 300 Myr there is a tendency to overestimate the extinction. This is the reason for the overestimate of the mass and the underestimate of the ages of these old clusters.

In general the ages and masses derived from fitting the cluster models are quite accurate: more than 99% of our synthetic clusters have an age determination that is accurate to within 0.25 dex and a mass determination that is accurate to within 0.2 dex. For real cluster samples the accuracy will depend on the magnitude distribution of the clusters, and hence on their photometric accuracy.

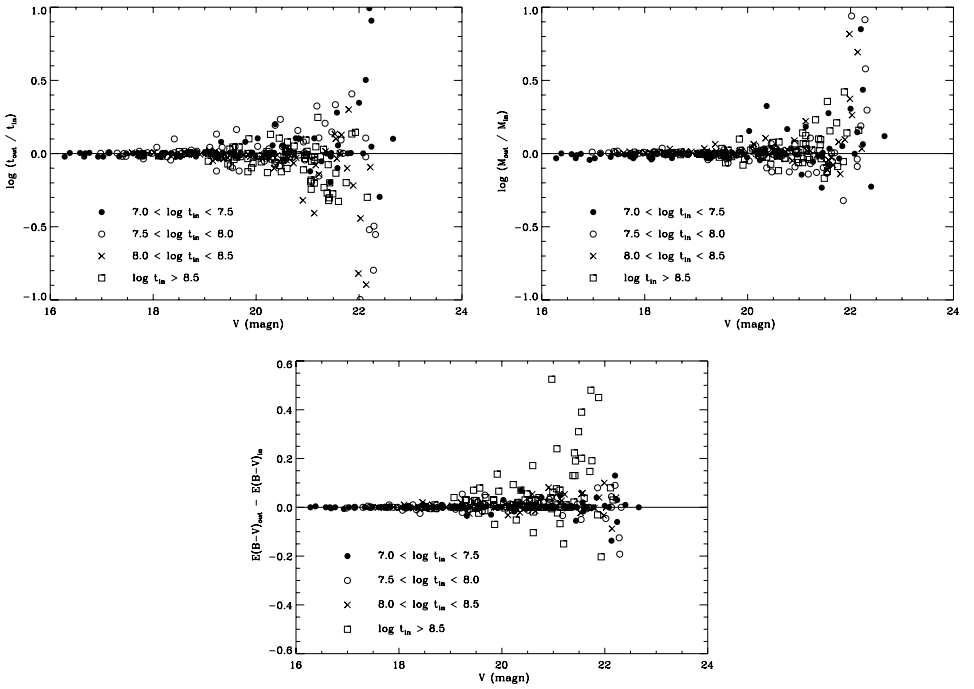

Figure 3.5: Comparison between input and output values of the ages (upper left panel, a), masses (upper right panel, b) and extinction values (lower panel, c) of the synthetic cluster sample. Different symbols indicate different age ranges.

Stochastic colour fluctuations

An additional uncertainty in the fitting of ages of star clusters using SSP models, is the stochastic colour fluctuations resulting from the fact that young low mass clusters will be dominated by a few high luminosity stars (e.g. Dolphin & Kennicutt 2002). Thus, the absence (or presence) of a small number of stars can significantly affect the observed integrated colours of a cluster. Unfortunately, due to the random nature of this effect it is impossible to determine which clusters in our sample are most heavily affected by this. However, if the stochastic colour fluctuations vary equally around the 'true' (i.e. fully sampled, high mass limit) colour, we do not expect our derived age distribution for the population as a whole to be affected by this. Finally, we note that our age distribution analysis (see § 3.6) has been restricted to clusters with derived masses above $10^{4.7} M_{\odot}$, e.g. the most massive clusters, where the stochastic colour fluctuations are expected to be smallest (Lançon & Mouhcine 2000). Stochastic effects are expected to affect the colour and magnitude of a 10 Myr, $10^5 M_{\odot}$ cluster by $\sigma_V = 0.08$ mag and $\sigma_{V-I} = 0.07$ (Dolphin & Kennicutt 2002). These small fluctuations are

within the observational uncertainties, and as such are not expected to significantly affect the derived parameters.

Dependence on the adopted models

The *3DEF* method assumes that the adopted models accurately reproduce the colours of star clusters as a function of age. In order to quantify this effect we have carried out the same analysis as discussed in § 3.4.3, but now using the Starburst99 models (Leitherer et al. 1999) for the artificial clusters, and then carrying out our fittting procedure using the `GALEV` models. These models were chosen because of the differing stellar evolutionary isochrones used when constructing their respective SSPs (i.e. the `GALEV` models adopt the Padova isochrones, while the Starburst99 models adopt the Geneva isochrones).

These tests resulted in 80% of the artificial clusters being fit within 0.5 dex of the input age and mass. The extinction is fit to within 0.2 mag in $E(B-V)$ for $>$ 80% of the artificial clusters. Thus we see that while there are significant differences between the models used, the parameters of the majority of clusters can be accurately recovered.

We also note that fitting our cluster sample using the Starburst99 models as templates, resulted in age and mass distributions which are consistent with the results presented here (Bastian & Lamers 2003). Namely, the high numbers of very young ($<$ 10 Myr) as well as the increase the cluster formation rate at $\sim 50-100$ Myr ago (see § 3.6).

3.4.4. Reduction of the sample based on energy distributions

Once we have obtained the best fit for each source (i.e. age, extinction and mass) we can then determine whether or not the object has a *good* fit, i.e. if it is a cluster. In previous studies (Paper I, de Grijs et al. 2003b) we used the selection criterion that the reduced χ^2 must be below 3.0. This was effective in eliminating most of the poor fits, but it also removed many of the brightest clusters because their photometric error was relatively low. In order to remove this problem, we have used the standard deviation, defined to be

$$\sigma^2(BVR) = \sum_i \frac{(m_i^{\rm mod} - m_i^{\rm obs})^2}{n_{\rm filters}} \tag{3.1}$$

where the sum runs over the F439W, F555W, and F675W bands only (the three bands in which all clusters were detected), as a criterion to test the accuracy of the photometric fit. The sum was restricted in order to maintain a fairly homogeneous set and to eliminate biases that would occur if bands with short exposures or low count rates (e.g. F255W) were included.

We then checked by eye the spectral energy distributions of the sources and their fits, in order to find a reasonable value for the minimum $\sigma^2(BVR)$, $\sigma^2_{\rm min}(BVR)$. As the "goodness" of the fit is rather arbitrary, we quantified the exact value of

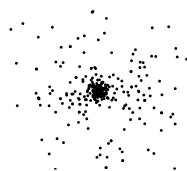

$\sigma^2_{\rm min}(BVR)$ by making a histogram of all the sources, approximating the histogram with a Gaussian (which is a relatively good fit) and taking the 1/e point. This point, and the value preferred by our visual inspection were almost identical at $\sigma^2_{\rm min}(BVR) = 0.05$.

In the remainder of the paper, when we refer to "clusters", we will mean sources that passed the following criteria:

- detected in the F439W, F555W, and F675W bands at at least 5σ above the background,
- photometric uncertainty < 0.2 mag in the F439W, F555W, and F675W bands,
- detected in at least one other band,
- well fit ($\sigma^2(BVR) < 0.05$) by an SSP model,
- brighter than the 90% completeness limits for each filter in which they are detected (see Table 3.2)

1150 clusters pass these criteria, which will be used to study the cluster population in M51. The majority of the sources (from the original 3504 sources detected) that have been removed from our sample were eliminated because they were fainter than one or more of our 90% completeness limits.

3.4.5. The elimination of stars on the basis of their energy distribution

In § 3.3.1 we argued that the expected number of very luminous stars that might contaminate our sample is relatively small. We have investigated the rejection of possible stellar sources from our sample on the basis of the energy distribution fitting. To this purpose we created energy distributions of stellar atmosphere models and analysed them in the same way in which we analysed the energy distributions of clusters.

We adopt the super-giant models calculated by Bessell et al. (1998), transformed to *WFPC2* magnitudes by Romaniello et al. (2002). Bessell et al. (1998) normalised the magnitudes to stars with a radius of 1 $R_\odot$ at a distance of 10 pc. They published 70 models with $T_{\rm eff}$ ranging from 3500 to 50000 K for a range of gravities from main sequence stars to super-giants. We adopted the energy distributions of these stellar models with the lowest gravity (without adding noise to their photometry) and then analysed the data as if the stars were clusters. We did this for stars that are observed in all six *WFPC2* bands (UV, U, B, V, R, I), and for stars observed only in the U, B, V, R bands or in the B, V, R, I bands.

We found that stars with effective temperatures higher than about 14,000 K all end up in the youngest age bin for clusters of $\log(t/{\rm yr}) \simeq 6.6$. If our sample is contaminated by massive stars, most of these will be blue, because they spend most

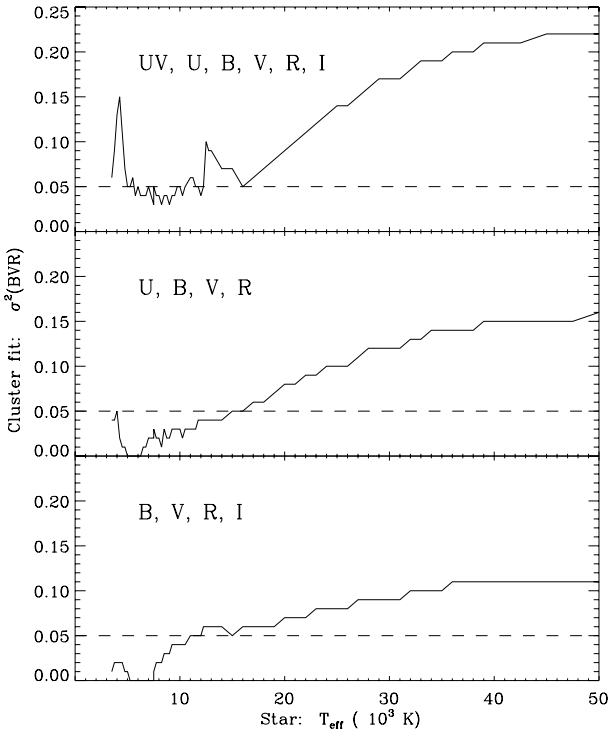

Figure 3.6: The elimination of possibly contaminating bright stars in our sample by means of the fitting of their energy distribution. The figure shows the values of the rejection criterion $\sigma^2(BVR)$ (Eq. 3.1) for stars of different temperatures in three different filter combinations. Notice that possibly contaminating stars with $T_{\rm eff} > 17\,000$ K will be effectively eliminated by our selection criterion $\sigma^2(BVR) < 0.05$.

of their time on or near the main sequence. If there is a red phase for such massive stars, the crossing time between the blue and the red phase is very short, only about 1% of the main-sequence phase. However stars with masses in excess of 50 $M_\odot$ are not expected to become red super-giants because that would bring them above the observed Humphreys-Davidson luminosity upper limit (Humphreys & Davidson 1979). We conclude that, *if* there is a sizable number of massive O-stars with $21.70 < V < 22.70$ mag, they will end up in the youngest age bin of our cluster sample.

Fig. 3.6 shows the values of $\sigma^2(BVR)$ as a function of the temperature of the stars, for stars observed in all six *WFPC2* bands, and for stars observed only in the B, V, R, I or U, B, V, R bands. Only stars below the dashed line pass our criterion of $\sigma^2(BVR) < 0.05$. We see that most of the stars will be rejected from our sample, except the coolest ones.

We concluded before (§ 3.3.1) that the expected contamination of our cluster sample of sources with $V < 21.70$ mag with bright stars is very small. Here we have

shown that our analysis of their energy distribution will eliminate a major fraction of these. The small number that may pass our selection criterion, are expected to end up in the youngest age bin.

3.4.6. The effect of metallicity

We have studied the effect of metallicity on the determination of the age, mass, and extinction of the clusters. To this purpose we follow the method of de Grijs et al. (2003b,c) and introduce metallicity into our models as a free parameter.

This technique has been applied recently to NGC 3310 (de Grijs et al. 2003c) with good results, and to NGC 6745 (de Grijs et al. 2003a) with somewhat less encouraging results as two metallicities were equally well represented in the final sample, due to the smaller number and narrower wavelength coverage of available passbands, and the inherent effects of the age–metallicity degeneracy. For NGC 3310 the authors report that the near-infrared colours of a cluster are a good indicator of metallicity, while optical colours do a better job at discerning ages (see also Anders et al. 2004).

To this end we have fit all sources in M51 which pass our criteria (see § 3.4.4) with models of four metallicities, namely Z = 0.004, 0.008, 0.02, and 0.05. We do not find any significant difference in the number of sources that pass our selection criteria ($\sigma^2(BVR) < 0.05$) between the different metallicity models. We find that 14%, 21%, 17%, and 48% of the sources in our sample are best fit (lowest $\sigma(BVR)^2$) by models of Z = 0.004, 0.008, 0.02, and 0.05 respectively. The largest percentage of the clusters being fit by twice solar metallicity models is consistent with the metallicity estimates of HII regions in M51 by Hill et al. (1997).

We note however, that many of the individual clusters within the same cluster associations show widely different metallicities. As this seems unphysical, we are forced to conclude that fitting on metallicity is not possible with the current data. We therefore choose to concentrate our analysis on the fits using the solar metallicity models (which is the median metallicity found in our sample), although we will discuss how our results depend on the assumed metallicity where applicable.

3.4.7. Recovery rates

In order to determine the recovery rate of the fitting method we use the artificial cluster sample generated in § 3.4.3. In Fig. 3.5 we found that the accuracy of the fit depended on the magnitude of the input cluster, with brighter clusters being fit with higher accuracy. Because of the input cluster IMF, which has many more fainter clusters than brighter ones, we need to quantify this affect. The recovery rate is defined to be the number of clusters found divided by the number of input clusters for a given age bin. Figure 3.7 shows the recovery rate as a function of age. This shows that we slightly over-predict the number of clusters in the age range of $\log(t/\mathrm{yr}) \in [6.62,6.87]$ and $\log(t/\mathrm{yr}) \in [7.37,7.62]$ by about 40 per cent. We underestimate the number of clusters in the age range of $\log(t/\mathrm{yr}) \in [6.87,7.12]$ by about 20%, and also tend to underestimate the number of clusters with ages greater than 10^8 yr. This is

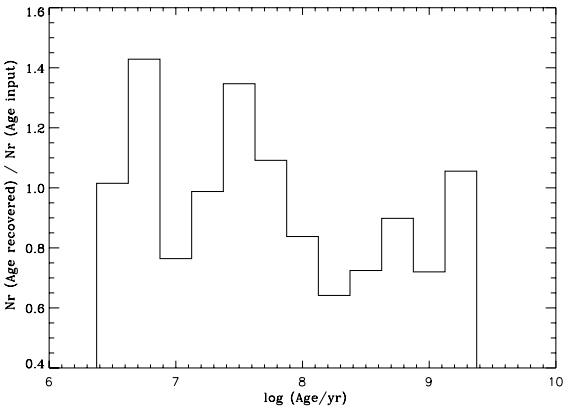

Figure 3.7: The recovery rate of our sample as a function of input age. We underestimate the number of clusters in the range of $6.9 < \log(t/\mathrm{yr}) < 7.1$ by about 25% and overestimate the number in the preceding age bin by $\sim 40\%$.

not a physical effect but due to the rapidly changing colours of the SSP `GALEV` models during this age range. We will use this recovery rate in § 3.6.2 where we study the cluster formation history of M51.

3.5. Extinction

Once we have derived ages, extinctions, and masses for all of the clusters, we can begin looking at general trends in the cluster population.

Figure 3.8 shows the distribution of the $E(B-V)$ values for different age groups. The left-hand side of the figure shows the number of clusters and the right-hand side shows their logarithmic values. The figure shows that at each age bin over half of the detected clusters have an extinction of $E(B-V) < 0.05$ mag, with the rest showing a rapidly declining distribution up to $E(B-V) \simeq 0.8$ mag. The logarithmic figures show about the same distribution of the clusters with $E(B-V) > 0.05$ mag, with $\mathrm{d}\log(N)/\mathrm{d}E(B-V) \simeq -2.0$. This relation is independent of age, although the highest extinction found decreases strongly with ages. This is presumably due to the fading of clusters as they age, bringing them closer to the detection limit, so older clusters with a significant amount of extinction will drop below the detection limit. Another effect that could contribute to the observed distribution is if young clusters have more extinction than older clusters, which is expected as young clusters form in gas rich environments.

The large numbers of clusters found with low extinction is qualitatively what is expected. The cluster IMF of $N(M) \sim M^{-\alpha}$, with $\alpha \simeq 2$, implies an increase in

cluster numbers towards the lower mass and fainter clusters. The magnitudes of these low mass clusters are close to the detection limit, so they can only be detected if their extinction is small. Thus our sample is complete to larger extinction values for brighter clusters, and for younger ages which are less affected by the detection limit (see Fig. 3.10). This effect will affect all cluster studies where the host galaxy is not optically thin (i.e. studies where one cannot see through the host galaxy at the given completeness limits).

In Fig. 3.9 we show the extinction as a function of age for the clusters in our sample. The solid points are the mean of all the points for each age bin and the error bars represent the variance about the mean. This figure shows that the average extinction is higher for young clusters ($\leq$ 20 Myr) and rather abruptly drops to a constant value for clusters older than 20 Myr. This is qualitatively what is expected as clusters emerge from their parent molecular cloud, although as we noted above, there is a selection effect which causes us to detect younger clusters to higher extinction values.

3.6. The age distribution of the clusters

It has been shown that the global properties of the host galaxy, such as an interaction or merger, can significantly affect the cluster formation rate (CFR) within a galaxy (e.g. de Grijs et al. 2003b). To search for such an effect within M51, we combined our cluster sample, with the detailed models of the interaction between M51 and its companion, NGC 5195, taken from the literature (SL00). SL00 propose a scenario in which NGC 5195 has had two close passages with M51, an early encounter at approximately 400-500 and a second at 50-100 Myr ago (the last passage). Their *double encounter* model reproduces the kinematic features of the system better than the single passage models (such as, e.g., the apparent counter-rotation of the southern HI-tail), as well as the morphological "kink" in the northern spiral arm.

3.6.1. The mass versus age diagram

Figure 3.10, top left panel, shows the age of each cluster plotted against its determined mass. (We remind the reader that this is the present mass of the cluster.) Note the presence of a clear lower mass limit which increases with age. This is due to the evolutionary fading of clusters as they age, which raises the minimum mass that the clusters should have to be brighter than our detection limit. Hence, the lack of old low-mass clusters is mainly an effect of fading due to stellar evolution (another important effect is cluster disruption, which will be treated in Paper III). The solid lines increasing to the right show the detection limit for $m_{\rm F555W} = 22.7$ mag, i.e. the adopted magnitude limit of the sample, and 21.7 mag.

The figure shows the apparent concentrations of the clusters in some very narrow age bins, i.e. at $\log(t/{\rm yr})$=7.2, 7.3 and near 7.8. This is not a physical effect but it is due to the way we select the best fitting models in the study of the cluster SEDs with

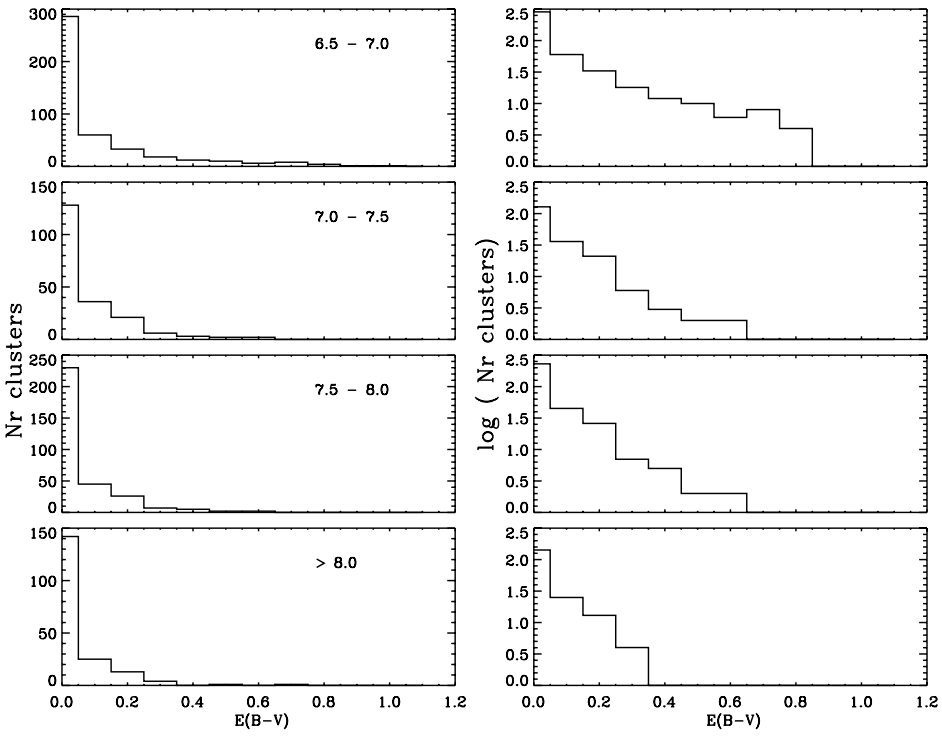

Figure 3.8: The histograms of the extinction for different age bins (given in the upper right of the panels in the left column, in logarithmic years). The left-hand panels show the linear distribution (N versus $E(B-V)$) and the right-hand panels show the logarithmic distribution ($\log(N)$ versus $E(B-V)$). Notice the strong peak near $E(B-V) \simeq 0$ mag and the steeply declining relation towards $E(B-V) \simeq 0.8$ mag.

the 3DEF-method (see § 3.4.3 and Paper I). In reality these peaks should spread over the neighbouring age bins.

The top right panel in Fig. 3.10 shows the relation between the age and masses of those clusters whose sizes are resolved. The general properties are the same as for the full sample, namely the increase in the lower mass limit as a function of increasing age, an excess of clusters with young ages (< 10 Myr), and an additional excess at 60 Myr. Therefore, we conclude that we are not biasing our study by including unresolved sources.

As mentioned above, certain artifacts of the age *vs.* mass distribution are likely caused by model and fitting effects, which do not reflect anything physical. Since this complicates the analysis, we attempt to correct for these effects using the simulations from § 3.4.7. To do this, we generate a number density grid in the age *vs.* mass space

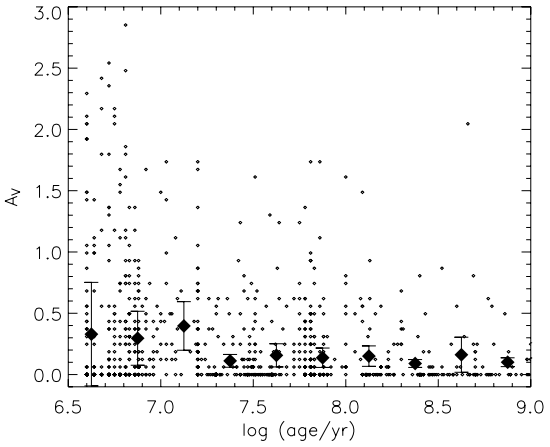

Figure 3.9: The extinction as a function of age for the clusters in our sample. The solid points are the mean for each age bin, while the error bars are the variance about the mean. Note that the extinction is higher for clusters with ages less than 20 Myr than for the older clusters.

for our observed cluster sample as well as for our simulated cluster sample (cluster IMF with slope -2.0, continuous cluster formation rate, and random extinction between $0 < E(B-V) < 1$ mag with a Gaussian probability function that has $\sigma = 0.20$ mag). The model number density is normalised in order that the average is the same as the observations (i.e. we normalise to the cluster formation rate). We then divide the observed cluster distribution by that of the simulated distribution. This technique will remove any features caused by the adopted models or the fitting method.

This process and the result are shown in Fig. 3.11. It shows the number density of the clusters in the mass versus age diagram in a logarithmic grey-scale, normalised in such a way that the number densities run from light to dark grey. The top left panel shows the density of the *observed* clusters in the mass versus age diagram. The top right panel shows the density of the *generated* cluster sample with a constant cluster formation rate and a power law cluster IMF. The lower panel shows the *ratio* of the observed to predicted cluster number densities in the diagram. For the top panels, dark shading represent high numbers of clusters, while for the bottom dark shading represents an over-density of observed clusters compared to that expected from the models. In order to fully interpret the final result, it is important to understand the simulated cluster sample. Two of the strongest features in Fig. 3.11b are the increase in the number density from the top of the panel to the bottom as well as from left to right. The increase in the number of clusters at lower masses (top to bottom in Fig. 3.11b) is due to the cluster initial mass function, which gives many more low-mass than high-mass clusters. The increase in the number (for a given mass bin) of

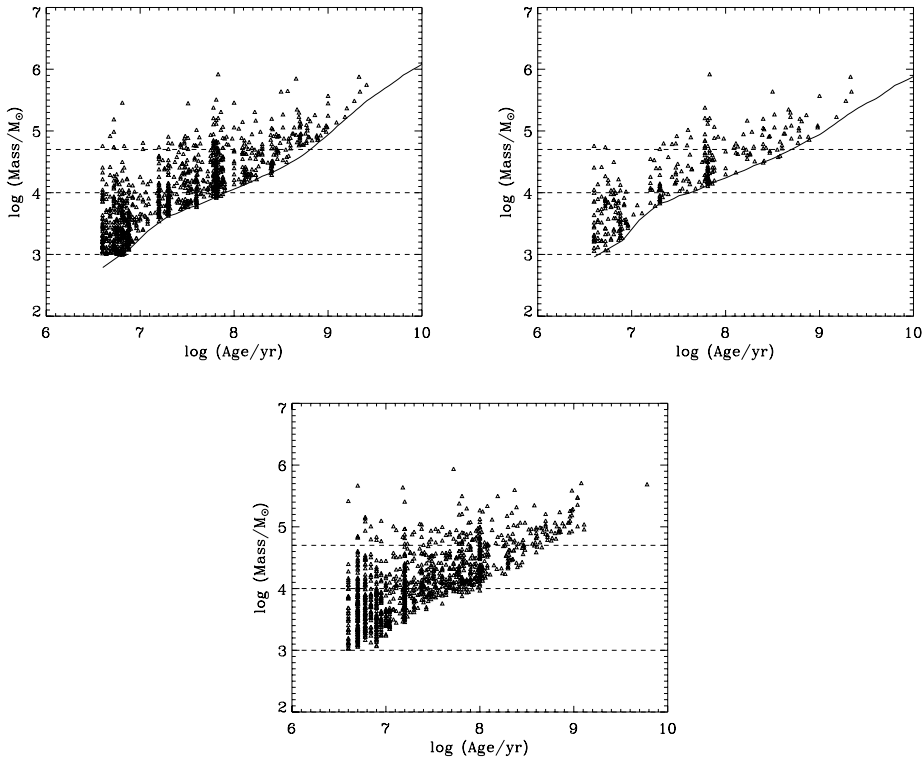

Figure 3.10: **Top left:** The present mass as a function of age for the 1078 clusters that pass our σ criterion and which have a present mass greater than 1000 $M_{\odot}$. The solid line is the predicted detection limits using the GALEV models, for m(F439W) = 22.6 mag. The horizontal dashed lines represent constant mass cutoffs used in Fig. 3.12. **Top right:** The same as above, but only for those clusters with measured sizes greater than 2 pc. The solid line is the predicted detection limit for m(F555W) = 22.0 mag **Bottom:** The present mass as a function of age while leaving metallicity run as a free parameter.

clusters from younger to older (left to right) is due to the logarithmic age-binning and the assumed constant cluster formation rate in linear time.

Once we divide our observed distribution (Fig. 3.11a) by the simulated distribution (Fig. 3.11b) we have the *true* age vs mass distribution which is shown in Fig. 3.11c. Since the effects of the cluster IMF and the logarithmic binning have been removed in this comparison, the decrease in number density from the lower left of Fig. 3.11c to the upper right is presumably caused by the disruption of the clusters. Additionally we find relative excesses in the number density at ages of $\sim$ 60 Myr and $\sim$ 6 Myr. These two features will be discussed in more detail in § 3.6.2 and § 3.7, respectively.

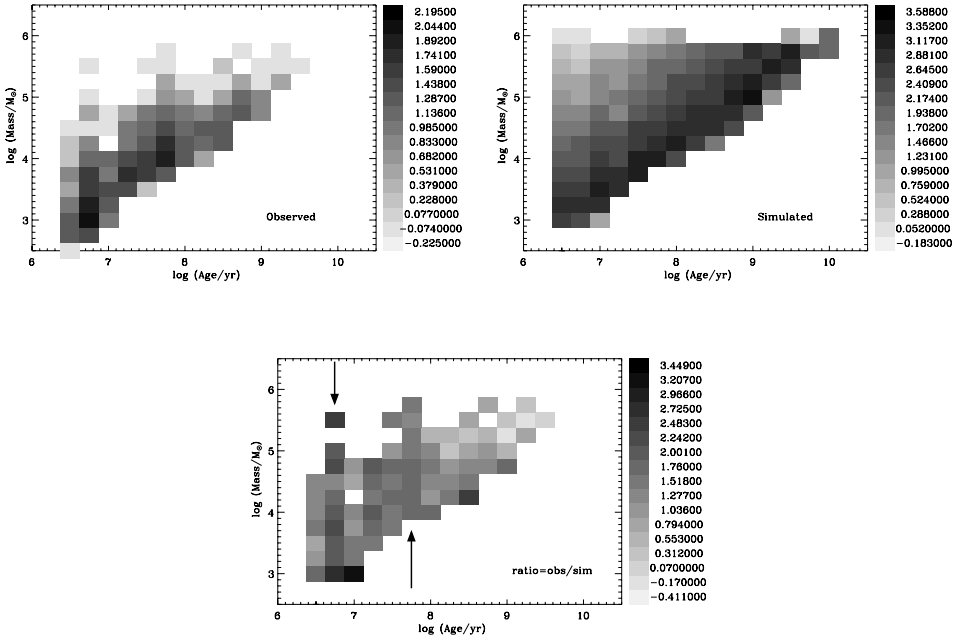

Figure 3.11: **Top left(a):** The present mass as a function of age for the 1152 clusters that pass our selection criterion. The shading represents the logarithmic number density, with the scale given on the right. **Top right(b):** Same as (a), but for the simulated cluster sample with a constant cluster formation rate (see § 3.4.3 for details). **Bottom(c):** The ratio between the observed distribution (top) and the predicted distribution (middle). The arrows indicate two age bins which have an over-density of clusters relative to the simulated cluster sample.

3.6.2. The cluster formation history

In the previous section we found an excess of clusters at ages $\sim$ 60 Myr, corresponding in time to the *last* passage of NGC 5195 and M51 in the SL00 models. In order to quantify this excess we will look at the age distribution directly (i.e. by collapsing the mass axis in Fig. 3.11c). As shown in § 3.6.1, for a given magnitude-limited sample, we are able to detect clusters to lower masses for younger ages than for older ages. Therefore, we will detect more younger than older clusters (assuming the standard cluster IMF which predicts many more lower mass than higher mass clusters), simply due to selection effects. Thus, in order to trace the true age distribution of the sample, the analysis must be restricted to masses above a certain limit, where the sample is complete for the age range of interest. This effect is shown in Fig. 3.12 by looking at the age distribution and applying the constant mass cuts

shown in Fig. 3.10. The mass cuts are at 10^3, 10^4, and $5{\times}10^4 M_\odot$, the last one chosen so that we are complete for ages younger than 1 Gyr.

The left-hand side of Fig. 3.12 shows the number of clusters detected per logarithmic age bin while the CFR (in number per Myr) is shown on the right-hand side. For the calculation of the CFR, we have corrected the age distribution of the detected clusters for the recovery rates (Fig. 3.7) in order to eliminate spurious effects. The difference in appearance between the two sides is due to the logarithmic binning of the left-hand side (e.g. each bin spans a larger age range than the preceding bin). Note that the distributions for different mass cuts appear very different.

If we look at the sample in which we are complete for the past Gyr (i.e. for masses $> 10^{4.7}$ $M_\odot$) we see a clear indication of an increase in the CFR $\sim$ 60 Myr ago. In addition, we also find the peak at $\sim$ 6 Myr, that was seen in Fig. 3.11c. This peak is presumably due to the presence of a large number of unbound clusters, and will be discussed in detail in § 3.7.

The increase in the CFR at $\sim$ 60 Myr ago for clusters with $\log(M/M_\odot) > 4.7$ occurs at the time of the proposed second encounter between M51 and NGC 5195. The CFR appears to have been 2 to 3 times higher during the burst period than in the period immediately preceding it. The CFR declines slightly after the initial rise, but remains significantly higher than before. In Fig. 3.12 we note the CFR rises extremely rapidly at the onset of the burst, and decays much more smoothly, consistent with a linear Gaussian distribution plotted on a logarithmic scale.

Duration of the burst

An increase in the CFR at the time of an interaction has been shown for other galaxies, e.g. NGC 6745, M82 and NGC 3310 (de Grijs et al. 2003a,b,c, respectively). While the duration of the burst of cluster formation in M51 is rather short lived, we note that this is similar to the distribution observed in NGC 3310 (de Grijs et al. 2003c) where the estimated duration of the increase in cluster formation rate was $\sim$ 20 Myr (it should be noted that their method of analysis was very similar to the one presented here). Presumably, the increase in the CFR in M51 was likely caused by the tidal interaction between M51 and NGC 5195 $\sim$ 60 Myr ago, supporting the *two encounter* model of SL00.

Tidal interactions can influence large portions of a galaxy within a relatively short time, and is the only known mechanism that could coordinate galaxy-wide starbursts on the timescales presented here. Recently, Murray et al. (2005) have shown that there is an Eddington-like maximum luminosity for starburst galaxies. This luminosity is a critical luminosity where there exists a balance between gravity and radiative pressure caused by the young stars formed. When a starburst is tidally triggered, as is the case in M51, the (starburst) luminosity can grow rapidly. When this growth happens on a shorter time scale than the dynamical (free fall) timescale of the starbursting system, in this case giant molecular clouds, the luminosity grows beyond the critical luminosity and star formation rate stops. This could explain the narrow burst length observed in the cluster formation rate. Solomon et al. (1987) give typical values

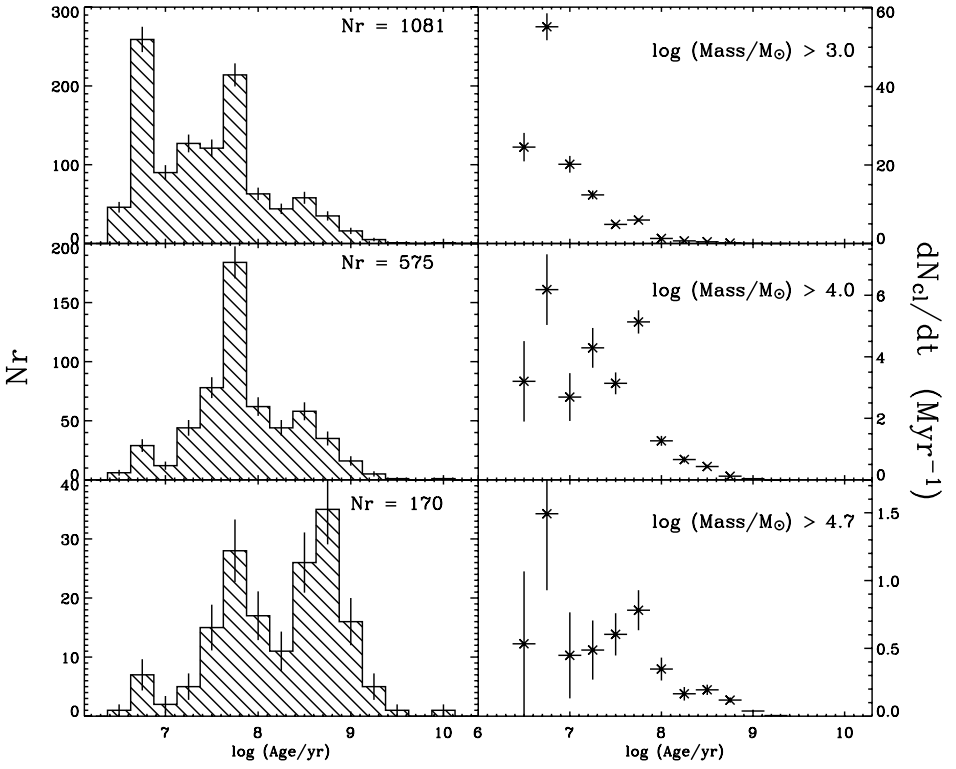

Figure 3.12: Differences between the age distribution and the formation distribution. Left: the number of clusters found per age bin for three mass limits. Right: the cluster formation rate (number per Myr) as a function of age, corrected for the recovery errors given in Fig. 3.7. Adopting different mass limits clearly biases the interpretation of the distribution.

for molecular clouds in the Galaxy. The dynamical time scale can be estimated by: $t_{\rm dyn} \simeq r_{\rm eff}/\sigma = {r_{\rm eff}}^{1/2}$, where σ is the velocity dispersion inside the cloud. Thus, $t_{\rm dyn}$ is between 6 - 15 Myr for molecular clouds in the mass range $10^6 - 10^{7.5} M_\odot$ as found in M51 (Rand & Kulkarni 1990), which are the most likely progenitors of star clusters in M51. This may explain the short duration of the burst in M51.

3.6.3. Spatial Dependence of the Cluster Formation Rate

Figure 3.13 shows that the cluster formation history does not differ significantly between the two sides of the galaxy, although the west side of the galaxy seems to have approximately twice as many clusters as the east side. This is not an effect of the differing detection limits between the two pointings, as we have restricted our analysis to magnitudes brighter than the 90% completeness limit of the shallowest

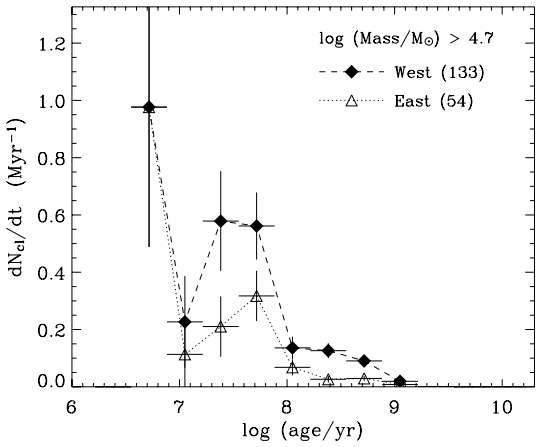

Figure 3.13: Spatial dependence of the cluster formation rate. We have not corrected the rates here for fitting errors. We note that the general trend in the formation rate is similar between the two sides of the galaxy.

observation.

The higher cluster formation rate on the west side of the galaxy is also reflected in the presence of large, isolated and young star cluster complexes located in the western spiral arms, that appear to be largely absent in the eastern spiral arms (Bastian & Gieles 2004). These complexes are typically less than ~ 6 Myr old, contain 3×10^4 to $3 \times 10^5 M_{\odot}$, and are associated with large concentrations of CO (Henry et al. 2003).

Henry et al. (2003) studied the present day star formation rate (SFR) and its relation to the molecular cloud content in the spiral arms of M51, based on *NICMOS* (Paα) and BIMA-SONG (CO 1-0) observations. They find that both the molecular cloud content and the SFR are higher in the NW and W spiral arm (regions 1a and 1b in their terminology) than in the SE and E arm (regions 2a and 2b). Thus the larger amount of clusters that we find in the western arm is consistent with the measured higher SFR on this side of the galaxy.

3.7. A population of short-lived clusters

As noted in § 3.6.2, the cluster formation history of M51 shows are large increase during that last $\sim$ 6 Myr (see Fig. 3.12). This can be interpreted in two ways, either M51 is experiencing a burst in cluster formation right now, or that a significant portion of the very young clusters ($<$ 10 Myr old) will disrupt within the next few Myr. Three additional observations argue for the latter scenario. First, a similar feature has been observed in the NGC 4038/39 system (Whitmore 2003). Second, we

know of many loose open star clusters within the Galaxy that are expected to disperse on timescales shorter than 10 Myr (e.g. Lada & Lada 1991). Lastly, $\sim$ 10 Myr is the timescale given for NGC 5253 for clusters to dissolve and disperse their stars into the field (Tremonti et al. 2001). Adopting this scenario, we can explore what percentage of the young clusters will disrupt within the next few Myr.

To do this we compare the observed "formation" rates in the first two bins of Fig. 3.12, i.e. the bins of $\log(t/\mathrm{yr})$=6.6 to 6.93, and 6.93 to 7.26. In Fig. 3.14 we show the percentage of the young clusters that are expected to disrupt before they age to older than 10 Myr, as a function of their mass. One striking feature of this figure, is that the percentage of the clusters disrupted is largely independent of mass within the uncertainties of the measurements.

The mean value of the number ratio of clusters in the logarithmic age bins of (6.93,7.26) compared to (6.6,6.93) for clusters with a mass in the range of $3.5 < \log(M/M_{\odot}) < 5.0$ is 68$\pm$ 15%. This is comparable to the fraction ($\sim$ 87%) of missing clusters less than 10^8 years (observed relative to predictions based on embedded star clusters in GMCs) in the solar neighbourhood estimated by Lada & Lada (1991). This missing fraction is presumably made up of unbound clusters that have dispersed. For clusters to disappear from our sample due to expansion, their radius should extend over more than $\sim$ 3 pixels (with the exact value depending on the cluster's brightness and the brightness of the local background), corresponding to a linear size of 48 pc. For a mean initial velocity dispersion of the stars in a cluster of about 10 km s^{-1}, this corresponds to a disruption time of about 5 Myr.

The largely mass independent destruction rate of the clusters is in stark contrast to other observed disruption patterns (Boutloukos & Lamers 2003) in which the disruption timescale is heavily dependent on the initial mass of the cluster. Boutloukos & Lamers (2003) found that the disruption time depends on the cluster mass to the power 0.6 for cluster systems in four different galaxies. Also theoretical disruption studies of young cluster populations (e.g. Vesperini 1998; Fall & Zhang 2001; Baumgardt & Makino 2003) have shown a strong dependence of the disruption timescale on the mass of the cluster. This implies that there are two distinct stages of disruption. The first, mass independent, operates on very short timescales and may be related to the sudden removal of gas from the system caused by super-novae and stellar winds (Boily & Kroupa 2003). This effect has been dubbed "infant mortality" (e.g. Whitmore 2004) and it corresponds to the rapid disruption of unbound clusters. The second stage of disruption, strongly mass dependent, operates on longer timescales and is a combination of different effects, including evaporation, tidal fields, and relaxation.

Indeed, we expect that the first period of disruption is largely mass independent in order that the mass functions (as interpreted through the luminosity function) of extremely young ($<$ 10 Myr) cluster systems such as in the Antennae (Whitmore et al. 1999b) is similar to that of intermediate-age populations (300 Myr - 3 Gyr) such as in NGC 7252 (Miller et al. 1997) and NGC 3610 (Whitmore et al. 2002).

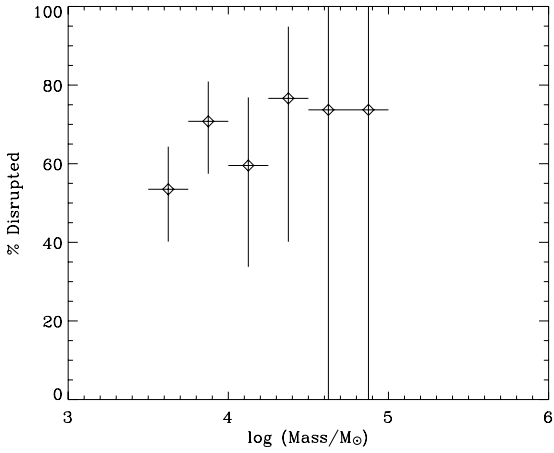

Figure 3.14: The fraction of the young (< 10 Myr old) clusters per mass bin that are expected to disrupt within the next ∼ 10 Myr.

3.8. Cluster sizes

Using the `ishape` algorithm by Larsen (1999), we have attempted to derive the effective radius of all clusters on the WF chips in M51 with an observed F439W magnitude brighter than 22.6 mag. We have restricted ourselves to these brighter clusters, as fainter clusters do not have a high enough signal-to-noise ratio for unambiguous model fits. Briefly, the algorithm convolves a two dimensional analytical model (e.g. a King profile) with the PSF and diffusion kernel of the F555W filter for a given WFPC2 chip. We have modelled the PSF of the F555W filter with `Tiny Tim`, at position $x = 400, y = 400$ for each of the three wide field chips. We have tested whether the fits change significantly if the PSF used is from a different portion of the chip, and find that the difference is marginal, on the order of 10% in the derived radius. The algorithm then compares the model with the observed cluster profile using a reduced χ^2 test. For each observed cluster, multiple King profiles, all with concentration factor 30, of varying sizes were compared and the best fit model was selected. We then converted the measured FWHM of the profile to effective radius, $r_{\rm eff}$ (Larsen & Richtler 1999).

Following Larsen (2004), the minimum value accepted for a 'resolved' cluster was a FWHM of 0.2 pixels. At the distance of M51, a FWHM of 0.2 pixels for a King profile with concentration factor 30 corresponds to an $r_{\rm eff}$ of 1.2 pc. We adopt the more conservative lower limit of 2 pc when making the subsample of resolved clusters from the full cluster sample. We caution that this size criterion biases the sample towards large clusters, but due to the resolution of the data, clusters smaller than this criterion do not have well determined radii. This results in 407 clusters that pass

the criteria given in § 3.4.4, have reliable size measurements of ≥ 2 pc and are located more than 3 pixels away from the nearest source. The final criterion was applied in order to avoid contamination by neighbouring sources in the size determination. The size criterion ($r_{\rm eff} \geq 2$ pc) eliminates 552 clusters from the sample. Of the 91 sources that were detected in four or more bands, did not pass our $\sigma^2(BVR)$ criterion, and were brighter than $V = 22.0$, 84% were unresolved. This provides further evidence that our cluster selection eliminates the majority of contaminating individual stars from our sample.

Additionally, we have tested the reliability of the derived fit as a function of the magnitude of the cluster. To do this we generated 20 artificial clusters with effective radii between 0.65 and 12.4 pc for magnitudes $V = 20, 21, 22$, and 23 mag (i.e., 80 clusters in total). We added these analytic profiles to the F555W images and re-fit them using the above method. Figure 3.15 shows the results of these tests. As a function of decreasing brightness, the first clusters to deviate from the input radius are the large clusters. This is due to the fact that the outer parts of the clusters will be lost in the background noise, and so larger clusters will be affected first.

The distribution of sizes for all clusters more than 3 pixels away from the nearest source, is shown in Fig. 3.16. The dashed line in the figure is a power-law fit to the data of the form $N(r){\rm d}r \propto r^{-\eta}{\rm d}r$, with $\eta = 2.2 \pm 0.2$, where the fit was carried out only on clusters with $r_{\rm eff} > 2$ pc (i.e. the resolved sample) and $r_{\rm eff} < 15$ pc (most larger sources were determined to be blends of sources upon visual inspection). We note that this fit overestimates the number of small clusters, a possible indication of a turnover in this distribution. We compare this to the size distribution of the Galactic globular clusters, by using the data available in the McMaster catalogue (Harris 1996a)[4]. Fig. 3.17 shows the size distribution (half-mass radius) of the Galactic globular clusters, along with the best fitting power-law with $\eta = 2.4 \pm 0.5$. We note that the size distribution of the M51 clusters is different from that reported for the young cluster system in the merger remnant NGC 3256, which is characterised by $\eta = 3.4$ (Ashman & Zepf 2001). In that same work, the authors report that the size distribution of the Galactic globular clusters has $\eta = 3.4$, significantly steeper than that found here (although using the same catalogue). This may have been caused by the erroneous addition of $+1$ to η in the fitting of the size distribution (seeElmegreen & Falgarone 1996 for a correction of a similar point of confusion in the data of Galactic GMCs). We therefore report that the size distribution of the old Globular clusters in the Galaxy and that of the young M51 clusters (and possibly that of the young NGC 3256 system) has the same form, within the errors. This distribution is, however, significantly different from the Galactic GMC size distribution, which is characterised by $\eta = 3.3 \pm 0.3$ (Elmegreen & Falgarone 1996), in contrast with what was reported by Ashman & Zepf (2001).

The similarity between the size distributions of MW GCs and young star clusters suggests that disruption processes (which have had a much longer time to act on the MW GCs) have not preferentially acted upon the larger clusters. Thus, cluster disrup-

[4]We used the revised February 2003 version, http://physun.physics.mcmaster.ca/Globular.html

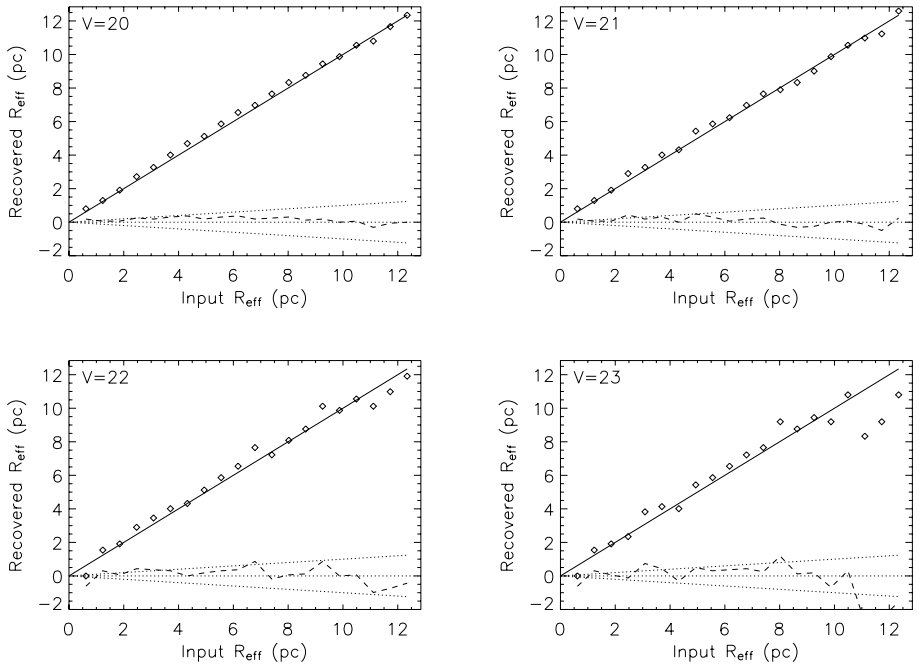

Figure 3.15: A test of the accuracy of the measurements of cluster radii. The derived effective radius as a function of both the input effective radius and the magnitude. A one-to-one relation is shown by the solid line. The difference between the recovered and the input radii is shown as the dashed line, while the dotted lines show the value 10% difference between the input and the recovered radii.

tion appears to be largely independent of size. Additionally, the strong resemblance between size distributions of M51 and the Galactic globular clusters lends support to the idea of a universal formation mechanism for star clusters.

3.9. Correlations with the cluster radius

With a dataset such as compiled in this work, it is interesting to search for correlations among the derived parameters. In particular we are interested in relations which may reflect the formation mechanism of star clusters. Much emphasis has been placed on the relation between the size of a cluster and the cluster's mass/luminosity (e.g. Zepf et al. 1999; Ashman & Zepf 2001). The GMCs that are presumed to be the birth place of young clusters follow the relation $r_{\rm cloud} \propto M_{\rm cloud}^{1/2}$ (Larson 1981). Young clusters, such as those in merging galaxies (Zepf et al. 1999) and in spiral galaxies (Larsen 2004) show only a slight correlation (if at all) between their radii and masses.

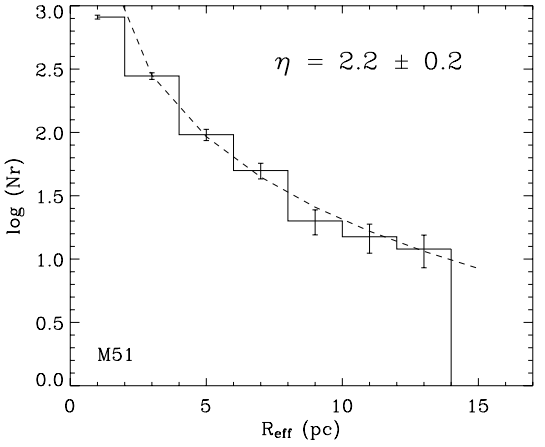

Figure 3.16: Size distribution of all clusters more than 3 pixels away from the nearest source. The dashed line is a power-law fit to the data of the form $N(r)\mathrm{d}r \propto r^{-\eta}\mathrm{d}r$, with $\eta = 2.2 \pm 0.2$. The fit was carried out for all clusters with $2.0 < r_{\rm eff} < 15.0$ pc. The power-law fits the data quite well for sources greater than 2 pc, although it over-estimates the number of small clusters (unresolved clusters were given a size of 0 pc) with respect to the observations.

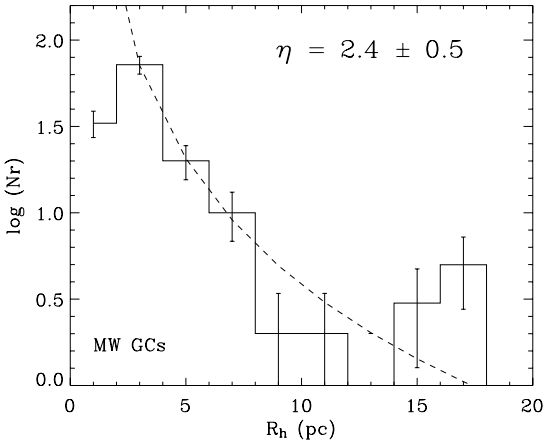

Figure 3.17: Size distribution (half mass radius) of the Galactic globular cluster population. The dashed line is a power-law fit to the data of the form $N(r)\mathrm{d}r \propto r^{-\eta}\mathrm{d}r$, with $\eta = 2.4 \pm 0.5$. The fit was carried out for all clusters with $2.0 < r_{\rm eff} > 15.0$ pc.

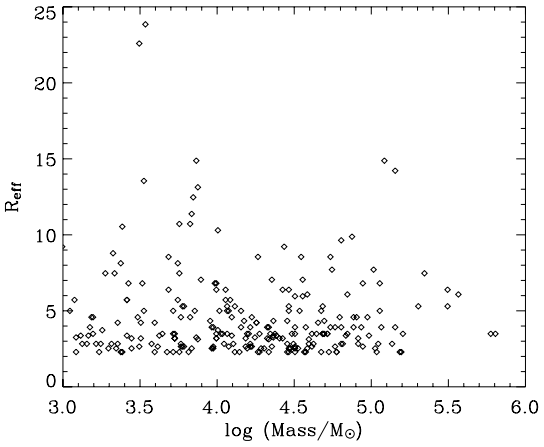

Figure 3.18: The cluster mass *vs.* radius for all clusters with $r_{\rm eff} > 2$ pc and located more than 3 pixels away from the nearest neighbouring source.

The results using our sample are shown in Fig. 3.18. There is no apparent direct relation between the mass and size of a cluster in M51.

Recently, Larsen (2004) has shown that young clusters in spiral galaxies have shallower luminosity profiles than older clusters, presumably due to an extended halo surrounding young clusters, although no correlation between size and age is found. In § 3.8 we presented our method used to derive the cluster sizes, which assumed a constant cluster profile, unlike the study of Larsen (2004) which also solved for the best fitting cluster profile. Figure 3.19 shows the effective radii *vs.* ages for the resolved clusters in our M51 sample. No strong correlation is found, although there is a slight tendency for younger clusters to be more extended than their older counterparts. We also note that if we include the unresolved clusters (assigning an effective radius of 1 pc) this slight trend is removed.

We have also attempted a multi-variable fit of the form:

$$r_{\rm eff} = b \times {\rm age}^x * {\rm mass}^y. \tag{3.2}$$

The derived exponents, x and y, are -0.051 ± 0.027 and 0.048 ± 0.031, respectively, if we restrict the sample to only the most robust measurements, $3 < r_{\rm eff}({\rm pc}) < 10$ and sources more than 5 pixels away from the nearest source. As before we see a slight trend of the size decreasing with increasing age as well as a slight increase in size with increasing mass, though both relations are quite shallow and have rather large uncertainties.

Van den Bergh et al. (1991) report that globular clusters in the Galaxy follow the relation $D_{\rm eff} \propto R_{\rm gal}^{1/2}$ (with a large scatter) where $D_{\rm eff}$ is the diameter within which half the light of the cluster is contained, in projection, and $R_{\rm gal}$ is the distance of the

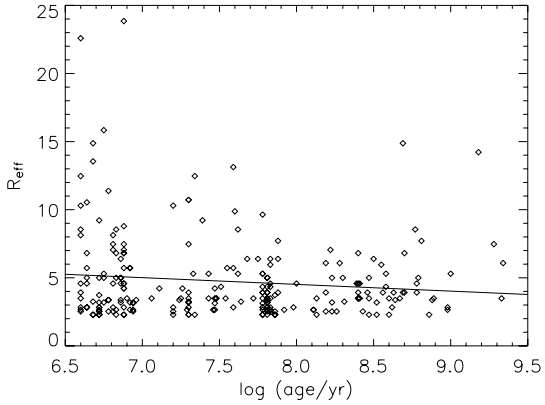

Figure 3.19: The age of the clusters *vs.* their effective radii. There is a slight tendency for younger clusters to be larger than their older counterparts, but the scatter is large.

cluster to the Galactic centre. They interpret this result as suggesting that compact clusters form preferentially near the c enters of galaxies where the density of gas clouds is higher than in the outer regions of the galaxy. We have searched our sample in two ways to see if a similar effect is present. We have looked for a relation between the effective radius of a cluster and its galactocentric distance (Fig. 3.20) as well as a trend between the stellar density (instead the effective radius) of each cluster and its galactocentric distance (Fig. 3.21). No clear relation can be seen. This may mean that the young clusters are forming by a different mechanism than globular clusters. This may simply be due to our sample coming mainly from the disc of M51 while the globular clusters presumably formed outside the Galactic disc. Alternatively, the relation found for old globular clusters in the Galaxy may be due to disruption effects which have had a much longer time to work on globular clusters than on the young disc population in the M51 sample.

3.10. Conclusions

We have analysed the star cluster population of the interacting galaxy M51. By comparing the broad-band magnitudes with those of SSP models, we have derived the ages, extinction values and masses of 1152 clusters with ages between 4 Myr and 10 Gyr, and masses between $10^{2.7} - 10^{6} M_{\odot}$. The main conclusions can be summarised as follows:

1. In order to examine the cluster formation history within a galaxy, a minimum mass cut-off must be applied, above which the sample is complete over the entire

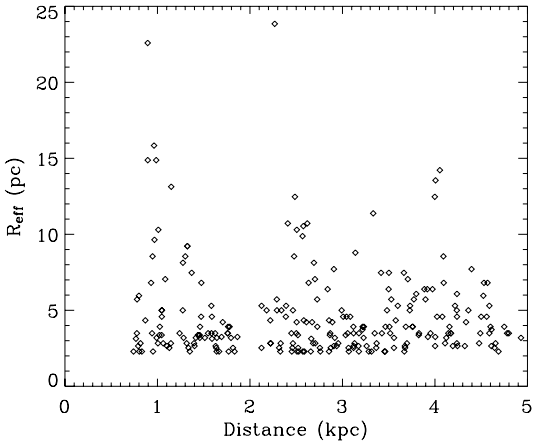

Figure 3.20: The effective radii of a clusters versus their distance to the nucleus of M51. No trend is apparent in the data.

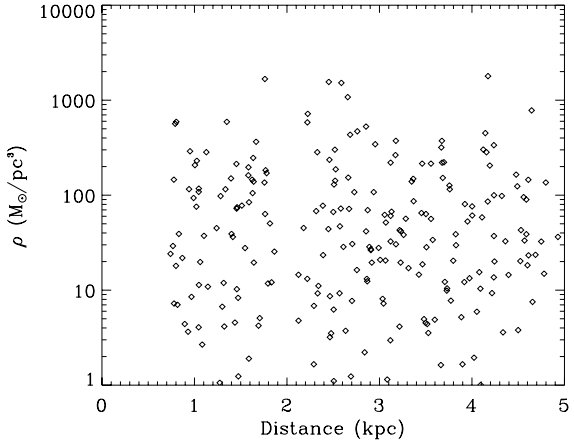

Figure 3.21: The density of the clusters versus their distance to the nucleus of M51. No trend is apparent in the data.

age range of interest. This avoids the bias introduced by the effects of the fading of clusters due to stellar evolution.

2. The cluster formation rate increased significantly approximately 60 Myr ago, which is coeval with the proposed *second encounter* between M51 and its companion NGC 5195. We interpret this as evidence supporting the multiple encounter model of Salo & Laurikainen (2000).

3. The number of young (< 10 Myr) clusters is much higher than would be expected for a constant cluster formation rate over the past 20-30 Myr. By comparing the formation rate during the past 10 Myr to that between 10-20 Myr, we find that $\sim 70\%$ of the young clusters will disrupt before they are 10 Myr old. This process appears to be independent of mass, which implies that it is a fundamentally different disruption mechanism from that which dominates the disruption of older clusters. Thus, there seem to be at least *two* distinct modes of cluster disruption. The first mechanism operates during the first ~ 10 Myr of the cluster's lifetime while the second operates on significantly longer timescales. We suggest that the first may be due to rapid gas removal from the emerging young cluster, based on the models of Boily & Kroupa (2003). This is similar to the fraction of unbound clusters in the solar neighbourhood. The second mechanism has been extensively modelled (e.g. Vesperini 1998; Fall & Zhang 2001; Baumgardt & Makino 2003) and includes two-body encounters within the cluster, disc shocking, and stellar evolutionary processes. This disruption mechanism was studied for M51 by Boutloukos & Lamers (2003), based on the cluster study in one of the *WFPC2* chips presented in Paper I. We will improve this disruption study in detail in Paper III, based on the new and largely extended cluster sample presented in this paper.

4. The western side of M51 contains a significantly higher number of star clusters, although the age and mass distributions of the clusters present do not show any large discrepancies. This trend is also reflected in the presence of large, isolated, and young star cluster complexes located in the west spiral arm, which appear to be absent on the east side of the galaxy. This is also consistent with the estimated star formation rates of Henry et al. (2003).

5. The cluster effective radius distribution can be well approximated by a power-law of the form $N(r)\mathrm{d}r \propto r^{-\eta}\mathrm{d}r$, with $\eta = 2.2 \pm 0.2$. This is remarkably similar to the distribution of old Milky Way Globular Clusters, which is characterised by $\eta \simeq 2.4 \pm 0.5$. These distributions are significantly different from the Galactic giant molecular cloud (GMC) distribution ($\eta = 3.3$). The agreement between the size distributions of the old Galactic globular clusters and the young clusters in M51 suggests that cluster disruption is largely independent of cluster size and argues for a universal cluster formation mechanism.

6. We have searched our dataset in order to look for correlations among the derived parameters. From this study we report that:

a) We find a strong correlation between the age of a cluster and its extinction, with the youngest clusters (< 10 Myr) having $< A_V > \approx 0.55$ mag, while the oldest clusters (~ 1 Gyr) have $< A_V > \approx 0.30$ mag. At an age of ~ 20 Myr the extinction drops suddenly, and then remains relatively constant for older ages. This is qualitatively expected as clusters emerge from the molecular cloud from which they formed.

b) A shallow relation is found between the effective radius of a cluster and its mass.

c) There is a marginal correlation between the age of a cluster and its effective radius, with young clusters being slightly larger than older ones.

d) Contrary to observations of globular clusters in the Galaxy, no correlation between the size of a cluster and its galactocentric radius is found. Additionally, no correlation between density and galactocentric radius is apparent in our dataset.

acknowledgements We thank Søren Larsen for useful discussions of the work and comments on the draft, both before and during the refereeing process. Additionally, we thank Michael Fall, Brad Whitmore, and Rupali Chandar for useful discussions, and Phillip Massey for help in estimating the contamination by field stars. We also thank Cees Bassa for making Figs. 3.1 & 3.2.

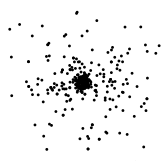

CHAPTER 4

The star cluster population of M51: Cluster disruption and formation history

M. Gieles, N. Bastian, H.J.G.L.M. Lamers and J.N. Mout

Astronomy and Astrophysics, v.441, p.949–960 (2005)

Abstract In this work we concentrate on the evolution of the cluster population of the interacting galaxy M51 (NGC 5194), more precisely the time-scale of cluster disruption and possible variations in the cluster formation rate. We present a method to compare observed age *vs.* mass number density diagrams with predicted populations including various physical input parameters like the cluster initial mass function, cluster disruption, cluster formation rate and star bursts. If we assume that the cluster formation rate increases at the moments of the encounters with NGC 5195, we find an increase in the cluster formation rate of a factor of $3.0^{+4.6}_{-1.2}$, combined with a disruption time-scale which is slightly higher than when assuming a constant formation rate ($t_4 = 2.0^{+2.3}_{-1.1} \times 10^8$ yr *vs.* $1.0^{+0.6}_{-0.5} \times 10^8$ yr). The measured cluster disruption time is a factor of 5 shorter than expected on theoretical grounds. This implies that the disc of M51 is not a preferred location for survival of young globular clusters, since even clusters with masses on the order of $10^6 M_\odot$ will be destroyed within a few Gyr.

4.1. Introduction

The goal of this series of papers is to understand the properties of the entire star cluster population of the interacting spiral galaxy M51. These properties include the age and mass distribution of the cluster population. Additional properties are the survival rate of the clusters, as well as any relations between the observed properties. These relations may be used to constrain cluster formation and destruction scenarios.

In order to study the above properties, we exploit the large amount of *HST* broad-band archival data on M51, which covers roughly 50% of the observed surface area of M51, and covers a broad spectral range (*UV* to *NIR*). The large spatial coverage is necessary in order to obtain a large sample of clusters for carrying out a statistical analysis, and the broad spectral range allows accurate determination of the individual cluster properties (Bik et al. 2003; Anders et al. 2004). A preliminary analysis of a subset of the M51 cluster population was carried out by Bik et al. (2003), hereafter Paper I, who introduced the method used to determine the cluster properties and derived the age and mass distributions of the cluster sample roughly 2 kpc to the north-east of the nucleus.

Bastian et al. (2005b), hereafter Paper II, extended the survey to include the entire inner ~ 5 kpc of M51, and found 1152 clusters, 305 of which had accurate size determinations. In that work we extended the age distribution analysis of Paper I and found evidence for a cluster formation rate increase $\sim 50 - 70$ Myr ago. This corresponds to the last close passage of NGC 5195 and M51 (Salo & Laurikainen 2000). Additionally we found that 68 $\pm$15% of the clusters forming in M51 will disrupt within the first ~ 10 Myr after their formation, independent of their mass, so-called *infant mortality*. For the resolved cluster sample, we found that the size distribution (the number of clusters as a function of their effective radius) can be well fit by a power-law: $N\,\mathrm{d}r_{\rm eff} \propto {r_{\rm eff}}^{-\eta}\,\mathrm{d}r_{\rm eff}$, with $\eta = 2.2 \pm 0.2$, which is very similar to that found for Galactic globular clusters. Finally, we did not find any relation between the age and mass, mass and size, or distance from the galactic centre and cluster size.

In this study we focus on the evolution of the population of clusters in M51, in particular the time-scale of cluster disruption and possible variations in the cluster formation rate. Cluster disruption of multi-aged populations, which excludes the galactic globular clusters, has been the subject of many earlier studies: e.g. Hodge (1987) for the SMC and Battinelli & Capuzzo-Dolcetta (1991) for the Milky Way. In this study we will take mass dependent disruption into account, since the time needed to destroy half of the cluster population, which has been estimated in earlier work, will strongly depend on the mean mass of the sample and the lower mass limit of the sample. In addition, we here want to study the effect of variations in the formation rate, which is usually kept constant.

Boutloukos & Lamers (2003) have developed a method to derive the disruption time-scale based on the age and mass distributions of a magnitude-limited cluster sample. They found that the disruption time of clusters in M51 is a factor of 15 shorter than the one for open clusters in the solar neighbourhood. Lamers, Gieles, & Portegies Zwart (2005b) showed that part of the difference can be explained by the difference in density of the cluster environment and that the disruption time of clusters depends on the clusters initial mass and the galaxy density as $t_{\rm dis} \propto M_i^{0.62}\,\rho_{\rm gal}^{-0.5}$, based on the results of N-body simulations. The disruption time of clusters in M51 was still about a factor of 10 lower than the predicted value. In this work we are particularly interested in seeing if a short disruption time-scale can be mimicked by an increasing cluster formation rate, and how the assumed disruption law influences the derived

time-scales. To this end we generated artificial cluster samples with parameterised global characteristics (e.g. time-dependent cluster formation rates, disruption laws, infant mortality rates, and mass functions). We then compare these models with the derived age and mass distributions of the cluster population of M51 to derive the best fit parameters for the population as a whole.

The structure of the paper is as follows: in § 4.2 the observations of the cluster population of M51 are presented. In § 4.3 we investigate to what extent the disruption time depends on different cluster and galaxy parameters. § 4.4 describes the steps we will take in our models, where the details of the models we used to generate artificial cluster populations will be explained in § 4.5. The results of the fits are given in § 4.6. A discussion of the implication of the results is given in § 4.7, and the conclusions are presented in § 4.8.

4.2. The observations

4.2.1. Fitting the observed spectral energy distribution

From archival *HST* broadband photometry we have derived the age, mass, and extinction of 1152 clusters in M51 (Paper II), using the three-dimensional maximum likelihood fitting (3DEF) method. Details about the 3DEF method can be found in Paper I. In summary, the spectral energy distribution of each cluster is compared with cluster evolution models. In this case the *GALEV* simple stellar population (SSP) models (Anders & Fritze-v. Alvensleben 2003; Schulz et al. 2002) for solar metallicity and Salpeter IMF are used. For each age a series of different extinction is then applied to the models and all combinations of age and extinction are compared to the data. The lowest χ^2 is kept, and from the absolute magnitude at that age, the mass is determined. Detailed tests of the accuracy and reliability of the derived parameters are presented in Paper II. In the present work, we further investigated the accuracy of our fitting method and used the data set to develop a model that describes the global properties of the cluster system.

4.2.2. The age and mass distribution of clusters

The ages and present masses of the 1152 clusters are plotted in the top left panel of Fig. 4.1. In order to be able to compare our observations with simulated cluster samples, we bin the data in logarithmic number density plots of the age *vs.* mass distribution. Clusters were counted in bins of 0.4 age dex by 0.4 mass dex (Fig. 4.1, top right panel), and the result illustrated in the bottom panel of Fig. 4.1. A few striking features can be learned from this diagram:

1. a burst in the cluster formation rate (CFR) between 50 and 70 Myr, corresponding to the most recent interaction with the companion galaxy NGC 5195;

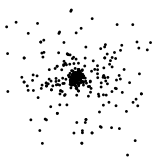

2. a short-lived young population with ages < 10 Myr. In Paper II we found that $\pm 68\%$ of these young clusters will dissolve within 10 Myr, independent of their mass;

3. evolutionary fading under the detection limit, which makes it harder to detect old low-mass clusters. The increasing line in Fig. 4.1 shows how the 90% completeness limit in the F439W band (22.6 mag.) corresponds to different masses at different ages;

4. an *apparent* increase in the mass of the most massive cluster with age. This is a binning effect: the older age bins span more time and therefore contain more clusters, and the chance of finding a more massive cluster at older ages is higher due to the *size of sample* effect (Hunter et al. 2003). We tried to use the method of Hunter et al. (2003) to derive the cluster formation rate, but found that the increase in the maximum mass is much too shallow. This probably means that M51 has reached the maximum cluster mass ($\sim 10^6 M_{\odot}$) when the relation of Hunter et al. (2003) does not apply anymore, since the maximum cluster mass found at a certain age is then no longer determined anymore by sampling statistics. This is the topic of a subsequent study (Gieles et al. 2006b).

We found that a large fraction ($\pm 68\%$) of the clusters younger than 10^7 yr dissolves independent of mass, probably due to the removal of the primordial gas (e.g. Kroupa 2005; Geyer & Burkert 2001; Lada & Lada 2003). After these critical 10^7 years, the surviving clusters will dissolve due to the tidal field of the host galaxy and external perturbations from, for example, encounters with giant molecular clouds (GMCs). The disruption of clusters is in that sense a two step process. Here we will use the resulting age/mass distribution to study the disruption of clusters with ages larger than 10^7 yr., i.e. the second step in the disruption process.

4.2.3. Artifacts introduced by the age-fitting method

We want to see whether the 3DEF method (§ 4.2.1), used to derive ages, masses, and extinction from the photometry, introduces systematic artifacts. More important, could it affect our results of the disruption time or formation rate? For instance, are there systematically old clusters fitted with young ages or the other way around?

The uncertainty in the derived ages, extinctions, and masses from broad-band photometry is caused mainly by two effects:

1. Differences between the real integrated colours of the clusters and the models, for example due to stochastic sampling of the stellar IMF, which cannot be taken into account in the SSP models, or errors in the stellar isochrones used;

2. Systematic errors introduced by the age-fitting method and the applied selection effects.

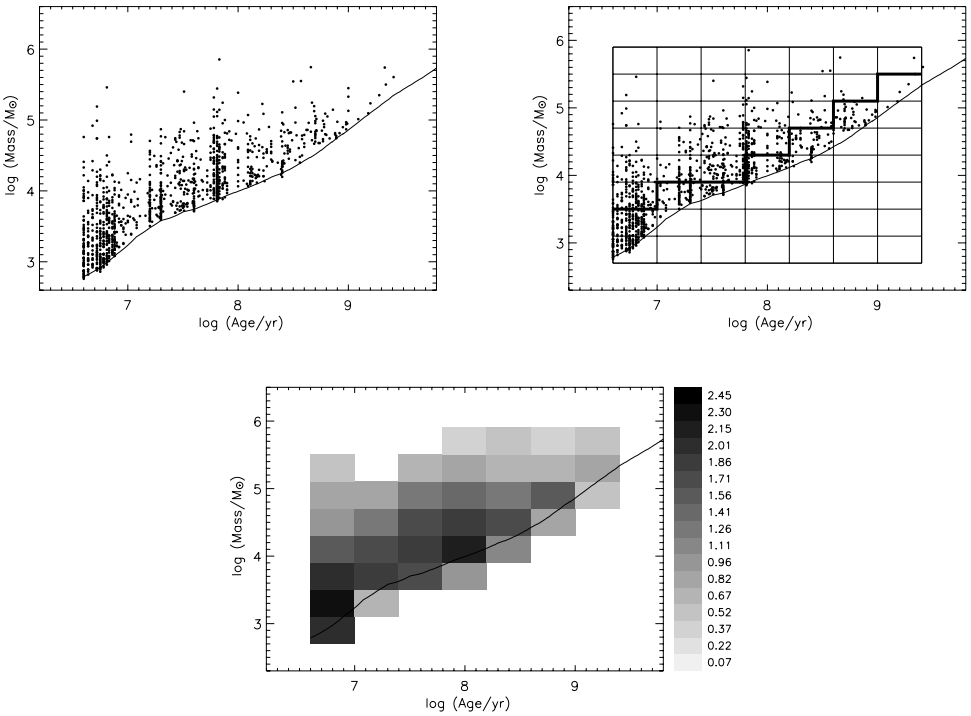

Figure 4.1: Ages and present masses of the 1152 clusters identified in Paper II. **Top left**: original data, where every point represents a cluster. **Top right:** same data as in the top panel over-plotted with the grid used to bin the data. Above the dark line are the bins not affected by the detection limit. **Bottom**: logarithmic density plot of the same sample, where dark regions represent more clusters. The right hand scale shows how the grey values correspond to the logarithm of number. The line in all three plots is the 90% completeness limit (F439W = 22.6 mag).

Of course, the first effect cannot be corrected for, unless we are able to compare photometric determined ages directly to spectroscopically determined ages, which is unfortunately not feasible for a whole population of clusters. In addition, although spectroscopically derived ages are more accurate, they are hampered by their own problems (Brodie et al. 1998). In addition, the age derivation will depend on the choice of the adopted SSP models. Variations in the metallicity and the IMF will affect the derived ages. A detailed comparison of the data with models of different metallicity was carried out in Paper II. An earlier study of the age distribution of M51 used Starburst99 models (Bastian & Lamers 2003), and they found a very similar age distribution.

The second effect can be quantified with the use of artificial cluster populations.

Earlier studies (e.g. Anders et al. 2004; de Grijs et al. 2005) have already shown the importance of using a long wavelength baseline (U to NIR) to age-date young clusters. Here we make an attempt to quantify possible systematic errors introduced by the age-fitting method and see whether we can correct for them or not.

To quantify the artifacts introduced by the fitting routine, an artificial cluster sample including simulated observational errors and extinction values was generated and fitted with the same fitting procedure as used for the data (§ 4.2.1). We started with a sample of clusters equally spread in log(age/yr) and $\log(M/M_{\odot})$ space. In total 201 time steps between log(age/yr) = 6 and log(age/yr) = 10 and 161 mass-steps between $\log(M/M_{\odot}) = 2$ and $\log(M/M_{\odot}) = 7$ were generated. The *GALEV* models have log(age/yr) = 6.6 as youngest model, so clusters with younger ages were given that age. The magnitudes as a function of age and mass were taken from the *GALEV* SSP models. Observational uncertainties were applied as a function of magnitude as was done in Paper II; the observed errors in the magnitudes of clusters in M51 can be well approximated by $\Delta\mathrm{mag}_{\lambda} = 10^{d_1+d_2\times\mathrm{mag}_{\lambda}}$. The values for d_1 and d_2 for the different filters are results from analytical functions fitted to the observed errors and magnitudes and are given in Table 4 of Paper II. Ideally, we then apply the same extinction to the model clusters as the M51 clusters have. Unfortunately, the only information we had was the extinction we measured, which of course could already be polluted with artifacts. To get an estimate of the uncertainty in the measured extinction, we started with a sample of clusters with no extinction applied. When we fit this population with the 3DEF method, we found that 20% of the sources was fitted with some extinction. This is quite a large number, but fortunately 90% of these sources have extinction values lower than $E(B-V) = 0.1$ mag. The maximum $E(B-V)$ found is 1 mag.

The next step is to apply an extinction model close to what we observe. To this end $E(B-V)$ extinction values were chosen randomly from a Gaussian distribution centred at 0 with $\sigma = 0.10$ for clusters younger than log(age/yr) = 7.3 and $\sigma = 0.05$ for clusters older than log(age/yr) = 7.3. The values for σ agree with the value we found for the mean extinction in Paper II. There we found that these values are the average extinction for these two age groups. The higher extinction for young ages is caused by the presence of the left-over dust around the cluster. Negative extinctions were set to 0, resembling the extinction distribution of the data where half of the clusters had $E(B-V) = 0$ (See Fig. 8 of Paper II). An age-dependent maximum extinction was applied of the form: $E(B-V)_{\max}(t) = 5 - 0.5 * \log(t)$. This is a little bit lower than the observed maximum extinction, but we know that some of the observed high values could be caused by wrong fits. This still resembles the observed extinction behaviour quite well. The resulting magnitudes were than cut off at our completeness limits in each filter. In this way we created the spectral energy distributions of a large artificial cluster sample with age, mass, and extinction known for each cluster. These were fitted with the 3DEF method (§ 4.2.1).

The result of the fitted simulation is shown in Fig. 4.2. A direct comparison with the observed age-mass diagram of M51 clusters (Fig. 4.1, top left) shows that there are features present in the data which are not visible in the fitted simulation. For

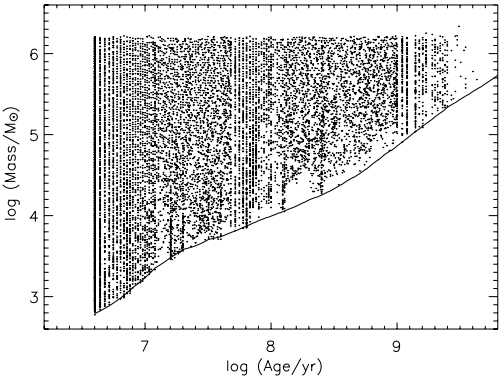

Figure 4.2: Age/mass diagram of artificial sample after fitting with the method described in § 4.2.1. The deviations from equally spaced dots in $\log(\mathrm{age/yr})/\log(M/M_{\odot})$ are caused by the applied observational errors and the fitting routine.

example, there is a gap at $6.9 < \log(\mathrm{age/yr}) < 7.1$ in the M51 cluster sample, which seems to appear at slightly higher ages in the fitted simulations ($7.1 < \log(\mathrm{age/yr}) < 7.2$). This suggests that the artifacts in the data are caused not only by our applied selection effects or our age-fitting technique. In the top left panel of Fig. 4.3 we show the fitted age versus the input age for the simulated cluster sample. A large number of clusters with wrong ages are fitted with a $\log(\mathrm{age/yr}) \simeq 7$. We found for 87% of the modelled clusters that the fitted age was the same as the input age within 0.4 dex (Fig. 4.3, Top right). For the mass, 97% was fitted correctly within 0.4 dex (Fig. 4.3, Bottom right) and 92% of the extinction values were fitted back within 0.05 mag. (Fig. 4.3, Bottom left). We have to realize that the strength of the artifacts depends on the number of input clusters at each age and mass bin. We have not attempted to match the observations in this stage, since we are only interested in relative errors. For example, the horizontal spur at $\log(\mathrm{age/yr}) \simeq 7$ in Fig. 4.3 (Top, left) is populated with clusters with input ages up till a few times 10^9 yr. The number of clusters with that age in our M51 sample is very low (see Fig. 4.1, top left).

4.2.4. Correcting the data for fitting artifacts

We will try to correct the data for possible artifacts, by using the (systematic) deviations found in § 4.2.3. Correcting the observed ages based on the absolute numbers deviating from the one-to-one relation is not useful, since the number of clusters that were used as input at each age and mass differs from the observed number. From the input sample we can derive how many clusters are (systematically) fitted with wrong ages and masses. Let the total number of bins in age/mass space be K. Here we define the number of bins as the number of bins which are not affected

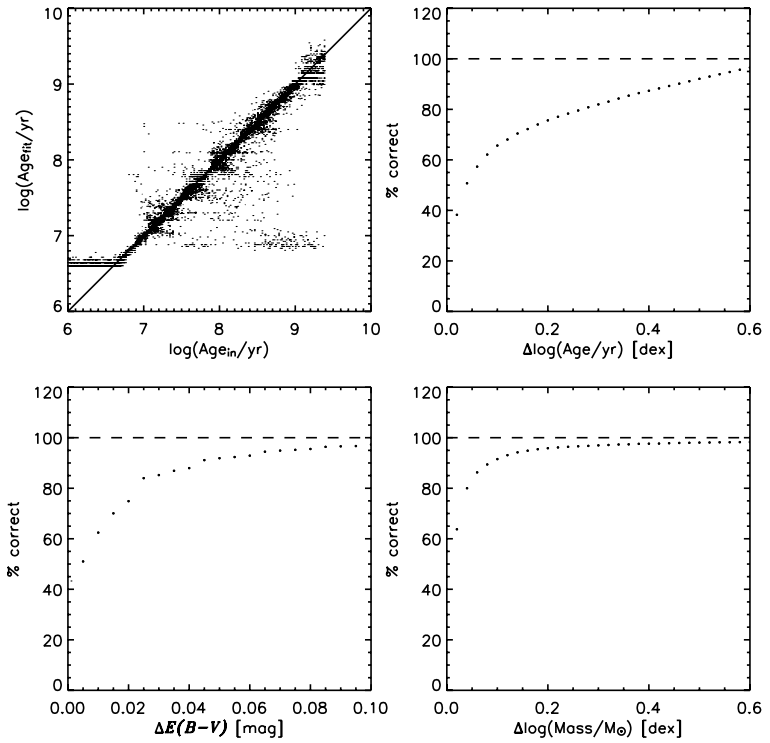

Figure 4.3: Result of fitting an artificial cluster sample with the 3DEF method. **Top left:** The fitted age is shown versus the input age for each cluster. Deviations from the one-to-one relation are caused by photometric errors which are applied to the input sample and misfitted extinction.**Top right:** The percentage of clusters fitted with the same age as the input value, plus some deviations, as a function of this deviation. **Bottom left:** similar, but then for extinction. **Bottom right:** similar but for the mass.

by the detection limit (see Fig. 4.1, top right panel). The number of clusters found in each bin is the sum of the contribution of clusters from all bins to this one, where the majority will be from the bin with the same input age and mass. When we write the number of clusters in each bin as a vector with K-entries, the fitted number of clusters can be written as a matrix multiplication of all contributions times the input number of clusters

$$\begin{pmatrix} N_1 \\ N_2 \\ \vdots \\ N_K \end{pmatrix}_{\rm obs} = \begin{pmatrix} C_{11} & C_{12} & \dots & C_{1K} \\ C_{21} & C_{22} & \dots & C_{2K} \\ \vdots & \vdots & \ddots & \vdots \\ C_{K1} & C_{K2} & \dots & C_{KK} \end{pmatrix} \begin{pmatrix} N_1 \\ N_2 \\ \vdots \\ N_K \end{pmatrix}_{\rm intr} \tag{4.1}$$

where $N_{\mathrm{intr},j}$ is the number of clusters generated in bin j, $N_{\mathrm{obs},i}$ the number of clusters fitted in bin i, and C_{ij} the contribution to bin i from bin j. Tests have shown that the best results are acquired when only taking bins into account which are not affected by the detection limit (see Fig. 4.1, top right panel). From the simulated and fitted sample we can derive the values for C_{ij} for all combinations of i and j. All values on the diagonal of C (i.e. C_{ij} where $i = j$) are close to 1, since most clusters are fitted with the same age, extinction, and mass. All other values are 0 or between 0 and 1. When we know the matrix C, the inverse can be used to correct the observations for systematic 3DEF fitting artifacts:

$$\vec{N}_{\mathrm{intr}} = C^{-1} \times \vec{N}_{\mathrm{obs}} \tag{4.2}$$

where $\vec{N}_{\mathrm{intr}}$ is the vector with the intrinsic number of clusters, C^{-1} the inverse of the contribution matrix as defined in Eq. 4.1, and $\vec{N}_{\mathrm{obs}}$ the vector with observed clusters. When we correct the observed vector and plot it in a 2D age-mass diagram again, then divide the corrected and uncorrected observations, we can see where deviations take place. Fig. 4.4 shows the ratio of corrected over uncorrected observations. The number of clusters in the age bins at log(age/yr) = 7.2 and 8.0 has been lowered by about 15%. The observations, however, show a gap at log(age/yr) = 7.2 (Fig. 4.1, top left), so the underestimation of clusters in that age bin is not caused by our fitting routine.

The corrected observations based on Eq. 4.2 are shown in Fig. 4.5. The burst at between 50-70 Myr is less pronounced, but still present. The differences with the uncorrected observations (Fig. 4.1, Bottom) are small, so we conclude that our age-fitting method (3DEF) and our applied selection affect is not severely affecting our age-mass diagrams in a systematic way. In particular, there is no large systematic shift from old to young clusters or the other way around. We therefore conclude that we can use the uncorrected data, as well as the corrected data, to compare with the synthetic cluster populations in § 4.5. In § 4.6.2 we show that both the corrected as the uncorrected data give the same results when fitting the analytical models to the data.

4.3. Exploration of the parameters which determine the disruption time

4.3.1. Cluster initial mass

If cluster relaxation drives the evaporation of clusters, then the more massive clusters live longer than their low mass counterparts. Boutloukos & Lamers (2003) propose an empirical way to determine the dependence of the cluster disruption time on the initial cluster mass, assuming a power-law dependence of the disruption on the cluster mass

$$t_{\mathrm{dis}} = t_4 \, (M_i/10^4 \, M_\odot)^\gamma \tag{4.3}$$

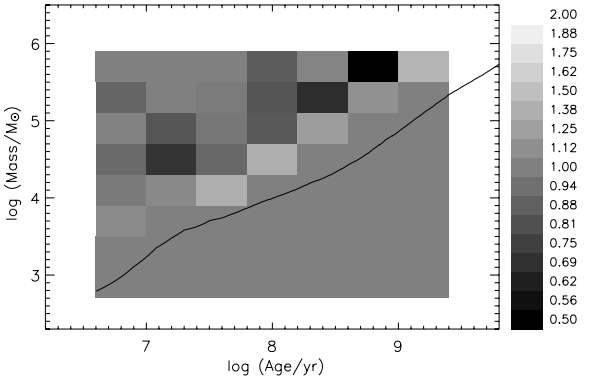

Figure 4.4: Ratio of the corrected observations over the uncorrected observations. The corrected data was calculated using Eq. 4.1 and Eq. 4.2. Light regions indicate where less clusters are found by the fitting procedure. Dark regions indicate where more clusters are fitted than inputted.

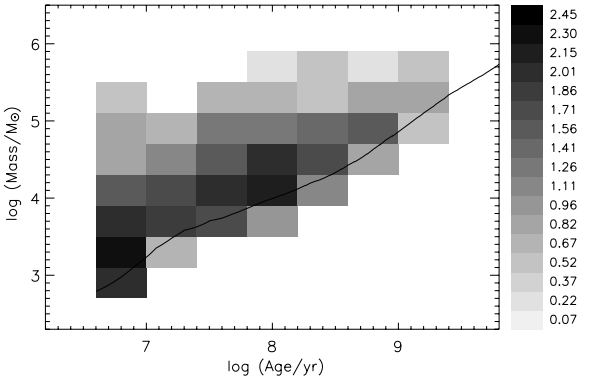

Figure 4.5: Corrected age and mass distribution. The raw data from Fig. 4.1 (Bottom) was multiplied with the inverse of the contribution matrix (Eq. 4.1)

where t_4 is the disruption time of a $10^4 M_\odot$ cluster, M_i the initial mass of the cluster, and γ a dimensionless index. The value of γ was determined by measuring the slope of the age and mass distributions of a cluster population. Their mean value for γ based on four different galaxies was $< \gamma >= 0.62 \pm 0.06$.

In a recent study by Lamers et al. (2005b), these observational results are compared with results of N-body simulations. The value of γ can be explained by tidally driven relaxation and was confirmed to be 0.62 by N-body simulations. The expla-

nation for this is that the disruption time of a cluster in a tidal field depends on the relaxation time ($t_{\rm rel}$) and on the crossing time ($t_{\rm cr}$) of the cluster as (Baumgardt 2001):

$$t_{\rm dis} \propto t_{\rm rel}^{x} \times t_{\rm cr}^{1-x}. \tag{4.4}$$

Using the expression for $t_{\rm rel}$ and $t_{\rm cr}$ from Spitzer (1987), this implies: $t_{\rm dis} \propto \beta(N/\ln N)^x$. Baumgardt & Makino (2003) found two combinations of β and x, depending on the concentration of the clusters. Lamers et al. (2005b) showed that for both combinations, $t_{\rm dis}$ could be well approximated with $t_{\rm dis} \propto N^{0.62} \propto M^{0.62}$, where N is the number of stars in the clusters and M the total mass of the cluster. King (1958) already had theoretical arguments to expect that the lifetime of clusters should depend on the mass as $t_{\rm dis} \propto M^{2/3}$. The agreement between observations and N-body simulations was first noted by Gieles et al. (2004). The physical background of why the disruption time does not scale directly with the relaxation time is given by Fukushige & Heggie (2000).

4.3.2. Cluster radius

Young clusters are not only affected by the external tidal field of the host galaxy, but they also undergo shocks from (giant) molecular clouds. Both these processes shorten the lifetime of clusters. For both cases, the radius of the cluster is an important parameter in determining how fast the cluster will disrupt. However, both processes depend in very different ways on the radius. From Eq. 4.4 and the expression for the relaxation time and crossing time, it follows that for the tidally driven relaxation the disruption time depends on the radius as $t_{\rm dis} \propto r_{\rm h}^{3/2}$. Larger clusters live longer since they have a longer relaxation time, so it takes more time for stars to reach the tidal radius and leave the cluster. Spitzer (1958) has shown that the time needed for a cluster to get unbound due to external shocks relates to the half mass radius of the cluster as $t_{\rm sh} \propto r_{\rm h}^{-3}$, so here larger clusters live shorter (for isolated clusters).

To see whether the radius of a cluster is an important parameter in disruption, we used the radii measurements of Paper II. There we measured the projected half light radius (or effective radius) $r_{\rm eff}$, which relates to the half mass radius as: $r_{\rm eff} = 3/4\, r_{\rm h}$ (Spitzer 1987). We made a number density plot of $r_{\rm eff}$ *vs.* age for all clusters (Fig. 4.6). There are clearly no old clusters with large radius, while the opposite is expected due to the size-of-sample effect (Hunter et al. 2003). This suggests that large clusters are disrupted preferentially, which in turn suggests that shocks may be the dominating disruption effect. However, when a large fraction of the clusters is removed, independent of radius, the upper radius also goes down. This is a result from number statistics: less clusters in a power law distribution will result in a lower maximum value. So what really matters here is whether the slope of the radius distribution changes in time or not. In Paper II it is shown that the cluster radius distribution of M51 is $N(r)\,dr \propto r^{-\eta}\,dr$, with $\eta = 2.2 \pm 0.2$. To see how the slope of

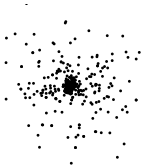

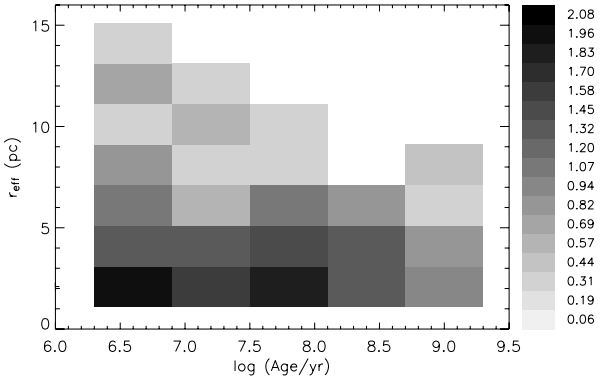

Figure 4.6: Number density plot of $r_{\rm eff}$ *vs.* age. The decreasing number going towards larger radii shows the power law behaviour of the radius distribution. The right hand side shows how the grey values correspond to the logarithm of number of clusters.

the distribution depends on age, we divide our cluster sample in young (log(age/yr) < 7.5) and old (log(age/yr) > 7.5). Dividing the sample at log(age/yr) $= 7.5$ yields two samples of more or less equal size, which gives similar errors in the fit to both distributions. When we determine this index η for only young clusters, we find $\eta = 2.0 \pm 0.4$, and for old clusters we find $\eta = 2.5 \pm 0.6$, which is very similar to the value found for the globular clusters in our Milky Way ($\eta = 2.4 \pm 0.2$, Paper II). Although the radius distribution seems to get steeper with age, the errors are too large to place a strong constraint on this. We therefore do not take the radius into account as a free parameter when modelling the cluster disruption. Future studies of M51 with higher resolution, for example with the *Advanced Camera for Surveys (ACS)*, could shed light on how the radius of clusters affects the lifetime.

4.3.3. Distance to the galactic centre

Lamers et al. (2005b) and Baumgardt & Makino (2003) have shown that the disruption time is expected to depend on the galactocentric distance of the cluster, the orbital velocity in the galaxy, and the ambient density of the galaxy as

$$t_{\rm dis} \propto R_{\rm G}/V \tag{4.5}$$
$$\propto \rho_{\rm amb}^{-0.5} \tag{4.6}$$

where $R_{\rm G}$ is the distance to the galactic centre, V the rotational velocity of the cluster in the host galaxy at that distance, and $\rho_{\rm amb}$ the ambient density of the galaxy at the location of the cluster. The relation with the ambient density holds only when a logarithmic potential is assumed. Since we are dealing with a disc galaxy, it is not

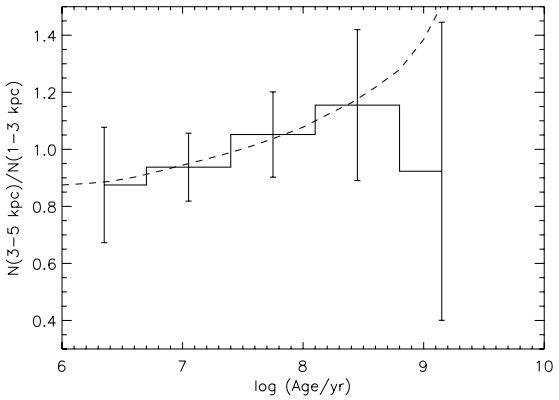

Figure 4.7: Ratio of the number of clusters (N) between 3-5 kpc and 1-3 kpc as a function of age. Over-plotted is a model predicting this ratio for two disruption times differing a factor of 1.8, based on Eq 4.8.

so straightforward to derive the ambient density from the spherically symmetric logarithmic potential. Therefore, we prefer the relation with the galactocentric distance and the velocity (Eq. 4.5). With Eq. 4.5 we are able to estimate if we would be able to observe a difference in disruption time at different locations in the galaxy. When we look at clusters between 1 and 3 kpc and at clusters between 3 and 5 kpc, the average value of R_G goes up by a factor of 2. The rotational velocity of M51 increases from 200 km s^{-1} to 225 km s^{-1} (Rand 1993), so from Eq. 4.5 we expect the disruption time in the two samples to be different by a factor of 1.8. In Fig. 4.7 we plot the ratio of the number of clusters at different ages for the outer region (3-5 kpc) and inner region (1-3 kpc). Over-plotted is the predicted ratio using Eq. 4.8 for a disruption time-scale that is different by a factor of 1.8. Just as for the radius dependence, we see that the distance to the galactic centre plays a role, but the data is not sufficient to include in our analysis.

In conclusion, we see evidence of radius and galactocentric distance-dependent disruption, but the noise is too large to include these parameters in the models. The mass of the cluster is the most dominating parameter in the determination of disruption time, and in the remainder of the study, we only use the mass dependence as a parameter we vary in the models.

4.4. Input parameters for modelling the cluster population of M51

So far, analytical models for finding the cluster disruption time have assumed that clusters were formed with a constant CFR, as is probably the case for Galactic open

clusters (Boutloukos & Lamers 2003; Battinelli & Capuzzo-Dolcetta 1991). Lamers et al. (2005a) predicted the age distribution of open clusters. In the case of M51, we have age and mass information available for each cluster, so predictions can be done for age and mass. In addition, assuming a constant CFR for M51 might be an oversimplification of the situation, since the galaxy is in interaction with NGC 5195. In the next sections we explore a broader parameter space.

Since there are strong arguments to believe that the mass dependence of the cluster disruption ($\gamma = 0.62$) is constant (Lamers et al. 2005b), we start by varying only the constant t_4, to be able to compare our results with clusters gradually losing mass with the *instantaneous disruption* assumption (Eq. 4.3) results of Boutloukos & Lamers (2003). Next, a two-dimensional parameter search for γ and t_4 is performed, to verify the assumed value for γ and to study the dependence of t_4 on the value of γ.

Once we have a first estimate of the disruption time, we will study how this value changes when we assume that the CFR has been increasing during the last Gyr or contains bursts at the moments of encounter with NGC 5195.

4.5. Analytical model for generating a cluster population

4.5.1. Setting up a synthetic cluster population

The synthetic cluster populations will be created in a similar way as in § 4.2.3. This time, however, we want to include realistic input physics, like the cluster IMF and different formation rates, so creating clusters equally spaced in log(age/yr) and $\log(M/M_\odot)$ will not be adequate. When creating clusters with a realistic CIMF, the number of clusters needed to fully sample the CIMF up to 10 Gyr ago is too high. Therefore each cluster was assigned a weight depending on the initial cluster mass and its age ($w(t, M_i)$), proportional to the expected number of clusters formed at each age and mass. The weight is a function of age and mass, scaled such that the youngest, most massive cluster has a weight of 1

$$w(t, M_i) = (t/t_{\rm min}) \times (\alpha - 1) \times (M_i/M_{\rm max})^{1-\alpha} \tag{4.7}$$

where $w(t, M_i)$ is the weight assigned to a cluster with age t and mass M_i, $M_{\rm max}$ the mass of the most massive cluster in the simulation, $t_{\rm min}$ the age of the youngest cluster in the simulation, and α the slope of the mass function. When α is chosen 2, i.e. $N(M) \sim M^{-2}$, the weight depends on age and mass simply as: $w(t, M_i) \propto t/M_i$. When the simulated clusters are binned, the weights of the clusters are counted, yielding a realistic log(age/yr) *vs.* $\log(M/M_\odot)$ diagram similar to Fig. 4.1 (Bottom). The advantage of using points spread equally in log(age/yr) and $\log(M/M_\odot)$, with weights assigned, is that the number of points per bin is constant and it is very easy to create a lot of populations with different formation rates, disruption time-scales, etc. in a short time.

In our case the clusters are given weights such that, after binning, the CIMF has a slope of $\alpha = 2.1$, as found for M51 (Paper I) and the Galactic open clusters (Battinelli et al. 1994). The weights enable us to model different formation and disruption scenarios (§ 4.6.2-§ 4.6.4).

4.5.2. Including stellar evolution and cluster disruption

Baumgardt & Makino (2003) have shown that stellar evolution (SEV) is an important contributor to the dissolution of young clusters, especially for clusters with low concentrations. They also confirm that clusters dissolve with a power-law dependence of their initial mass as $t_{\rm dis} \sim M_i^{\gamma}$, where $\gamma = 0.62$, in agreement with the empirical determination by Boutloukos & Lamers (2003). In this study instantaneous disruption after the disruption time was assumed as a first approximation and they find that the typical disruption time (t_4, see Eq. 4.3) varies a lot for different galaxies. In a recent study (Lamers et al. 2005a), it was shown that there is a simple analytical description of the mass of a cluster as a function of time. It takes into account the effect of mass loss due to stellar evolution, based on the mass loss predicted by the *GALEV* SSP models (Anders & Fritze-v. Alvensleben 2003; Schulz et al. 2002) and cluster mass loss due to the tidal fields. The mass of the cluster as a function of time can be approximated well by

$$M_p(t) = ((M_i \mu_{\rm sev})^{\gamma} - \gamma \frac{t}{t_0})^{1/\gamma} \tag{4.8}$$

where $M_p(t)$ is the present mass of the cluster as a function of its age, M_i the initial mass of the cluster, $\mu_{\rm sev} \equiv M_p(t)/M_i$ is the fraction of remaining mass after mass loss due to stellar evolution has been subtracted, and t_0 relates to t_4 as $t_4 = t_0 \times 10^{4\gamma}$. The mass as a function of time, according to the analytical formula, agrees perfectly with the predictions following from N-body simulations. Lamers et al. (2005a) have also shown that with this analytical model the age distribution of galactic open clusters can be explained very well.

4.6. Fitting observed age-mass distribution to predictions

4.6.1. Determining reduced χ^2 values from 2D fits

Artificial cluster samples with realistic input physics (e.g. a CIMF, cluster disruption, bursts, etc.) can now be generated and compared with the observed age and mass number density distribution.

After calculating the analytically generated cluster population, the model was binned into number density plots in the same way as the observed data (see § 4.2.2) taking the weights into account. In order to compare the simulated (2D) age-mass

density plots with the observations, we used the Poisson Probability Law (PPL) introduced by Dolphin & Kennicutt (2002) for similar purposes

$$\mathrm{PPL} = 2\sum_{i=0}^{N} m_i - n_i + n_i \ln \frac{n_i}{m_i} \tag{4.9}$$

where N the number of bins, m_i is the predicted number by the analytical model in bin i, and n_i the observed number of clusters in bin i. The value of PPL is similar to χ^2, in the sense that lower values imply better fits. We always divide the PPL value by the number of bins minus the number of degrees of freedom, which is equivalent to the reduced χ^2, so that χ^2_ν. We will refer to χ^2_ν when we discuss results of fits.

4.6.2. Determining the cluster disruption time assuming a constant formation rate of clusters

To determine the *typical* cluster disruption time, t_4, defined in § 4.5, we generate a cluster sample with a constant CFR and then calculate the cluster masses as a function of age according to Eq. 4.8 for various values of t_4. Here we are interested in the disruption time of clusters that have survived that first 10^7 yr in which the natal cloud is being removed by stellar winds, therefore we excluded the youngest age bin in the fits. Figure 4.8 shows a clear χ^2_ν minimum around $t_4 = 1.0^{+0.6}_{-0.5} \times 10^8$ yr, where the upper and lower errors are defined by $\chi^2_{\nu,\mathrm{accept}} \leq \chi^2_{\nu,\mathrm{min}} + 1$, which is equivalent to the 1 σ error. In addition, we fitted the same models but then corrected for age-fitting artifacts (§ 4.2.4). The shape of this χ^2_ν curve is the same as for the raw data, though the values are higher. This shows that the uncertainties of our age-fitting method do not alter the value found for the disruption time-scale.

To see how the value of t_4 depends on the value of γ, we simulated a grid of cluster populations and varied t_4 and γ. A 2D χ^2_ν plot is shown in Fig. 4.9. The minimum is at $\gamma = 0.65^{+0.16}_{-0.25}$ and $t_4 = 1.0^{+0.84}_{-0.35} \times 10^8$ yr, agreeing very well with the value of $\gamma = 0.62$, which was stated earlier based on theoretical arguments and other observational results. The plot also shows that there is a diagonal bar-shaped minimum for different combinations of t_4 and γ. One could argue that multiple combinations could be possible, which will yield a somewhat higher value for t_4. The fit, however, is very sensitive to the choice of bin size when varying two variables. We excluded the mass bins higher than $5 \times 10^5 M_\odot$, since we were probably dealing with a truncation of the mass function. If sampling effects were to determine the upper mass at different ages (Hunter et al. 2003), the maximum mass should increase much more than we observe in the top left panel of Fig. 4.1. This effect makes the mass function steeper above $\log(M/M_\odot) \simeq 5.3$; therefore the region in the age/mass diagram is not suitable to fitting the (sensitive) mass-dependent disruption. An alternative way to measure γ would be to measure the slopes of the age and mass distribution separately, as was done in Boutloukos & Lamers (2003). We fitted these slopes and found the same value for γ as for the 2D fit shown in Fig. 4.9. Again, for the mass, we do not include the high mass end for similar reasons as mentioned before. This method is

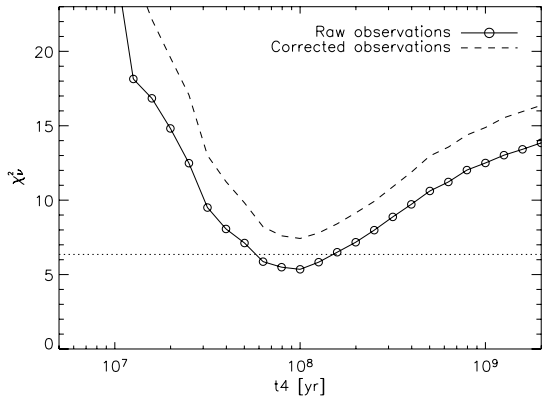

Figure 4.8: χ^2_ν values for different disruption times. A clear minimum is visible at $t_4 = 1.0^{+0.6}_{-0.5} \times 10^8$. The dotted line indicates $\chi^2_{\nu,\min} + 1$. The dashed line shows a fit to the data after correcting for age-fitting artifacts (§ 4.2.4). In these simulations we have chosen γ to be 0.62, based on theoretical arguments (§ 4.5).

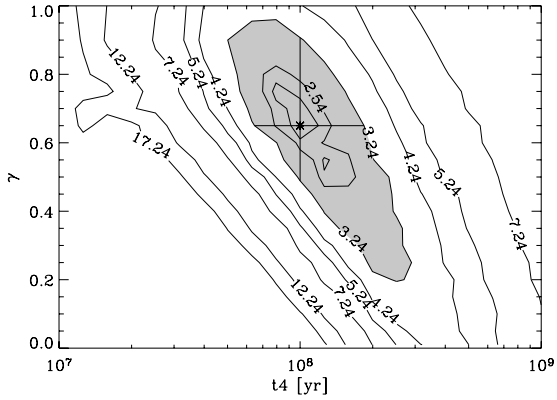

Figure 4.9: Two dimensional χ^2_ν plot of γ *vs.* t_4. The cross and the shaded area indicate the region where $\chi^2_{\nu,\min} < \chi^2_\nu < \chi^2_{\nu,\min} + 1$ in t_4 and γ.

less sensitive to the choice of bin size, since we can fit the slope of the age and mass distribution independently of the value of the disruption time. We chose to include the result of the simultaneous fit of t_4 and γ, because it nicely illustrated how these two variables relate.

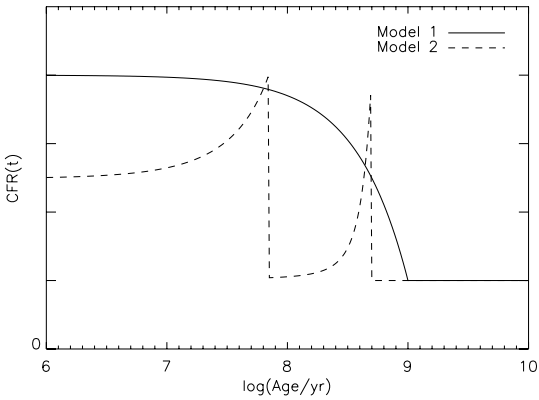

Figure 4.10: Illustration of the applied CFR increase in § 4.6.3 for two different models. Model 1.: The CFR is taken to be constant before 1 Gyr ago and then increases linearly in time until $t = 0$. Model 2.: The CFR increases with steps at the two moments of encounter with NGC 5195. Here the height of the step is the variable.

4.6.3. The effect of an increasing cluster formation rate

Since NGC 5195 is probably bound to M51 and, therefore, slowly falling in (Salo & Laurikainen 2000), one could argue that the short disruption time-scale found in § 4.6.2 is actually caused by an increasing cluster formation rate (CFR). Bergvall et al. (2003) show that interacting galaxies, such as M51 (i.e. non-merging), can have an increased star formation rate on the order of a factor of 2-3. We, therefore, model different cluster populations with increasing CFR(t) rates of various strengths, where we assume that an increasing star formation rate results in an equally large increase in the CFR(t). We study two different models with increasing CFR: 1.) a linear increasing CFR starting 1 Gyr ago (§ 4.6.3) and 2.) a CFR that increases with bursts at the moments of encounter with NGC 5195 (§ 4.6.3). Figure 4.10 gives a schematic illustration of how the CFR varies with time for the two models.

Linearly increasing cluster formation rate

In the linear model, the CFR(t) starts to increase 1 Gyr ago, which is before the moment of the *early* close encounter with NGC 5195 (400-500 Myr ago, Salo & Laurikainen 2000). We expect the CFR to start increasing before the moment of the closest encounter, since the two galaxies are already interacting before the first perigalactic passage. We calculated models with different CFR increases and disruption times, and plotted the χ^2_ν values for various values of CFR($t = 0$)/CFR($t = 10^9$ yr) and t_4 in the left panel of Fig. 4.11.

The minimum χ^2_ν value is at $t_4 = 2.0^{+5.2}_{-1.1} \times 10^8$ yr and there is an increase in the CFR of $7.0^{+68.1}_{-5.0}$. For low values of t_4 the equal χ^2_ν lines are vertical. This can

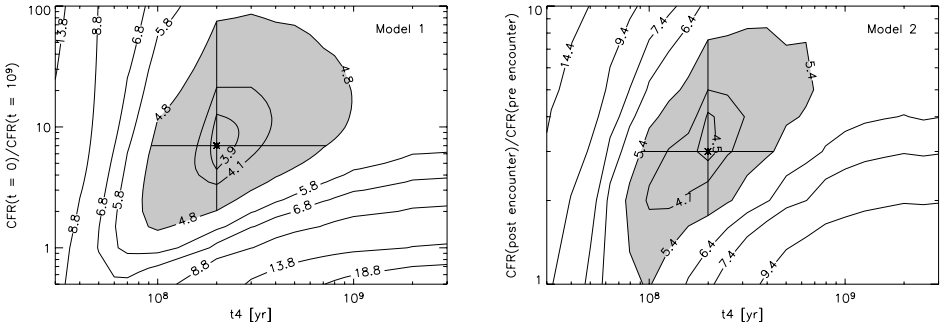

Figure 4.11: χ^2_ν values for different combinations of CFR increase and disruption time (t_4). The left panel shows the results of Model 1 where the CFR increases linearly between $t =$ 1 Gyr and $t =$ present time. The right panel shows the result for Model 2, where the CFR increases with steps at the moment of encounter with NGC 5195. The cross and the shaded area indicate the region where $\chi^2_{\nu,\min} < \chi^2_\nu < \chi^2_{\nu,\min} + 1$

be explained by the fact that, *if* the disruption time is short, no fingerprints of the ancient formation rate are present in the current population. They are simply erased by disruption. The reason that the equal χ^2_ν contours are circular around the minimum is that the disruption of clusters depends on the mass of the clusters (Eq. 4.3), unlike an increase in the formation rate.

Cluster formation rate with bursts

An alternative formation scenario would be that the CFR increases with a burst at the moments of encounter with NGC 5195 and then an exponential decay in the CFR (see model 2 in Fig. 4.10). We chose the moments of increase at $t = 7 \times 10^7$ yr and $t = 5 \times 10^8$ yr ago, based on the results of Salo & Laurikainen (2000), and the typical decay time of the burst is 10^8 yr (Paper II). The CFR step and t_4 are varied in different models.

The right panel of Fig. 4.11 shows that the lowest χ^2_ν value is at $t_4 = 2.0^{+2.3}_{-1.1} \times 10^8$ yr. This is a factor of 2 higher than when the increasing CFR is not taken into account, but it is the same value as was found for the linear increase in the CFR. The value is still a factor of 5 lower than predicted by N-body simulations (Baumgardt & Makino 2003; Lamers et al. 2005b). The best value for the increase in CFR at the moment of encounter is $3.0^{+4.6}_{-1.2}$. The latter value agrees very well with what is generally observed for the increase in star formation rate of interacting galaxies (Bergvall et al. 2003). Since one of the bursts is clearly observed and a linearly increasing CFR is not so physical, we prefer Model 2 above Model 1. In the next section we compare several properties of this model with the observations.

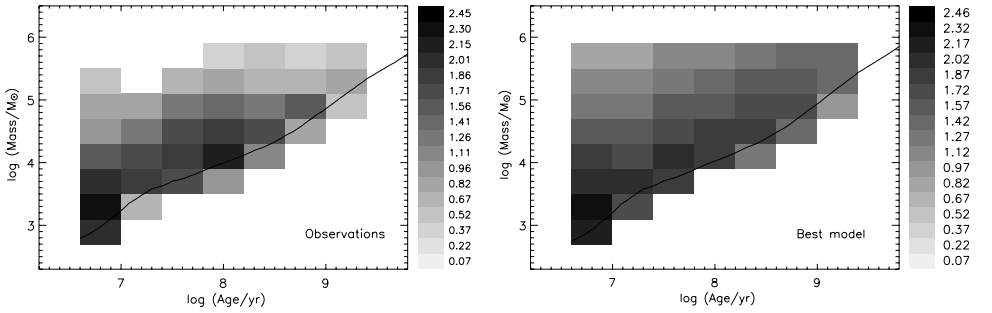

Figure 4.12: Comparison between the observed (*left*) and the modelled (*right*) age *vs.* mass number density plots. In both plots the 90% completeness limit of the F439W band is indicated with a line. The right hand side shows how the different grey values correspond to the logarithm of number. The total number in the simulations is scaled to the total number of observed clusters above the 90% completeness limit (1152).

4.6.4. Comparison between the best fit model and the observations

We show a direct comparison between the age-mass diagrams of the best fit model (§ 4.6.3) and the observations in Fig. 4.12. The densities are scaled such that the total number of simulated clusters equals the total number of observed clusters (1152). A few bins in the observations are empty but not empty in the simulations. The reason for this is that the simulated cluster sample contains bins with values lower than 1. Apart from this, the general trend of grey values in this 2D plot is very similar in both cases.

Another interesting property of the observations is the formation rate. In Paper II we showed the number of clusters at different ages for different mass cut-offs. For clusters with masses higher than $10^{4.7} M_{\odot}$, we get a realistic impression of the cluster formation rate. This is because we are complete until 1 Gyr for these masses (see top left panel of Fig. 4.1) and because the most massive clusters are not that affected by disruption. In Fig. 4.13 (left) we show the number of clusters in different age bins for the observations and the best fit model. The general trend of the observations is followed very well by the model. A better way to show the formation rate is to divide each age bin by the width of the bin. Then we get the number of clusters formed per unit of time (Myr), as is shown in the right panel of Fig. 4.13. In this figure the over-density of young clusters ($\log(\mathrm{age/yr}) < 7$) is more obvious and the burst at 7×10^7 year is more visible. The first burst of cluster formation (5×10^8 years ago) is not visible anymore, since clusters with these ages are already affected by the (short) disruption time. This reinforces that it is very hard to detect variations in the cluster formation rate when the disruption time is that short. The largest difference is seen for the bin with $\log(\mathrm{age/yr}) = 7$ and 8.25. The model predicts more clusters

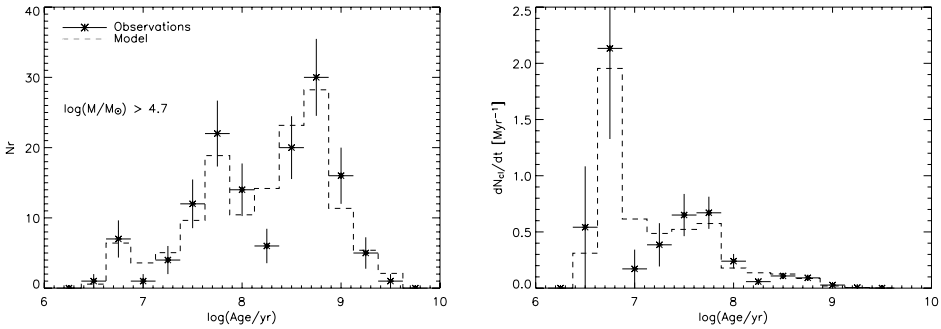

Figure 4.13: Comparison of the age distribution of clusters with masses larger than $10^{4.7} M_{\odot}$ and the one derived from the best fit model. *Left:* Number of clusters per age bin. *Right:* The cluster formation rate (number per Myr).

in these bins than are observed. This can be explained by fitting artifacts which yield an (unphysical) under-density of clusters (§ 4.2.3). The model is still within the 3 σ error of the observations, however.

4.7. Implication of the derived disruption time

We have shown that the clusters disruption time for a typical cluster with mass of $10^4 M_{\odot}$ is around 10^8 years in M51. When increasing formation rates are taken into account the disruption time increases by a factor of 2. This is significantly longer than Boutloukos & Lamers (2003) find for clusters in a smaller region of M51 ($t_4 = 4 \times 10^7$ yr). This could be because they did not separate the dissolution due to infant mortality rate from the evaporation by the tidal field from the galaxy. Clusters with ages younger than 10^7 year are not taken into account in this study, since they are affected by dissolution due to the removal of primordial gas. Theoretical predictions show that clusters of $10^4 M_{\odot}$ in a tidal field of the strength of M51 should have a disruption time of about 10^9 years (Lamers et al. 2005b; Baumgardt & Makino 2003). This value is found from observations of clusters in the solar neighbourhood (Boutloukos & Lamers 2003). What causes the clusters in M51 to dissolve about 5 times faster than predicted? A few effects that have not been incorporated in the N-body models that predict the disruption times in tidal fields are:

1. **Variations in the stellar IMF**. When clusters are formed with a so-called top heavy IMF as is observed in the starburst galaxy M82 (Smith & Gallagher 2001), clusters will disperse much faster, since the disruption time depends on the number of stars in the clusters as $t_{\rm dis} \propto N^{0.62}$ (§ 4.3.1). Suppose the stellar IMF starts at 1 $M_{\odot}$ instead of $0.1 M_{\odot}$, then the number of stars for a given cluster mass will be about a factor 10 lower. This will make the disruption time

a factor $10^{0.62} \simeq 4$ lower, which would nicely explain the factor 5 difference in disruption time we observe.

2. **External perturbations**. The N-body models of Baumgardt & Makino (2003) calculated the disruption time of clusters in a smooth external potential from the host galaxy. In reality, the cluster will also experience additional external perturbations, for example, the encounters with molecular clouds. The clusters in our sample are in the inner 5 kpc of the galaxy, where most of the giant molecular clouds reside (Henry et al. 2003; Kuno et al. 1995). The encounters with molecular clouds can speed up the disruption of clouds significantly (e.g. Terlevich 1987; Theuns 1991).

3. **Out-of-equilibrium formation of clusters**. All clusters in the N-body models start in virial equilibrium and in tidal equilibrium with the host galaxy. Kroupa (2005) has shown that after the gas removal phase, the clusters are not in virial equilibrium anymore, and the outer parts of the cluster have expanded. It will be easier to dissolve these clusters then when all stars are in tidal equilibrium and within the tidal radius imposed by the host galaxy.

4. **Variations in the central concentration**. The N-body models of Baumgardt & Makino (2003) start clusters with concentration values of $W_0 = 5$-7. This is the average concentration of globular clusters in our Milky Way (Harris 1996a). When clusters start with much lower concentration, the core of the clusters is less compact and the cluster will be more vulnerable external perturbations. The concentration of clusters in M51 cannot be determined due to lack of resolution, but we know from young open clusters in the Milky Way that they have much smaller concentration indices than the globular clusters (Binney & Tremaine 1987).

So far, the clusters in M51 have not been checked for variations in the IMF in the way it was done for clusters in other galaxies (e.g. Smith & Gallagher 2001; Larsen 2004; Maraston et al. 2004. Also, no N-body experiments have been performed including the effect of a tidal field and perturbations by giant molecular clouds. Arguments 3 and 4 are based upon unknown observables of young clusters and they could hold for clusters in other galaxies as well.

When the disruption of clusters is indeed as short as we derived, young massive clusters ($M_i \simeq 10^6 M_\odot$) will not survive longer than $3.5{\times}10^9$ yr. This means that the disc of M51 is not the right location for young globular clusters to survive over a Hubble time.

4.8. Conclusions

We have compared the cluster population of M51 with theoretical predictions including evolutionary mass loss, cluster disruption, variable cluster formation rate, and a magnitude limit. The age *vs.* mass diagrams of the observed cluster populations

were binned to acquire two dimensional number density plots, which can be compared with simulated cluster samples. The results can be summarised as follows:

1. Artifacts introduced by our age-fitting routine do not systematically bias our sample towards either young or old clusters. We present a method to correct observations of a cluster population for artifacts introduced by the age-fitting method applied.
2. The size of the largest star cluster decreases with age, from 15 pc for clusters with $\log(\text{age/yr}) < 7$ to 10 pc for clusters with ages around 1 Gyr. In addition, the slope of the radius distribution seems to get steeper in time: $\eta = 2.0 \pm 0.4$ for clusters younger than $\log(\text{age/yr}) = 7.5$ and $\eta = 2.5 \pm 0.6$ for clusters with $\log(\text{age/yr}) > 7.5$. Both these results seem to suggest that smaller clusters have a larger chance of surviving. However, the radius distribution of globular clusters in our Milky Way is very similar to the values found: $\eta = 2.4 \pm 0.2$. Samples with higher spatial resolution and more clusters are needed to study the radius dependence.
3. There are more old clusters at larger distances from the galactic centre. The ratio of the number of clusters in the outer parts of the galaxy (3-5 kpc) over the number of clusters in the inner part (1-3 kpc) per age bin increases with a factor of 1.8 in age (from $\log(\text{age/yr}) = 6.5$ to $\log(\text{age/yr}) = 8.5$), which is to be expected since the disruption time depends on the distance to the galactic centre.
4. Assuming that the cluster disruption time depends on the initial mass of the cluster as $t_{\rm dis} \propto M_i^{\gamma}$, and using $\gamma = 0.62$ based on theoretical and observational studies (Lamers et al. 2005b), we find a typical disruption for a $10^4 M_{\odot}$ cluster of $t_4 = 1.0^{+0.6}_{-0.5} \times 10^8$ yr, where we assumed a constant cluster formation rate.
5. When γ and t_4 are varied together, the value found for γ is similar to that predicted by Lamers et al. (2005b), based on observational and N-body studies. A value of $\gamma = 0.65^{+0.16}_{-0.25}$ and $t_4 = 1.0^{+0.84}_{-0.35} \times 10^8$ yr are the best combination.
6. We studied the degeneracy between formation increase and disruption. Models where the cluster formation rate increases linearly in time do not affect the disruption time-scale much (t_4 gets a factor 2 higher). When we include bursts at the moments of encounter with NGC 5195, the typical disruption time is also a factor of 2 higher.
7. When clusters of $10^4 M_{\odot}$ are disrupted within 2×10^8 years, and considering the power-law dependence of the disruption time scale with the initial cluster mass, even clusters with a mass of $10^6 M_{\odot}$ will not survive longer than 3.5 Gyr. This means that the disc of M51 is not a preferred location to form a new generation of globular clusters. This might explain why so far there are no old (> Gyr) massive ($> 10^6 M_{\odot}$) clusters known in the discs of spiral galaxies, although they are still forming: e.g. Westerlund 1 in the Galactic disc (Clark & Negueruela 2004) and the young globular cluster in NGC 6946 (Larsen et al. 2001).

CHAPTER 5

Disruption time scales of star clusters in different galaxies

H.J.G.L.M. Lamers, M. Gieles and S.F. Portegies Zwart

Astronomy and Astrophysics, v.429, p.173–179 (2005)

Abstract The observed average lifetime of the population of star clusters in the Solar Neighbourhood, the Small Magellanic Cloud and in selected regions of M51 and M33 is compared with simple theoretical predictions and with the results of N-body simulations. The empirically derived lifetimes (or disruption times) of star clusters depend on their initial mass as ${t_{\rm dis}}^{\rm emp} \propto {M_{\rm cl}}^{0.60}$ in all four galaxies. N-body simulations have shown that the predicted disruption time of clusters in a tidal field scales as ${t_{\rm dis}}^{\rm pred} \propto t_{\rm rh}^{0.75} t_{\rm cr}^{0.25}$, where $t_{\rm rh}$ is the initial half-mass relaxation time and $t_{\rm cr}$ is the crossing time for a cluster in equilibrium. We show that this can be approximated accurately by ${t_{\rm dis}}^{\rm pred} \propto M_{\rm cl}^{0.62}$ for clusters in the mass range of about 10^3 to 10^6 $M_\odot$, in excellent agreement with the observations. Observations of clusters in different extra-galactic environments show that $t_{\rm dis}$ also depends on the ambient density in the galaxies where the clusters reside. Linear analysis predicts that the disruption time will depend on the ambient density of the cluster environment as $t_{\rm dis} \propto \rho_{\rm amb}^{-1/2}$. This relation is consistent with N-body simulations. The empirically derived disruption times of clusters in the Solar Neighbourhood, in the SMC and in M33 agree with these predictions. The best fitting expression for the disruption time is $t_{\rm dis} = C_{\rm env} (M_{\rm cl}/10^4 M_\odot)^{0.62} (\rho_{\rm amb}/M_\odot {\rm pc}^{-3})^{-0.5}$, where $M_{\rm cl}$ is the initial mass of the cluster and $C_{\rm env} \simeq 300 - 800$ Myr. The disruption times of star clusters in M51 within 1 - 5 kpc from the nucleus, is shorter than predicted by about an order of magnitude. This discrepancy might be due to the strong tidal field variations in M51, caused by the strong density contrast between the spiral arms and inter-arm regions, or to the disruptive forces from giant molecular clouds.

5.1. Introduction

The age distribution of star clusters in the disc of the Milky Way, can only be explained if galactic clusters disrupt on a time scale on the order of a few times 10^8 years (Oort 1958; Wielen 1971, 1988). Clusters in the LMC and SMC survive longer than those in the solar neighbourhood (e.g. Elson & Fall 1985, 1988; Hodge 1987.

The disruption time of clusters is expected to depend on both the *internal cluster conditions*, such as the initial mass, density and velocity dispersion and the stellar initial mass function (IMF), and on the *external conditions*, such as the orbit in the galaxy and tidal heating by encounters with for example giant molecular clouds. Recently, Boutloukos & Lamers (2003), hereafter called BL03, have derived an empirical expression for the disruption time of clusters as a function of their initial mass in selected regions in four galaxies. They found large differences in the disruption times between these regions. This allows a crucial test of the theoretical disruption times of clusters predicted with N-body simulations.

The purpose of this paper is three-fold:
(a) to explain the empirical dependence of the cluster disruption times on cluster mass;
(b) to explain the strong dependence, found by BL03 of the disruption time on the conditions in the host galaxies;
(c) to confront the predicted disruption theory with the empirically derived disruption relations.

In § 5.2 we describe the predicted dependence of the disruption times of star clusters on their initial mass and on their environment. In § 5.3 we review the method used for the determination of the disruption times based on a statistical analysis of large cluster samples and the resulting expressions for the disruption times in four galaxies. In § 5.4 we discuss the observed dependence of the disruption times on the environment of the clusters in their host galaxies and we compare it with the predictions. We discuss the peculiar case of the clusters in M51. The conclusions are in § 5.5.

5.2. The predicted dependence of the disruption time on cluster parameters and environment

The evolution of an isolated star cluster is characterised by three distinct phases: (1) infant mortality (the dissolution of unbound clusters) within about 10 Myr (Bastian et al. 2005b; Whitmore 2004), (2) stellar evolution dominates the cluster mass loss in the first $\sim 10^8$ years (see Takahashi & Portegies Zwart 2000) followed by (3) a relaxation dominated phase in which the cluster mass loss is driven by its internal dynamical evolution and the external influence of the tidal field of the host galaxy. If the cluster survives the first two phases, its lifetime will be dominated by the third phase as it generally lasts much longer, until complete dissolution. During this episode mass loss is about constant with time and appears to depend weakly on the density

profile of the cluster (Spitzer 1987; Portegies Zwart et al. 2001a, but see Portegies Zwart et al. 1998, for some complications near the end of the lifetime of the star cluster). During the third phase there are two important effects which drive the cluster dissolution. These are internal two-body relaxation and the interaction between the cluster and the tidal field of the host Galaxy.

Internal two-body relaxation drives the cluster evaporation on a very long time scale of many initial half-mass relaxation times (Baumgardt et al. 2002). The half-mass relaxation time scale can be written as (Spitzer 1987):

$$t_{\rm rh} = 0.138 \frac{N^{1/2} r_{\rm hm}^{3/2}}{\langle m \rangle^{1/2} G^{1/2} \ln \Lambda} \propto \frac{N}{\ln \Lambda} \left(\frac{{r_{\rm h}}^3}{G M_{\rm cl}} \right)^{1/2} \tag{5.1}$$

where N is the initial number of stars in the clusters, $\langle m \rangle = M_{\rm cl}/N$ is the mean mass of the stars and $r_{\rm h}$ is the half-mass radius. The Coulomb logarithm Λ is approximately proportional to N (see Giersz & Heggie 1996; Spinnato et al. 2003).

The mass loss rate for clusters in a tidal field is much higher and the lifetime shorter than for clusters in isolation. Baumgardt (2001) found that for clusters in a tidal field the disruption time depends not only on the relaxation time but also on the crossing time $t_{\rm cr}$ because, due to their circulation within the cluster, stars with sufficient energy still need a considerable time to reach the outskirts of the cluster from where they can escape. He showed that the disruption time can be approximated as

$$t_{\rm dis} \simeq t_{\rm rh}^{x} \, t_{\rm cr}^{1-x} \tag{5.2}$$

where the crossing time for a cluster in equilibrium is

$$t_{\rm cr} \propto r_{\rm hm}^{3/2} / \sqrt{G M_{\rm cl}}. \tag{5.3}$$

and so $t_{\rm cr} \propto t_{\rm rh} \ln \Lambda / N$.

Baumgardt (2001) showed on theoretical arguments that x is expected to be about 3/4. A more accurate estimate of the value of $0 < x < 1$ can be found empirically from N-body simulations (see below). Combining Eqs. 5.1, 5.2 and 5.3 an expression for the disruption time can be derived of the form

$$t_{\rm dis} = C \left[\frac{N}{\ln (\gamma N)} \right]^{x} \left[\frac{{r_{\rm h}}^3}{G M_{\rm cl}} \right]^{1/2} \tag{5.4}$$

where we replaced Λ with γN, with $0.01 < \gamma < 0.4$.

Baumgardt & Makino (2003), hereafter BM03, have performed an extensive set of simulations of clusters in the Galactic halo tidal field and fitted the results to find the constant C and the value of x in the approximation of Eq. 5.4. They used a logarithmic potential of the form $\phi(R_{\rm G}) = V_{\rm G}^2 \ln(R_{\rm G})$, where $R_{\rm G}$ is the distance to the galactic centre and $V_{\rm G}$ is the circular velocity. Their clusters started with a tidal radius equal to the tidal radius of the external field,

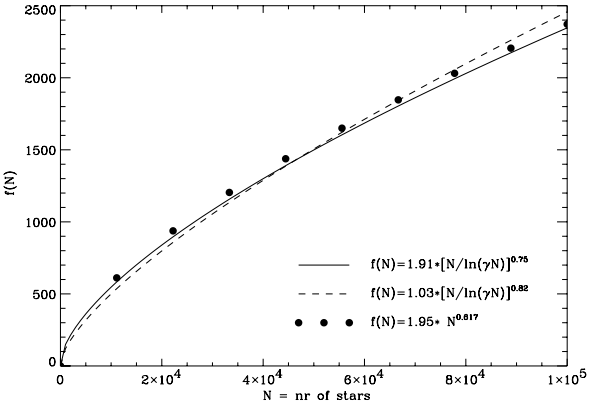

Figure 5.1: The function $\beta\{N/\ln(0.02N)\}^x$ of equation 5.6 for the two combinations of β and x for clusters with $W_0 = 5$ (solid line) and 7 (dashed) from BM03 and the power law approximation 1.95 $N^{0.617}$ (dots).

$$r_{\rm t} = \left(\frac{GM_{\rm cl}}{2V_{\rm G}^2}\right)^{1/3} R_{\rm G}^{2/3} \tag{5.5}$$

If we assume the tidal radius scales linearly with the half-mass radius, which holds for clusters with the same density profile, Eq. 5.5 can be combined with Eq. 5.4, which yields

$$\frac{t_{\rm dis}}{\rm Myr} = \beta \left[\frac{N}{\ln(\gamma N)}\right]^x \frac{R_{\rm G}}{\rm kpc} \left(\frac{V_{\rm G}}{220\,{\rm km\,s^{-1}}}\right)^{-1} \tag{5.6}$$

where β is a constant whose value can be found empirically.

BM03 fitted this relation to the results of their simulations of clusters at different distances from the Galactic centre. For clusters that initially followed a King (1966) profile with central concentration $W_0 = 5.0$ they found $\beta = 1.91$ and $x = 0.75$. For clusters with $W_0 = 7.0$ they found $\beta = 1.03$ and $x = 0.82$. For γ a value of 0.02 was adopted. We found that the factor $\beta\{N/\ln(0.02N)\}^x$ in Eq. 5.6 for both combinations of β and x can be approximated by a power law $1.95N^{0.62}$ with high accuracy. This is illustrated in Fig. 5.1.

The density of the clusters depends on the ambient density which depends on the adopted potential field. The *ambient density*, for the potential field adopted in the study by BM03 can be found by applying Poisson's law which gives

$$\rho_{\rm amb} = \frac{1}{4\pi G}\left(\frac{V_{\rm G}}{R_{\rm G}}\right)^2 \tag{5.7}$$

Combining this with Eq. 5.6, and assuming an initial mean stellar mass of $\langle m \rangle = 0.54 M_\odot$, as done by BM03 based on the stellar IMF of Kroupa (2001), we can write the disruption time as a function of cluster mass and local ambient density:

$$t_{\rm dis} \simeq 810 \left(\frac{M_{\rm cl}}{10^4\ M_\odot} \right)^{0.62} \rho_{\rm amb}^{-1/2} \quad {\rm Myr} \tag{5.8}$$

with $M_{\rm cl}$ in units of $M_\odot$ and $\rho_{\rm amb}$ in $M_\odot {\rm pc}^{-3}$. The constant indicates the time when 95 per cent of the initial cluster mass is lost. If the initial mean stellar mass is 0.70 $M_\odot$, predicted by the stellar IMF from Scalo (1986), the constant decreases from 810 to 690. (For clusters in elliptical orbits with ellipticity ϵ moving within a logarithmic potential field the disruption time is shorter by factor $1 - \epsilon$, if $\rho_{\rm amb}$ is the density at the apogalactic radius.) The positive exponent 0.62 indicates that the disruption time increases with mass, as expected.

The results of N-body simulations and their predicted dependence on the ambient density are plotted in Fig. 5.2. These are based on N-body simulations of clusters of $10^4\ M_\odot$ from different authors. These simulations are from Portegies Zwart et al. (1998, 2002) and BM03. All simulations were performed with `NBODY4` (Aarseth 1999; BM03) and the `Starlab` (Portegies Zwart et al. 2001b)[1] software environment with both codes running on the *GRAPE* family of special purpose computers (Makino et al. 2003). The models by Portegies Zwart et al. (2002) were calculated for star clusters near the Galactic centre, i.e. they are representative for a high density ambient medium.

The dashed line shown in this figure represents the mean relation derived by BM03 and described by Eq. 5.8. This line passes through the data of their individual models.

The full line is the mean relation predicted by Portegies Zwart et al. (2001a). It is derived from the argument that the lifetime of a cluster will depend on the two-body relaxation time near the tidal radius as $t_{\rm dis} \simeq 0.3 t_{\rm rt}$. The tidal radius can be obtained from Eq. 5.5, but the required average cluster density $\rho_{\rm cl}$ is not readily available from the observations. Since the cluster is in equilibrium with its environment one can estimate $\rho_{\rm cl}/\rho_{\rm amb} \simeq 3$ for a standard Roche-solution by assuming that the clusters follow a King (1966) model and that the tidal radius of the King model equals the Jacobi radius of the star cluster in the tidal field of the Galaxy (see e.g. Binney & Tremaine 1987). This predicts that the constant in Eq. 5.8 is about 330 Myr. This is 0.4 times as small as the value derived from the models by BM03 . The line passes through the data of the individual models of Portegies Zwart et al. (1998, 2002).

The simulations by Portegies Zwart et al. (1998, 2002) result in shorter disruption times than the simulations by BM03, by about a factor of 2.5. This difference can be explained by variations in the initial conditions and between the two codes. The initial mass function used in Portegies Zwart et al. (2002) is taken from Scalo (1986) and has a mean stellar mass of $\langle m \rangle \simeq 0.7 M_\odot$. BM03 adopted the initial mass function of Kroupa (2001), which has a mean stellar mass of 0.54 $M_\odot$. Portegies Zwart et al. (1998) and BM03 use King (1966) models for the initial density distribution, whereas

[1] see also `http://www.manybody.org`

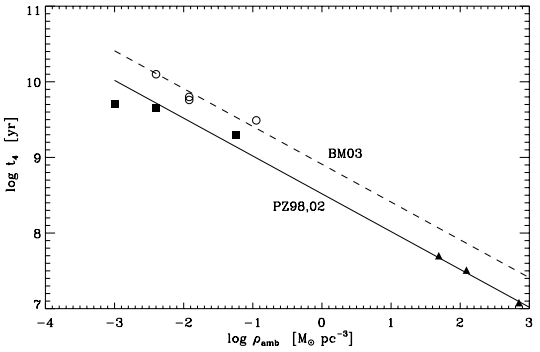

Figure 5.2: The predicted dependence of the disruption time, t_4, of clusters of initial mass of 10^4 $M_\odot$ on the mean ambient density, $\rho_{\rm amb}$. The symbols refer to N-body simulations; filled squares are from Portegies Zwart et al. (1998) (from left to right models IR16, IC16 and FH16), filled triangles are calculations for star clusters near the Galactic centre from Portegies Zwart et al. (2002) (from left to right models R150W4, R90W4 and R34W4). The open circles represent models from BM03 (from left to right models V, I, II and IV with 16384 stars). The dashed line is the relation predicted by BM03, Eq. 5.8, and the full line is the relation predicted by Portegies Zwart et al.

Portegies Zwart et al. (2002) adopt self consistent Heggie & Ramamani (1995) models. But also the stellar evolution in the calculations are slightly different: the stellar evolution in BM03 is based on Pols et al. (1998) whereas the calculations of Portegies Zwart et al. use the stellar evolution predicted by Eggleton et al. (1989). Moreover, the end of the cluster lifetime is defined differently in the various calculations: BM03 and Portegies Zwart et al. (2002) uses the time when 5 percent of the initial mass remains, whereas Portegies Zwart et al. (1998) use the time when 10 percent of the initial mass remains. The most important difference, however, is in the treatments of the tidal field and the way stars escape from the cluster. Portegies Zwart et al. (1998) did not include a full tidal potential, but a simple cut-off radius. This easily leads to a shorter disruption time for the cluster. BM03 and Portegies Zwart et al. (2002), on the other hand adopt a self-consistent tidal field up to the quadrupole moment.[2]

A few notes about these estimate:
(a) The constant of expression (5.8) was derived for clusters moving in circular orbits in the Galactic potential field. Clusters in elliptical or inclined orbits will experience disc or bulge shocking that reduces their lifetime (Spitzer 1987; Fall & Zhang 2001; BM03). However the proportionality with mass and density remains the same.

[2]In an extensive *collaborative* experiment Heggie et al. (1998) perform a detailed comparison between the N-body codes used by Portegies Zwart and Baumgardt (and others). The difference in cluster lifetime is between 20 and 40%. (see `http://www.maths.ed.ac.uk/~douglas/experiment.html`)

(b) Encounters with giant molecular clouds (GMCs) or spiral density waves are not included in these calculations. In situations where these effects are likely to occur, e.g. for clusters in orbits in a galactic plane, the constant will be smaller than estimated above.

Based on these considerations we can expect the following expression for the disruption times of star clusters due to tidal interactions in different extra-galactic environments

$$t_{\rm dis} \; = \; C_{\rm env} \left(\frac{M_{\rm cl}}{10^4 \, M_\odot} \right)^{0.62} \left(\frac{\rho_{\rm amb}}{M_\odot \ {\rm pc}^{-3}} \right)^{-1/2} \tag{5.9}$$

where $C_{\rm env} \simeq 300 - 800$ Myr. If encounters with giant molecular clouds or disc shocking (for clusters in orbits tilted with respect to the galactic plane) becomes important, the disruption times might be shorter than given by Eq. 5.9.

5.3. The empirically determined disruption times

The disruption times of systems of star clusters in different extra-galactic environments have been determined statistically by BL03 from samples of star clusters in four galaxies. We will summarise their method and results.

Suppose that the disruption times of clusters in some region of a galaxy can be written as

$$t_{\rm dis} = t_4 \times (M_{\rm cl}/10^4)^\gamma \tag{5.10}$$

where $M_{\rm cl}$ is the initial cluster mass (in $M_\odot$) and t_4 is the disruption time (in yrs) of a cluster with an initial mass of $M_{\rm cl} = 10^4 \ M_\odot$. Assume also that the cluster formation rate is constant over the period of time for which t_4 and γ are determined, and that all clusters had the same initial stellar IMF. Then, the values of γ and t_4 can be derived from the mass and age histograms of cluster samples with a well determined brightness limit. BL03 have applied this method for an empirical determination of γ and t_4 in specific regions of M51, M33, (observed with $HST/WFPC2$) and in the SMC and the solar neighbourhood. The method has been improved by Lamers et al. (2005a) and by Gieles et al. (2005), who showed that the distribution of the observed clusters in a mass versus-age-diagram provides a more powerful method for deriving t_4 and γ than the mass and age histograms separately.

The results are given in Table 5.3. Column 2 gives the range of galactocentric distances of the cluster sample. Columns 3, 4 and 5 give the number of clusters and their age and mass range. Columns 6 and 7 give the resulting values of the disruption time t_4 and γ. Column 8 gives the ambient density of the host galaxy at the location of the cluster samples used for the determination of the disruption time (see § 4).

In the determination of γ we adopted a cluster IMF with $\alpha = 2.0$ (Zhang & Fall 1999; Bik et al. 2003; de Grijs et al. 2003a). The values of t_4 and γ of the SMC is

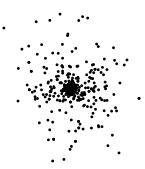

from BL03. The values for M51 have been redetermined by Lamers et al. (2005a) on the basis of the extended cluster sample of Bastian et al. (2005b) and the improved method mentioned above. The values for M33 have been redetermined, on the basis of the extended cluster sample by Chandar et al. (2001, 2002). The new value of t_4 for this galaxy is considerably higher than originally derived by BL03, due to the largely improved cluster sample and a redetermination of the cluster ages. The values for the Solar neighbourhood have been redetermined by Lamers et al. (2005a), based on the clusters sample by Kharchenko et al. (2005).

Notice that the values of γ of the four galaxies are the same, within the uncertainty, but the values of t_4 differ strongly. The mean value of the empirically determined value of γ and its uncertainty is

$$\langle \gamma_{\rm emp} \rangle \;=\; 0.60 \pm 0.02. \tag{5.11}$$

where 0.02 is the uncertainty in the mean value, which is much smaller than the uncertainty in the individual measurements. This exponent agrees very well with $\gamma_{\rm pred} = 0.62$ predicted by BM03, Eq. 5.8, on the basis of their numerical simulations. The agreement between the observed and the predicted value of γ was first pointed out by Gieles et al. (2004), but based on slightly different theoretical arguments.

5.4. The dependence of the disruption time on the conditions in the host galaxy

Table 1 shows that the constant t_4, which is the disruption time of a clusters of $M_{\rm cl} = 10^4 M_\odot$, differs greatly between the regions in the galaxies that were studied. This indicates that the disruption time depends strongly on the local conditions in the host galaxy. In § 5.3 we have shown that t_4 is expected to scale with the inverse square-root of the mean density in the host galaxy, if evolutionary mass loss, relaxation driven evaporation and tidal stripping are the dominant mass loss mechanism for clusters. In this section we compare this predicted dependence with the empirically derived values of the disruption time t_4.

5.4.1. The ambient density in the host galaxies

We estimate the ambient density $\rho_{\rm amb}$ at the galactocentric distances of the observed environments for which BL03, Gieles et al. (2005) and Lamers et al. (2005a) determined the value of t_4.

M51:
The clusters are at galactocentric distances of 1 to 5 kpc. The column density of M51 decreases exponentially as $\sigma = 540 \exp(-r/4.65)\ M_\odot\ {\rm pc}^{-2}$, with r in kpc (Salo & Laurikainen 2000). The total disc mass within a ring of 1 to 5 kpc is 2.0×10^{10} $M_\odot$ and the mean surface density in that annulus is $2.6 \times 10^2\ M_\odot\ {\rm pc}^{-2}$. Van der Kruit (2002) has shown that spiral galaxies have a vertical scale-height of 1/7 times

Table 5.1: The parameters of the disruption time: $t_{\rm dis} = t_4 \times (M_{\rm cl}/10^4)^{\gamma}$

Galaxy	$R_{\rm Gal}$ kpc	Nr	Age range log (yrs)	Mass range log $M_\odot$	$\log t_4$ log (yrs)^a	γ	$\log \rho_{\rm amb}$ $M_\odot$ pc^{-3}	
M51	1.0 - 5.0	1152	6.3 – 9.0	2.6 – 5.6	7.85 ± 0.22 (7.6)	0.57 ± 0.10	-0.70 ± 0.30	2
M33	0.8 - 5.0	147	6.5 – 10.0	3.6 – 5.6	8.80 ± 0.20 (8.1)	0.60 ± 0.15	-0.66 ± 0.30	3
Galaxy	7.5 - 9.5	184	7.2 – 9.5	—	8.75 ± 0.20 (9.0)	0.60 ± 0.12	-1.00 ± 0.04	1,4
SMC	0 - 4	314	7.6 – 10.0	—	9.90 ± 0.20 (9.9)	0.61 ± 0.08	-2.10 ± 0.30	1
					Mean	0.60 ± 0.02		5

(a) The value in parenthesis is the original value from BL03
(1) t_4 and γ from age distribution only
(2) Improved determination of t_4 and γ by Gieles et al. (2005), based on new cluster sample of Bastian et al. (2005b)
(3) Improved determination of t_4 and γ by based on extended cluster samples by Chandar et al. (2001, 2002)
(4) Improved determination by Lamers et al. (2005a)
(5) The quoted error is the uncertainty in the mean value

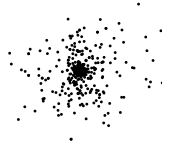

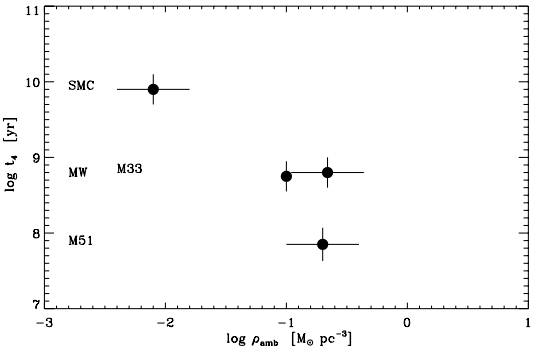

Figure 5.3: The relation between the measured values of the disruption time t_4 of clusters with an initial mass of 10^4 $M_\odot$ and the mean ambient density $\rho_{\rm amb}$ in $M_\odot$ pc^{-3}, of the galaxies at the galactocentric distances where the studied clusters were located.

the radial scale-length. This implies a value of $h_z = 0.66$ kpc and a mean mid-plane density between 1 and 5 kpc of 0.20 $M_\odot$ pc^{-3}. The structural parameters of M51 derived by Athanassoula et al. (1987) result in a very similar estimate of the mid-plane density.

M33:
The sample of clusters is located at galactocentric distances between 1 and 5 kpc. More than 90 percent of the clusters are between 1 and 4 kpc. The column density of M33 decreases exponentially as $\sigma = 525\exp(-r/1.45)$ $M_\odot$ pc^{-2}, with r in kpc (Athanassoula et al. 1987). The total disc mass within a ring of 1 to 4 kpc is 4.2×10^9 $M_\odot$ and the mean surface density is 90 $M_\odot$ pc^{-2}. Adopting an effective thickness of the disc of 1/7 of the radial scale-length, i.e. 0.21 kpc, we find a mean mid-plane density of 0.22 $M_\odot$ pc^{-3}.

Solar Neighbourhood:
The mean gas and stellar density in the solar neighbourhood, derived from Hipparcos data is 0.10 ± 0.01 $M_\odot$ pc^{-3} (Holmberg & Flynn 2000).

SMC:
The sample of clusters is distributed throughout the SMC. With a total mass of about 2×10^9 $M_\odot$ (Mathewson & Ford 1984) and a radius of the central core of 4 kpc (Caldwell & Laney 1991) we find a mean density of 8×10^{-3} $M_\odot$ pc^{-3}.

The ambient densities are listed in Table 5.3, where we have adopted an uncertainty of a factor 2 in the densities, except for the solar neighbourhood. The relation between t_4 and the ambient densities is shown in Figure 5.3. The figure shows a clear trend of decreasing disruption time with increasing ambient density.

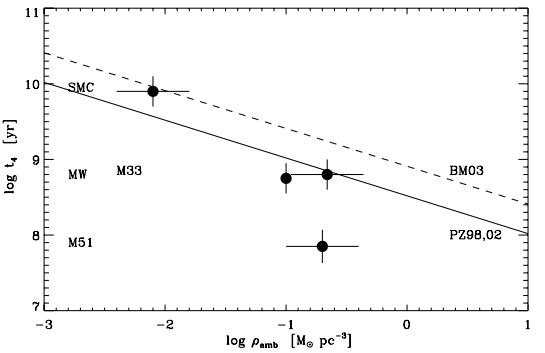

Figure 5.4: Comparison between the observed (large dots) and predicted (lines) disruption time t_4 of clusters with an initial mass of 10^4 $M_\odot$ as a function of the mean density $\rho_{\rm amb}$ in $M_\odot$ pc^{-3} of the host galaxy. The solid curve present the predictions by Portegies Zwart et al. (1998, 2002) and the dashed line by BM03 .

5.4.2. Comparison between observed and predicted disruption time scales

We compare the observed values of t_4 for the different galaxies with the predictions based on N-body simulations, discussed in § 5.3. These simulations were done for clusters in Galactic environments. However, by using the expected scaling laws (§ 5.3), we can apply the results of these simulations to the conditions in the galaxies where the cluster disruption times were measured.

In Fig. 5.4 we compare the observed relation between t_4 and $\rho_{\rm amb}$ with the predicted mean relations derived from N-body simulations of clusters of 10^4 $M_\odot$ from Portegies Zwart et al. (1998, 2002) and BM03, shown in Fig. 5.2.

The empirically derived values of t_4 roughly follow the relations predicted by the N-body simulations within the uncertainty of the data, except for the clusters in M51, whose disruption time is almost an order of magnitude shorter than expected.

There are several possible explanations for the short cluster lifetimes in M51, some of which originate from variations in the birth conditions of the clusters or from star formation histories of the host galaxy. For example, the constant used in Eq. 5.9 depends via $\langle m \rangle$, quite sensitively on the adopted initial mass function. If we adopt a Salpeter (1955) initial mass function with a lower mass limit of $1\,M_\odot$, instead of $0.1\,M_\odot$, the mean stellar mass increases by about an order of magnitude. Such dramatic change to the initial mass function results via Eqs. (5.4) in a reduction of the cluster lifetime by about a factor 3. Such a lower mass cut-off for the initial mass function is controversial, but is suggested in young star clusters like MGG-11 (McCrady et al. 2003) and MGG-F, both in M82 (Smith & Gallagher 2001) and in

several of the young star clusters in the Antennae galaxies (Mengel et al. 2002).

Since M51 experienced a recent star formation event, about 60 Myr ago (Bastian et al. 2005b), possibly part of the discrepancy can be explained by variations in the IMF. (This starburst event was taken into account in the determination of the disruption time for M51 by Gieles et al. (2005). Young star formation environments also tend to have higher metallicity, which drives stronger winds and therefore more stellar mass loss. Another possible explanation for the short disruption time of clusters in M51 is related to the strength of the tidal field variations. M51 has the highest density contrast between the arm and inter-arm regions of any spiral galaxy (Rix & Rieke 1993), so the tidal field variations experienced by star clusters will be higher than normal, which might explain the short disruption time of the star clusters in M51. This last effect is studied by Gieles et al. (2006a,d).

5.5. Conclusions

We analysed the disruption time of star clusters in the Solar Neighbourhood, the SMC and in selected regions of M33 and M51. We find the following result.
(a) Within each region, there is a clear relation between the empirically derived cluster disruption time and the cluster mass of the type $t_{\rm dis} \propto M^{\gamma}$. The mean empirical value of $\gamma_{\rm emp} = 0.60 \pm 0.02$ agrees very well with the predicted value of $\gamma_{\rm pred} = 0.62$, derived from direct N-body simulations of galactic star clusters.
(b) Comparing the disruption times in different galaxies, we find that the disruption time depends on the ambient density in the environment where the clusters reside. N-body simulations of clusters at different galactocentric distances predict that the disruption time decreases with the ambient density as $t_{\rm dis} \propto {\rho_{\rm amb}}^{-0.5}$. The empirical values of three galaxies, SMC, M33 and the Solar neighbourhood agree roughly with this prediction. However, the disruption time of star clusters in the inner 4 kpc of M51 is shorter than predicted by about an order of magnitude. The difference is most likely due to large tidal field variations, due to the high density contrast in the spiral arms and inter-arm regions of M51, or due the starburst triggered by the last encounter with its companion NGC 5195.

The disruption time of star clusters of initial mass $M_{\rm cl}$ in circular orbits in an environment with a mean ambient density $\rho_{\rm amb}$ is given by Eq. 5.9. The disruption time may be shorter in starburst regions.

acknowledgements We thank Nate Bastian for discussions and comments on the manuscript, Albert Bosma and Piet van der Kruit for advice on the densities of spiral galaxies and Holger Baumgardt for providing the results of his numerical simulations. We are grateful to the referee, Douglas Heggie, for constructive suggestions that improved the paper. This work was supported by a grant from the Netherlands Research School for Astronomy (NOVA) to HJGLML and by a grant from the Royal Netherlands Academy of Sciences (KNAW) to SPZ.

Part II

N-body simulations of the disruption of star clusters

CHAPTER 6

Theory of gravitational shocks

Abstract Tidal forces are important contributors to the dissolution of star clusters. In this chapter of the thesis I explain the basic principles of tidal perturbations on star clusters due to fast moving external potentials. This happens when massive objects, such as giant molecular clouds or massive black holes, pass the cluster at small distances or when a cluster crosses a density wave, such as the galactic disc or a spiral arm. If the crossing time of the external potential is much faster than the internal crossing time of stars in the cluster, the perturbation is referred to as a *shock* and the resulting velocity increase of stars in the cluster can be calculated in the *impulsive approximation*. The problem then reduces to a relatively simple mathematical exercise. I derive expressions for the (kinetic) energy gain of a cluster after the passage of a massive object (i.e. *tidal shocks*) and after crossing a density wave (*compressive gravitational shocks*). In both cases, the energy gain per unit of cluster mass (ΔE), scales with the mean square position of stars in the cluster ($\bar{r^2}$) and the relative velocity (V) between the cluster and the perturbing potential as: $\Delta E \propto g^2\,\bar{r^2}/V^2$, where g is the acceleration due to the perturber. For tidal shocks, $g \propto M/p^2$, with M the mass of the perturber (GMC or black hole) and p the encounter distance. For the compressive gravitational shocks $g = g_{\rm m}$, with $g_{\rm m}$ the maximum acceleration experienced by the cluster due to the density wave.

6.1. Introduction

In Chapters 2 and 3 we showed that star clusters do not form and evolve in isolation. Therefore, to understand cluster evolution and explain the observed disruption times of Chapters 4 and 5, we need to take into account the effect of external perturba-

tions on star clusters. In some situations, for example in the Small Magellanic Cloud (SMC, see Chapter 5), the effect of the tidal field of the host galaxy is the dominant contributor to the dissolution of clusters. This effect has been studied extensively by many people, using a variety of techniques to solve for the gravitational N-body problem (e.g. Chernoff & Weinberg 1990; Gnedin & Ostriker 1997; Portegies Zwart et al. 1998; Baumgardt & Makino 2003). Modern N-body simulations consider a realistic stellar mass function, stellar evolution, the effect of the Galactic tidal field and use particle numbers that are close to realistic values of massive clusters ($N \simeq 10^5$). This is feasible due to recent developments of dedicated hardware, in the form of the *GRAPE* computers (Makino et al. 2003), to accelerate force calculations. However, when comparing observed disruption times to the results of simulations of clusters in tidal fields (Chapter 5), only for the SMC good agreement is found. For clusters in the other galaxies considered, i.e. M33, M51 and the solar neighbourhood, the observed disruption times are shorter than expected from the strength of the tidal field only. The tidal field strength can be derived quite accurately from the orbital velocity of the clusters in the galaxy ($V_{\rm G}$) and the location in the galaxy ($R_{\rm G}$), since they relate to the enclosed galaxy mass within the orbit of the cluster as $M(R_{\rm G}) = {V_{\rm G}}^2 R_{\rm G}/G$, where G is the gravitational constant. The Galaxy potential can be derived from $M(R_{\rm G})$. Note that measurements of $V_{\rm G}$ also include possible contributions from dark matter to the tidal field.

However, by approximating the tidal field of a galaxy by a smooth analytical potential, as done in most simulations, contributions from local irregularities in the density distribution are neglected. Looking at the image of M51 in Chapter 1 (Fig. 1.3), it is apparent that the immediate surroundings of young clusters are highly irregular. Clusters will travel through the spiral arms, there are molecular clouds (visible as dark dust lanes in this image) and other (massive) clusters. Since clusters and clouds have a relative velocity dispersion of $\sim 10\,{\rm km\,s^{-1}}$, encounters will occur. Massive clouds can be a factor of 10^{3-4} times more massive than clusters, causing an encounter to affect the cluster more than the cloud.

In this chapter I give a theoretical background of what physically happens with a star cluster when it is disturbed by such irregularities. It serves as an introduction to the following two chapters in this thesis, which deal with N-body simulations of star cluster disruption. § 6.2 explains the effect of passages of massive objects on clusters, which would happen when giant molecular clouds (GMCs) (Chapter 8) or massive black holes pass a star cluster. § 6.3 deals with the effect of a passing density waves. This is usually applied to globular clusters that cross the Galactic disc, but we apply this to young clusters in the disc that cross spiral arms (Chapter 7).

6.2. Tidal shocks

"The tidal force of passing interstellar clouds accelerates the stars in a galactic clusters, increases the total cluster energy, and leads to the expansion and ultimate disruption of clusters." This is the first sentence of the abstract of a seminal paper

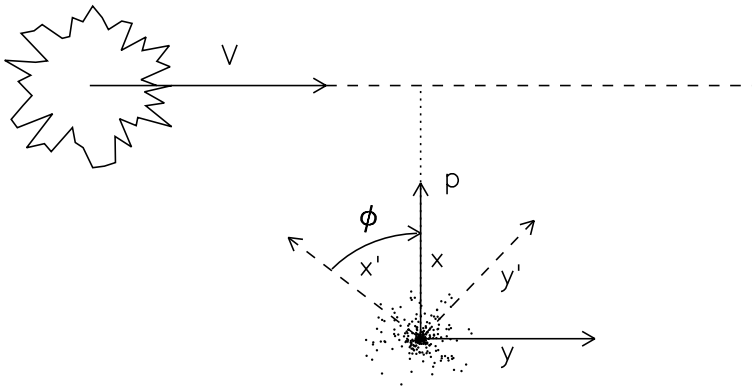

Figure 6.1: Schematic representation of a cloud travelling with velocity V with respect to cluster. The tidal forces are expressed in the rotating co-ordinate frame (x', y', z') with the x'-axis pointing towards the cloud. These are later converted to the static (x, y, z) frame with the x-axis points toward the cloud when it is at closest distance (p).

by Spitzer (1958) on the disruption of Galactic (open) clusters. This paper and a series of follow-up papers by Spitzer and collaborators form the basis of studies on the disruption of clusters by external (time-dependent) tidal fields. Although it is commonly accepted that stars in a cluster are accelerated when a massive object passes, I have experienced that many astronomers, when given a pen and paper, can not derive the explanation of this effect. (Try it!)

With some simple assumptions we can derive the energy gain of a cluster due to tidal heating. If the object (GMC or black hole) passes the cluster sufficiently rapidly, we can compute the increase in velocity ($\Delta\mathbf{v}$) of stars in the cluster as though the stars hold their position during the fast passage. This is referred to as the *impulse approximation*.

Let us define a co-ordinate system centred at the cluster centre and with the x-axis toward to the cloud when it is at its distance of closest approach, p (see Fig. 6.1). The y-axis is taken parallel to the velocity of the cloud relative to the cluster (V)[1]. The z-axis is then perpendicular to the plane of Fig. 6.1. Let R be the distance between the cloud centre and the cluster centre. By choosing $t = 0$ at the moment of closest approach, we can write

[1]small v, r and m refer to the velocity, position and mass of the star in the centre-of-mass frame of the cluster. Capital V, R and M refer to the velocity, position and mass of the cloud with respect to the centre of the cluster.

$$R^2 = p^2 + V^2 t^2. \tag{6.1}$$

The tidal force on a star is defined in a rotating reference frame, with the x'-axis pointing towards the cloud. The tidal forces on stars arise because there is a force gradient in the cluster along the x'-axis. Assuming the cloud is a point-mass, its strength on a star with mass m at distance r from the cluster centre on this axis can be derived by linearising Newton's law, yielding the familiar inverse cube law for tidal forces

$$F_t = \frac{2GM_{\rm n}mr}{R^3}, \tag{6.2}$$

with $M_{\rm n}$ the mass of the cloud. The tidal forces are pointing away from the cluster centre, causing an expansion of the cluster in that direction. In the plane perpendicular to the x'-axis, the forces are directed inwards. At a distance r from the cluster centre along the y'-axis and the z'-axis, the inward force is equal to $(GM_{\rm n}m/R^2)(r/R)$, or $F_t/2$ with negative sign. Hence, the vector notation of the tidal acceleration on a star at position x', y', z' is

$$\mathbf{a}_t = \frac{GM_{\rm n}}{R^3}\,[2x', -y', -z']. \tag{6.3}$$

The angle between the two co-ordinate frames is $\tan(\phi) = Vt/p$. By translating the tidal forces to the (x, y, z) frame and integrating over time, we get the total velocity increment of a star at position (x, y, z) from the cluster centre

$$\Delta\mathbf{v} = \frac{2GM_{\rm n}}{p^2V}[x, 0, -z]. \tag{6.4}$$

There is no velocity increment in the y direction, due to symmetry of the tidal forces in this direction. (Stars at $+y$ positions will feel a tidal force along y with negative sign before $t = 0$ and a positive tidal force after $t = 0$. For stars at $-y$ the other way around.) Note that the sign difference between x and z, which was forgotten by Spitzer, will leave an cluster elongated in the x direction after the encounter. This effect can be seen in Fig. 8.6 of Chapter 8.

Using $\bar{x}^2 + \bar{z}^2 = \frac{2}{3}\bar{r^2}$, with $\bar{r^2}$ the mean square position of stars in the cluster, we can express the total increase in cluster energy per unit mass as

$$\Delta E = \sum_i \frac{1}{2}(\Delta v_i)^2 = \frac{1}{3}\left(\frac{2GM_{\rm n}}{p^2V}\right)^2 \bar{r^2}. \tag{6.5}$$

In Chapter 8 we compare this result to the results of N-body simulations and we show that it is very accurate for encounters with p larger than a few cloud radii, i.e. when the assumption of a point-mass cloud is valid. Since close encounters are very important in the disruption of clusters, because $\Delta E \propto p^{-4}$, we extend Eq. 6.5 to more realistic density profiles for the cloud in Chapter 8.

Nevertheless, the great agreement between the N-body simulations of Chapter 8 and Eq. 6.5 for point-masses show that that the impulse assumption is valid in a cluster-cloud encounter.

6.3. Compressive gravitational shocks

Ostriker, Spitzer, & Chevalier (1972) used the impulse approximation to calculate the disruptive effect of the Galactic disc on globular clusters. They introduced this effect as *compressive gravitational shocks*, which nowadays is commonly referred to as *disc shocks*. The term shock arose because the energy is gained on a very short time scale, typically shorter than the crossing time of stars in the cluster.

Following Ostriker et al. (1972), let the gravitational acceleration by the disc be dependent on Z only: $g(Z)$, where Z is the height above the disc. Let Z_c be the Z position of the cluster centre and define the position of an individual star as $z = Z - Z_c$. If v_z is the corresponding projected stellar velocity relative the cluster centre, then

$$\frac{\mathrm{d}v_z}{\mathrm{d}t} = g(Z) - g(Z_c) \approx z\frac{\mathrm{d}g}{\mathrm{d}Z}(Z_c), \tag{6.6}$$

where it is assumed that z is sufficiently small compared to the range over which Z varies, so that the second order term is negligible. Poisson's law relates the density, $\rho(Z)$, to the potential as

$$\frac{\mathrm{d}^2\phi}{\mathrm{d}Z^2} = 4\pi G\rho(Z). \tag{6.7}$$

Since $g = -\mathrm{d}\phi/\mathrm{d}Z$, the derivative of g scales with the density as $\mathrm{d}g/\mathrm{d}Z \propto -\rho(Z)$. Hence, a density increase leads to a negative $\mathrm{d}v_z/\mathrm{d}t$ in Eq. 6.6, i.e. the cluster gets compressed.

When using $\mathrm{d}Z = V_z\mathrm{d}t$ and the impulse assumption that z is constant during the crossing of the disc, the stellar velocity increment after one disc crossing (Δv_z) is achieved by integrating Eq. 6.6. We then obtain

$$\Delta v_z = \frac{z}{V_z} \mid g(Z_c) \mid_{-Z_m}^{+Z_m}, \tag{6.8}$$

where Z_m is the value of Z where $g(Z)$ reaches its maximum value, g_m. Assuming that $g(Z)$ is an odd function, the total energy gain per unit of cluster mass is

$$\Delta E = \frac{2z^2{g_\mathrm{m}}^2}{V^2} = \frac{2\bar{r^2}g_\mathrm{m}^2}{3V^2}. \tag{6.9}$$

In Fig. 6.2 we illustrate the effect. The acceleration $g(Z)$ is shown as a full line, with the maximum $+g_\mathrm{m}$ and minimum $-g_\mathrm{m}$ indicated. The absolute acceleration on the cluster before and after $Z = 0$ is indicated. We choose three fiducial points in the front, in the cluster centre and in the back of the cluster. If the cluster is between $-g_\mathrm{m}$ and $+g_\mathrm{m}$, the forces are always pointing towards the centre of the disc. In the reference frame of the cluster, however, the tidal forces are all pointing inwards, causing a compression. Due to the extra kinetic energy, stars will travel further out than they would do based on their initial velocity, causing the cluster to expand. When stars get in higher orbits, the mean potential energy is lower. Virialisation

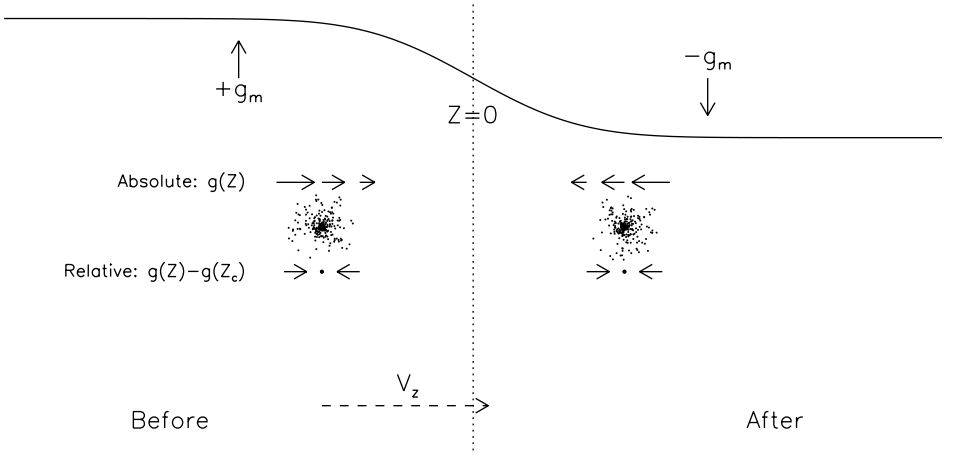

Figure 6.2: Schematic representation of a cluster crossing a density wave. The acceleration g as a function of Z is indicated as a full line, with the maximum and minimum values indicated. Inside that region all forces on the cluster are pointing towards $Z = 0$, where $g = 0$. In the frame of the cluster, the tidal forces are all inwards.

then slows down the stars, resulting in a lower mean kinetic energy of the cluster compared to the initial value.

This chapter serves as an introduction of the general concept of gravitational "shocks". The effect of these shock on the disruption of clusters is the topic of the following three chapters. In Chapter 7 we will also show that the impulse approximation is not always valid, since spiral arms can be very broad and the relative velocity can be low. Then the assumption of static stellar positions is sometimes not valid. Then stars, especially in the core of the cluster, are heated adiabatically, which in general results in a lower overall energy gain.

CHAPTER 7

The effect of spiral arm passages on the evolution of stellar clusters

M. Gieles, E. Athanassoula and S.F. Portegies Zwart

Monthly Notices of the Royal Academic Society, submitted

Abstract We study the effect of spiral arm passages on the evolution of star clusters in planar and circular orbits around the centres of galaxies. We consider the effect of crossings through the high density shocked gas in the spiral arms, which results in a compression of the cluster. A cluster close to the centre or the outskirts of a galaxy experiences frequent high velocity perturbations due to the spiral arms. Clusters orbiting close to the corotation radius ($R_{\rm CR}$) experience fewer spiral arm crossings than those orbiting in the other regions. Near $R_{\rm CR}$, however, the perturbations are of longer duration and, therefore, have a stronger compressive effect on the cluster. The energy injected during each spiral arm passage can exceed the total binding energy of a cluster, but, since most of the energy goes in high velocity escapers from the cluster halo, only relatively little mass is lost. A single perturbation that injects the same amount of energy as the initial (negative) cluster energy causes at most $\sim 40\%$ of the stars to escape. We find that a perturbation that delivers 100 times the initial cluster energy is needed to completely unbind a cluster in a single passage. The net effect of spiral arm perturbations on the evolution of a low mass ($\lesssim 100\,M_\odot$) star clusters is profound. In the solar neighbourhood the disruptive effect of spiral arm perturbations are more important than in a similar but two-armed galaxy, since the Milky Way has four spiral arms. The time scale of disruption by subsequent spiral arm perturbations scales with the galactocentric distance (R) and $R_{\rm CR}$ as the inverse of $R\,|1-R/R_{\rm CR}|$, which has a minimum at $R_{\rm CR}$. Since the solar neighbourhood is near $R_{\rm CR}$, spiral arm perturbations are relatively important there. Still the disruption time due to spiral

arm crossings is about an order of magnitude higher than what is observed for the solar neighbourhood, making spiral arm perturbations a moderate contributor to the dissolution of open clusters.

7.1. Introduction

The distinct difference between open and globular clusters has vanished since the discovery of young massive clusters in merging and interacting galaxies (e.g. Holtzman et al. 1992; Whitmore et al. 1999b). There is, however, still an evident difference in evolution. Star clusters formed in discs, which in our Galaxy are referred to as open clusters, experience external perturbations by giant molecular clouds (GMCs) and by spiral arms and other disc density perturbations. These are not present in the halo of a galaxy, where most of the globular clusters reside. To understand how cluster populations, such as the open clusters in the solar neighbourhood (Kharchenko et al. 2005) and such as the ones found in spiral galaxies like M51 (Bastian et al. 2005b) and NGC 6946 (Larsen et al. 2001), evolve, it is important to understand the effect of these external perturbations.

The number of Galactic open clusters as a function of age shows a lack of old open clusters, first pointed out by Oort (1958). This lack can partially be explained by the rapid fading of clusters with age due to stellar evolution, which makes it harder to observe them at older ages. Still, fading can not explain the difference between the observed and the expected number of old ($\gtrsim 1\,\mathrm{Gyr}$) open clusters, implying that a significant fraction must have been destroyed (Wielen 1971; Lamers et al. 2005a). In addition to two-body relaxation, clusters in tidal fields dissolve by the combined effect of: A.) Mass loss due to stellar evolution, reducing the mass and hence the binding energy of the cluster; B.) the tidal field of the host galaxy, imposing a tidal boundary, increasing the escape rate of stars; C.) bulge/disc shocks, pushing stars over the tidal boundary and D.) additional perturbations induced by irregularities in the galaxy, such as GMCs and spiral arms. The importance of the first three effects has been studied in detail by many people (for example Chernoff & Weinberg 1990; Gnedin & Ostriker 1997; Gnedin, Lee, & Ostriker 1999; Takahashi & Portegies Zwart 2000; Baumgardt & Makino 2003), using different techniques (e.g. Fokker-Planck calculations or N-body simulations).

These studies were mainly aimed at understanding the evolution of globular clusters residing in the Galactic halo. The observed short disruption time ($\sim 100\,\mathrm{Myr}$) of disc clusters in the grand-design spiral galaxy M51 (Gieles et al. 2005) is an order of magnitude lower than expected from the tidal field of the galaxy (Lamers, Gieles, & Portegies Zwart 2005b). Even for clusters in the solar neighbourhood, N-body simulations predict disruption times five times longer than observed. These N-body simulations, however, ignore the presence of spiral arms (for example Takahashi & Portegies Zwart 2000 and Baumgardt & Makino 2003). In this paper, we study the contribution of spiral density waves to the cluster dissolution time.

Spiral arms are believed to be density waves rotating around the galaxy centre

with an angular pattern speed ($\Omega_{\rm p}$) which is independent of the distance R to the galactic centre (see Athanassoula 1984 for a review). The radius at which $\Omega_{\rm p}$ is equal to the angular velocity in the disc ($\Omega(r) = V_{\rm disc}/R$, where $V_{\rm disc}$ the circular velocity in the disc) is called the corotation radius ($R_{\rm CR}$). As gas travels through such a density wave, it gets shocked and compressed to five to ten times higher densities (Roberts 1969). This is observable as narrow sharp dust lanes in optical images of (nearly) face-on spiral galaxies which are far from edge-on.

A cluster on a circular orbit around the centre of the galaxy will, in the inertial frame, have a velocity equal to the circular velocity $V_{\rm disc}$. In the reference frame of the spiral arm, its velocity (hereafter drift velocity, $V_{\rm drift}$) is equal to

$$\begin{aligned} V_{\rm drift} &= |V_{\rm disc} - \Omega_{\rm p} R| \\ &= V_{\rm disc}\,|1 - R/R_{\rm CR}|\,. \end{aligned} \tag{7.1}$$

The absolute value of $V_{\rm drift}$ decreases going from the galaxy centre to $R_{\rm CR}$, where it is zero, and increases again beyond that radius. The time it takes for a cluster to travel from one arm to the next is defined as the drift time: $t_{\rm drift}(R) \equiv 2\pi R/(m\,V_{\rm drift}(R))$, where m is the number of spiral arms in the galaxy. Thus, near to $R_{\rm CR}$, a cluster experiences few passages but of long duration, while at considerably smaller, or considerably larger radii it undergoes many short-lasting spiral arm passages with high velocity. As it moves from the low density inter-arm region to the high density in the arms, the cluster gets compressed due to tidal forces. These accelerate the cluster stars, some of which may reach the escape velocity and become unbound.

This is comparable to what happens to a globular cluster that crosses the Galactic disc (Ostriker, Spitzer, & Chevalier 1972). There are, however, important qualitative differences between spiral arm perturbations and disc shocks. In particular, globular clusters cross the disc with a velocity almost independent of R. On the contrary, the velocity of the cluster with respect to the spiral depends strongly on the distance to the centre. Similarly, the scale-height of a disc is independent of R, provided the galaxy is not barred (van der Kruit & Searle 1981a,b, 1982a,b; de Grijs & van der Kruit 1996). For spiral arms, on the contrary, it is the angular width of the arm that is roughly independent of radius, so that the linear width of a spiral arm is proportional to the radius.

The passage duration determines the nature of the perturbation of the arm on the cluster. If the time to cross the arm ($T_{\rm cr}$) is much longer than the crossing time of stars in the cluster ($t_{\rm cr}$), the stars can adiabatically adjust to the density increase. When $T_{\rm cr}$ is much shorter than $t_{\rm cr}$, the stars get an impulsive velocity increase due to tidal forces. Stars in the cluster core have a short $t_{\rm cr}$ and, therefore, get adiabatically heated. The boundary between adiabatic and impulsive heating in the cluster is determined by the ratio $t_{\rm cr}/T_{\rm cr}$. If this ratio is low, a higher fraction of stars is heated impulsively.

In this paper we study the effect of spiral arm passages on clusters and investigate the importance of relative velocity with respect to the arm. This paper is organised

as follows: In Section 7.2 the physical parameters of spiral arms are derived from observations. Simple analytical estimates of the effects of compressive perturbations are given in Section 7.3. They are confronted with results of N-body simulations in Section 7.4. In Section 7.5 the results of the simulations are used to derive cluster mass loss and disruption times due to the spiral arm perturbations. The conclusions are presented in Section 7.6.

7.2. Spiral arm parameters

7.2.1. Stellar arms

Disc clusters are found to have short disruption times both in our Galaxy and in M51. Therefore, we will hereafter consider two fiducial spiral galaxies, one Milky-Way-like – which we will call for brevity Milky Way, or MW – and the other M51-like – which we will call grand design spiral. We will adopt for both a constant rotational velocity of $V_{\rm disc} = 220\,{\rm km\,s^{-1}}$, that is, we limit ourselves to the regions where their respective rotation curves are flat.

Spiral patterns are present in both young and old populations, as already noted by Zwicky (1955) and later by Schweizer (1976). The old Population II stars in the disc show a broad spiral pattern with a relatively low arm-interarm flux contrast ($\Gamma_{\rm flux}$). The young, blue, Population I stars, which form preferentially in the spiral arms, show more irregular spiral patterns with higher $\Gamma_{\rm flux}$. This is because of the low mass to light ratio and the short life of Population I stars. Estimates of the arm-interarm density contrast (Γ) of the stellar population in the disc of M51 were made by Rix & Rieke (1993) and by Gonzalez & Graham (1996), using the K-band light as tracer of stellar mass. Their results are in good agreement and show that the maximum value for Γ is around $2-3$. Similar values have been found for other grand design spirals (e.g. NGC 4254, see Kranz, Slyz, & Rix 2001). We expect our own Galaxy to have smaller values of Γ. Indeed, Drimmel & Spergel (2001) find a value of $\Gamma \simeq 1.3$ from model comparisons to K-band measurements.

M51 has a clear two-armed ($m = 2$) grand-design spiral, presumably due to the interaction with its companion NGC 5195. The structure of our Galaxy is more complex. It has a bar (see Dehnen 2002 for a review and references therein) and a spiral structure which could rotate with a pattern speed different from that of the bar (Tagger et al. 1987; Sygnet et al. 1988). Drimmel (2000) and Drimmel & Spergel (2001) modelled the COBE-DIRBE data and propose that the old stellar population has a two armed spiral, while the gas and young and stars form a four-armed spiral (for the latter see also Georgelin & Georgelin 1976). Studies in which all components (bar and spirals) have the same pattern speed find that the solar neighbourhood is well beyond corotation (Dehnen 2000; Fux 2001), but models allowing for a different pattern speed for the bar and spiral components give a better view of the complex structure in our Galaxy. Bissantz et al. (2003) calculate the gas response to a composite bar plus spiral model and find best agreement for the observations with a pattern speed of $60\,{\rm km\,s^{-1}\,kpc^{-1}}$ for the bar and $20\,{\rm km\,s^{-1}\,kpc^{-1}}$ for the spiral. Similar values are

found by Martos et al. (2004). This places the solar neighbourhood well beyond the bar corotation, but just within the spiral corotation. With an adopted solar radius of $R_0 = 8.5\,\mathrm{kpc}$ and the adopted value for $V_{\rm disc} = 220\,\mathrm{km\,s^{-1}}$ the solar neighbourhood is at $R \simeq 0.8\,R_{\rm CR}$. Compared to the Milky Way, M51 has been modelled very little and no clear-cut value has been given for its pattern speed. Recently, Zimmer, Rand, & McGraw (2004) and Egusa, Sofue, & Nakanishi (2004) determined the pattern speed of four grand design two-armed spirals and they find values, between 30 and 40 $\mathrm{km\,s^{-1}\,kpc^{-1}}$. We adopt $R_{\rm CR}$= 6 kpc, resulting in a pattern speed of $\sim 37\,\mathrm{km\,s^{-1}\,kpc^{-1}}$.

To further quantify the effect of a spiral-arm passages on the evolution of star clusters, we also need to consider the width of the arms. To enable a quantitative discussion about spiral-arm width, we define $\Delta\,\phi_{1/2}$ as the annular full width at half maximum of the arm. The typical values of $\Delta\,\phi_{1/2}$ measured from optical images of six spiral galaxies by Schweizer (1976), is almost independent of R and $\Delta\,\phi_{1/2} \simeq 20°$. Seigar & James (1998) studied K-band images of a sample of 45 face-on spiral galaxies and found for two-armed spiral galaxies typical values of $\Delta\,\phi_{1/2}$ between 20° and 40°. These values are slightly higher than found by Schweizer (1976), which is probably because the K-band is a better tracer of the old stellar populations, for which $\Delta\,\phi_{1/2}$ is larger. For $\Delta\,\phi_{1/2} = 30°$, the value of $T_{\rm cr}$ depends on $V_{\rm drift}$ and R as $T_{\rm cr} \simeq 0.5R/V_{\rm drift}$. For the solar neighbourhood $T_{\rm cr} \simeq 80\,\mathrm{Myr}$. For our M51-like galaxy, the values for $T_{\rm cr}$ at $[0.1/0.3/0.5] \times R_{\rm CR}$ are $[2.7, 14, 68]\,\mathrm{Myr}$. The values for $T_{\rm cr}$ are all higher than the typical $t_{\rm cr}$ of clusters, that is, a few Myrs. Therefore, the stars in the cluster can respond adiabatically when it crosses the arm and it does not have the short lasting compressive effect as a galactic disc has on globular clusters.

7.2.2. Gaseous arms

The gaseous spiral pattern is different from the stellar one. Gas gets shocked in the potential well of the stellar arms, where it gets compressed to up to ten times higher densities (Roberts 1969). These high gas densities manifest themselves in optical observations of spiral galaxies as thin dust lanes on the leading side of the arm within $R_{\rm CR}$. After the shock, the density decreases exponential-like to a value slightly lower than the mean gas density, as is illustrated in Fig. 7.1. Such stringly peaked high gas densities act as a compressive perturbation on the cluster (Section 7.3), which can be compared to disc shocks of globular clusters. The disc crossing is referred to as a shock in that context because of the short duration of the perturbation. That is, the time to cross the disc is much shorter than $t_{\rm cr}$. Since we here also discuss shocks by gas in the arm we avoid confusions and refer to perturbations instead of shocks. In addition, in Section 7.3 we will show that, due to the variation of $T_{\rm cr}$ with R, the perturbations are of highly varying duration.

Besides the higher densities, also the typical values of $\Delta\,\phi_{1/2}$ of the gaseous spiral arm is much smaller than the one of the stars. Roberts (1969) argues that the width can be calculated by the time-scale of formation and evolution of massive stars, that is, a few tens of Myr, since these stars are visible in the optical, so they must have traveled

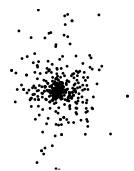

Table 7.1: Adopted parameters for spiral arms in grand design two-armed spiral galaxy and in the Milky Way

	Grand design	Milky Way
m	2	4
$V_{\rm disc}$ (km s^{-1})	220	220
Ω_p (km s^{-1} kpc^{-1})	36.7	24.5
$R_{\rm CR}$ (kpc)	6	9
$\Delta\,\phi_{1/2}$(stars)	30°	15°
$W_{1/2}$(gas) (pc)	250	250
$\Gamma_{\rm stars}$	2-3	< 2
$\Gamma_{\rm gas}$	10	10
$\langle\rho_{\rm HI}\rangle$ ($M_\odot$ pc^{-3})	0.033	0.033

out of the high density environment where they formed. Studies of the molecular spiral arms in M31 and M51 by Nakai et al. (1994) and Nieten et al. (2006), give values of the full-width at half maximum ($W_{1/2}$) of 500 pc and 1000 pc, respectively. Since these values are close to the resolution of the beam, the sharp peak in density (Fig. 7.1) is presumably not resolved. Hydrodynamical simulations of barred galaxies revealed narrower density peaks of the gas (see Fig. 11 of Athanassoula 1992), very close to what was predicted by Roberts (1969) and what is shown in Fig. 7.1. We also measured the width of the dust lane on an optical picture of M51 and the width of the HI on the 8 arcsec resolution map of Rots et al. (1990) and find that they are both compatible with a width of 250 pc. We, therefore, adopt $W_{1/2} = 250$ pc for the gaseous arms.

Measurements of the neutral hydrogen content in a sample of spiral galaxies in the Virgo cluster (Cayatte et al. 1994) show that the *surface* density of HI gas ($\Sigma_{\rm HI}$) within $R \simeq 10$ kpc in gas rich spirals is nearly constant with R and of the order of $\Sigma_{\rm HI} \simeq 10\,M_\odot{\rm pc}^{-2}$. A recent study of the Milky Way (Levine, Blitz, & Heiles 2006) gives similar values for $\Sigma_{\rm HI}$ in the solar neighbourhood. Levine et al. (2006) also find that Γ is almost independent of R. Their measurements of the arm-interarm surface density contrast (Π), combined with the measured vertical compression factor in the spiral arms are consistent with $\Gamma = 10$ for the gas.

From $\Sigma_{\rm HI}$ and the vertical scale height of gas ($H_{\rm z}$) we can derive the mean midplane density of HI ($\langle\rho_{\rm HI}\rangle$), since $\langle\rho_{\rm HI}\rangle = \Sigma_{\rm HI}/2H_{\rm z}$, assuming an exponential vertical density distribution. Van der Kruit (1988) finds a vertical scale height of $H_{\rm z} \simeq 150$ pc, resulting in $\langle\rho_{\rm HI}\rangle \simeq 0.033\,M_\odot$ pc^{-3}. The peak density (ρ_0) is then

$$\rho_0 \simeq \Gamma\,\langle\rho_{\rm HI}\rangle, \tag{7.2}$$

where we assume Γ is the ratio of ρ_0 to $\langle\rho_{\rm HI}\rangle$.

All parameters of spiral arms, used in our models, are summarised in Table 7.1.

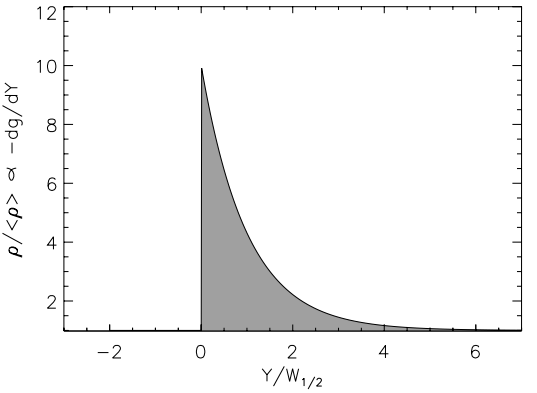

Figure 7.1: Schematic illustration of the gas density along azimuthal trajectories through a spiral arm, where the gas travels from left to right in this figure. The grey shaded area is the gas density predicted by Roberts (1969). When the scale length of a Gaussian function (H) is $1/\sqrt{\pi}$ times the scale length of the exponential function ($W_{1/2}$), the areas under the two curves are the same.

7.2.3. Potential-density relations for the arms

The density of gas along the clusters orbit has a sharp raise at the point where the shock occurs and an exponential-like decrease after the shock (see Fig. 7.1 and Fig. 5 of Roberts 1969). For simplicity we assume a one-dimensional density perturbation of Gaussian form

$$\rho(Y) = \rho_0 \, \exp(-Y^2/H^2), \tag{7.3}$$

with H the scale length and Y is the azimuthal distance. In Section 7.3 we will show that the compressive tidal forces on the cluster are determined by the integration of $\rho(Y)$ with respect to Y, where Y is the direction of motion of the cluster. A Gaussian function with a surface equal to an exponential function has the same compressive effect on the cluster. When defining the exponential function as $\rho(Y) = \rho_0 \, \exp(-Y/W_{1/2})$, for $Y > 0$, and the Gaussian function of Eq. (7.3), then the surfaces are equal when $H = W_{1/2}/\sqrt{\pi}$. With Table 7.1 we thus find that $H \simeq 150\,\mathrm{pc}$ for the gaseous arms.

By using Poisson's law and Eq. 7.3 we can derive the related potential along the trajectory of the cluster

$$\phi(Y) = 2\pi G \rho_0 H \left[\sqrt{\pi} Y erf(Y/H) + H \exp(-Y^2/H^2)\right], \tag{7.4}$$

with G the gravitational constant. The acceleration ($g(Y)$) that is felt by the cluster due to spiral arm passage is equal to $-\mathrm{d}\phi/\mathrm{d}Y$ and with Eq. 7.4 it follows that

$$g(Y) = -2\pi^{3/2} G \rho_0 H erf(Y/H). \tag{7.5}$$

The Gaussian density form (Eq. 7.3) implies a constant acceleration far from the centre of the density wave. This is not physical for spiral arms, since the attractive force due to the arm should decrease with distance from it and should reach zero in between two arms. Therefore, we only consider the effect of the density wave in the vicinity of its centre ($-2H < Y < +2H$), that is, where $g(Y)$ varies and hence tidal forces are at work causing a compression of the cluster (Section 7.3).

The values of $\Delta\,\phi_{1/2}$ and $W_{1/2}$ are always measured in the tangential direction, that is, along the orbit of the cluster. The width perpendicular to the spiral arm is therefore smaller and depends on the pitch angle. Given the uncertainties in the arm width measurements and since the typical radius of star clusters ($\sim 3-4\,\mathrm{pc}$) is much smaller than the $W_{1/2}$ of the spiral arm, it does not matter that clusters cross the arm with a certain angle. In order to avoid having the pitch angle as an extra parameter, we study perpendicular passages through a density wave. The effect of the pitch angle is taken into account in the choice of the azimuthal scale length H.

7.3. Simple analytical estimates for one-dimensional tidal perturbations

7.3.1. The impulsive approximation

The energy gain of a globular cluster crossing the Galactic disc was derived by Ostriker et al. (1972) using the impulse approximation. They assumed that the stars do not move during the passage of the density wave, that is, that $t_{\rm cr}$ is much longer than $T_{\rm cr}$.

Assume a one-dimensional acceleration along the Y-axis ($g(Y)$), a cluster with its centre at $Y_{\rm c}$ and an individual star at a distance $y = Y - Y_{\rm c}$ from the cluster centre. The tidal acceleration of a star due to the density wave is then

$$\frac{{\rm d}v_{\rm y}}{{\rm d}t} = g(Y) - g(Y_{\rm c}) \simeq y\frac{{\rm d}g}{{\rm d}Y} = \frac{y}{V}\frac{{\rm d}g}{{\rm d}t}, \tag{7.6}$$

where we have substituted ${\rm d}Y = V{\rm d}t$, with V the relative velocity between the cluster and the density wave and where g is expanded around the cluster centre. This is accurate as long as the cluster is much smaller than the width of the density wave. Note that the tidal acceleration scales with the density variation ($\rho(Y)$) since $g = -{\rm d}\phi/{\rm d}Y$ and $\rho(Y) \propto {\rm d}^2\phi/{\rm d}Y^2$ through Poisson's law. Therefore, the tidal forces scale with $-\rho(Y)$ (Eq. 7.6) and are always directed inwards for a density increase. Combined with the impulsive assumption, Ostriker et al. (1972) introduced the name *compressive gravitational shock*. As mentioned in Section 7.2, the term shock was introduced due to the short duration of the perturbation. This does not necessarily have to be the case, since for cluster close to $R_{\rm CR}$ $T_{\rm cr}$ can be long.

Integrating Eq. (7.6) then yields an expression for the velocity increment of a star of the form

$$\Delta v_{\rm y} = \frac{y}{V}\,|\,g(Y_c)\,|_{-Y_{\rm m}}^{+Y_{\rm m}}\,. \tag{7.7}$$

In here $Y_{\rm m}$ is the point where g reaches its maximum $g_{\rm m}$. If g is an odd function and does not change much for $Y < -Y_{\rm m}$ and $Y > +Y_{\rm m}$ the total energy gain per unit mass of a cluster after a tidal perturbation is

$$\Delta E_{\rm imp} = \frac{2\, g_{\rm m}^2\, \bar{r^2}}{3\, V^2}, \tag{7.8}$$

where we have substituted $\bar{y^2} = \frac{1}{3}\bar{r^2}$, where $\bar{r^2}$ is the mean square position of stars in the cluster. From Eq. 7.5 it follows that $g_{\rm m}$ is

$$g_{\rm m} = 2\pi^{3/2} G \rho_0 H. \tag{7.9}$$

As mentioned in Section 7.2.3 the constant acceleration at large distances of the Gaussian density is not physical in the case of spiral arms. However, we are interested in the density change and the related change in g from $-g_{\rm m}$ to $+g_{\rm m}$ close to the centre of the density wave is approximately correct.

7.3.2. Validity of the impulsive approximation

Constant velocity assumption

One of the assumptions made by Ostriker et al. (1972) and later in more detailed studies (see for example Weinberg 1994c; Murali & Weinberg 1997; Gnedin & Ostriker 1997, 1999) on the tidal perturbation due to the Galactic disc on globular clusters is that the velocity, $V(Y)$, remains constant during the crossing. This is probably not such a bad assumption for the globular clusters, since they cross the disc with high initial relative velocity ($\sim 200\,{\rm km\,s^{-1}}$). For spiral arms, however, the relative velocity is between zero at $R_{\rm CR}$ and almost $V_{\rm disc}$ close to the galaxy centre and at large distances from it. For low $V_{\rm drift}$ there is large relative increase of velocity, making the assumption of a constant velocity invalid (Eq. 7.6 and 7.8). The most accurate solution to this would be to express V as a function of g and integrate Eq. 7.6. This, however, is even for this simple functional form quite hard.

Alternatively, we can estimate the change in $V(Y)$ from $\phi(Y)$ (Eq. 7.4). The variation of $V(Y)$ depends on $\phi(Y)$ as

$$V(Y) = \sqrt{V_0^2 + 2\,[\phi_0 - \phi(Y)]}, \tag{7.10}$$

with ϕ_0 and V_0 a reference potential and velocity, respectively. The variation of $g(Y)$ follows from the spatial derivative of $\phi(Y)$. We need to integrate $1/V$ with respect to g (Eq. 7.6), to get the total $\Delta v_{\rm y}$ of an individual star. In Fig. 7.2 we show the variation of $1/V$ with g for a constant V (dotted) line and one that considers an acceleration due to the potential (full line). The shaded surface is the result of the integration of $1/V$ with respect to g. This surface is almost equal to $\simeq 2g_{\rm m}/V_{\rm max}$.

Using Eq. 7.4 we can find an expression for $\Delta\phi$ of the form

$$\Delta\phi = \phi(Y_0) - \phi(0) = 2\pi G \rho_0 H \left[\sqrt{\pi} Y_0 - H\right] \tag{7.11}$$

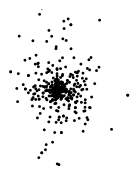

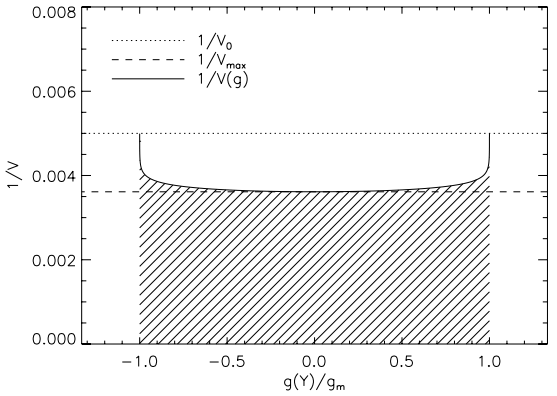

Figure 7.2: The variation of $1/V$ with $g(Y)$ (Eq. 7.6) for a constant V_0 and $V_{\rm max}$ (dotted and dashed, respectively) and for the true $1/V(g)$ (full line), derived from the $\phi(Y)$ (Eq. 7.4).

where Y_0 is the starting position of the cluster, where it has velocity V_0 with respect to the density wave. Equation 7.11, combined with Eq. (7.10), can be used to find the value of $V_{\rm max}$. This suggests that $V_{\rm max}$, i.e. the maximum velocity of the cluster relative to the spiral arm, should be used instead of V_0 to get the correct energy gain from Eq. 7.8. In Section 7.4 we validate this with N-body simulations.

The effect of adiabatic damping

The value of $t_{\rm cr}$ depends on the distance of the stars to the cluster centre (r). In the core of the cluster $t_{\rm cr}$ is much shorter than close to the tidal radius ($r_{\rm t}$). For stars with short period orbits, the effect of the shock is largely damped due to adiabatic invariances. Therefore, there is almost no net energy gain in the core. On the other hand the stars in the outer region will largely be heated impulsively. To define the transition between the impulsive and adiabatic regions, we can define an adiabatic parameter (Spitzer 1987)

$$x \equiv \frac{\omega H}{V}, \tag{7.12}$$

where ω is the angular velocity of stars inside the clusters. This is defined as $\omega(r) = \sigma(r)/r$, with $\sigma(r)$ the velocity dispersion of stars at position r. (Note that the original definition of the adiabatic parameter by Spitzer 1987 contains an additional factor 2. We choose to define x as the ratio of the time it takes the cluster to cross a distance H to the time it takes a star to cross a distance r inside the cluster, e.g. $T_{\rm cr}/t_{\rm cr}$ as did Gnedin & Ostriker (1999).) When $x << 1$ the term shock is justified, and for $x >> 1$ the perturbation is largely adiabatic.

Spitzer (1958) gives an estimate of the conservation of adiabatic invariants in the harmonic potential approximation. This assumes all stars are initially at the same distance r from the cluster centre and have the same oscillation frequency ω. The energy gain for each star can then be written as a function of the result of the impulsive approximation (Section 7.3.1) and an adiabatic correction factor $A(x)$ (Eq. 5 of Kundic & Ostriker 1995)

$$\Delta E = \Delta E_{\rm imp}\, A(x), \tag{7.13}$$

with $\Delta E_{\rm imp}$ the result of Eq. (7.8). The correction factor $A(x)$ in the harmonic approximation is (for example Spitzer 1987, Eqs. 5-28)

$$A_{\rm s}(x) = \exp(-2x^2). \tag{7.14}$$

We refer to $A_{\rm s}(x)$ as the Spitzer correction. (The original definition of $A_{\rm s}(x)$ by Spitzer has a factor 0.5 instead of 2, this because of the different definition of x in Eq. 7.12.)

Weinberg (1994a,b,c) showed that this exponential decrease of the energy with x underestimates the heating effect. This is due to the fact that the basic assumption of the harmonic potential approximation is not valid when the system has more than one degree of freedom, so that small perturbations can still grow. When the cluster is represented as a multidimensional system of nonlinear oscillators, some perturbation frequencies become commensurable with the oscillator frequencies of stars. This results in a correction factor $A(x)$ that is not exponentially small for large x but, instead, has a power-law dependence on x. The simplest form, as shown by Gnedin & Ostriker (1997), can be written as

$$A_{\rm w}(x) = (1 + x^2)^{-3/2}. \tag{7.15}$$

We refer to $A_{\rm w}(x)$ as the Weinberg correction. The index $-3/2$ is also dependent on the duration of the shock (Gnedin & Ostriker 1999).

Besides this shift in energy (ΔE), there is also a quadratic term that affects the dispersion of the energy spectrum of the cluster. The effect of shock-induced relaxation was mentioned by Spitzer & Chevalier (1973) and later studied in more detail by Kundic & Ostriker (1995). It is beyond the scope of this study to include all this detailed physics and we refer the reader to the aforementioned papers for details.

In Section 7.4 we will compare results from N-body simulations to both adiabatic correction factors (Eqs. 7.14 and 7.15).

7.4. N-body simulations

In this Section, we confront the simple analytical estimates given in Section 7.3 with a series of N-body simulations of clusters that cross a density wave of Gaussian form (Eq. 7.3). The potential and acceleration are derived from the one-dimensional Gaussian density profile, as described in Section 7.2.3.

7.4.1. Set-up of the simulations

Description of the code

The N-body calculations were carried out by the `kira` integrator, which is part of the `Starlab` software environment (McMillan & Hut 1996; Portegies Zwart et al. 2001b). `Kira` uses a fourth-order Hermite scheme and includes special treatments of close two-body and multiple encounters of arbitrary complexity. The special purpose *GRAPE-6* systems (Makino et al. 2003) of the Observatoire de Marseille and of the University of Amsterdam are used to accelerate the calculation of gravitational forces between stars.

Units and scaling

The cluster energy per unit mass (E_0) is defined as $E_0 = \eta G M_{\rm cl}/(2r_{\rm h})$, with $\eta \simeq 0.4$, $M_{\rm cl}$ the mass of the cluster and $r_{\rm h}$ its half-mass radius, depending on the cluster model. All clusters are scaled to N-body units, such that $G = M_{\rm cl} = 1$ and $E_0 = -1/4$, following Heggie & Mathieu (1986). The virial radius ($r_{\rm v}$) is the unit of length and follows from the scaling of the energy, since $r_{\rm v} \equiv GM_{\rm cl}/(2|U|) = 1$, where U is the potential energy per unit of cluster mass. We assume virial equilibrium at the start of the simulation, which implies $U = 2E_0$ and, therefore, $r_{\rm v}(t = 0) = 1$.

Cluster parameters

For the density distribution of the cluster we assume a King (1966) profile. Such a profile fits the radial luminosity profile of our Galactic clusters. Open clusters in our Galaxy have a lower concentration index than globular clusters. When we define the concentration index as $c = \log(r_t/r_c)$, with $r_{\rm t}$ the tidal radius and $r_{\rm c}$ the core radius of the cluster, typical values for open clusters are $0.5 < c < 0.9$ (King 1962) or even lower (Binney & Tremaine 1987). A concentration index $c = 0.7$ corresponds to a dimensionless central potential depth of $W_0 = 3$. The average concentration index of globular clusters is $c \simeq 1.5$ (Harris 1996b), corresponding to $W_0 = 7$. Here, we adopt a dimensionless central potential depth of $W_0 = 5$. This corresponds to a concentration index of $c = \log(r_{\rm t}/r_{\rm c}) \simeq 1.03$. For a $W_0 = 5$ cluster it follows that $\eta = 0.41$. The corresponding radii are $r_{\rm h} = 0.81$ and $\bar{r^2} = 1.36$ in N-body units (Section 7.4.1).

Code testing

To test our code, we run a single perturbation with $H = 100$ and $V_0 = 200$ and ρ_0 chosen such, that $\Delta E/|E_0| = 0.05$ (Eqs. 7.8 and 7.9). The cluster consists of $N = 65\,536$ equal mass particles. The cluster is positioned at $Y_0 = -2H$ and the velocity is directed towards the density wave. When the cluster is at $+2H$, there are almost no tidal forces anymore, but there is still an acceleration towards the density wave (Eq. 7.5). To prevent a second crossing, we turn the external tidal field off. The cluster is evolved for an additional $10t_{\rm cr}$ after the perturbation. In Fig. 7.3 we

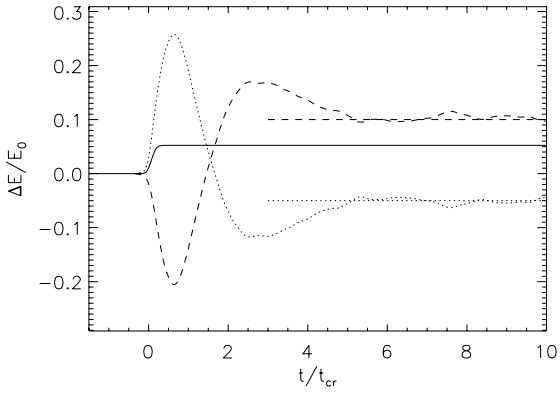

Figure 7.3: Variation of fractional energy gain ($\Delta E/|E_0|$), shown as a full line and the kinetic and potential component shown as dotted and dashed lines, respectively. The cluster has $N = 65\,536$ particles and started in virial equilibrium. Parameters for the density wave are described in the text (Section 7.4.1).

show the variation of the energy gain[1] (ΔE) as a full line and the internal kinetic energy (ΔT) and potential energy (ΔU) as dotted and dashed lines, respectively. Due to the compressive nature of the tidal forces, all stars gain kinetic energy in the $-y$ direction, resulting in an increasing T. Consequently, the stars move deeper in the potential of the cluster, resulting in a decreasing U. The cluster is in virial equilibrium before the perturbation, that is, the virial ratio is equal to one ($Q = -2T/U = 1$). The value of Q increases due to the perturbation. After the perturbation the cluster revirialises, due to relaxation, reducing Q initially to $Q < 1$, around $t \simeq 3t_{\rm cr}$. After a few oscillations the virial ratio is close to one again, leaving a cluster with $\Delta T = -\Delta E$ and $\Delta U = +2\Delta E$.

7.4.2. Parameters of the runs

We choose to use the same clusters as before. The value of ω varies strongly within the cluster, from $\gtrsim 100$ deep in the core down to ~ 0.01 at $r_{\rm t}$. We, therefore, calculate the mass weighted mean value of ω, i.e. $\bar{\omega}$, by numerically solving

$$\bar{\omega} = \frac{4\pi}{M_{\rm cl}} \int_0^{r_{\rm t}} r^2 \rho(r) \omega(r) {\rm d}r. \tag{7.16}$$

For a King profile with $W_0 = 5$, $\bar{\omega} = 0.68$. This is about a factor of two higher than $1/t_{\rm cr}$, with $t_{\rm cr} = 2\sqrt{2}$ at $r_{\rm v}$ (in N-body units). The point where $\omega(r) = 0.68$ is slightly

[1] When we discuss cluster energy, we refer to the sum of the *internal* potential and *internal* kinetic energy, that is, where the energy of the centre of mass motion and the contribution of the external tidal field have been subtracted.

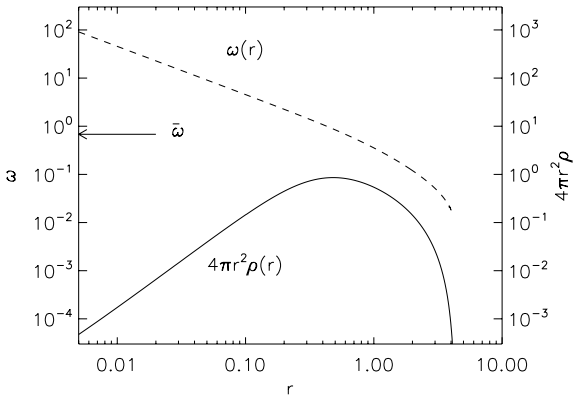

Figure 7.4: Variation of w as a function of r for a cluster with $W_0 = 5$ (dashed line). The mass contribution $4\pi r^2\rho(r)$ is shown as a full line. The solution of Eq. 7.16 is indicated with an arrow.

inside the half-mass radius: $r(\omega = \bar{\omega}) = 0.72r_{\rm h}$. Fig. 7.4 illustrates the variation of $\omega(r)$ (dashed line) and $4\pi r^2\rho(r)$ (full line) for a $W_0 = 5$ cluster.

The value of ρ_0 was chosen such that the predicted $\Delta E_{\rm imp}$ (Eq. 7.8) is always 1/8 of $|E_0|$, which is $+1/32$ (in N-body units) (Section 7.4.1). This is possible since ρ_0 is a free parameter in Eqs. 7.8 and 7.9 after V_0 and H are defined by our grid.

The cluster is positioned at a distance $Y_0 = -2H$ initially and then gets a velocity V_0 in the Y-direction.

7.4.3. Testing the validity of the impulsive approximation

We ran two series of 12 simulations, both for the same sequence of x values (Eq. 7.12), ranging from 0.003 to 15. This was achieved, in the first series by fixing $V_0 = 50$ and varying H and in the second series by fixing $H = 50$ and varying V_0 accordingly. We have assumed the cluster energy gain (ΔE) to scale with $1/V_0^2$ (Eq. 7.8). It is to be expected that ΔE decreases for larger x, because the maximum velocity is larger (Section 7.3.2) for larger x, due to the longer duration of the perturbation.

In Fig. 7.5 we show $\Delta E/|E_0|$ as a function of x, defined in terms of V_0. The result for constant V_0 and H are shown in the left and right panel, respectively. The square symbols are the results of the N-body simulations. The dashed line shows the prediction of $\Delta E_{\rm imp}$ (Eq. 7.8) based on a constant velocity. Excellent agreement between the simulations and the analytical predictions using the impulsive approximation is found for $x \lesssim 0.03$, for both series. With the full line we show the predicted energy gain when we use $V_{\rm max}$ in Eq. 7.8, which we derived from Eqs. 7.10 and 7.11. Indeed the energy gain decreases for larger x, since $V_{\rm max}/V_0$ increases for

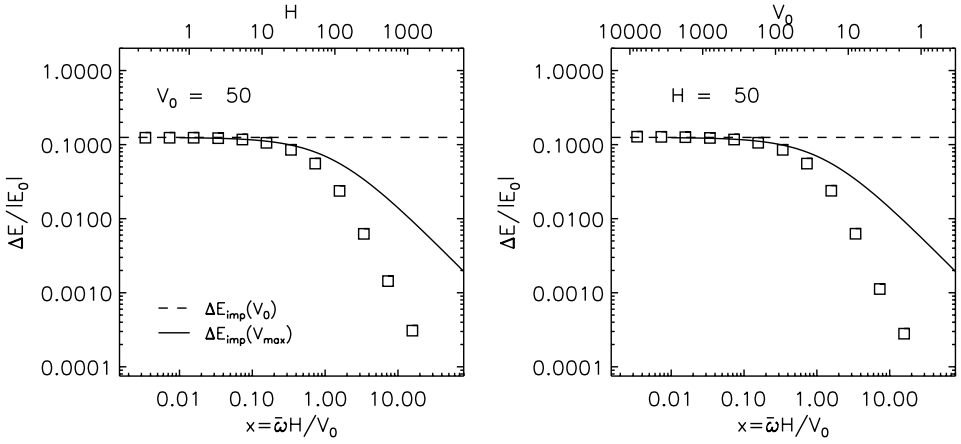

Figure 7.5: Fractional energy gain ($\Delta E/|E_0|$) as a function of the adiabatic parameter x (Eq. 7.12) resulting from the N-body simulations described in Section 7.4.2 (squares), the impulsive approximation (Eq. 7.8) based on V_0 (dashed line) and on $V_{\rm max}$ (full line). In the left panel the value for V_0 was fixed and H was varied to vary x. In the right panel it was done the other way around.

perturbations with longer duration. This prediction of $\Delta E_{\rm imp}(V_{\rm max})$ explains the results of the simulations very nicely for $x \lesssim 0.5$. For $x \gtrsim 0.5$ the energy gain in the simulations is lower than predicted by the impulsive approximations. This is caused by adiabatic invariances in the cluster core (Section 7.3.2). In Section 7.4.4 we compare the results of the simulations to the theoretical predictions that include adiabatic damping.

7.4.4. Adiabatic invariances

To quantify deviations from the impulsive approximation, that is, the effect of damping by adiabatic invariances, we show in Fig. 7.6 the resulting $\Delta E/|E_0|$ of the simulations from Section 7.4.3, but now using $V_{\rm max}$ in the definition of x (Eq. 7.12) and $\Delta E_{\rm imp}$ (Eq. 7.8). The values of $\Delta E/|E_0|$ from the simulations are multiplied by $(V_{\rm max}/V_0)^2$. If all simulations were in the impulse regime, the energy gain would be constant ($\Delta E/|E_0| = 1/2$), which is shown as a dashed line. (Note that the dashed line in Fig. 7.6 is the same as the full line in Fig. 7.5). The theoretical predictions with adiabatic correction are shown for the result of Spitzer (Eq. 7.14) and Weinberg (Eq. 7.15) as dotted and full lines, respectively. As was already clear from Fig. 7.5, the simulations can be well explained by the impulsive approximation for $x \lesssim 0.5$. The decrease of $\Delta E/|E_0|$ for $x \gtrsim 0.5$ is well explained by the predictions made by Weinberg (1994a,b,c), that is, Eq. (7.15) (full line).

Since close to $R_{\rm CR}$ the values of $V_{\rm drift}$ are low, and therefore $x > 1$ (Section 7.2),

it is important to include a correct description of adiabatic damping to understand the effect of spiral arm perturbations on clusters. Including the simple correction as derived by Spitzer (Eq. 7.14) underestimates the energy gain of perturbations with low $V_{\rm drift}$. The impulsive approximation (Eq. 7.8) overestimates the energy gain by orders of magnitude.

7.5. Cluster mass loss and disruption by spiral arm perturbations

7.5.1. Energy gain *vs.* mass loss

The energy gained in a compressive perturbation is absorbed mainly by the stars in the outer parts, since for these stars r is large (Eq. 7.8). This implies that the fractional energy gain ($\Delta E/|E_0|$) is not necessarily equal to the fractional mass loss ($\Delta M/M_0$)[2]. In fact, $\Delta E/|E_0|$ is higher than$\Delta M/M_0$, since stars escape with velocities higher than the escape velocity. Since this energy is taken by escaping stars, it can not be used to unbind more stars. This was also found for encounters between star clusters and GMCs (Gieles et al. 2006d).

We simulate perturbations with $\Delta E/|E_0|$ between 10^{-3} and 100 for clusters with $N = 2048$. The values of H and V_0 were fixed at 10 and 100, respectively. The value of ρ_0 was varied to achieve the desired energy gain. The simulations are run without a tidal field for five crossing times after the perturbations. The final number of unbound stars is then compared to $\Delta E/|E_0|$ from the simulations. In Fig. 7.7 we show $\Delta M/M_0$ as a function of $\Delta E/|E_0|$ following from the simulations (circles). The dotted line shows a one-to-one relation. For $\Delta E/|E_0| < 1$ the relation between $\Delta M/M_0$ and $\Delta E/|E_0|$ is almost linear, but with $\Delta M/M_0$ a factor of 7.5 lower than $\Delta E/|E_0|$. For $\Delta E/|E_0| > 1$ the relation flattens to $\Delta M/M_0 = 1$, that is, a value corresponding to a completely unbound cluster. This relation can be described well by a simple function of the form

$$\Delta M/M_0 = 1 - \exp(-f\Delta E/|E_0|), \tag{7.17}$$

with $f \simeq 1/7.5$ (dashed line). The reason of this flattening is that the assumption of the impulsive approximation is not valid anymore for such strong perturbations. The stars in the centre of the cluster are heated adiabatically (Fig. 7.4) and remain bound after the perturbation. A value of $\Delta E/|E_0|$ of almost 100 is necessary to completely unbind the cluster with a single passage.

Stars that do not get unbound can get in higher energy orbits, where in the presence of a tidal field they can be beyond $r_{\rm t}$. Since in these simulations we ignore the Galactic tidal field, we follow the number of stars that is pushed over $r_{\rm t}$. We adopt a physically more relevant definition of $\Delta M/M_0$ that considers all unbound stars plus stars that are still bound to the cluster, but have positions larger than

[2]We define the mass loss, ΔM, to be positive.

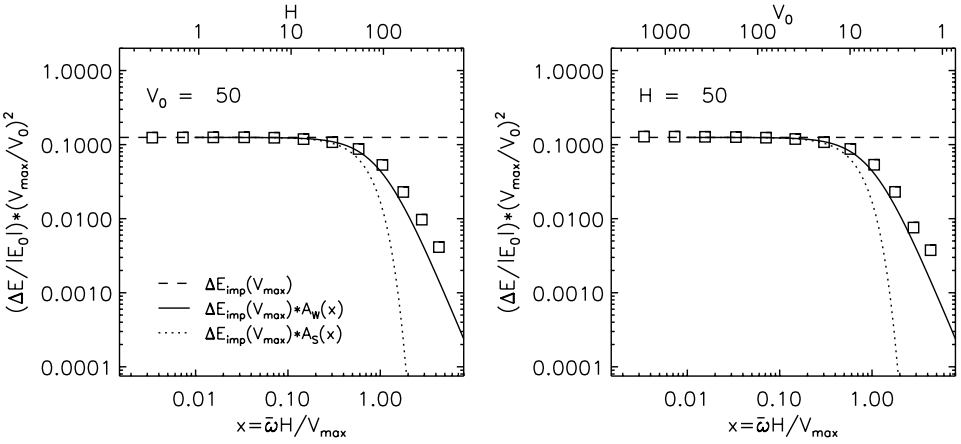

Figure 7.6: Same as in Fig. 7.5, but now $\Delta E/|E_0|$ is multiplied by $(V_{\rm max}/V_0)^2$ to make the predicted energy gain using the impulsive approximation constant for all simulations. Deviations are now caused by adiabatic damping (Section 7.3.2). The impulse approximation (dashed line) now predicts a constant $\Delta E/|E_0|$ (Eq. 7.8). The adiabatic correction of Spitzer (Eq. 7.14) and Weinberg (Eq. 7.15) are shown as a dotted line and as a full line, respectively.

$r_{\rm t}$. The relation between this $\Delta M/M_0$ and $\Delta E/|E_0|$ is shown as squares in Fig. 7.7. These values are higher, but still a factor of 2.5 lower than $\Delta E/|E_0|$, and the results can be approximated by Eq. (7.17), with $f \simeq 1/2.5$ (full line). To translate the energy gains predicted from the analytical estimates to mass loss of the cluster we adopt Eq. 7.17 with $f = 0.4$. With this we will estimate the mass loss and resulting disruption time of clusters due to spiral arm perturbations in Section 7.5.2.

7.5.2. The cluster disruption time

A toy model for spiral arms in the disc

The strength of a spiral arm perturbation on a cluster depends on $V_{\rm drift}$, H and ρ_0. In Sections 7.2.2 and 7.2.3 and Table 7.1 we adopted a constant arm-interarm density contrast $\Gamma = 10$ and scale length of $H = 150\,{\rm pc}$ for gaseous arms, leaving $V_{\rm drift}$ as main R dependent variable.

From Eq. 7.2 and $\langle \rho_{\rm HI} \rangle$ from Section 7.2.2 we find $\rho_0 = 0.33\,M_\odot\,{\rm pc}^{-3}$. The value of $V_{\rm max}$ in the arm is found from $V_{\rm drift}$ and considering an acceleration by the arm from $Y_0 = -2H$ to $Y = 0$ (Eq. 7.10). With these parameters and Eqs. 7.13 and 7.15 we can now calculate the energy gain for clusters that cross spiral arms at different R.

With the relation between $\Delta M/M_0$ and $\Delta E/|E_0|$ from Section 8.4.5, that is, Eq. 7.17 with the factor $f \simeq 0.4$, we can estimate the mass loss of the cluster at

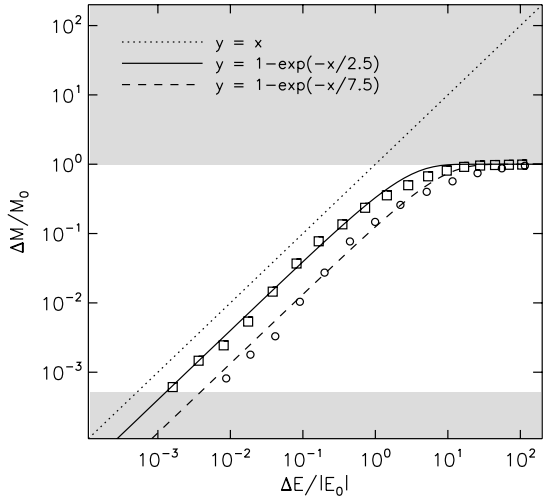

Figure 7.7: Fractional mass loss defined as the fractional loss of bound stars ($\Delta M/M_0$) *vs.* fractional energy gain ($\Delta E/|E_0|$) from the simulations (circles). The dashed line is a simple functional form that makes $\Delta M/M_0$ a factor of 7.5 lower than $\Delta E/|E_0|$ for $\Delta E/|E_0| < 1$ and flattens to 1 for $\Delta E/|E_0| > 1$. The $\Delta M/M_0$ defined as the number of stars beyond r_t is shown as squares. A functional fit is shown as a full line. A one-to-one relation is shown as dotted line. The results of the simulations are expected between the grey shaded regions, since the maximum value for $\Delta M/M_0$ is 1, that is, total disruption of the cluster and the minimum value is 1/2048, that is, a single star got unbound by the perturbation.

different R. We assume here that $\Delta M/M_0$ is independent of N, which is to be expected since the derivations of $\Delta E/|E_0|$ (Eqs. 7.8 and 7.13) are independent of N as well. They do depend on the distribution of stars in the clusters, that is, the cluster density profile or concentration index. There might be a small N dependence in the boundary between the impulsive and the adiabatic regime, since clusters with low N are able to adjust faster to a changing potential.

The cluster disruption time

Ostriker et al. (1972) define the cluster disruption time due to many repeated disc shocks (t_dd) using the impulsive approximation by dividing the initial cluster energy E_0 by the energy injection per unit time: $t_\mathrm{dd} = |E_0|/\langle \mathrm{d}E/\mathrm{d}t \rangle$. For the cluster energy they assume $E_0 = -0.2\,G\,M_\mathrm{cl}/r_\mathrm{h}$ (Note that this implies $\eta = 0.4$, see Section 7.4.1). Combined with Eq. 7.8 and the fact that clusters have two disc passages per orbital period (P), t_dd can be expressed as

$$t_{\rm dd} = \frac{3\,G\,M_{\rm cl}\,P\,V^2}{20 g_{\rm m}^2\,{r_{\rm h}}^3}, \tag{7.18}$$

This time scale is defined as the time needed to unbind the cluster by (periodically) injecting energy in the cluster by disc shocks.

This expression can be rewritten to derive a disruption time due to periodic spiral arm perturbations ($t_{\rm ds}$). We explicitly use the mass loss per spiral arm passage (Eq. 7.17), which we approximate as $\Delta M/M_0 = f(\Delta E/|E_0|)$, with $f \simeq 0.4$ (Section 8.4.5). The expression for $t_{\rm ds}$ can then be derived from

$$t_{\rm ds} = \frac{\Delta t}{f}\frac{|E_0|}{\Delta E}, \tag{7.19}$$

with ΔE from Eq. (7.13) (with the adiabatic correction factor) and $\Delta t = t_{\rm drift}(R)$. Using the definition of E_0 from Section 7.4.1, we can write $\Delta E/|E_0|$ as

$$\begin{aligned} \Delta E/|E_0| &= \frac{2{g_{\rm m}}^2\bar{r^2}}{3{V_{\rm max}}^2}\frac{2r_{\rm h}}{\eta G M_{\rm cl}}A_{\rm w}(x) \\ &= \frac{4{g_{\rm m}}^2}{3{V_{\rm max}}^2}\frac{{r_{\rm h}}^3}{\eta G M_{\rm cl}}\frac{\bar{r^2}}{{r_{\rm h}}^2}A_{\rm w}(x), \end{aligned} \tag{7.20}$$

where we included a factor $\bar{r^2}/{r_{\rm h}}^2$ to get a dependence on $M_{\rm cl}/{r_{\rm h}}^3$ as in Eq. (7.18). For a cluster with $W_0 = 5$ cluster $\bar{r^2}/{r_{\rm h}}^2 = 2$.

The adiabatic correction factor ($A_{\rm w}(x)$) of Eq. (7.20) is calculated using the results of Section 7.4. We use the parameters for the $W_0 = 5$ cluster as described in Sections 7.4.1 and 7.4.2, that is, $\eta = 0.41$ and $\bar{\omega} = 0.58$. We consider clusters with $M_{\rm cl} = 10^2\,M_\odot$, $10^3\,M_\odot$ and $10^4\,M_\odot$ all with $r_{\rm h} = 3.75\,{\rm pc}$. The constant radius is based on recent observations of young clusters in spiral galaxies (Larsen 2004). Using the scaling relations of Section 7.4.1, the values of $\bar{\omega}$ for these clusters are $0.046, 0.14$ and $0.46\,{\rm Myr}^{-1}$, respectively. In panel A) of Fig. 7.8 we show the result for the impulsive approximation, that is $A(x) = 1$, in the top panel and Weinbergs correction factor ($A_{\rm w}(x)$) in the bottom panel.

In panel B) of Fig. 7.8 we show the energy gain of Eq. 7.20 using values of $A(x)$ from panel A). For the cluster with $M_{\rm cl} = 10^2\,M_\odot$ inclusion of the correct $A_{\rm w}(x)$ does not make much difference. For the cluster with $M_{\rm cl} = 10^3\,M_\odot$, $A_{\rm w}(x)$ decreases to 0.2 at $R_{\rm CR}$ and for the most massive cluster ($M_{\rm cl} = 10^4\,M_\odot$) the effect of the spiral arm passage is largely damped for almost all values of R. This is because $t_{\rm cr}$ is shorter in a more massive cluster, assuming a constant radius.

If we translate $\Delta E/|E_0|$ to $\Delta M/M_0$ with Eq. 7.17 we prevent that the mass loss is larger than the cluster mass. Panel C) shows $\Delta M/M_0$ in the impulsive approximation (top) and with the adiabatic correction factor (bottom). The cluster with $M_{\rm cl} = 10^2\,M_\odot$ can get completely unbound by a single spiral arm passage ($\Delta M/M_0$=1).

An expression for $t_{\rm ds}$ can be obtained by combining Eqs. 7.19 and 7.20

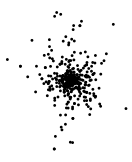

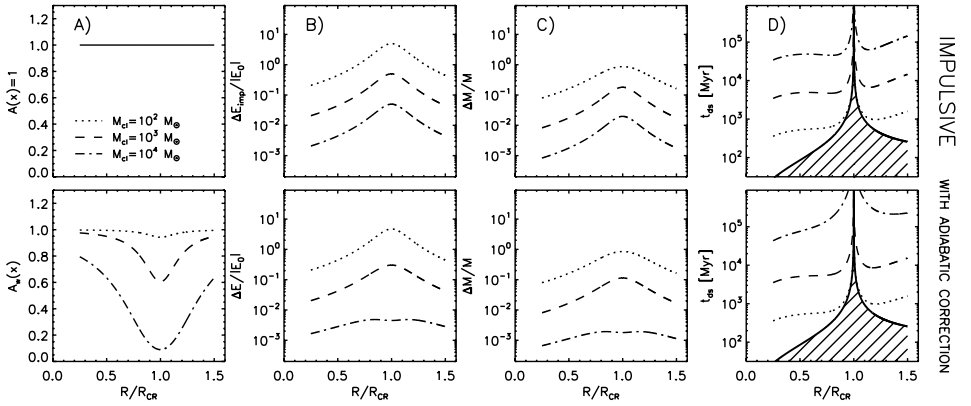

Figure 7.8: Variation of spiral arm parameters with R in a two armed grand design spiral galaxy. In the top row results are shown using the impulsive approximation, that is $A(x) = 1$, and in the bottom panel we used $A_{\rm w}(x)$ of Eq. (7.15). The adiabatic correction factor is shown in panel A). Panel B) shows $\Delta E/|E_0|$ for a single shock at different R. The peak around $R_{\rm CR}$ is because of a minimum in $V_{\rm max}$ around $R_{\rm CR}$. From $\Delta E/|E_0|$ we derive $\Delta M/M_0$ through Eq. 7.17 and the result is shown in panel C). The disruption time at different R, $t_{\rm ds}(R)$ (Eq. 7.21), is shown in panel D).

$$t_{\rm ds}(R) = \frac{3{V_{\rm max}}^2}{4g_{\rm m}^2}\,\frac{\eta}{f}\,\frac{1}{A_{\rm w}(x)}\,\frac{GM_{\rm cl}}{{r_{\rm h}}^3}\,\frac{r_h^2}{\bar{r}^2}\,t_{\rm drift}, \tag{7.21}$$

where $V_{\rm max} \simeq V_{\rm drift}(R)$ (Eq. 7.1) and $t_{\rm drift} = 2\pi R/(mV_{\rm drift})$, with m the number of spiral arms in the galaxy. In panel D) of Fig. 7.8 we show the result of $t_{\rm ds}$ as a function of R for a two-armed spiral galaxy ($m = 2$). For clusters inside the corotation radius, i.e. $R < R_{\rm CR}$, the value of $t_{\rm ds}$ is nearly constant. This is because we have assumed the arm parameters not to vary with R (Section 7.2.2). The variables that are a function of R in Eq. (7.21) are $V_{\rm max}$ and $t_{\rm drift}$. The product ${V_{\rm max}}^2 t_{\rm drift}$ from Eq. (7.21) varies with R approximately as $R|1 - R/R_{\rm CR}|$, since $t_{\rm drift} \propto R/V_{\rm drift}$ and $V_{\rm max} \simeq V_{\rm drift}$ (Eq. 7.1). The product $R|1 - R/R_{\rm CR}|$ increases from 0 at $R = 0$ to a maximum at $R_{\rm CR}/2$ to decrease again beyond $R = R_{\rm CR}/2$. Since at $R_{\rm CR}$ there is never a spiral arm crossing $t_{\rm ds}$ is infinite there.

7.6. Discussion and conclusions

Much work has been done on the combined effect of stellar evolution, a realistic stellar mass function and a spherically symmetric Galactic tidal field to understand the dissolution of star clusters. The resulting cluster disruption times of these models (for example Baumgardt & Makino 2003) are longer than the observed values for

open clusters in the solar neighbourhood (Lamers et al. 2005a) and in the central region of M51 (Gieles et al. 2005). Our study is aimed at understanding the effect of perturbation by spiral arm passages and to see whether they can contribute to this difference.

From the age distribution of open clusters in the solar neighbourhood clusters Lamers et al. (2005a) derived a disruption time of 1.3×10^3 Myr for a $10^4\,M_\odot$ cluster, which they refer to as t_4. A similar analyses was performed by Gieles et al. (2005) using the age and mass distribution to derive the disruption time of clusters in the central region M51. They find $t_4 \simeq 150 \pm 50$ Myr for clusters with $R < 6$ kpc, that is, within $R_{\rm CR}$ (Section 7.2). These observed disruption time scales can be compared to the results of Baumgardt & Makino (2003). They derive the disruption time for clusters on a circular motion in the Galaxy. They consider a realistic stellar mass function and stellar evolution and the tidal field of the Galaxy. They used a smooth analytical description of the Galaxy potential and find $t_4 = 6.9 \times 10^3$ Myr for clusters in the solar neighbourhood, that is, almost a factor of five longer than what is observed. For the parameters of M51, the predicted value of t_4 is ten times longer than the observed value.

Neither the spiral arm perturbations on a simple cluster, without mass function and stellar evolution (Section 7.5.2), nor the effect of the Galactic tidal field on a realistic cluster can, on their own, explain the observed disruption time. We can compare the disruptive effect of the spiral arm perturbations to the observed values. In Fig. 7.6 we show the $t_{\rm ds}$ as a function of cluster mass $M_{\rm cl}$ for the solar neighbourhood (top panel) and a grand design spiral galaxy, such as M51 (bottom panel). The parameters of Sections 7.2 and 7.5.2 are used, that is, $m = 4$ and $R \simeq 0.9 R_{\rm CR}$ for the solar neighbourhood and $m = 2$ and $R \simeq 0.5 R_{\rm CR}$ for the clusters in M51. The full lines represent the resulting disruption times using the impulsive approximation and the dashed lines show the result for $t_{\rm ds}$ when the correct adiabatic correction is applied. As we showed in Section 7.5.2 the impulsive result applies to clusters with $M_{\rm cl} \lesssim 3 \times 10^3\,M_\odot$ in the solar neighbourhood, because of the long crossing time $t_{\rm cr}$ of stars in such clusters. For the cluster in a grand design spiral at $R = 0.5 R_{\rm CR}$ the adiabatic correction is important for clusters of slightly higher masses, since at that location $V_{\rm drift}$ is higher (Eq. 7.1). In the solar neighbourhood $t_{\rm ds}$ becomes constant for $M_{\rm cl} \lesssim 10^2\,M_\odot$. This is because a single arm crossing can destroy clusters with such low masses and $t_{\rm ds}$ becomes equal to $t_{\rm drift}$. The disruption times from the observations of Lamers et al. (2005a) and Gieles et al. (2005) for the solar neighbourhood and M51 are indicated as hashed regions in the top and bottom panel, respectively. The area of the hashed region is defined by the errors in the observations and the mass range of the observed cluster sample. Note that both studies found an empirical mass dependence of $t_{\rm dis} \propto {M_{\rm cl}}^{0.6}$.

For the solar neighbourhood the disruption time due to the spiral arm perturbations is about an order of magnitude higher than the observed result. For M51 the difference is almost three orders of magnitude. This suggest that spiral arm perturbations contribute little to the disruption of the (low mass) open clusters in the solar neighbourhood and can definitely not explain the observed short disruption time of

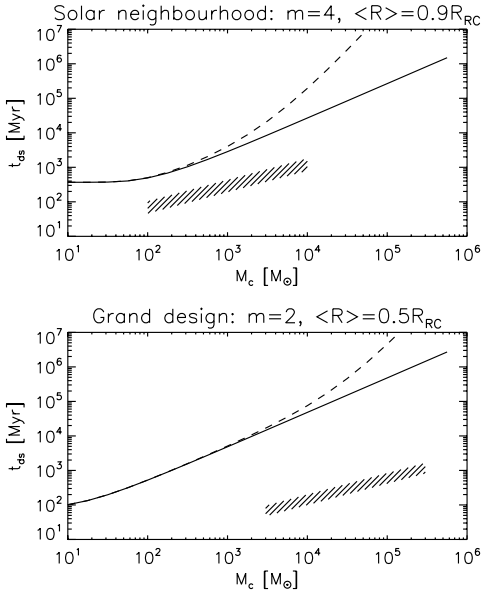

Figure 7.9: Disruption time due to spiral arm passages ($t_{\rm ds}$) for different $M_{\rm cl}$ in the solar neighbourhood (top panel) and in a grand design spiral galaxy (bottom). The full lines show the result using the impulsive approximation, that is, Eq. 7.21 with $A(x) = 1$. The dashed lines show $t_{\rm ds}$ with $A_{\rm w}(x)$ (Fig. 7.8). The shaded areas are the observed disruption times and mass range of the observed clusters from Lamers et al. (2005a) (top) and Gieles et al. (2005) (bottom).

clusters in M51 (Gieles et al. 2005).

There should thus be a further disruptive agent, which we have not considered so far. The central region of M51 has a rich population of giant molecular clouds (GMCs) (for example Garcia-Burillo et al. 1993) whose velocity with respect to the cluster is relatively small ($\sim 10\,{\rm km\,s^{-1}}$). Even at the relatively large distance from the Galactic centre of the solar neighbourhood there are GMCs with masses $\gtrsim 10^6\,M_\odot$ (for example Solomon et al. 1987).

In an accompanying study (Gieles et al. 2006d) encounters between clusters and (massive) GMCs are studied. We find that such encounters are more effective in destroying clusters on time scales that are comparable to the observed values. Lamers & Gieles (2006) have combined these results with the results from this paper to explain the age distribution of open clusters in the solar neighbourhood.

Acknowledgements We thank Oleg Gnedin, Nate Bastian, Henny Lamers, Douglas Heggie, Jean-Charles Lambert and Albert Bosma for useful discussion. This work was done with financial support of a *Marie-Curie Training Fellowship* with number HPMT-CT-2001-00338, the Royal Netherlands Academy of Arts and Sciences (KNAW), the Dutch Research School for Astrophysics (NOVA, grant 10.10.1.11 to HJGLM Lamers). EA and MG also acknowledge INSU/CNRS, the PNG and the OAMP for funds to develop the computing facilities used for the simulations in this paper. Part of the simulations were done on the MoDeStA platform in Amsterdam.

CHAPTER 8

Star cluster disruption by giant molecular clouds

M. Gieles, S.F. Portegies Zwart, H. Baumgardt, E. Athanassoula
H.J.G.L.M. Lamers, M. Sipior and J. Leenaarts

Monthly Notices of the Royal Academic Society, v.371, p.793–804 (2006)

Abstract We investigate encounters between giant molecular clouds (GMCs) and star clusters. We propose a single expression for the energy gain of a cluster due to an encounter with a GMC, valid for all encounter distances and GMC properties. This relation is verified with N-body simulations of cluster-GMC encounters, where the GMC is represented by a moving analytical potential. Excellent agreement is found between the simulations and the analytical work for fractional energy gains of $\Delta E/|E_0| < 10$, where $|E_0|$ is the initial total cluster energy. The fractional mass loss from the cluster scales with the fractional energy gain as $(\Delta M/M_0) = f(\Delta E/|E_0|)$, where $f \simeq 0.25$. This is because a fraction $1-f$ of the injected energy goes to the velocities of escaping stars, that are higher than the escape velocity. We therefore suggest that the disruption time of clusters, $t_{\rm dis}$, is best defined as the time needed to bring the cluster mass to zero, instead of the time needed to inject the initial cluster energy. We derive an expression for $t_{\rm dis}$ based on the mass loss from the simulations, taking into account the effect of gravitational focusing by the GMC. Assuming spatially homogeneous distributions of clusters and GMCs with a relative velocity dispersion of $\sigma_{\rm cn}$, we find that clusters loose most of their mass in relatively close encounters with high relative velocities ($\sim 2\,\sigma_{\rm cn}$). The disruption time depends on the cluster mass ($M_{\rm c}$) and half-mass radius ($r_{\rm h}$) as $t_{\rm dis} = 2.0\,S\,\left(M_{\rm c}/10^4\,M_\odot\right)\,(3.75\,{\rm pc}/r_{\rm h})^3\,{\rm Gyr}$, with $S \equiv 1$ for the solar neighbourhood and S scales with the surface density of individual GMCs ($\Sigma_{\rm n}$) and the global GMC density ($\rho_{\rm n}$) as $S \propto (\Sigma_{\rm n}\rho_{\rm n})^{-1}$. Combined with the observed relation between $r_{\rm h}$ and $M_{\rm c}$, i.e. $r_{\rm h} \propto {M_{\rm cl}}^{\lambda}$, $t_{\rm dis}$ depends on $M_{\rm c}$ as $t_{\rm dis} \propto {M_{\rm c}}^{\gamma}$. The index γ is then defined as $\gamma = 1 - 3\lambda$. The observed shallow relation

between cluster radius and mass ($\lambda \simeq 0.1$), makes the value of the index $\gamma = 0.7$ similar to that found from observations and from simulations of clusters dissolving in tidal fields ($\gamma \simeq 0.62$). The constant of 2.0 Gyr, which is the disruption time of a $10^4\,M_\odot$ cluster in the solar neighbourhood, is about a factor of 3.5 shorter than found from earlier simulations of clusters dissolving under the combined effect of galactic tidal field and stellar evolution. It is somewhat higher than the observationally determined value of 1.3 Gyr. It suggests, however, that the combined effect of tidal field and encounters with GMCs can explain the lack of old open clusters in the solar neighbourhood. GMC encounters can also explain the (very) short disruption time that was observed for star clusters in the central region of M51, since there $\rho_{\rm n}$ is an order of magnitude higher than in the solar neighbourhood.

8.1. Introduction

Star clusters are subjected to various disruptive effects, which prevent low mass star clusters ($M_{\rm cl} < 10^4\,M_\odot$) from surviving for a Hubble time. From observations this was first noted by Oort (1958) and later by Wielen (1971), who showed that there is a lack of open star clusters older than a few Gyr in the solar neighbourhood. Later, more quantitative results were obtained for the life time of star clusters (e.g. Hodge 1988 and de Grijs & Anders 2006 for clusters in the LMC; Boutloukos & Lamers 2003 for the SMC and M33; Lamers et al. 2005a and Piskunov et al. 2006 for the solar neighbourhood and Gieles et al. 2005 for the central region of M51). From the theoretical side, the evolution and disruption of star clusters has been the subject of many studies using a variety of techniques to solve the gravitational N-body problem (e.g. Ostriker, Spitzer, & Chevalier 1972; Chernoff & Weinberg 1990; Gnedin & Ostriker 1997; Takahashi & Portegies Zwart 2000; Baumgardt & Makino 2003).

Lamers, Gieles, & Portegies Zwart (2005b) compared observationally determined disruption times in four galaxies to the corresponding times following from the N-body simulations of clusters in tidal fields of Baumgardt & Makino (2003) and Portegies Zwart et al. (1998, 2002). They found that, based on the results of the simulations, the disruption time ($t_{\rm dis}$) should depend on the cluster mass $M_{\rm c}$ as $t_{\rm dis} \propto [M_{\rm cl}/\ln(M_{\rm cl})]^{0.75} \propto {M_{\rm cl}}^{0.62}$. The index (0.62), which is referred to as γ, was also determined from the observed age and mass distributions of different cluster populations (Boutloukos & Lamers 2003) and the mean value from the observations is $\bar{\gamma} = 0.62 \pm 0.06$. The value of $t_{\rm dis}$ scales with the disruption time of a $10^4\,M_\odot$ cluster as $t_{\rm dis} = t_4\,(M_{\rm cl}/10^4\,M_\odot)^\gamma$. Good agreement for t_4 between simulations and observations was found only for the star clusters in the SMC. In the solar neighbourhood, the observed t_4 for open clusters ($t_4 = 1.3$ Gyr, see Lamers et al. 2005a) is a factor of 5 lower than expected from the disruption time due to the galactic tidal field, combined with a realistic stellar mass function and with stellar evolution ($t_4 = 6.9$ Gyr, see Baumgardt & Makino 2003). An even larger disagreement of almost an order of magnitude was found for $t_{\rm dis}$ of clusters in the central region of M51 (Gieles et al.

2005).

The fact that the observed disruption times are shorter could be a result of time-dependent external perturbations, such as spiral arm passages and encounters with giant molecular clouds (GMCs), which were ignored in the simulations of Baumgardt & Makino (2003). Terlevich (1987) and Theuns (1991) showed that a single encounter with a massive GMC could disrupt a star cluster of a few hundred $M_\odot$ and Gieles, Athanassoula, & Portegies Zwart (2006a) showed that in the solar neighbourhood passages of spiral arms contribute significantly to the disruption of open clusters.

In this study we investigate the disruption of clusters by encounters with GMCs. We want to quantify whether GMCs can explain the difference between the observed values of t_4 and the ones following from the simulations without the time-dependent external effects. Moreover, would simulations including encounters with GMCs preserve the numerical value of the index $\gamma \simeq 0.62$, where the observations and previous simulations already agree?

The paper is organised as follows: In § 8.2 we introduce the initial conditions for the clusters and GMCs and define the parameters involved in a cluster-GMC encounter. In § 8.3 we give analytical calculations of the energy gain for a cluster due to various types of encounters. These analytical formulae for the energy gain are verified with N-body simulations and compared to the mass loss of the cluster in § 8.4. The results of the N-body simulations are used in § 8.5 to derive an expression for the cluster disruption time in environments with different GMC densities. The conclusions and discussion are presented in § 8.6.

8.2. Initial conditions

8.2.1. GMC properties

In this study we consider encounters between molecular clouds and star clusters. Since 90% of the total molecular gas mass in our Galaxy is in giant molecular clouds (GMCs) with mass $M_\mathrm{n} > 10^4\,M_\odot$ (Solomon et al. 1987) and encounters with low mass clouds do not affect a star cluster much (e.g. Wielen 1985), we consider only the massive GMCs. In § 8.3 we show that the cluster energy gain due to an encounter with a GMC scales with the GMC mass squared ($M_\mathrm{n}{}^2$), supporting our assumption to consider only the massive clouds (i.e. the GMCs). Solomon et al. (1987) showed that there is a relation between the size and mass of galactic GMCs of

$$M_\mathrm{n} = 540 \left(\frac{R_\mathrm{n}}{\mathrm{pc}}\right)^2 M_\odot, \tag{8.1}$$

where M_n is the mass of the GMC and R_n is its radius[1]. The internal density profile is of the form $\rho(r) \propto r^{-1}$. Eq. 8.1 implies a constant mean surface density of $\Sigma_\mathrm{n} = 170\,M_\odot \mathrm{pc}^{-2}$.

[1]Throughout this paper we use the subscript "n" (from nebula or nuage) to indicate the parameters of the GMC and "c" for the cluster.

We use the spherically symmetric Plummer model (Plummer 1911) to describe the GMC, since it is mathematically convenient to use in analytical calculations (§ 8.3). The potential of this model is

$$\Phi(r) = -G\,M/\sqrt{r^2 + a^2}, \tag{8.2}$$

where G is the gravitational constant, M is the total mass and a is the Plummer radius. If we choose the Plummer radius of a GMC equal to half the radius from Eq. 8.1, i.e. $a_{\rm n} = 0.5\,R_{\rm n}$, the resulting profile is very similar to what would follow from a density profile of the form $\rho(r) \propto r^{-1}$. In Fig. 8.1 we compare the descriptions for a Plummer model (Eq. 8.2) and constant surface density profile (Eq. 8.1) for the potential in the top panel, the acceleration in the middle panel and the density profile in the bottom panel. The Plummer model has the advantage that the first derivative of the force is differentiable for each r, which is necessary for the N-body simulations.

8.2.2. Star cluster properties

For the star cluster we also choose a Plummer model (Eq. 8.2). The number of particles is $N = 2048$ with a total mass of $M_{\rm cl} = 1000\,M_\odot$ and all stars the same mass, resulting in a realistic mean stellar mass of $0.49\,M_\odot$ (e.g. Kroupa 2001). The virial radius is set to 2 pc. For a Plummer model, the virial radius relates to the Plummer radius of the cluster as $r_{\rm v} = 16\,a_{\rm c}/(3\pi)$. The cluster half-mass radius relates to $a_{\rm c}$ as $r_{\rm h} \simeq 1.305\,a_{\rm c}$. Therefore, the values of $a_{\rm c}$ and $r_{\rm h}$ in physical units are 1.18 pc and 1.54 pc, respectively. The energy gain of a cluster due to an encounter with a GMC will be compared to the total initial cluster energy, i.e. the sum of kinetic and potential energy. This is defined as $E_0 = -\eta\,G{M_{\rm c}}^2/(2r_{\rm h})$, with $\eta \simeq 0.4$, depending on the cluster model. For a Plummer model $E_0 = (3\pi/64)\,G{M_{\rm c}}^2/a_{\rm c}$, hence $\eta \simeq 0.38$.

8.2.3. Encounter definitions

Two particles with a relative velocity at infinity that is non-zero will experience a hyperbolic encounter. The motion of the reduced mass particle is schematically represented in Fig. 8.2. The impact parameter and the velocity at infinity are referred to as b and v_0, respectively. The distance of closest approach and the maximum velocity are called the encounter parameter p and $V_{\rm max}$, respectively. Conservation of angular momentum relates v_0 and $V_{\rm max}$ as

$$V_{\rm max} = v_0 \frac{b}{p}. \tag{8.3}$$

Consider a GMC with a Plummer model according to Eq. 8.2 and mass $M_{\rm n}$ and a cluster with mass $M_{\rm c}$ which is a point source. From conservation of energy and Eq. 8.3, it follows that b and p are related as

$$b = p\sqrt{1 + \frac{2G(M_{\rm n} + M_{\rm c})}{v_0^2\sqrt{p^2 + {a_{\rm n}}^2}}}. \tag{8.4}$$

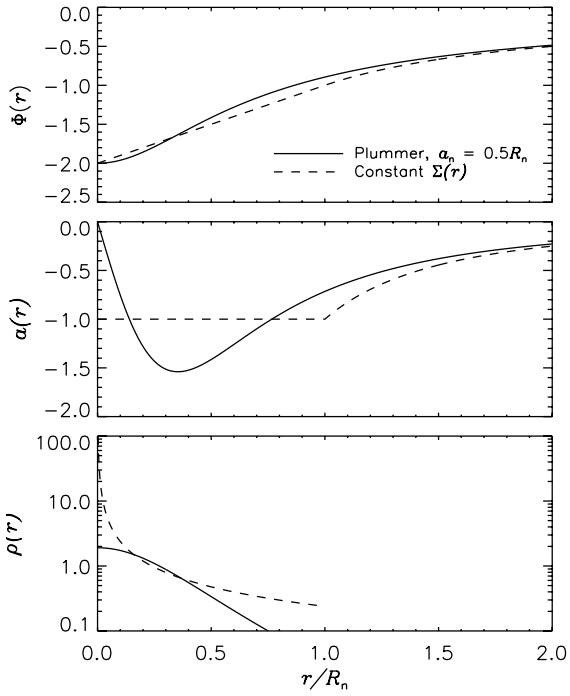

Figure 8.1: Comparison between the radial profiles of the potential (*top*), acceleration (*middle*) and density (*bottom*) for a constant surface density GMC with $M_\mathrm{n} = R_\mathrm{n} = 1$, following from Eq. 8.1 and $\rho_\mathrm{n} \propto r^{-1}$ (dashed line) and for a Plummer model with radius $a_\mathrm{n} = 0.5\,R_\mathrm{n}$ (full line).

Note that b is now a mixed function of encounter and impact variables. In the next sections we will show that the encounter parameter p and V_max determine the internal energy gain. Since we want to perform N-body simulations that result in an encounter with a certain desired p and V_max, we use Eq. 8.3 and Eq. 8.4 to express p and V_max in terms of b and v_0. In addition, in our simulations we will not start with the GMC at infinity, hence we will need to take into account the potential energy contribution at the beginning of the simulation. Since the final expressions for b and v_0 as a function of $p, V_\mathrm{max}, M_\mathrm{n}$ and M_cl are quite complex, but follow from simple mathematical exercises, we do not give them here.

There exists an analytical expression for the energy gain of a cluster due to an head-on encounter and due to a distant encounters. In the next section these relations will be extended to the full range of encounter parameters, i.e. including close encounters. The exact boundary between close and distant encounters is hard to define. Here we

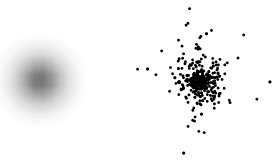

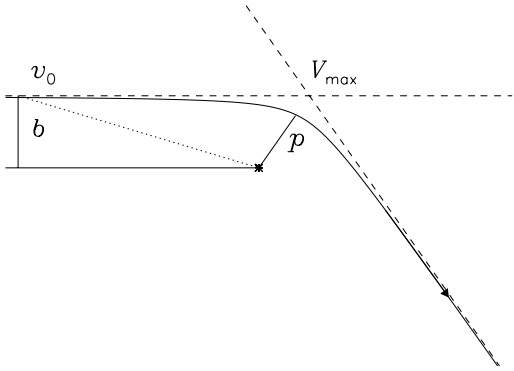

Figure 8.2: Motion of the reduced particle in a hyperbolic encounter. The impact parameter b and the velocity at infinity v_0 are denoted on the left side of the picture and the encounter parameter p and maximum relative velocity $V_{\rm max}$ are indicated at the point of closest approach.

will distinguish three types of encounters: (1) head-on encounters for which $p = 0$; (2) close encounters, where $0 < p/a_{\rm n} < 5$ and (3) distant encounters, which is for $p \geq 5a_{\rm n}$.

8.3. Cluster energy gain and mass loss due to an encounter with a GMC

8.3.1. Distant encounters

Spitzer (1958, hereafter S58) derived an expression for the energy gain of a cluster due to a distant encounter with a GMC. He assumed that the GMC is a point mass and that the encounter velocity is much faster than the internal velocity of the stars in the cluster, which is referred to as the *impulsive approximation*. The cluster energy gain can then be expressed in the encounter, GMC and cluster parameters as

$$\Delta E = \frac{1}{3}\left(\frac{2GM_{\rm n}}{p^2 V_{\rm max}}\right)^2 M_{\rm c}\bar{r^2}. \tag{8.5}$$

Here $\bar{r^2}$ is the mean-square position of the stars in the cluster[2].

Theuns (1991) used combined hydro-dynamical and N-body calculations of a GMC-cluster encounter, to show that Eq. 8.5 is very accurate. He also notes the

[2]S58 makes no distinction between b, v_0 and $p, V_{\rm max}$. In § 8.4 we show that p and $V_{\rm max}$ are the most convenient ones to use for calculating the energy gain.

inconvenience of the ill defined $\bar{r^2}$ parameter. In principle $\bar{r^2}$ follows from the cluster profile, but this variable is very sensitive to variations of the positions of stars far from the cluster centre, hence it is not constant during the simulation because of scattering of stars out of the cluster. Even in simulations covering a short time span, $\bar{r^2}$ will increase due to stars that get at larger distances from the centre due to two-body encounters in the core.

Aguilar & White (1985) have shown with N-body calculations of encounters between two Plummer models with radii a_1 and a_2, that the predictions of Eq. 8.5 hold when $p \geq 5 \max(a_1, a_2)$. In § 8.4 we examine with N-body simulations in what regime the results of Eq. 8.5 are valid, and at what moment during the encounter the value for $\bar{r^2}$ should be taken.

8.3.2. Head-on encounters

Gravitational focusing will deflect many cluster orbits which start with $b > 5\,a_\mathrm{n}$ to encounters with $p < 5\,a_\mathrm{n}$, for which the relation of S58 (Eq. 8.5) does not hold. To obtain an expression for the energy gain for close encounters, we first explore the opposite of distant encounters, namely head-on encounters (i.e. $p = 0$). In those encounters the extent of the GMC has to be taken into account, since assuming a point mass GMC would severely overestimate the energy gain. The energy gain in close encounters should be an interpolation between the distant encounter and head-on results.

Following Binney & Tremaine (1987) (Chap. 7.2, hereafter BT87) we can derive the cluster energy gain for an head-on encounter between a cluster and a GMC, both described by a Plummer model. Let (R, z) be cylindrical coordinates, with the z-axis coinciding with the GMC trajectory. Due to symmetry, the stars in the cluster get a velocity increase only perpendicular to the trajectory of the GMC, of size

$$\Delta v\,(R) = -\frac{2GM_\mathrm{n}R}{V_\mathrm{max}(R^2 + {a_\mathrm{n}}^2)}, \tag{8.6}$$

where analogous to the case of the distant encounters we use V_max for the relative velocity between the cluster and the GMC. Eq. 8.6 can be used to calculate the energy gain of the cluster:

$$\Delta E = \pi \int_0^\infty [\Delta v\,(R)]^2\,\Sigma(R)\,R\,\mathrm{d}R. \tag{8.7}$$

Here $\Sigma(R)$ is the surface density of the cluster obtained by projecting parallel to the line of motion of the GMC. Since the cluster is described by a Plummer model, $\Sigma(R)$ is

$$\Sigma(R) = \frac{M_\mathrm{c}{a_\mathrm{c}}^2}{\pi}\,(R^2 + {a_\mathrm{c}}^2)^{-2}, \tag{8.8}$$

so the energy gain of the cluster due to an encounter between two Plummer models is

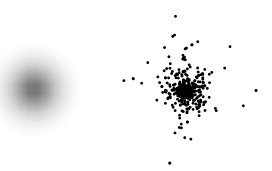

$$\Delta E = \left(\frac{2GM_{\rm n}a_{\rm c}}{V_{\rm max}}\right)^2 M_c \int_0^\infty \frac{R^3}{(R^2+{a_{\rm n}}^2)^2\,(R^2+{a_{\rm c}}^2)^2}{\rm d}R. \tag{8.9}$$

The result of the integration is a function of $a_{\rm c}$ and $a_{\rm n}$ and is equal to $1/12a^4$ when $a_{\rm n} = a_{\rm c} = a$. In that case, Eq. 8.9 reduces to the result found by BT87:

$$\Delta E_{\rm BT} = \frac{1}{3}\left(\frac{GM_{\rm n}}{V_{\rm max}\,a}\right)^2 M_c. \tag{8.10}$$

When $a_{\rm n} \neq a_{\rm c}$, the result of the integration is a function of $a_{\rm c}$ and $a_{\rm n}$. Introducing a new variable $\chi \equiv a_{\rm n}/a_{\rm c}$, the ratio of the GMC and cluster radii, Eq. 8.9 can be written as

$$\Delta E = \frac{1}{3}\left(\frac{GM_{\rm n}}{V_{\rm max}\,a_{\rm c}}\right)^2 M_c \frac{12(\chi^2-1)-6(\chi^2+1)\,\ln(\chi^2)}{(1-\chi^2)^3}, \tag{8.11}$$

where in the first factor we recognise the result for $a_{\rm c} = a_{\rm n}$ (Eq. 8.10) and the rest is a correction factor $C(\chi)$ which is only a function of χ. We can write a more general expression for the energy gain of head-on encounters

$$\Delta E = \Delta E_{\rm BT}\; C(\chi), \tag{8.12}$$

with

$$C(\chi) = \begin{cases} \frac{12(\chi^2-1)-6(\chi^2+1)\,\ln(\chi^2)}{(1-\chi^2)^3} & \text{for } \chi \neq 1 \\ 1 & \text{for } \chi = 1 \end{cases} \tag{8.13}$$

The expression for $C(\chi)$ is rather complicated, but for realistic values of χ (i.e. $2 < \chi < 10$), $C(\chi)$ can be approximated with high accuracy by $C(\chi) \simeq 2\,\chi^{-3}$ (see Fig. 8.4).

With Eq. 8.12 and Eq. 8.13 we have a general expression for the energy gain of head-on GMC-cluster encounters, when both are described by Plummer models, valid for any radius and mass of the cluster and the GMC. In § 8.4.3 we will confront Eq. 8.12 and Eq. 8.13 with results from N-body simulations.

8.3.3. A general expression for the cluster energy gain

The energy gain for a close encounter, i.e. an encounter for which the cluster moves through the cloud within a few $a_{\rm n}$ from the GMC centre, should be a smooth interpolation between the result for a head-on (Eq. 8.12) and distant encounters (Eq. 8.5). When replacing $4\bar{r^2}/p^4$ in Eq. 8.5 by $C(\chi)/{a_{\rm c}}^2$, we get the result for head-on encounter (Eq. 8.12). One way of connecting the two is to add a term in the denominator of Eq. 8.5, preventing the result to diverge to infinity at $p = 0$, so that it converges to Eq. 8.12, is

$$\Delta E = \frac{1}{3}\frac{4\bar{r^2}}{\left(p^2+\sqrt{4\,\bar{r^2}a_{\rm c}^2/C(\chi)}\right)^2}\left(\frac{GM_{\rm n}}{V_{\rm max}}\right)^2 M_c. \tag{8.14}$$

If we use the approximation given in § 8.3.2 for $C(\chi)$ (i.e. $C(\chi) \simeq 2\,\chi^{-3}$) and the fact that $\sqrt{\bar{r^2}} \simeq 1.8\,r_{\rm h}$, $a_{\rm c} \simeq r_{\rm h}/1.305$ and the real GMC radius $R_{\rm n}$ relates to $a_{\rm n}$ as $R_{\rm n} = 2\,a_{\rm n}$, we can rewrite Eq. 8.14 as

$$\Delta E \simeq \frac{4.4\,r_{\rm h}^2}{\left(p^2 + \sqrt{r_{\rm h}\,{R_{\rm n}}^3}\right)^2} \left(\frac{GM_{\rm n}}{V_{\rm max}}\right)^2 M_c. \tag{8.15}$$

In the next section, this relation will be compared to results of N-body simulations for encounters with p ranging from 0 to $10\,a_{\rm n}$.

8.4. Validation with N-body simulations

8.4.1. Description of the code

The N-body calculations were carried out by the `KIRA` integrator, which is part of the `Starlab` software environment (McMillan & Hut 1996; Portegies Zwart et al. 2001b). `KIRA` uses a fourth-order Hermite scheme and includes special treatments of close two-body and multiple encounters of arbitrary complexity. The special purpose *GRAPE-6* systems (Makino et al. 2003) of the University of Amsterdam are used to accelerate the calculation of gravitational forces between stars.

The potential, acceleration and jerk of the stars due to the GMCs are derived from Eq. 8.2 and calculated for each star individually, based on its position and velocity with respect to the GMC. We assume the GMCs are moving potentials which do not interact. Indeed, we are interested in the star cluster and since we consider GMCs that are $\sim 100 - 1000$ times more massive than the cluster, the gravitational pull from the star cluster on the GMCs is negligible and will therefore not affect its orbit. Although GMCs have finite life times ($\simeq 10 - 30\,$Myr), the encounter durations are sufficiently small ($\simeq 1\,$Myr) to not be affected by this.

8.4.2. Description of the runs

We want to avoid sudden jumps in the contribution of the GMC to the cluster potential energy at the beginning and at the end of the simulations. In principle, our GMC should start at infinity, have an encounter with the star cluster and then continue until infinity. Since we do not want to evolve the cluster to long before the encounter, to restrict simulation time and to avoid too much internal dynamical evolution, we put the GMC initially at a distance of $D = 500\,a_{\rm c}$ from the cluster and give it zero mass. While the GMC travels from D to $0.9\,D$, approaching the cluster, we increase its mass gradually from 0 to $M_{\rm n}$. Similarly, after the encounter and while the GMC travels from $0.9\,D$ to D we decrease its mass gradually from $M_{\rm n}$ to 0. To give the cluster time to get back to equilibrium and to give stars with velocities higher than the escape velocity time to leave the cluster we evolve it further for a time equal to half that elapsed after the encounter.

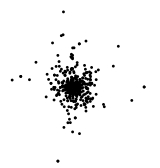

Table 8.1: Summary of the N-body simulations. All runs mentioned are done 4 times and average results are used. (1) GMC mass, with $M_{\rm c} = 10^3\,M_\odot$; (2) ratio of the GMC radius and cluster radius ($\chi = a_{\rm n}/a_{\rm c}$, where $a_{\rm c}$=1.18 pc); (3) impact parameters in units of GMC radius; (4) impact velocity in units of internal cluster velocity dispersion ($\sigma_{\rm rms}$); (5) and (6) are the encounter distance and velocity, following from columns (3),(4) and Eq. 8.4 and Eq. 8.3; (7) Figures where the results of the runs are shown.

(1) $M_{\rm n}/M_{\rm cl}$	(2) χ	(3) $b/a_{\rm n}$	(4) $v_0/\sigma_{\rm rms}$	(5) $p/a_{\rm n}$	(6) $V_{\rm max}/\sigma_{\rm rms}$	(7) Figure
10	1	0	17.9	0	20	8.4
	2	0	19.0	0	20	
	3	0	19.3	0	20	
	4	0	19.5	0	20	
	5	0	19.6	0	20	
	6	0	19.7	0	20	
	7	0	19.7	0	20	
	8	0	19.8	0	20	
	9	0	19.8	0	20	
	10	0	19.8	0	20	
200	1	10.8	27.7	10	30	8.5
		15.8	28.5	15	30	
		20.8	28.9	20	30	
10	5.8	0	19.6	0	20	8.3
100	5.8	3.3	14.2	3	15	8.6
100	5.8	0	38.44	0	40	8.7,8.8,8.9,8.10
		0	16.67	0	20	
		0	4.67	0	10	
		0.324	38.52	0.3125	40	
		0.371	16.85	0.3125	20	
		0.708	5.30	0.3125	10	
		0.645	38.74	0.625	40	
		0.720	17.35	0.625	20	
		1.117	6.72	0.625	10	
		1.278	39.14	1.25	40	
		1.372	18.22	1.25	20	
		1.722	8.71	1.25	10	
		2.530	39.52	2.5	40	
		2.628	19.03	2.5	20	
		2.914	9.09	2.5	10	
		5.030	39.76	5	40	
		5.122	19.53	5	20	
		5.361	9.19	5	10	
		10.026	39.89	10	40	
		10.107	19.79	10	20	
		10.306	9.64	10	10	

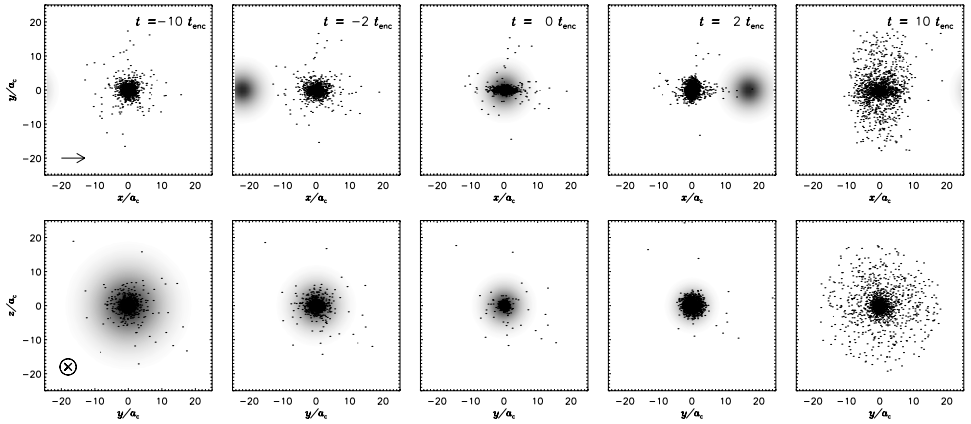

Figure 8.3: Snapshots of a star cluster undergoing a head-on encounter with a GMC of $M_{\rm n} = 10^4\,M_\odot$ with $V_{\rm max} = 20\,\sigma_{\rm rms}$. The motion of the GMC is along the x-axis the line of sight is perpendicular to (*top panels*) and along (*bottom panels*) the GMC trajectory. The arrows in the left lower corner of the left panels are parallel to the direction of motion of the GMC. The GMC is shown with grey shades based on the surface density of a GMC with $a_{\rm n} = 5.8\,a_{\rm c}$. The time with respect to the moment of encounter is indicated in each panel of the top row, where $t_{\rm enc} \equiv 2a_{\rm n}/V_{\rm max}$. The snapshots are taken in the centre-of-mass frame of the cluster and the viewing distance is $40\,a_{\rm c}$.

To test the different analytical expressions of § 8.3 for the energy gain of the cluster, we perform series of head-on ($p = 0$), distant ($p > a_{\rm n}$) and close encounters with different GMC radii and encounter parameters. The initial velocity (v_0) and impact parameter (b) of the GMC are calculated from the desired values of p and $V_{\rm max}$, using the expressions for gravitational focusing of § 8.2.3. The cluster properties are described in § 8.2.2. A summary of all runs is given in Table 8.1. The results will be discussed in § 8.4.3-8.4.5.

All clusters are scaled to N-body units, such that $G = M = 1$ and $E_0 = -0.25$, following Heggie & Mathieu (1986). Then $r_{\rm v}$ is the unit of length and follows from the scaling of the energy, since $r_{\rm v} \equiv GM_{\rm cl}/(4|E_0|) = 1$, where E_0 is the total (potential and kinetic) initial energy of the cluster. We assume virial equilibrium at the start of the simulation, which implies $r_{\rm v}(t = 0) = 1$.

8.4.3. Head-on encounters

We perform N-body simulations of head-on encounters between a cluster and a GMC, both described by a Plummer model. GMCs with different Plummer radii $a_{\rm n}$ were used to compare simulations to the analytical result of Eq. 8.12. The energy

gain of the cluster[3] is always expressed in units of the initial cluster energy, i.e. the fractional energy gain ($\Delta E/|E_0|$). Since we are here interested in the effect of the GMC radius on $\Delta E/|E_0|$, we fix the mass of the GMC at a constant value. The results can then be compared with the predicted value from Eq. 8.12. More specific, when we divide the energy gain for the different cases by the value that was predicted by BT98 (e.g. Eq. 8.10), we should get the factor $C(\chi)$ of Eq. 8.13. In § 8.4.5 we show that there is no good agreement between the simulations and the analytical predictions when $\Delta E/|E_0| >> 1$. To keep $\Delta E/|E_0| < 1$ for all GMC radii, we choose $M_{\rm n} = 10^4\,M_\odot$, which is somewhat lower than a realistic value for $M_{\rm n}$. We choose integer values for χ from 1 to 10, where Eq. 8.10 and Eq. 8.12 should be valid for $\chi = 1$ and $\chi \neq 1$, respectively. The encounter velocity for all simulations is $V_{\rm max} = 20\,\sigma_{\rm rms}$, where $\sigma_{\rm rms} = 1\,{\rm km\,s^{-1}}$ is the internal velocity dispersion of stars in the cluster.

In Fig. 8.4 we show the results of $\Delta E/|E_0|$ from the N-body simulations for different χ with diamond symbols, the value of BT87 with a filled circle (left) and the result of Eq. 8.12 with the full line. The latter relation is also shown with a dashed line, but with an approximation for $C(\chi)$ of the form $C(\chi) = 2\,\chi^{-3}$. This approximation is very close to the real $C(\chi)$ for $2 \leq \chi \leq 9$. Excellent agreement between the analytical work and the N-body results is found in all cases.

In Fig. 8.3 we show snapshots of a cluster during a head-on encounter with a GMC. In the top panels the line of sight is perpendicular to the trajectory of the GMC, whose direction is parallel to the x-axis. The attractive force of the GMC parallel to its trajectory before and after the encounter cancel out, resulting in displacement of stars only perpendicular to the line of motion of the GMC. In the bottom panels the line of sight is along the motion of the GMC, and it can be seen that the stars escape and form a disc like structure of unbound particles around the cluster. The time with respect to the encounter moment is indicated in each panel in the top row, in units of $t_{\rm enc}$, where $t_{\rm enc} \equiv 2a_{\rm n}/V_{\rm max}$.

8.4.4. Distant and close encounters

For the simulations of distant encounters we choose $M_{\rm n} = 10^5\,M_\odot$. The tidal forces of the GMC deform the cluster into a cigar like shape, as can be seen in Fig. 8.6. In Fig. 8.5 we show with the full lines the evolution of the internal energy of the cluster for encounters with three different values for p as a function of time, in units of the encounter time ($t_{\rm enc} \equiv p/V_{\rm max}$). (Note that for head-on encounters $t_{\rm enc} \equiv 2a_{\rm n}/V_{\rm max}$.) We define time ($t$) such that the moment of closest approach is at $t = 0$. The value of $V_{\rm max}$ for these runs is $40\,\sigma_{\rm rms}$ and the GMC radius is equal to the cluster radius. The GMC radius is chosen small in this example in order not to have too large values of p when the ratio $p/a_{\rm n}$ is large. Otherwise, the energy gain would be too small. The results of Eq. 8.5 for these encounters are over-plotted

[3]We start the cluster in the origin, resulting in a centre of mass velocity after the passage of the GMC. In the comparison with the analytical models, when we refer to cluster energy, we refer to the sum of the *internal* potential and *internal* kinetic energy, i.e. the energy after the centre of mass motion has been subtracted.

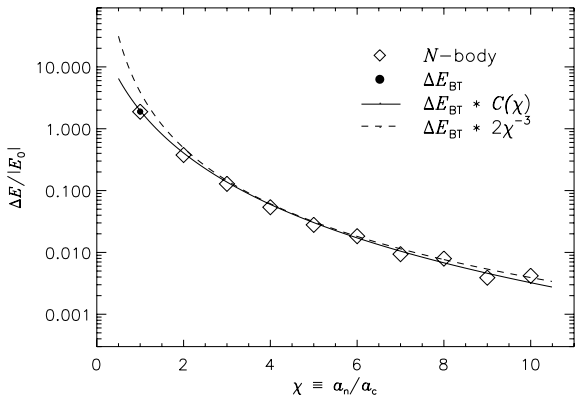

Figure 8.4: Fractional energy gain ($\Delta E/|E_0|$) for a star cluster due to head-on encounters with GMCs with $M_{\rm n} = 10^4\,M_\odot$ for different $\chi \equiv a_{\rm n}/a_{\rm c}$ and with $V_{\rm max} = 20\,\sigma_{\rm rms}$. The analytical approximation of BT87 (Eq. 8.10) for head-on encounters between identical Plummer models is indicated with a filled circle (left). The N-body results are shown with diamonds. The analytical prediction of Eq. 8.12 with the correction factor $C(\chi)$ for different cloud radii is shown with the full line. The predicted energy gain with an approximation for $C(\chi)$ (i.e. $C(\chi) = 2\,\chi^{-3}$) is shown with the dashed line.

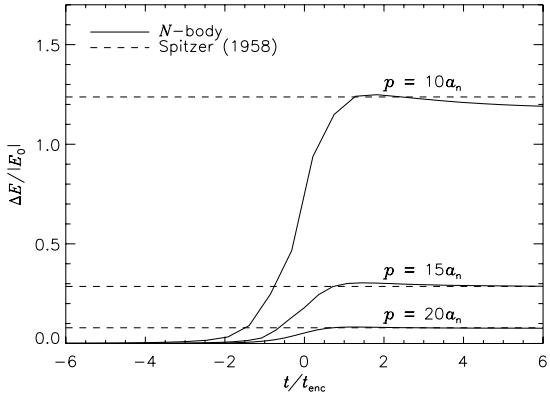

Figure 8.5: The evolution of the energy gain of a cluster during distant cloud encounters (full lines) with $M_{\rm n} = 2 \times 10^5\,M_\odot$, $V_{\rm max} = 30\,\sigma_{\rm rms}$ and three different impact parameter p. The dashed lines indicate the final energy gains predicted by S58 (Eq. 8.5).

as the dashed lines. The value of $\bar{r^2}$ changes during the simulations due to internal dynamical effects and because of deformation of the cluster by the GMC. This last effect is clearly visible in Figs. 8.3 and 8.6. Since the result of Eq. 8.5 is very sensitive

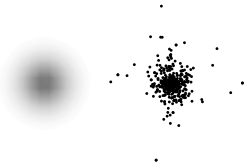

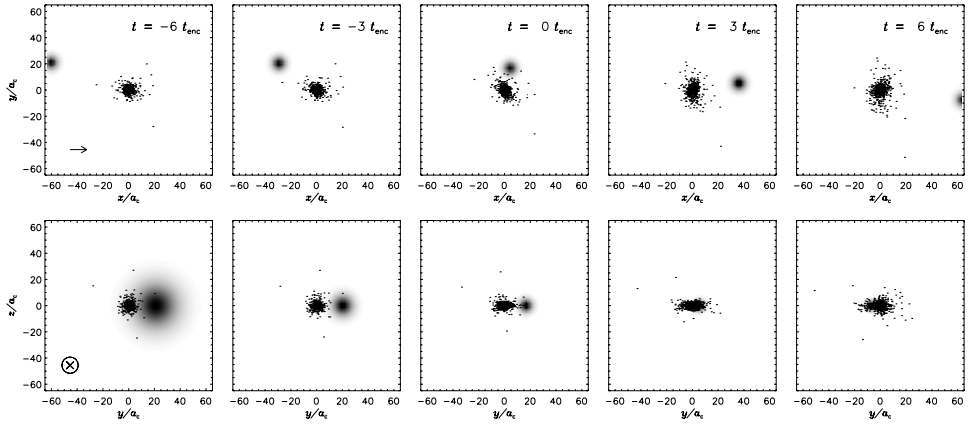

Figure 8.6: Snapshot of a star cluster during a distant encounter with a GMC with $M_{\rm n} = 100\,M_{\rm cl}$, $p = 3\,a_{\rm n}$ and $V_{\rm max} = 15\,\sigma_{\rm rms}$ in the centre of mass frame of the cluster. The motion of the GMC is along the x-axis, starting at $b = y = 20\,a_{\rm c}$, and the line of sight is perpendicular to (*top panels*) and along (*bottom panels*) the GMC trajectory. The arrows in the left lower corner of the left panels are parallel to the direction of motion of the GMC. The GMC is shown with grey shades based on the surface density of a GMC with $a_{\rm n} = 5.8\,a_{\rm c}$. The time with respect to the moment of encounter is indicated in each panel of the top row, where $t_{\rm enc} \equiv p/V_{\rm max}$. The snapshots are taken in the centre-of-mass frame of the cluster and the viewing distance is $60\,a_{\rm c}$.

to the value of $\bar{r^2}$, we performed tests to find at which time $\bar{r^2}$ should be taken to get the best agreement between Eq. 8.5 and the simulations. If we take this value too early, Eq. 8.5 will underestimate the energy gain compared to the result of the simulation. This because dynamical evolution will increase $\bar{r^2}$. When using a value $\bar{r^2}$ which is determined during the encounter (i.e. $t \simeq 0$), the energy gain from Eq. 8.5 overestimates the true value. We found that best agreement was found when using $\bar{r^2}$ at $t = -2\,t_{\rm enc}$. From Fig. 8.5 it can be seen that this is moment where the energy of the cluster starts to increase, whereas the cluster energy is almost constant before that moment.

The variations of the relative velocity between the cluster and the GMC are smaller than the variations in $\bar{r^2}$, and for that reason the result of Eq. 8.5 is less sensitive to the time that we choose the velocity. Since most of the energy is injected between $-t_{\rm enc}$ and $+t_{\rm enc}$ (Fig. 8.5), the best agreement is obtained when the relative velocity at $t = 0$, i.e. $V_{\rm max}$, is used.

To test the validity of the interpolation between the distant and the head-on encounters (Eq. 8.14), we performed N-body simulations of various encounters with impact parameter p ranging from 0 to 10 times the GMC radius $a_{\rm n}$. The encounter velocity was chosen $40\sigma_{\rm rms}$, such that the fractional energy gain is always lower than 1 (Eq. 8.12). The impact parameter b and initial velocity v_0 of the GMC where

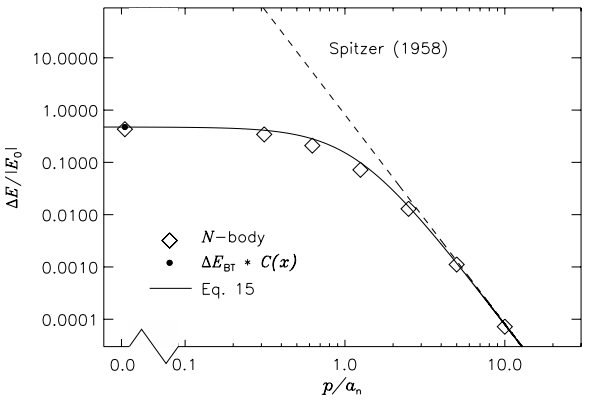

Figure 8.7: Fractional energy gain of a cluster as a function of the impact parameter p and for $V_{\rm max} = 40\,\sigma_{\rm rms}$. The results of the N-body simulations are shown with diamonds. The analytical result for head-on encounters, including the correction for the radius of the GMC is shown with a filled circle (left). The result for distant encounters from S58 is shown with the dashed line. The result from the interpolation between the two analytical predictions (i.e. Eq. 8.5 and 8.12), i.e. Eq. 8.14, is shown with the full line.

calculated using Eq. 8.4. The GMC mass is $10^5\,M_\odot$ and we used the observed mass-radius relation for GMCs (Eq.8.1), resulting in $\chi = 5.8$ and therefore $C(\chi) = 0.01$ (Eq. 8.13). In Fig. 8.7 we show the result of $\Delta E/|E_0|$ from the N-body simulations (diamonds) and the analytical prediction of Eq. 8.14 (full line). The predictions for the two extreme values of p, i.e. for distant and for head-on encounters are shown with the dashed line and the filled circle (left), respectively. The analytical expression Eq. 8.14 agrees very well with the results from the N-body simulations. It can be seen that the prediction of S58 is accurate for $p \geq 5\,a_{\rm n}$, in agreement with what was found by Aguilar & White (1985). Note that in Fig. 8.7 we have used $a_{\rm n}$ as a scale length to normalise p. This is possible since GMCs have finite sizes. If we were dealing with objects of infinitesimal size, as e.g. black holes, this scaling would not be possible. Thus, Fig. 8.7 can not be applied to those cases. For large p ($p >> a_{\rm n}$) the energy gain only depends on p. This is demonstrated by the good agreement with the point source approximation of S58, since for these cases $a_{\rm n} = 0$.

To see if the agreement between our predicted energy gain from Eq. 8.14 and N-body simulations holds for lower velocities, we performed a similar series N-body simulations as shown in Fig. 8.7 for $V_{\rm max} = 10\sigma_{\rm rms}$ and $20\sigma_{\rm rms}$. The values of $\Delta E/|E_0|$ for these three different values of $V_{\rm max}$ and different values of p is shown in Fig. 8.8. For the lower velocities we again find very good agreement. However, when the fractional energy gain is larger than 1, the N-body simulations show a smaller energy gain than the predictions. The difference is larger for larger energy gains. Similar results were obtained by Gieles et al. (2006a) for one-dimensional shocks due to spiral arms. This

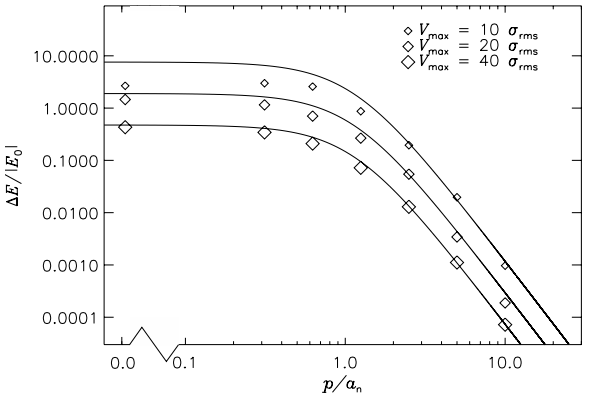

Figure 8.8: Fractional energy gain of a cluster as a function of the impact parameter p in units of $a_{\rm n}$ and for different values of $V_{\rm max}$. The results of the N-body simulations are shown with diamonds, where the size of the diamonds corresponds to the encounter velocity. The analytical results from Eq. 8.14 are shown with the full lines.

is probably because the impulsive approximation does not hold anymore. When the GMC is very massive, or when the relative velocity is low, the stars in the cluster are displaced too much before the encounter. The symmetry assumption of the encounter of the impulse approximation then does not hold anymore.

The energy gain from the encounter is absorbed mainly by the stars far from the cluster centre, which can gain velocities much higher than the escape velocity. A bound core will remain, even when $\Delta E/|E_0| >> 1$. Both topics will be discussed in more detail in § 8.4.5.

8.4.5. Relation between predicted energy gain and mass loss

In the previous section we found good agreement between the N-body simulations and our analytical formula for $\Delta E/|E_0|$ of a cluster due to encounters with GMCs with different p and $V_{\rm max}$ as long as $\Delta E/|E_0| < 1$ (see Eq. 8.14). In Fig. 8.8 we show that deviations occur whenever the energy gain is larger than the initial cluster energy. We did a few more simulations of head-on encounters with higher GMC masses and compare all the predicted energy gains to the results from the simulations. The results are shown in Fig. 8.9. A one-to-one relation (dashed line) holds until $\Delta E/|E_0| \simeq 5$. A simple functional ($y = x\,[1 - \exp(-12/x)]$), which starts to deviate from a one to one relation around $y \simeq 5$ and levels off at $y = 12$ is also shown in Fig. 8.9 and describes the results well.

To derive a realistic disruption time of clusters due to encounters with GMCs, we need to know how the energy gain relates to the number of stars, or mass, that is lost from the cluster in the different encounters. In Fig. 8.10 we show the fractional

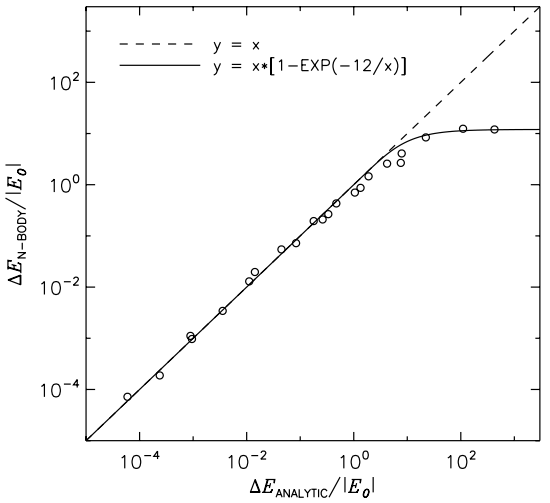

Figure 8.9: Relation between the fractional energy gain from the simulations and the analytical prediction of Eq. 8.14 (circles). A one-to-one relation is over-plotted as the dashed line. A simple functional form, describing a linear function that saturates at a value of 12, fits the result at the high energy part well.

mass loss ($\Delta M/M_0$) as a function of $\Delta E/|E_0|$. The dashed line indicates a one-to-one relation and the full line is a fit to the results. The grey areas indicate the regions where $\Delta M/M_0$ cannot be defined, since the cluster can not loose less then one star (i.e. $M_0/2048$, lower region), and it can not loose more than the total initial cluster mass (i.e. M_0, upper region). The fit shows an almost linear relation, where $\Delta M/M_0$ is a fraction $f = 0.22$ of $\Delta E/|E_0|$. Given the good agreement between the predicted energy gain and the one from the simulations, we can conclude that a fraction $f = 0.22$ of the input energy is used to unbind stars. This implies that a fraction $(1 - f)$ of $\Delta E/|E_0|$ went into the velocity of the escaping stars, so that these have escaped with velocities much higher than the local escape velocity. Combined with the saturation of Fig. 8.9, this shows that some encounters with $\Delta E \gtrsim 10\, E_0$, called overkill encounters (Wielen 1985, 1988), can completely disrupt a cluster. We will further discuss this topic in § 8.5.3.

Since we consider isolated clusters, one might argue that there can be stars that have remained bound, but that would have been pushed over the tidal radius if the cluster was located in a galaxy. Assuming a disc galaxy with a flat rotation curve, with rotational velocity of $V_0 = 220\,\mathrm{km\,s^{-1}}$, the tidal radius of a cluster depends then on its mass and galactocentric distance (R) as $r_{\rm t} = \left(GM_{\rm cl}/2V_0^2\right)^{1/3} R^{2/3}$. The estimated values of $r_{\rm t}$ for our cluster at $R = [0.5, 1, 2] \times R_0$, where $R_0 = 8.5\,\mathrm{kpc}$, i.e. the solar neighbourhood, are $r_{\rm t} \simeq [13.8, 21.8, 34.6]\,\mathrm{pc}$, respectively. We counted

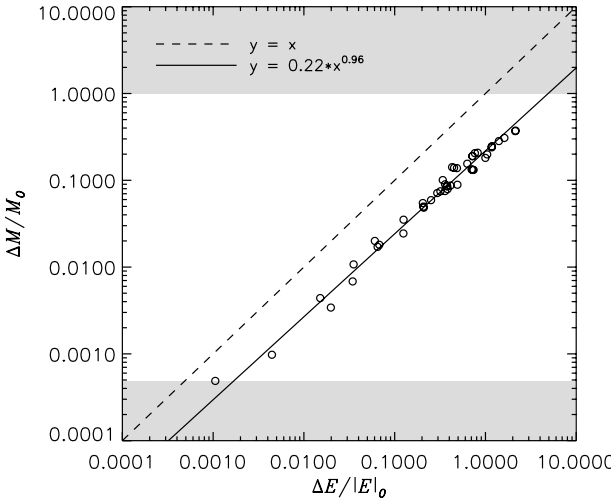

Figure 8.10: Relation between the fractional mass loss ($\Delta M/M_0$) and the fractional energy gain ($\Delta E/|E_0|$) for the simulations of § 8.4 (circles). The dashed line shows a one-to-one relation and the full line is a fit to the simulations. The grey areas indicate the regime where $\Delta M/M_0$ can not be defined.

for our simulations the number of extra stars ($\Delta N/N_0$) which after the encounter beyond these three radii. There is a linear relation between $\Delta N/N_0$ and $\Delta M/M_0$, where the ratio of the two quantities is $[1.3, 1.1, 1.0]$ for the three different tidal limits, respectively. So the effective value of f is somewhat higher when we take into account the tidal limit of the cluster. For the solar neighbourhood a good estimate would be $f = 0.22 \times 1.1 \simeq 0.25$. For clusters in the centres of galaxies the tidal radius is small and f can be a factor ~ 1.5 higher. From now on we will assume a linear relation $\Delta E/|E_0| = f\,\Delta M/M_0$, with $\simeq 0.25$, which takes into account stars that have become unbound in isolation and/or are pushed over the tidal limit. This will be used in § 8.5 to derive the mass loss of clusters in environment with GMCs and the resulting cluster disruption time.

Hitherto, the cluster disruption time has always been defined as the time needed to bring the cluster energy to zero by periodically injecting energy with shocks (e.g. Ostriker et al. (1972) for the disruption time by disc shocks and Spitzer & Chevalier (1973) for the disruption by GMCs). We have shown that this overestimates the disruption time by a factor of $1/f \simeq 4$. A more accurate disruption time, taking into account this factor f is derived in the following section.

8.5. Cluster disruption time due to GMC encounters

With the description of the mass loss from a cluster due to different types of encounters with GMCs of §§ 8.3,8.4 we can derive the disruption time of star clusters in an environment with GMCs, such as the solar neighbourhood.

8.5.1. Clusters in an environment with GMCs

When considering a distribution of GMCs and clusters with a relative velocity dispersion $\sigma_{\rm cn} = \sqrt{\sigma_{\rm n}^2 + \sigma_{\rm c}^2}$, the probability of a relative velocity in the range $v_0, v_0 + {\rm d}v_0$ can be expressed as (BT87, Eq. 7-60)

$$ {\rm d}P = \frac{4\pi v_0^2}{(4\pi {\sigma_{\rm cn}}^2)^{3/2}} \exp\left(-\frac{v_0^2}{4{\sigma_{\rm cn}}^2}\right) {\rm d}v_0. \tag{8.16} $$

Assuming a spatially homogeneous distribution of GMCs, the rate of encounters in the range $b, b + {\rm d}b$ is then

$$ \dot{C} = n_{\rm clouds}\, v_0\, 2\pi\, b\, {\rm d}b\, {\rm d}P \tag{8.17} $$

$$ = \frac{n_{\rm clouds}\, 8\pi^2\, b\, {\rm d}b}{(4\pi {\sigma_{\rm cn}}^2)^{3/2}} \exp\left(-\frac{v_0^2}{4{\sigma_{\rm cn}}^2}\right) v_0^3\, {\rm d}v_0, \tag{8.18} $$

where $n_{\rm clouds}$ is the number density of clouds. The energy of the cluster increases at a rate

$$ \dot{E} = \int_0^\infty \int_{b_{\rm min}}^{b_{\rm max}} \dot{C}(b, v_0)\, \Delta E(b, v_0) {\rm d}b {\rm d}v_0, \tag{8.19} $$

where $\Delta E(b, v_0)$ follows from Eq. 8.14 after converting b and v_0 to p and $V_{\rm max}$ due to gravitational focusing. This integral can be calculated numerically.

In Fig. 8.11 we illustrate this using the parameters for clusters and GMCs used in the N-body simulations of § 8.4, i.e. $M_{\rm n} = 10^5\, M_\odot$, $a_{\rm n}$=6.8 pc and $\sqrt{\bar{r^2}} \simeq 1.8$ pc. We assume that young clusters and GMCs have the same velocity dispersion, i.e. $\sigma_{\rm n} = \sigma_{\rm c} = 7\,{\rm km\,s^{-1}}$ (Stark 1984; Piskunov et al. 2006). The velocity dispersion of the motion of GMCs with respect to clusters, is then $\sigma_{\rm cn} = \sqrt{\sigma_{\rm n}^2 + \sigma_{\rm c}^2} \simeq 10\,{\rm km\,s^{-1}}$. In the left panel of Fig. 8.11 we show the impact rate $\dot{C}$ of Eq. 8.18 in units of $n_{\rm clouds}$ as a function of b and v_0, in units of $a_{\rm n}$ and $\sigma_{\rm cn}$, respectively. In the middle panel we show $\Delta E/|E_0|$ for individual encounters as a function of $b/a_{\rm n}$ and $v_0/\sigma_{\rm cn}$, where we have converted b and v_0 to p and v_0 first, and then substituted these values in the equation for energy gain (Eq. 8.14). The rate of energy gain as a function of $b/a_{\rm n}$ and $v_0/\sigma_{\rm cn}$ is the product of the encounter rate times the energy gain per encounter and is shown in the right panel. The isocontours indicate the regions where 10, 50 and 75% of the total energy per unit time is produced. This total energy was not determined from this graph, but from a numeric integration of a similar figure, but with an area

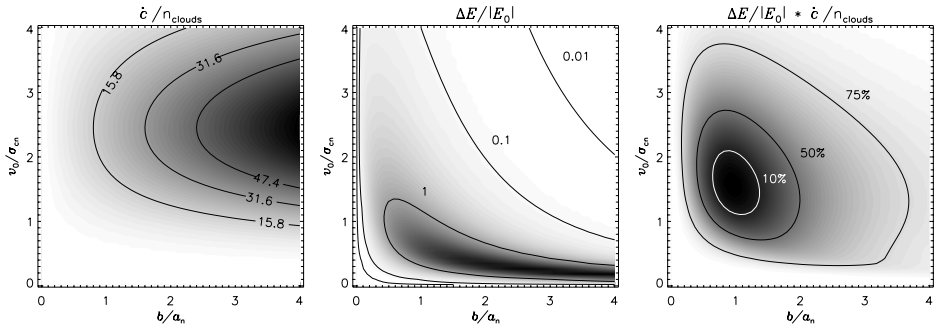

Figure 8.11: *Left:* The encounter rate ($\dot{C}$, Eq. 8.18), relative to $n_{\rm clouds}$, for different values of b and v_0. *Middle:* Fractional energy gain (Eq. 8.14) for encounters with different b and v_0. *Right:* Rate of energy increase, resulting from the multiplication of $\dot{C}$ and ΔE.

that is 100 times bigger. Most of the energy is injected by fast ($v_0/\sigma_{\rm cn} \simeq 2$) and close ($b/a_{\rm n} \simeq 1$) encounters. The encounter velocities ($V_{\rm max}$) are even higher than $2\sigma_{\rm cn}$ due to gravitational focusing and this means that the impulse approximation is valid for these encounters. In § 8.4.4 we found that the distant encounter regime of S58 holds for $p \geq 5\,a_{\rm n}$. The peak in the right panel of Fig. 8.11 around $b \simeq a_{\rm n}$ illustrates that the approximations of S58 for a point source GMC are not applicable for the encounters that inject the majority of the energy. In that regime it is important to use the more accurate description for the energy gain found in § 8.3.3 (Eq. 8.14).

BT87 solved Eq. 8.19 by substituting the energy gain for distant encounters of S58. They then integrate b from $R_{\rm n}$ to infinity and correct for the missing close encounters with a factor g of order unity. The advantage of this solution is that the result has ${R_{\rm n}}^2$ in the denominator, which can be combined with $M_{\rm n}$ and $n_{\rm clouds}$ to express the final result in the observable molecular gas density ($\rho_{\rm n}$) and surface density of individual GMCs ($\Sigma_{\rm n}$). Our results allow us to quantify the parameter g of BT87 by integrating Eq. 8.19 numerically from 0 to infinity and from $R_{\rm n}$ to infinity. When gravitational focusing is ignored, the value of g depends only on $M_{\rm n}$, since in that case $p = b$ and $V_{\rm max} = v_0$. Including gravitational focusing makes g dependent on $\sigma_{\rm cn}$ as well, since then encounters with initial $b > R_{\rm n}$ can result in $p < R_{\rm n}$. Intuitively one thinks that the inclusion of gravitational focusing will increase the value of g, since there are more encounters with $p < R_{\rm n}$ to correct for. However, the encounter velocity $V_{\rm max}$ is always higher than v_0, which will make the energy gain of the cluster for these encounters lower. In Fig. 8.12 we show the resulting g for various values of $M_{\rm n}$ ignoring gravitational focusing (full line) and for three values of $\sigma_{\rm cn}$. The horizontal dashed line indicates the estimated value of BT87 for g. For the solar neighbourhood (i.e. $M_{\rm n} \simeq 10^5\,M_\odot, \sigma_{\rm cn} \simeq 10\,{\rm km\,s^{-1}}$) our results show that $g \simeq 2.5$, slightly lower than predicted by BT87.

Using the relation between energy gain and mass loss of § 8.4.5 we can define the

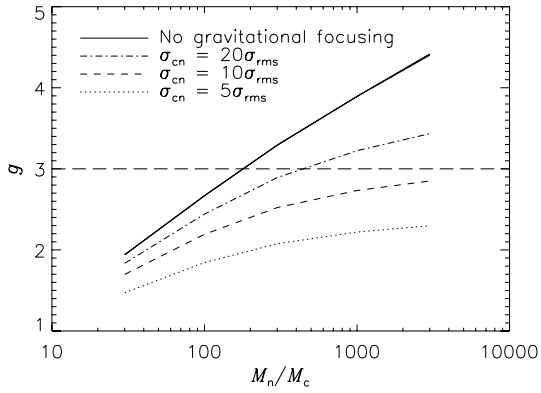

Figure 8.12: The correction factor g for close encounters (see text for details) as a function of GMC mass. The full line shows the result when gravitational focusing is ignored, and the other lines show the results for 3 different values of $\sigma_{\rm cn}$ when gravitational focusing is considered. The predicted value of $g = 3$ of BT87 is indicated with the dashed horizontal line.

mass loss rate of the cluster as

$$\dot{M}_{\rm c} = f\frac{\dot{E}}{E}\,M_{\rm c}, \tag{8.20}$$

where $f = 0.25$ is a dimensionless constant that relates fractional energy gain to fractional mass loss (see Fig. 8.10 and § 8.4.5). The initial cluster energy is $E_0 = -\eta\,GM^2/(2r_{\rm h})$, where $\eta \simeq 0.4$, depending on the cluster profile (Spitzer 1987).

We can derive a relation for the mass loss, using the expression for $\dot{E}$ of BT87 (their Eq. 7-66), where we substitute $\Sigma_{\rm n} \equiv M_{\rm n}/(\pi {R_{\rm n}}^2)$, $\rho_{\rm n} \equiv M_{\rm n}\,n_{\rm clouds}$ and $\dot{M} = f\,\dot{E}$

$$\dot{M}_{\rm c} = \frac{8\pi^{3/2} g\,f}{3\sigma_{\rm cn}\eta} G\,(\Sigma_{\rm n}\rho_{\rm n})\left(\frac{\bar{r^2}}{r_{\rm h}^2}\right){r_{\rm h}}^3, \tag{8.21}$$

where the ratio $\left(\bar{r^2}/r_{\rm h}^2\right)$ depends on the cluster model. For the Plummer cluster that we used $\left(\bar{r^2}/r_{\rm h}^2\right) \simeq 4$ and for King profiles with dimensionless potential depth values of $W_0 = [3, 5, 7, 9]$ it follows that $\left(\bar{r^2}/r_{\rm h}^2\right) \simeq [1.5, 2, 3.5, 3.7]$. From Eq. 8.21 we can derive the disruption time of clusters, by defining

$$t_{\rm dis} = M_{\rm c}/\dot{M}_{\rm c} = \frac{3\sigma_{\rm cn}\eta}{8\pi^{3/2} g\,f\,G}\left(\frac{1}{\Sigma_{\rm n}\rho_{\rm n}}\right)\left(\frac{r_{\rm h}^2}{\bar{r^2}}\right)\frac{M_{\rm c}}{{r_{\rm h}}^3}. \tag{8.22}$$

For the constants in Eq. 8.22 we have to make several assumption. First, we assume $f = 0.25$, as was found in § 8.4.5. For $\sigma_{\rm cn}$ we take $10\,{\rm km\,s^{-1}}$, based on observations of GMCs in the solar neighbourhood (Stark & Brand 1989) and open clusters (Piskunov et al. 2006). For the cluster profile we assume a King profile with $W_0 = 3$,

corresponding to $c \equiv \log(r_{\rm t}/r_{\rm c}) \simeq 0.7$, which is the mean concentration of the galactic open clusters (King 1962). King profiles are more realistic due to the tidal truncation, which the Plummer model does not have. For the $W_0 = 3$ profile considered here, $\left(r_{\rm h}^2/\bar{r^2}\right) \simeq 0.67$ and $\eta = 0.42$ (BT87).

8.5.2. Dependence on the relation between cluster mass and radius

The solution for $t_{\rm dis}$ of Eq. 8.22 is very sensitive to the choice of $r_{\rm h}$. Observations of (young) extra-galactic star clusters show that the projected half-light radius ($r_{\rm eff}$) of the majority of star clusters is confined to a narrow range of 2-4 pc (e.g. Bastian et al. 2005b; Larsen 2004) and a very shallow relation between the radius and the mass. A factor of two difference in radius and nearly equal masses still results in a factor of eight difference in $t_{\rm dis}$. This implies that clusters that are a few times larger than the mean radius are very unlikely to survive and cluster that are a few times smaller will be almost insensitive to encounters by GMCs. We choose the use the recently observed relation between radius and mass of Larsen (2004), who fits a function of the form $r_{\rm eff} = A\,{M_{\rm c}}^{\lambda}$ to a sample of young star clusters in nearby spiral galaxies and finds that $A = 1.12 \pm 0.35$ and $\lambda = 0.10 \pm 0.03$. There is a large scatter around the fit relation, which, combined with the high sensitivity of $t_{\rm dis}$ on $r_{\rm h}$ (Eq. 8.22), makes it hard to relate mass to radius. However, since the relation of Larsen (2004) reflects the median relation between $r_{\rm eff}$ and $M_{\rm c}$, the conversion will probably hold for a large cluster population. To convert $r_{\rm eff}$ to $r_{\rm h}$ we use the relation $r_{\rm h} = 4/3\, r_{\rm eff}$ (Spitzer 1987) and with that we can rewrite the result of Larsen (2004) as

$$r_{\rm h} = 3.75 \left(\frac{M_{\rm c}}{10^4\,M_\odot}\right)^{\lambda}, \tag{8.23}$$

with $\lambda \simeq 0.1$. Substituting Eq. 8.23 in Eq. 8.22 and inserting all constants, yields an expression for the disruption time that is independent of $r_{\rm h}$ and depends on the assumed index that relates $r_{\rm h}$ and $M_{\rm cl}$

$$t_{\rm dis} = 2.0 \left(\frac{5.1\,{M_\odot}^2\,{\rm pc}^{-5}}{\Sigma_{\rm n}\rho_{\rm n}}\right) \left(\frac{M_{\rm c}}{10^4\,M_\odot}\right)^{\gamma} {\rm Gyr}, \tag{8.24}$$

with $\gamma = 1 - 3\lambda$. We normalised the product $\Sigma_{\rm n}\rho_{\rm n}$ to the value for the solar neighbourhood ($\Sigma_{\rm n} = 170\,M_\odot{\rm pc}^{-2}$ and $\rho_{\rm n} = 0.03\,M_\odot{\rm pc}^{-3}$, Solomon et al. 1987). When taking the 1 sigma upper bound value of $\lambda \simeq 0.13$ from Larsen (2004), the index $1 - 3\lambda = 0.61$ agrees very well with the value of 0.62 found from observations (Lamers et al. 2005b) and from N-body simulations of clusters in the solar neighbourhood, dissolving under the combined effect of a tidal field, a realistic mass function and stellar evolution (Baumgardt & Makino 2003; Takahashi & Portegies Zwart 2000). These simulations adopted a slightly different relation between $r_{\rm h}$ and $M_{\rm c}$ since they assumed that at a given galactocentric distance the cluster size scales with the tidal radius ($r_{\rm h} \propto {M_{\rm c}}^{1/3}$). The multiplicative constant of Eq. 8.24 is a factor of about 7

higher than what was found from earlier studies (e.g. S58; Spitzer & Chevalier 1973; BT87). The difference can largely be explained by our factor $f \simeq 0.25$ from § 8.4.5, that relates energy gain to mass loss. The remaining difference is caused by the lower value we found for g and a slightly different value for the product $\Sigma_{\rm n}\rho_{\rm n}$.

8.5.3. Disruption by single encounters

In the derivation of $t_{\rm dis}$ in the previous sections we integrated over the full range of b and v_0 in Eq. 8.19 to get an expression for the rate of energy gain of a cluster due to GMC encounters. Doing so, we implicitly assume that disruption is caused by a large number of encounters. However, if the cluster is completely disrupted by the first encounter with a GMC, Eq. 8.22 will overestimate $t_{\rm dis}$. Fig. 8.10 shows that a single encounter can indeed disrupt the cluster (see also Wielen 1985 and Terlevich 1987). If cluster disruption was always caused by single encounters, then Eqs. 8.22 and 8.24 would overestimate the disruption time in all cases. The most accurate approach is to include the saturation function of Fig. 8.9 in the relation between energy gain and mass loss (Eq. 8.20), i.e. to exclude encounters with $\Delta E \gtrsim 10\,E_0$. This results in $\Delta M/M_0$=1 for $\Delta E/|E_0| \gtrsim 10$. However, this would not have allowed us to come to the convenient linear dependence of $t_{\rm dis}$ on $\rho_{\rm n}$ and $\Sigma_{\rm mol}$ in Eq. 8.22.

Alternatively, we here estimate the typical time scale for a cluster to be disrupted by one single encounter ($t_{\rm dis}^{\rm single}$). Following Wielen (1985), we can calculate the critical encounter distance ($p_{\rm crit}$) for which one encounter will result in total disruption of the cluster. Based on Eq. 8.15, on the expression for the cluster energy $|E_0| = \eta\, G{M_{\rm c}}^2/(2r_{\rm h})$ and on the relation between $\Delta E/|E_0|$ and $\Delta M/M_0$ from § 8.4.5 we can derive $p_{\rm crit}$ by solving for p in $\Delta E/|E_0| = 1/f$, such that

$$ {p_{\rm crit}}^2 = \left(\frac{8Gf}{3\eta}\,\frac{\bar{r^2}}{r_{\rm h}^2}\right)^{1/2} \frac{M_{\rm n}}{V} \left(\frac{M_{\rm c}}{{r_{\rm h}}^3}\right)^{-1/2} - K. \tag{8.25} $$

In here $K = \sqrt{r_{\rm h}\,{R_{\rm n}}^3}$, which is the term in the denominator of Eq. 8.15 that makes ΔE converge to the correct value for head-on encounters ($p = 0$). Wielen (1985) did not include this term, since he assumed point-mass GMCs (Eq. 8.5). (Note that Eq. 8.15 is equal to Eq. 8.5 when $K = 0$). The number of encounters with encounter parameter p depends on the GMC number density ($n_{\rm clouds}$) as

$$ N = \pi p^2\, n_{\rm clouds}\, V\, \Delta t. \tag{8.26} $$

We can solve for Δt by setting $N = 1$ and $p = p_{\rm crit}$, which is then the time it takes for a disruptive encounter to occur

$$ t_{\rm dis}^{\rm single} = \frac{1}{\pi {p_{\rm crit}}^2\, n_{\rm clouds}\, V}. \tag{8.27} $$

In here gravitational focusing is ignored. Following Wielen (1985) and assuming point-mass GMCs, i.e. $K = 0$, we find an expression of $t_{\rm dis}^{\rm single}$ of the form

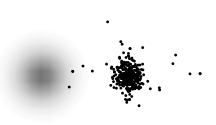

$$t_{\rm dis}^{\rm single} = \left(\frac{3\eta}{8Gf\pi^2}\frac{r_{\rm h}^2}{\bar{r^2}}\right)^{1/2}\left(\frac{M_{\rm c}}{{r_{\rm h}}^3}\right)^{1/2}\frac{1}{\rho_{\rm n}}, \quad (8.28)$$

where we have used $\rho_{\rm n} \equiv M_{\rm n} n_{\rm clouds}$ again. At first sight this relation for the disruption time looks similar to what we derived in the previous section (Eq. 8.22). The main difference is the scaling with the cluster density ($M_{\rm c}/{r_{\rm h}}^3$). In Fig. 8.13 we show a comparison between $t_{\rm dis}^{\rm single}$ of Eq. 8.28 (dotted line) and $t_{\rm dis}$ of Eq. 8.22 (full line) for different $M_{\rm c}$. Here we used a constant $r_{\rm h}$=3.75 pc and the same values for f, η and $(\bar{r^2}/r_{\rm h}^2)$ as in § 8.5. The value of $t_{\rm dis}^{\rm single}$ is smaller than the result of Eq. 8.24 for clusters with $M_{\rm c} > 5 \times 10^3\,M_\odot$. This implies that for massive clusters the life time is limited by the first disruptive encounter, rather than the successive heating by multiple encounters. For cluster of lower mass, the time it takes to disrupt by encounters with $p > p_{\rm crit}$ is shorter than $t_{\rm dis}^{\rm single}$. This mass dependence is counter intuitive at first, but is explained by the difference in scaling with $M_{\rm c}$ (Eqs. 8.22 and 8.28). Note that the crossing point (Fig. 8.13) does not depend on $\rho_{\rm n}$, since Eqs. 8.22 and 8.28 depend in the same way on $\rho_{\rm n}$.

In Fig. 8.13 we also plot the result of $t_{\rm dis}^{\rm single}$ by substituting Eq. 8.25 with $K = \sqrt{r_{\rm h}{R_{\rm n}}^3}$ in Eq. 8.27, based on $M_{\rm n} = 10^5\,M_\odot$ (dashed line) and $M_{\rm n} = 10^6\,M_\odot$ (dotted-dashed line) and Eq. 8.1. Here we use the same value for $\rho_{\rm n}$, and then assume that all mass is in clouds with $M_{\rm n} = 10^5\,M_\odot$ and $10^6\,M_\odot$, respectively, to solve for $n_{\rm clouds}$ (Eq. 8.27). For low mass clusters, these solutions for $t_{\rm dis}^{\rm single}$ agree with the result of Wielen (1985), since there $p_{\rm crit} \gtrsim {\rm few}R_{\rm n}$, where the assumption of point-mass GMCs is valid (see Fig 8.7). For clusters with $10^2 < M_{\rm c}/M_\odot < 10^4$, the solution for $t_{\rm dis}^{\rm single}$ is higher than that of the point-mass assumption. This is because $p_{\rm crit}$ is smaller when extended GMCs are considered. In close encounters the extent of the GMC, i.e. K, is more important (Eq. 8.14). There is no solution for clusters with $M_{\rm c} > 5 - 10 \times 10^4\,M_\odot$, meaning that it is not possible to disrupt these clusters by a single encounters with a GMC with masses up to few times $10^6\,M_\odot$.

The fact that the solutions for $t_{\rm dis}^{\rm single}$ for realistic (extended) GMCs are always larger than $t_{\rm dis}$ from Eq. 8.22 justifies our assumptions of § 8.5.1. However, Fig. 8.13 shows that for a cluster with $M_{\rm c} = 10^{3-4}\,M_\odot$ the two solutions are close, meaning that clusters are destroyed by just a few encounters. This means that individual clusters will have strongly varying lifetimes. Our results of § 8.5 will, however, be valid as a statistical mean.

8.6. Conclusions and discussion

We have derive an expression for the cluster disruption time ($t_{\rm dis}$) due to encounters with GMCs, based on the results of N-body simulations of different types of encounters between a cluster and a GMC. The expression for $t_{\rm dis}$ (Eq. 8.24) allows us to estimate the disruptive effect of GMCs in different environments and to compare it to other effects such as the galactic tidal field, stellar evolution and spiral arm

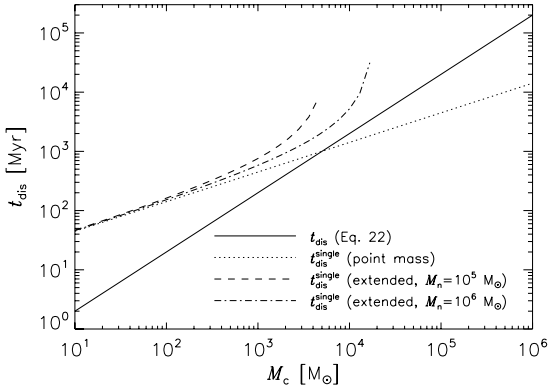

Figure 8.13: Comparison between $t_{\rm dis}$ of Eq. 8.22 (full line) and the single encounter disruption time ($t_{\rm dis}^{\rm single}$). The dotted line shows the result of Wielen (1985) for point-mass GMCs and the dashed and dotted-dashed lines show the results for extended GMCs with $M_{\rm n} = 10^5\,M_\odot$ and $10^6\,M_\odot$, respectively.

shocks. From Eq. 8.24 we see that the disruption time for a $10^4\,M_\odot$ cluster in the solar neighbourhood is $t_4 = 2.0\,$Gyr. This is a factor of 3.5 shorter than what was found by Baumgardt & Makino (2003) for the combined effect of a realistic mass function, stellar evolution and the galactic tidal field ($t_4 = 6.9\,$Gyr). Note that the index γ is comparable, if we take the upper bound value of $\lambda = 0.10 \pm 0.03$, since Baumgardt & Makino (2003) found $t_{\rm dis} \propto [M_{\rm cl}/\ln(M_{\rm cl})]^{0.75}$. Lamers et al. (2005b) showed that $[M_{\rm cl}/\ln(M_{\rm cl})]^{0.75} \propto {M_{\rm cl}}^{0.62}$. The same mass dependence was also found from the age and mass distribution of cluster samples in different galaxies by Boutloukos & Lamers (2003) and from the age distribution of clusters in the solar neighbourhood by Lamers et al. (2005a). For this last sample they found a shorter scaling value of $t_4 = 1.3\,$Gyr. Eq. 8.24 combined with the observed relation between $r_{\rm h}$ and $M_{\rm cl}$ (Eq. 8.23) suggests that the combined mass loss by GMC encounters and evaporation in a tidal field preserves the index $\gamma \simeq 0.62$. A similar scaling between $t_{\rm dis}$ and $M_{\rm cl}$ was found for the disruption time by spiral arm passages. The combination of all these effects and a comparison to the observed age distribution of open clusters in the solar neighbourhood will be discussed in more detail by Lamers & Gieles (2006).

The result of Eq. 8.24 can easily be applied to environments/galaxies with different molecular gas densities ($\Sigma_{\rm mol}$). The mid-plane density ($\rho_{\rm n}$) of GMCs scales with $\Sigma_{\rm mol}$ as $\rho_{\rm n} = \Sigma_{\rm mol}/2h$, where h is the vertical scale length of molecular gas, which is around 100 pc in the solar neighbourhood (Dame et al. 1987). Assuming that h is the same in M51, and therefore $\rho_{\rm n} = \Sigma_{\rm mol}/200\,$pc, we can predict t_4 due to GMCs encounters once we know $\Sigma_{\rm mol}$ in M51 and compare this to the value of t_4 for clusters in M51 (Gieles et al. 2005). Garcia-Burillo et al. (1993) find $\Sigma_{\rm mol} = 90\,M_\odot\,{\rm pc}^{-2}$ for the central region of M51, which is 14 times higher than in the solar neighbourhood

(Solomon et al. 1987). This implies $t_4 \simeq 2100\,\mathrm{Myr}/14 = 150\,\mathrm{Myr}$. Note that this value is an upper limit, since we have assumed that the surface density of individual GMCs (Σ_n) is independent of Σ_mol, while this could be higher in environments with higher Σ_mol. In addition, the values of f and g in Eq. 8.22 will probably be higher in the centre of M51 (see § 8.4.5 and § 8.5), which will make t_dis shorter. Also, we have assumed the same density profile as for the Galactic open cluster, i.e. $W_0 = 3$. A density profile of $W_0 = 7$, as found for the Galactic globular clusters, would reduce t_dis by a factor of two (Eq. 8.5). The resulting value of t_4, however, is very close to the value of $t_4 = 100 - 200\,\mathrm{Myr}$, determined observationally by Gieles et al. (2005) from the age and mass distribution of star clusters in M51. Based on this work we think that we can explain the short disruption times of clusters in the centre of M51, if GMC encounters are the dominant disruption effect.

Acknowledgement We thank the referee, Roland Wielen, for useful comments and pointing us to the problem of single disruptive encounters (§ 8.5.3). We enjoyed discussions with Nate Bastian, Søren Larsen and Sverre Aarseth. This work was done with financial support of the Royal Netherlands Academy of Arts and Sciences (KNAW), the Dutch Research School for Astrophysics (NOVA, grant 10.10.1.11 to HJGLM Lamers) and the Netherlands Organisation for Scientific Research (NWO, grant 635.000.001). The simulations were done on the MoDeStA platform in Amsterdam. MG thanks the Sterrekundig Instituut "Anton Pannenkoek" of the University of Amsterdam for their hospitality during many pleasant visits.

CHAPTER 9

Clusters in the solar neighbourhood: how are they destroyed?

H.J.G.L.M. Lamers and M. Gieles

Astronomy and Astrophysics, v.455, p.L17–L20 (2006)

Abstract We predict the survival time of initially bound star clusters in the solar neighbourhood taking into account: (1) stellar evolution, (2) tidal stripping, (3) shocking by spiral arms and (4) encounters with giant molecular clouds. We find that the predicted dissolution time is $t_{\rm dis} = 1.7 \times (M_{\rm i}/10^4\,M_\odot)^{0.67}$ Gyr for clusters in the mass range of $10^2 < M_{\rm i} < 10^5\,M_\odot$. The resulting predicted shape of the logarithmic age distribution agrees very well with the empirical one, derived from a complete sample of clusters in the solar neighbourhood within 600 pc. The required scaling factor implies a star formation rate of $4 \times 10^2\ M_\odot\,{\rm Myr}^{-1}$ or a surface formation rate of $3.5\ \times 10^{-10}\,M_\odot{\rm yr}^{-1}{\rm pc}^{-2}$ for stars in bound clusters with an initial mass in the range of 10^2 to $3 \times 10^4\,M_\odot$.

9.1. Introduction

The first empirical determination of the lifetime of clusters in the solar neighbourhood is by Oort (1958), who noticed the lack of clusters older than a few Gyr in the solar neighbourhood. Later, Wielen (1971) derived a dissolution time of 0.2 Gyr from the age distribution of clusters. Since most of the observed clusters within about 1 kpc from the sun have a mass in the range of 10^2 to a few $10^3\ M_\odot$ the value derived by Wielen is for clusters in that mass range. Theory predicts that the dissolution time of clusters depends on their initial mass in that massive clusters survive longer than low mass clusters (e.g. Spitzer 1958, Wielen 1985, Chernoff & Weinberg 1990, Gnedin & Ostriker 1997 and references therein). Baumgardt & Makino (2003) (hereafter BM03)

showed from N-body simulations that the dissolution time of clusters in the tidal field of the galaxy depends on their initial mass, M_i, as $t_{\rm dis} \sim M_i^{0.62}$. Independently, this same power-law dependence was also derived empirically in a study of cluster samples in four galaxies by Boutloukos & Lamers (2003).

The dissolution time of clusters in the solar neighbourhood was recently redetermined by Lamers et al. (2005a) (hereafter L05), based on a new cluster sample of Kharchenko et al. (2005). They found a dissolution time of $t_{\rm dis} = t_4 (M_{\rm i}/10^4 M_\odot)^{0.62}$ with $t_4 = 1.3 \pm 0.5$ Gyr. This is a factor 5 shorter than the 6.9 Gyr predicted for $M_i = 10^4\, M_\odot$ by the N-body simulations of BM03 for clusters in the solar neighbourhood. The simulations of BM03 include a realistic stellar mass function, stellar evolution and detailed treatment of binary evolution and close encounters of stars. The apparent discrepancy between the observations of L05 and BM03 shows that other, probably external, disruptive effects must play an important role in destroying star clusters in the solar neighbourhood.

In this paper we explain the lifetime of clusters in the solar neighbourhood, by taking into account the combined effects of stellar evolution, tidal stripping, encounters with giant molecular clouds (GMCs) and spiral arm shocks. We use stellar population models to describe the stellar evolution and the results of BM03 for tidal stripping. For the effects of GMCs and spiral arms we adopt the new estimates from the recent studies by Gieles et al. (2006d) (hereafter GPZB06) and Gieles et al. (2006a) (hereafter GAPZ06), which are based on N-body simulations.

The structure of the paper is as follows:
In § 9.2 we discuss the predicted mass loss from star clusters by stellar evolution, tidal stripping, encounters with GMCs and spiral arm shocks. We calculate the mass evolution of clusters due to these four effects. In § 9.3 we compare our results with the observed age distribution of clusters in the solar neighbourhood. The discussion and conclusions are given in § 9.4.

9.2. The decreasing mass of star clusters

9.2.1. Mass loss by stellar evolution

The mass loss from clusters due to stellar evolution has been calculated for cluster evolution models by several groups. We adopt the `GALEV` models for single stellar populations with a Salpeter type mass function in the range of $0.15 < M/M_\odot < 85$ (Schulz et al. 2002; Anders & Fritze-v. Alvensleben 2003). These models are based on stellar evolution tracks from the Padova group, which include overshooting, mass loss due to stellar winds and super-novae. (Bertelli et al. 1994; Girardi et al. 2000). L05 have shown that the fraction of the initial cluster mass that is lost by stellar evolution, $q_{\rm ev}(t) = \Delta M/M_{\rm i}$, can be approximated accurately by

$$\log q_{\rm ev}(t) = (\log t - a_{\rm ev})^{b_{\rm ev}} + c_{\rm ev} \quad \text{for} \quad t > 12.5 \text{ Myr}. \tag{9.1}$$

For solar metallicity models with a Salpeter mass function $a_{\rm ev} = 7.00$, $b_{\rm ev} = 0.255$ and $c_{\rm ev} = -1.805$. This function describes the mass loss fraction of the models at $t > 12.5$ Myr with an accuracy of a few percent. The mass loss at younger ages is negligible because stars with $M_* > 30 M_\odot$ hardly contribute to the mass of the cluster. The mass loss of a cluster by stellar evolution is

$$\left(\frac{{\rm d}M}{{\rm d}t}\right)_{\rm evol} = -M(t)\frac{{\rm d}q_{\rm ev}}{{\rm d}t} \tag{9.2}$$

9.2.2. Mass loss by the galactic tidal field

BM03 have calculated a grid of N-body simulations of clusters in circular and elliptical orbits in the tidal field of our Galaxy for different initial cluster masses, galactocentric distances R, and different cluster density profiles. The stars follow a Kroupa initial mass function and stellar evolution is taken into account during the evolution. Gieles et al. (2004) have shown that for all the models of BM03 the dissolution time can be expressed as a function of the initial cluster mass as

$$t_{\rm dis} = t_4\ (M_{\rm i}/10^4\, M_\odot)^{0.62}, \tag{9.3}$$

where t_4 is a constant that depends on the tidal field strength of the galaxy in which the cluster moves and on the ellipticity of its orbit. (If the tidal field were the only disruptive process then t_4 would be the lifetime of a cluster with $M_{\rm i} = 10^4\, M_\odot$.) The mass loss due to the Galactic tidal field can then be written as

$$\left(\frac{{\rm d}M}{{\rm d}t}\right)_{\rm tidal} = \frac{-M(t)}{t_{\rm dis}} = \frac{-(M/10^4 M_\odot)^{0.38}}{t_4/10^4}\, M_\odot\, {\rm Myr}^{-1} \tag{9.4}$$

We adopt the value of $t_4 = 6.9\,$Gyr from BM03 for clusters in circular orbits at $R_0 = 8.5$ kpc.

9.2.3. Mass loss by spiral arm shocking

GAPZ06 studied the dissolution of star clusters by spiral arms by means of N-body simulations. They used and adjusted the analytical expression of Ostriker et al. (1972) for the dissolution time of star clusters due to disc shock, to derive an expression for the dissolution time of star clusters by spiral arms ($t_{\rm ds}$). Mass loss by spiral arm shocks will occur just at the moment the cluster crosses the spiral arm. Assuming that spiral arms move with a constant pattern speed ($\Omega_{\rm p}$) and that the matter in the disc has a constant circular velocity ($V_{\rm disc}$), the relative velocity between the two ($V_{\rm drift}$) depends on the location in the galaxy (R). Density waves that pass with a low velocity have a large effect on the star clusters (e.g. Ostriker et al. 1972). Therefore, the disruptive effect of spiral arm shocks is most important close to the co-rotation radius ($R_{\rm CR}$), i.e. the point where the disc and the spiral arms have the same rotational velocity. We adopt the "average" spiral arm model of GAPZ06, which is based on a the study of Elmegreen et al. (1989) of the spiral galaxies M81

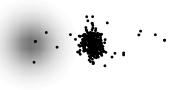

and M100, to derive the density contrast of the spiral arm. Dias & Lépine (2005) found $\Omega_{\rm p} = 25.9\,{\rm km\,s^{-1}\,kpc^{-1}}$ for the spiral arms in the Galaxy, from a study of the nearby star clusters, and a co-rotation radius ($R_{\rm CR}$) almost coinciding with the solar radius $R_{\rm CR}/R_0 = 1.06 \pm 0.08$. Based on the adopted values of $R_0 = 8.5\,{\rm kpc}$, $V_{\rm disc} = 220\,{\rm km\,s^{-1}}$ and the assumption that our Galaxy has 4 spiral arms (Vallée 2005), GAPZ06 used $V_{\rm drift} = 12.5\,{\rm km\,s^{-1}} = 12.7\,{\rm pc\,Myr^{-1}}$ and $t_{\rm drift} = 1.05\,{\rm Gyr}$. Taking into account the ratio $f = (\Delta M/M)/(\Delta E/E) = 0.3$ between the energy gain and the mass loss, predicted by GAPZ06 we find for the solar neighbourhood that

$$\begin{aligned} t_{\rm ds} &= 20 \left(\frac{M}{10^4\,M_\odot}\right) \left(\frac{3.75\,{\rm pc}}{r_{\rm h}}\right)^3 {\rm Gyr} \\ &= 20 \left(M/10^4\,M_\odot\right)^{1-3\lambda} {\rm Gyr}, \end{aligned} \tag{9.5}$$

where we have substituted the observed mass-radius relation of clusters in nearby spiral galaxies of Larsen (2004): $r_{\rm h} = 3.75\ (M/10^4 M_\odot)^\lambda$, with $\lambda = 0.10 \pm 0.03$. The mass loss of clusters due to spiral arm shocks is then

$$\left(\frac{{\rm d}M}{{\rm d}t}\right)_{\rm sp} = \frac{-M(t)}{t_{\rm ds}} = -0.5 \left(\frac{M(t)}{10^4\,M_\odot}\right)^{3\lambda} M_\odot\,{\rm Myr^{-1}}. \tag{9.6}$$

Notice that for $\lambda = 0.1$ the mass loss due to shocking by spiral arms has almost the same mass dependence, i.e. $\propto M^{0.3}$, as the mass loss by the tidal field (viz. $M^{0.38}$). We will use the mass loss relation Eq. 9.6 as a statistical mean.

9.2.4. Mass loss by giant molecular cloud encounters

GPZB06 studied the encounters between GMCs and clusters with N-body simulations. They derived an expression for the energy gain and the resulting mass loss for the full range of encounter distances, from head-on to distant encounters. Adopting a mean GMC density in the galactic plane near the sun of $\rho_n = 0.03 M_\odot {\rm pc}^{-3}$, a surface density of GMCs $\Sigma_n = 170 M_\odot\ {\rm pc}^{-2}$ (Solomon et al. 1987) and a mean velocity dispersion of clusters and GMCs of $\sigma_v \simeq 10\ {\rm km\,s^{-1}}$, they derived a dissolution time ($t_{\rm GMC}$) for clusters by GMC encounters in the solar neighbourhood of

$$t_{\rm GMC} = 2.0 \left(\frac{M}{10^4\,M_\odot}\right) \left(\frac{3.75\ {\rm pc}}{r_{\rm h}}\right)^3 {\rm Gyr}. \tag{9.7}$$

If we assume the same mass-radius relation as before we find that the mass loss rate due to encounters with GMCs is

$$\left(\frac{{\rm d}M}{{\rm d}t}\right)_{\rm GMC} = \frac{-M(t)}{t_{\rm GMC}} = -5.0 \left(\frac{M(t)}{10^4\,M_\odot}\right)^{3\lambda} M_\odot\,{\rm Myr^{-1}}. \tag{9.8}$$

Notice that the mass dependence is the same as for dissolution by spiral arm shocking, but that the effect is ten times stronger.

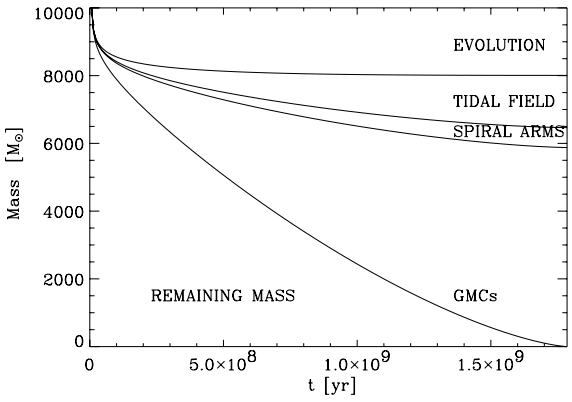

Figure 9.1: The mass evolution of a cluster with an initial mass of $10^4\,M_\odot$ in the solar neighbourhood. The mass loss due to the four separate effects is indicated. Encounters with GMCs are the dominant dissolution effect in the solar neighbourhood.

9.2.5. The predicted mass evolution of clusters in the solar neighbourhood

The decrease of mass due to the combined effects of stellar evolution, tidal stripping, spiral arm shocks and GMC encounters can then be described as

$$\frac{\mathrm{d}M}{\mathrm{d}t} = \left(\frac{\mathrm{d}M}{\mathrm{d}t}\right)_{\rm ev} + \left(\frac{\mathrm{d}M}{\mathrm{d}t}\right)_{\rm tidal} + \left(\frac{\mathrm{d}M}{\mathrm{d}t}\right)_{\rm sp} + \left(\frac{\mathrm{d}M}{\mathrm{d}t}\right)_{\rm GMC}, \tag{9.9}$$

with the terms given by Eqs. 9.2, 9.4, 9.6 and 9.8. We have solved this equation numerically for clusters of different masses. The results are shown in Fig. 9.1 for a cluster with an initial mass of $10^4\ M_\odot$. The figure shows the total mass loss as well as the mass lost by each mechanism independently. Encounters with GMCs are the dominant dissolution effect in the solar neighbourhood, contributing about as much as the three other effects combined.

Figure 9.2 shows the ages of clusters when their remaining mass is 0 and 100 $M_\odot$ as a function of the initial mass. The almost linear part from $\log(M_{\rm i}/M_\odot) = 3.5$ to 5 has a slope of about 0.67. The figure also shows the dissolution times by the Galactic tidal field, predicted by BM03 for clusters with an initial concentration factor $W_0 = 5$ in a circular orbit at $R_0 = 8.5$ kpc. Our predicted timescales are about a factor 5 smaller, which agrees with the empirically determined dissolution time (L05).

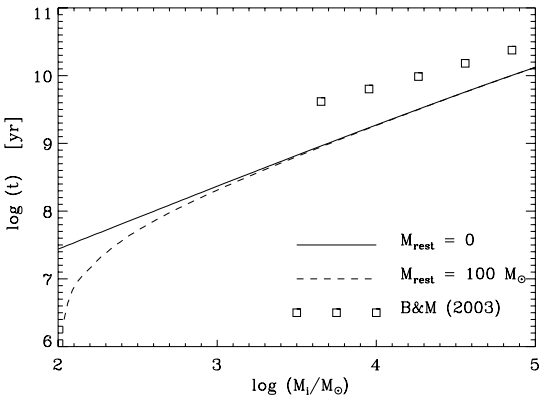

Figure 9.2: The predicted dissolution times of clusters in the solar neighbourhood due to the combined effects of stellar evolution, tidal field, spiral arm shocks and encounters with GMCs, as a function of the initial mass. Full line: total dissolution time. Dashed line: time when the remaining mass is 100 $M_\odot$. Squares and dotted line: dissolution time due to stellar evolution and the Galactic tidal field only, predicted by BM03. Cross with error bar: the value of t_4 empirically derived by L05.

9.3. Comparison with observed age distribution of clusters in the solar neighbourhood

Given the initial mass distribution of the clusters, their formation rate, CFR(t), and the time it takes for a dissolving cluster to fade below the detection limit, we can predict the distribution of observable clusters as a function of age or mass. L05 have derived an expression for the general case of a cluster sample that is set by a magnitude limit. Here we are interested in the prediction for a cluster sample that is complete down to a mass limit of 100 $M_\odot$, because this is the mass limit of the unbiased sample of clusters within 600 pc of Kharchenko et al. (2005) (see L05).

For a constant CFR and a power law cluster IMF with a slope of $-\alpha = -2$ (Lada & Lada 2003) the number of clusters with $M > 100\ M_\odot$ as a function of age is

$$N_{>100}(t) = C\ (M_{\rm lim}(t)^{-1} - M_{\rm max}^{-1}), \tag{9.10}$$

where $M_{\rm lim}(t)$ is the *initial* mass of clusters that reach $M(t) = 100\,M_\odot$ at age t. (Clusters of age t with a smaller initial mass have $M < 100\,M_\odot$ by now.) $M_{\rm max}$ is the maximum *initial* mass of the clusters that are formed. The constant C is related to the star formation rate (SFR) in bound clusters as SFR $= C \ln(M_{\rm max}/M_{\rm lim})$ for $-\alpha = -2$.

Figure 9.3 shows a comparison between the observed age distribution of clusters with $M > 100\,M_\odot$ within 600 pc (from L05) with the predicted distribution for

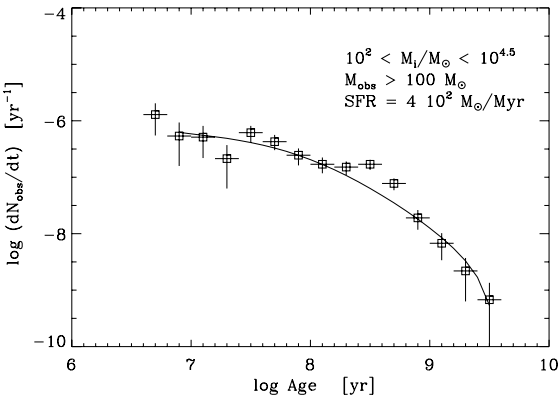

Figure 9.3: The observed age distribution of an unbiased sample of clusters with $M > 100\,M_\odot$ in the solar neighbourhood within 600 pc (Kharchenko et al. 2005; L05) in units of nr yr^{-1} is given by squares with the Poisson error bars. The full line shows the predicted distribution for a cluster sample with a maximum mass of $M_{\rm max} = 3\ 10^4\ M_\odot$ and a SFR of $4\ 10^2\,M_\odot\,\mathrm{Myr}^{-1}$.

$M_{\rm max} = 3\ 10^4 M_\odot$. This value of $M_{\rm max}$ is adopted because the observed distribution shows a steep drop at $\log\ t \simeq 9.5$ (with only one cluster in the last bin) and Fig. 9.2 shows that this corresponds to $M_{\rm i} = 3\ 10^4\,M_\odot$. (However, see discussion in § 9.4).

The flattening of the predicted distribution at the low age end is due to the fact that clusters with an initial mass in the range of about 100 to 300 $M_\odot$ quickly reach 100 $M_\odot$ (see Fig. 9.2). The bump in the observed distribution around $\log(t) \simeq 8.5$ is due to a local starburst (see L05 and Piskunov et al. 2006). Notice the good agreement in the shapes of the predicted and observed distributions!

The vertical shift that is applied to the predicted curve to match the observed one gives a value of $C = 10^{-4.15}$ in Eq. 9.10, which corresponds to a SFR of $4\ 10^2\,M_\odot\,\mathrm{Myr}^{-1}$ for bound clusters in the range of $10^2 < M_{\rm i}/M_\odot < 3\ 10^4$ within 600 pc from the sun.

9.4. Discussion and summary

We studied the dissolution of star clusters in the solar neighbourhood due to four effects: stellar evolution, tidal stripping, spiral arm shocks and encounters with GMCs. For this study we adopted the descriptions of GAPZ06 and GPZB06 for the dissolution of star clusters by spiral arms and encounters with GMCs. We found that the last effect plays a dominant role in the solar neighbourhood.

The cluster dissolution time due to spiral arms and GMCs depends on the density of the clusters, i.e. on $M/{r_{\rm h}}^3$. This implies that the dissolution time is $t_{\rm dis} \sim M^\gamma$ with $\gamma = 1 - 3\lambda$ if the radius of a cluster depends on its mass as $r_{\rm h} \sim M^\lambda$. We adopted

$\lambda \simeq 0.1$ as found by Larsen (2004) for clusters in spiral galaxies and so $\gamma \simeq 0.7$ for dissolution by both spiral arms and GMCs. This value is very similar to $\gamma = 0.62$ predicted for dissolution by the tidal field only (BM03) and empirically derived for cluster samples in four galaxies by Boutloukos & Lamers (2003). If there was no mass radius dependence for clusters in the solar neighbourhood, e.g. $\lambda = 0$, then the predicted age distribution would have a shallower slope than shown in Fig. 9.3, since more old (massive) clusters would have survived.

Our calculated dissolution times of clusters in the solar neighbourhood are about a factor five smaller than predicted by BM03 for stellar evolution and tidal field only. This is reminiscent of the short dissolution time of clusters in the central region of the interacting galaxy M51, where the empirical dissolution time is even ten times shorter than can be explained by stellar evolution and tidal fields (Gieles et al. 2005). GMCs severely limit the lifetime of clusters in that galaxy also (see the discussion in GPZB06).

The steep drop in the observed age distribution at $t \simeq 2$ Gyr yrs can be explained by an upper mass limit for the initial cluster mass in the solar neighbourhood of about $3\ 10^4\ M_\odot$. However, this value is uncertain because it depends crucially on the completeness of the used sample at ages above 1 Gyr. (The sample contains only six clusters older than 1 Gyr.) The mass versus age distribution of our adopted sample, shown in Fig. 8 of L05, suggests that the lower mass limit of the observed clusters increases steeply for clusters older than 1 Gyr. Since the predicted value of $\mathrm{d}N/\mathrm{d}t$ at any age depends on $M_{\rm lim}$ and $M_{\rm max}$ as given in Eq. 9.10, and $M_{\rm lim}$ increases when the lower mass limit increases, an increase in this limit implies an increase in $M_{\rm max}$ derived from the observed age distribution. Based on this argument and the small number of clusters older than about 1 Gyr in the observed sample, we conclude that the derived value of $M_{\rm max} = 3\ 10^4\, M_\odot$ should be considered as a lower limit of the real maximum initial mass.

The vertical shift applied to the predicted age distributions to match the observed one indicates a star formation rate of $4\ 10^2\ M_\odot\,\mathrm{Myr}^{-1}$ in bound clusters of $M_{\rm i} > 100\,M_\odot$ within a distance of 600 pc, corresponding to a surface formation rate of $3.5\ 10^{-10}\ M_\odot \mathrm{yr}^{-1}\mathrm{pc}^{-2}$. This is a factor 2 to 3 smaller than the SFR derived from the study of embedded stars by Lada & Lada (2003) because many of the stars are born in unbound clusters that dissolve within 10 Myr.

The very good agreement between the predicted and observed age distribution of clusters shows that dissolution of clusters in the solar neighbourhood is dominated by encounters with GMCs, as was already suggested by Oort (1958).

Acknowledgments This work is supported by a grant from the Netherlands Research School for Astronomy (NOVA).

Part III

A maximum to the masses of regular star clusters

CHAPTER 10

The luminosity function of star clusters: implications for the maximum mass and luminosity

M. Gieles, S.S. Larsen, N. Bastian and I.T. Stein

Astronomy and Astrophysics, v.450, p.129–145 (2006)

Abstract We introduce a method to relate a possible truncation of the star cluster mass function at the high mass end to the shape of the cluster luminosity function (LF). We compare the observed LFs of five galaxies containing young star clusters with synthetic cluster population models with varying initial conditions. The LF of the SMC, the LMC and NGC 5236 are characterised by a power-law behaviour $N\,\mathrm{d}L \propto L^{-\alpha}\,\mathrm{d}L$, with a mean exponent of $\langle\alpha\rangle = 2.0 \pm 0.2$. This can be explained by a cluster population formed with a constant cluster formation rate, in which the maximum cluster mass per logarithmic age bin is determined by the size-of-sample effect and therefore increases with log(age/yr). The LFs of NGC 6946 and M51 are better described by a double power-law distribution or a Schechter function. When a cluster population has a mass function that is truncated below the limit given by the size-of-sample effect, the total LF shows a bend at the magnitude of the maximum mass, with the age of the oldest cluster in the population, typically a few Gyr due to disruption. For NGC 6946 and M51 this suggests a maximum mass of $M_{\rm max} = 0.5 - 1 \times 10^6 M_\odot$, although the bend is only a 1-2 σ detection. Faint-ward of the bend the LF has the same slope as the underlying initial cluster mass function and bright-ward of the bend it is steeper. This behaviour can be well explained by our population model. We compare our results with the only other galaxy for which a bend in the LF has been observed, the "Antennae" galaxies (NGC 4038/4039). There the bend occurs brighter than in NGC 6946 and M51, corresponding to a maximum cluster mass of $M_{\rm max} = 1.3 - 2.5 \times 10^6\,M_\odot$. Hence, if the maximum cluster mass

has a physical limit, then it can vary between different galaxies. The fact that we only observe this bend in the LF in the "Antennae" galaxies, NGC 6946 and M51 is because there are enough clusters available to reach the limit. In other galaxies there might be a physical limit as well, but the number of clusters formed or observed is so low, that the LF is not sampled up to the luminosity of the bend. The LF can then be approximated with a single power-law distribution, with an index similar to the initial mass function index.

10.1. Introduction

The study of young extra-galactic star clusters has become a whole new field of research since the discovery of young massive clusters. The *Hubble Space Telescope (HST)* has made it possible to resolve these objects and to undertake systematic studies of the nature of these objects. Young clusters with masses in the range of our Milky Way globular clusters ($10^4 - 10^6 M_\odot$) have been found in merging galaxies like the "Antennae" (Whitmore & Schweizer 1995), interacting galaxies like M51 (Larsen 2000; Bastian et al. 2005b), starburst galaxies (Meurer et al. 1995; de Grijs et al. 2003a) and even non-interacting spiral galaxies (Larsen & Richtler 1999).

Recently, a relatively young and very massive cluster was discovered in the merger remnant NGC 7252 (Whitmore et al. 1993). Its (dynamical) mass was confirmed to be as high as $\sim 10^8 M_\odot$ (Maraston et al. 2004). This suggests that there are clusters that fill the gap between the mass range of star clusters and that of dwarf galaxies. However, it remains to be seen if every galaxy is able to produce such massive cluster or if there are physical limitations to the maximum mass of star clusters in different environments.

The LF of star clusters is a powerful tool when studying populations of star clusters. It indirectly gives us information about the underlying mass function (MF). Zhang & Fall (1999) showed for the young clusters in the "Antennae" galaxies that the cluster initial mass function (CIMF) can be well approximated by a power-law distribution: $N(M)\,\mathrm{d}M \propto M^{-\alpha'}\,\mathrm{d}M$, with an exponent[1] of $-\alpha' = -2$. They derived the ages of the clusters using reddening-free parameters, which is necessary to extract the initial mass function from the total luminosity function. The exponent of the CIMF ($-\alpha'$) is found to be close to -2 in a wide range of galaxy environments down to masses of $\sim 10^3 M_\odot$ (de Grijs et al. 2003c). This resembles the mass function of molecular clouds (Solomon et al. 1987), consistent with clusters forming from molecular clouds. The LF can also be approximated with a power-law distribution: $N(L)\,\mathrm{d}L \propto L^{-\alpha}\,\mathrm{d}L$, where values for the exponent $-\alpha$ are found in a range of -2.4 up till -1.7 (Larsen 2002, hereafter L02; Whitmore 2003). In general the indices of the bright LFs are smaller (i.e. steeper) than the index of the CIMF (L02). One of the unanswered questions is whether the difference in slope between the mass function

[1]Through the remainder of this Chapter we will use α' for the exponent of the cluster initial mass function and α for the exponent of the total cluster luminosity function.

and LF have a physical meaning or if it is a result of different measurement techniques and artifacts like the contamination by stars at lower luminosities.

Whitmore et al. (1999b) observe a distinct bend in the LF of young star clusters in the "Antennae" galaxies, where the slope faint-ward is shallower than the slope bright-ward of the bend. The exact slopes depend on the different ways of correcting for stellar contamination. They argue that this could be the progenitor turn-over of the peak that is observed in the luminosity function of old globular clusters which appears at $M_V \simeq -7.2$, corresponding to a mass of $2 \times 10^5 M_\odot$. The difficulty with directly relating the LF to a CIMF is that the LF consists of clusters of different ages, and the mass-to-light ratio of clusters changes drastically when clusters age. Between 10^7 and 10^9 year, a star cluster of constant mass fades about 4 magnitudes in the V-band. Recently, Mengel et al. (2005) observed the clusters in the "Antennae" galaxies in the Ks-band. They also find a double power-law behaviour in the LF and argue that the mass function has a turn-over.

When there is no physical limit to the cluster mass or if there are not enough clusters to sample the CIMF up to any such limit, the mass of the most massive cluster will be determined by the total number of clusters and the slope of the CIMF (Hunter et al. 2003, hereafter H03). A similar idea was posed by Weidner et al. (2004), who suggest that the maximum cluster mass in a galaxy is determined by the star formation rate in that galaxy. It has not been shown yet in a large sample of galaxies that the most massive cluster is a result of size-of-sample effects. H03 only showed that this is the case in the SMC and the LMC. In this study we add M51 to the sample in order to see if the most massive object in this galaxy is also a result of size-of-sample effect or if there is a physical limit above which clusters cannot form in this galaxy. In addition, we use a method to relate a possible truncation of the mass function at the high mass end with the shape of cluster LF. To this end we introduce an analytical model to generate a cluster population and derive the LF for different cluster formation histories, disruption mechanism and CIMFs. We will show that even if the initial mass function of clusters is truncated, the brightest clusters in the sample may will still be determined by sampling statistics as found by Whitmore (2003) and L02.

The paper is organised as follows: In § 10.2 we introduce the data used for this study. In § 10.3 we present the masses and luminosities as a function of log(age/yr) for three galaxies in the sample. The LFs of cluster populations in five different galaxies are presented in § 10.4. We introduce in § 10.5 a cluster population model with which we can reproduce LFs based on various variables. The relation between maximum cluster mass and maximum cluster luminosity is discussed in § 10.6. A discussion in presented in § 10.7. The conclusions are presented in § 10.8.

10.2. Data

10.2.1. SMC and LMC

The ages and masses of clusters in the LMC and SMC were derived by H03 from ground based broad-band photometry. The data was taken by the Michigan Curtis Schmidt telescope by Massey (2002) and covers a large field of the LMC and SMC (11.0 kpc^2 and 8.3 kpc^2, respectively). Aperture photometry was used to derive U, B, V and R magnitudes. The colours and magnitudes were corrected for foreground reddening ($E(B-V) = 0.13$ mag for the LMC and $E(B-V) = 0.09$ mag for the SMC). The ages and masses where derived by comparing the colours with the Leitherer et al. (1999) models. For more details on the data reduction and age derivation we refer to H03.

10.2.2. NGC 5236 and NGC 6946

Data for these two galaxies was taken from L02 and we refer to that paper for details about the data reduction and analysis. Briefly, clusters were identified on V-band equivalent (F555W and F606W) *HST/WFPC2* images and aperture photometry was carried out using a 3 pixels aperture. Cluster candidates were confirmed by a visual inspection of the images. For NGC 5236 and NGC 6946 there were 1 and 3 *HST/WFPC2* pointings available, corresponding to 7.1 kpc^2/53 kpc^2, respectively.

10.2.3. M51

We used the age, mass and luminosity data of more than 1000 clusters in M51 found by Bastian et al. (2005b). Briefly summarised, aperture photometry was performed on F336W, F439W, F555W, F675W, F814W, F110W and F160W (roughly U, B, V, R, I, J and H) images of the *HST/WFPC2* and *HST/NICMOS3* cameras. The magnitudes and colours were compared with the `GALEV` simple stellar population models (Anders & Fritze-v. Alvensleben 2003; Schulz et al. 2002) for different combinations of age and extinction. For detailed tests of the accuracy of the ages and the dependence on photometric errors and choice of models we refer to Bastian et al. (2005b). With 2 *HST/WFPC2* pointings we cover 69 kpc^2 of the inner region of the galaxy.

10.3. Masses and luminosities at different ages

10.3.1. Maximum masses at different ages

Predictions

The most direct way to study a possible truncation of the cluster mass function at the high mass end is to look at the masses of clusters as a function of the logarithm of the ages. When the cluster initial mass function (CIMF) is a power-law distribution

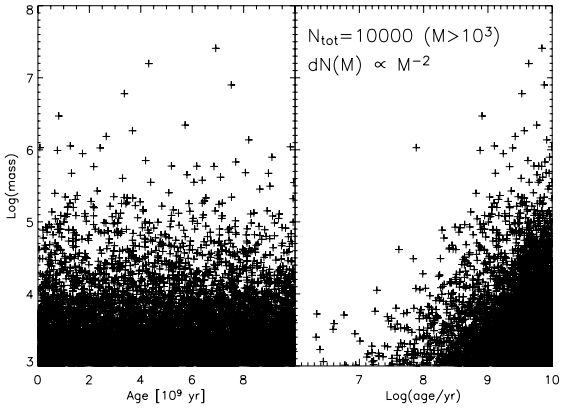

Figure 10.1: Result of a Monte Carlo simulation where 10 000 clusters are sampled from a power-law mass distribution and evenly distributed between $0 < t < 10^{10}$. In the **left-hand** panel the masses are plotted *vs.* age and in the **right-hand** panel *vs.* log(age/yr). In the latter bi-logarithmic plot an increase is visible with a slope of 1 (dashed line), which follows from Eq. 10.1.

($N\mathrm{d}M \propto M^{-\alpha'}\mathrm{d}M$) and not truncated, the maximum mass in the sample is purely determined by the size-of-sample effect. A single age distribution of clusters with a minimum mass $M_{\rm min}$ consisting of N clusters, will statistically have a maximum mass of $M_{\rm max} = N^{1/(\alpha'-1)}\,M_{\rm min}$. H03 showed that the maximum mass per logarithmic age bin should increase with log(age/yr) (assuming a constant cluster formation rate), since each logarithmic age bin corresponds to a longer time interval at older ages and hence more clusters. The number of clusters at higher log(age/yr) increases when assuming a constant cluster formation rate as: $N\,\mathrm{d}\log(t) \propto t\,\mathrm{d}\log(t)$. So, the maximum mass of a sample of clusters formed with a constant cluster formation rate should increase with age (t) as

$$M_{\rm max}\,\mathrm{d}\log(t) \propto t^{1/(\alpha'-1)}\,\mathrm{d}\log(t). \qquad (10.1)$$

This is illustrated in Fig. 10.1. We statistically generated 10 000 clusters from a CIMF with exponent -2 between $6 < \log(\mathrm{age/yr}) < 10$. In the left panel we plotted the results as a function of age and in the right-hand panel as a function of log(age/yr). The increase of the maximum mass predicted by Eq. 10.1 is only visible in the right-hand panel.

Observations

For three galaxies in our sample (SMC, LMC and M51) we have ages and masses of the individual clusters available from earlier studies. For details on the derivation

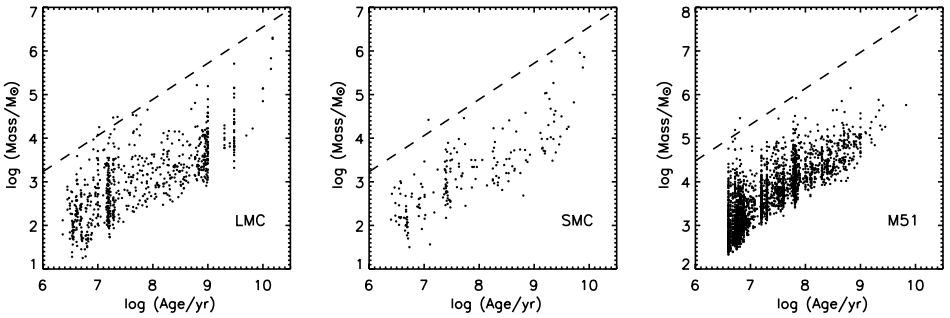

Figure 10.2: Cluster masses for different log(age/yr) for the LMC (**left**), the SMC (**middle**) and M51 (**right**). All samples are limited by a detection limit. Since clusters fade when they age, the lower mass limit goes up in time. the expected increase of the maximum cluster mass as a function of time based on the size-of-sample effect and an exponents for the initial cluster mass function of $-\alpha' = -2$.

of the ages we refer to § 10.2 and references therein. In Fig. 10.2 we plot the masses of the clusters as a function of log(age/yr) for the LMC (left), SMC (middle) and M51 (right). The completeness limit increases with age to higher masses due to fading of clusters caused by stellar evolution. The first impression may be that the unequal number of clusters in each age bin is incompatible with a constant CFR. However, the observed age distribution is a function not only of the cluster formation rate, but also of the detection limit and disruption of clusters. In addition, the age-fitting method yields some we irregularities. For examples all galaxies seem to have an over-density of clusters at log(age/yr)=7.2. This is a known fitting artifact (e.g. Gieles et al. 2005). Therefore, the unequal number of clusters does not contradict a constant cluster formation rate.

The dashed line shows the slope of the predicted increase of the maximum mass, based on $\alpha' = 2$ and Eq. 10.1. For the LMC and SMC the maximum cluster mass as a function of log(age/yr) can be well approximated by the size-of-sample prediction, as was shown already by H03. For M51 however we see that for ages higher than 10^8 year, there are more old high mass clusters predicted based on the size-of-sample effect than observed. However, the observations show that there are no clusters more massive than $\sim 10^6 M_\odot$.

We also performed a linear fit to the maximum mass *vs.* log(age/yr). This is shown in Fig. 10.3. The most massive cluster in every log(age/yr) bin is indicated with a dot. The fit is shown with a full line. The LMC clusters older than log(age/yr)= 9.5 were not included in the fit, because there seems to be an age gap in the cluster distribution between 3 and 10 Gyr. For the SMC and LMC the fit is consistent with the size of sample effect and a CIMF exponent of $-\alpha' = -2.4$, which was found already by H03 for the SMC and LMC. This is a rather steep slope for the CIMF and H03 showed that a fit to the first bins (log(age/yr) < 8) yields a value of $-\alpha' = -2$. It might

be that for higher ages we are seeing a lack of old massive clusters. Note also that we here assume a constant formation rate of cluster and no mass loss of the clusters after formation. We will look at the effect of this assumption in § 10.3.1. For M51 we find a much shallower slope (0.26) than expected on account of the size-of-sample effect. If this slope was caused by the mass function, it should have an exponent of $-\alpha' = -4.3$, which would be a much steeper slope than found in any other study. In fact, the CIMF has been determined for M51 by Bik et al. (2003) from young clusters and was found to be -2.1 ± 0.3.

The effect of mass loss, infant mortality rate and variable cluster formation rates

In the conversion of the $M_{\rm max}$ *vs.* log(age/yr) relation to a CIMF slope we assume that the clusters have not lost any mass after their formation and that the clusters were formed with a constant formation rate. In reality, only 10-30% of the clusters will survive the initial 10 Myr, clusters will lose mass due to stellar evolution (SEV) and tidal effects and the cluster formation rate (CFR) might not be constant at all. To quantify these effect, we generated a series of maximum masses consistent with the size-of-sample effect and a mass function exponent of -2, assuming a constant CFR. We then evolve each cluster mass as a function of its age according to the analytical formulas introduced by Lamers et al. (2005a). The mass of the cluster as a function of time can be well approximated by

$$M_p(t) = \left[(M_i \mu_{\rm sev})^\gamma - \gamma\, 10^{4\gamma} \left(\frac{t}{t_4} \right) \right]^{1/\gamma}, \qquad (10.2)$$

where $M_p(t)$ is the present mass of the cluster as a function of its age, M_i is the initial mass of the cluster, $\mu_{\rm sev} \equiv M(t)/M_i$ is the fraction of remaining mass after mass loss due to stellar evolution has been subtracted. The value of $\mu_{\rm sev}$ is based on the `GALEV` models and analytically parameterised (see Lamers et al. (2005a) for details). t_4 is the disruption time of a $10^4 M_\odot$ cluster and γ is a dimensionless index indicating the dependence of the disruption time of clusters on the initial mass; $t_{\rm dis} \propto M_i^\gamma$. The value for γ is found to be 0.62 based on observations and N-body simulations (Lamers et al. 2005b). Equation 10.2 describes the mass of a cluster as a function of time based on a variable final disruption time, taking mass loss due to stellar evolution and tidal evaporation into account.

We consider two scenarios: 1.) the SMC/LMC case and 2.) the M51 case. This is because the masses and disruption times are very different. For the SMC/LMC case we choose the maximum mass to be $M_{\rm max} = 10^3 M_\odot$ at log(age/yr) = 6.5, corresponding to the observed maximum mass at young ages. For the M51 case we choose a higher maximum mass; $M_{\rm max} = 5 \times 10^4 M_\odot$ at log(age/yr) = 6.5, also based on the observed masses at young ages. We then assume a typical disruption time of clusters for the SMC and LMC of $t_4 = 3 \times 10^9$ yr and $t_4 = 2 \times 10^8$ yr for M51. The disruption times are based on the observationally determined values of Boutloukos & Lamers (2003) (SMC) and Gieles et al. (2005) (M51) and the predicted values of

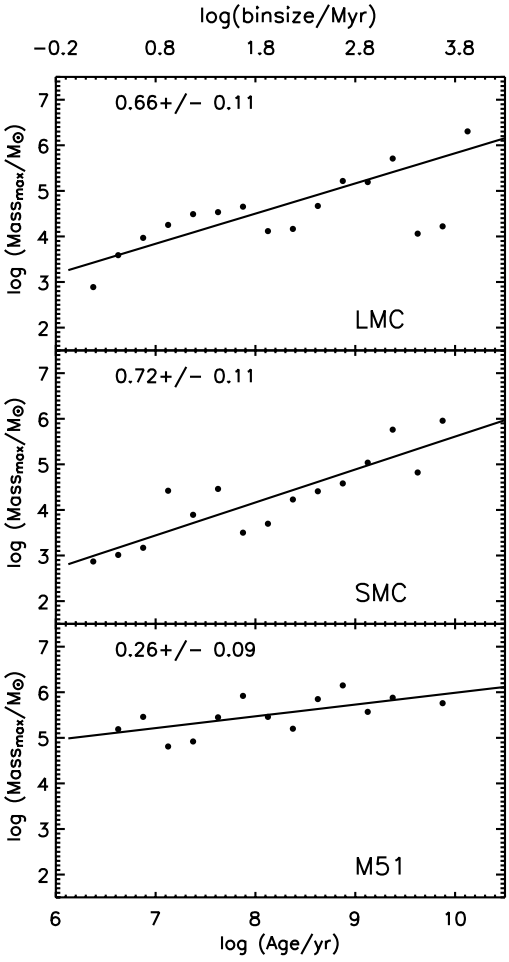

Figure 10.3: Mass of the most massive cluster (dots) in log(age/yr) bins of 0.25 dex for all three galaxies. The fit to the most massive clusters is shown with the full line in all panels. The values of the slopes are indicated. The top panel shows how the binsize increases with increasing log(age/yr), introducing the size-of-sample effect.

Baumgardt & Makino (2003) (LMC). In Fig. 10.4 we show the slope of the cluster maximum masses as a function of log(age/yr) as predicted by the size-of-sample effect with a full line and the shallower increase after the clusters have been evolved in time for different scenarios. In the top panels we show the effect of stellar evolution and disruption for the two different scenarios. The disruption time of clusters in M51 is almost a factor of 15 shorter than for clusters in the SMC/LMC, but since the

masses are higher and disruption is mass dependent ($t_{\rm dis} \propto M_i^{0.62}$), the effect of the evolution is similar in both cases. Since this simple model can easily be extended to more realistic scenarios, we now include the effect of a high infant mortality rate in M51 in the bottom left panel of Fig. 10.4. Bastian et al. (2005b) estimate that 70% of the clusters does not survive the first 10 Myr, independent of their mass, so we increase the maximum mass for bins below 10 Myr with a factor of 3.3 to simulate the higher masses at young ages. The result is shown in the bottom left panel of Fig. 10.4. The inclusion of infant mortality makes the slope again slightly shallower. However, still not even close to the observed value. The last effect we consider, is a steady increase in the CFR. Since the maximum mass is proportional to the CFR, an increase in the CFR could result in more young massive clusters. To get to the slope of 0.26 as observed in M51 (bottom panel of Fig. 10.3), we apply an additional increase in the CFR. We assume that increase exponentially in time as CFR $\propto t^{\delta}$. To get to a slope of 0.26 as observed, we need $\delta = -0.5$, which means the CFR has increased a factor of 22 in the last few Gyr. M51 is in interaction with NGC 5195 which might have enhanced the CFR. In earlier work, however, we have determined the CFR increase to be in the order of a factor of 3-5 (Gieles et al. 2005), which is in good agreement with independent determinations of the increase of the star formation rate for these kind of interacting systems, based on Hα measurements (Bergvall et al. 2003). Also, the increase in the CFR seems to be more in bursts rather than an exponential increase in time. A burst in the CFR will not affect the slope of Fig. 10.3, it will just show up as a peak. Worth noting is that the two peaks of M51 (Fig. 10.3) at log(age/yr)=7.8 and log(age/yr)=8.8. They coincide with the predicted moments of encounter with NGC 5195, ∼75 Myr and ∼450 Myr ago (Salo & Laurikainen 2000).

With this we show that part of the deviation from a slope of 1 in Fig. 10.3 is caused by stellar evolution, cluster mass loss due to tidal effects and infant mortality rate, but even the short disruption time and high infant mortality rate of M51 can not explain the observed shallow increase of the maximum cluster mass with log(age/yr) (Fig. 10.3, bottom), without assuming an unrealistically high increase in the CFR.

10.3.2. The cluster mass function

If the CIMF is truncated, the total MF of clusters should also show a truncation. As a check, we make the mass function, i.e. $\mathrm{d}N/\mathrm{d}M$ as a function of mass, for the SMC, LMC and M51. Since the detection limit cuts the sample at different masses (Fig. 10.2), we need to generate a mass and age limited sample. We choose minimum mass and maximum age combinations of $[\log(M_{\rm min}/M_{\odot}), \log({\rm age}_{\rm max}/{\rm yr}] = [3.1, 9], [3.5, 9]$ and $[4.2, 8.7]$ for the LMC, the SMC and M51 respectively. The resulting mass functions are shown in Fig. 10.5. The three mass functions where fitted with a single power-law, with variable slope and vertical scaling and with a power-law with exponential cut-off: $N\mathrm{d}M \propto M^{-\alpha'} \exp(-M/M_*)\,\mathrm{d}M$, where the cut-off mass M_* is an extra variable. This function is similar to the Schechter (1976) function, which will later be used to fit the luminosity function of clusters. The χ^2_{ν} results of the truncated and untruncated power-law fits are compared by showing the ratio. The

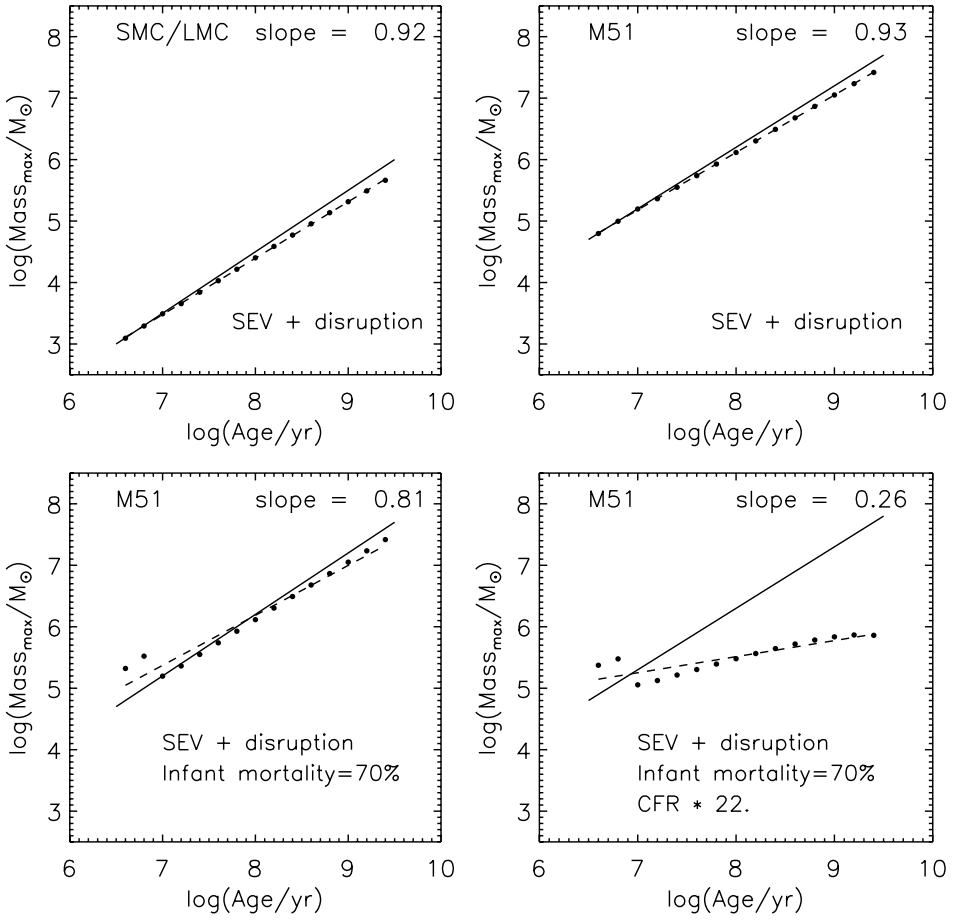

Figure 10.4: A simulated set of initial maximum masses as a function of log(age/yr) (full line) for the SMC/LMC case and the M51 case with different effects. The full line represent what is expected based on the size of sample effect and $-\alpha' = -2$ and therefore has a slope of 1 (see Eq. 10.1). The initial masses were evolved in time taking into account mass loss due to stellar evolution and tidal effects. The evolved masses (dots) are fit and the slope is indicated with dashed lines.

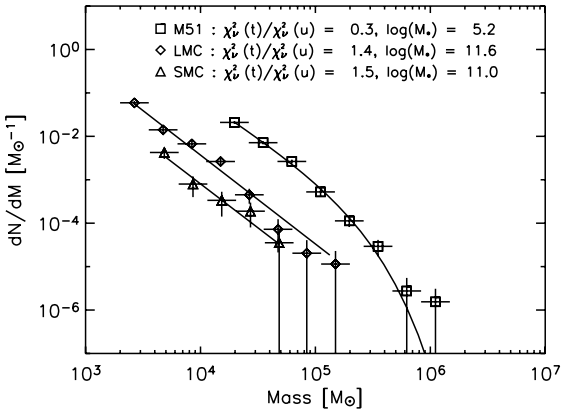

Figure 10.5: Mass functions of the LMC, SMC and M51 for an age and mass limited sample. The result of a truncated power-law fit is over-plotted and the corresponding M_* is indicated. The χ^2_ν of the truncated and untruncated power-law fits are compared by showing the ratio.

fit of the truncated power-law is over-plotted. For the SMC and LMC, however, this fit is similar to an untruncated power-law fit. The M51 mass function is better fitted with a truncated power-law. The values we find for $-\alpha'$ are $-2.05\pm0.01, -2.03\pm0.02$ and -1.70 ± 0.08 for the SMC, LMC and M51 respectively. The value for M51 can be explained by mass dependent cluster disruption. If star clusters are formed with a CIMF with index -2, then the total mass function will have the same index, as long as the disruption time scale is longer than the maximum age in the sample. For the SMC and LMC the maximum age in the sample is 10^9 yr, and the disruption time scale is $>> 10^9$ yr (Baumgardt & Makino 2003; Boutloukos & Lamers 2003). For M51, however, the disruption time is shorter than the maximum age in the sample (Gieles et al. 2005). Since the low mass clusters disrupt faster than the high mass clusters, the mass function gets shallower at older ages. Therefore we find that the MF has an index which is greater than -2.1, which is the index of the CIMF of M51 (Bik et al. 2003).

10.3.3. Maximum luminosities at different ages

Another way of looking at the size-of-sample effect, is by plotting the M_V magnitudes of all clusters as a function of log(age/yr). In Fig. 10.6 we plot the magnitudes for the three cluster populations shown in Fig. 10.2. The advantage of looking at magnitudes instead of masses, although they are directly linked by the age and mass dependent magnitudes from SSP models, is that this figure helps to understand the LF, which will be discussed in § 10.4. The solid line indicates the fading of a single mass cluster based on the `GALEV` models, i.e. without tidal disruption. We shifted the

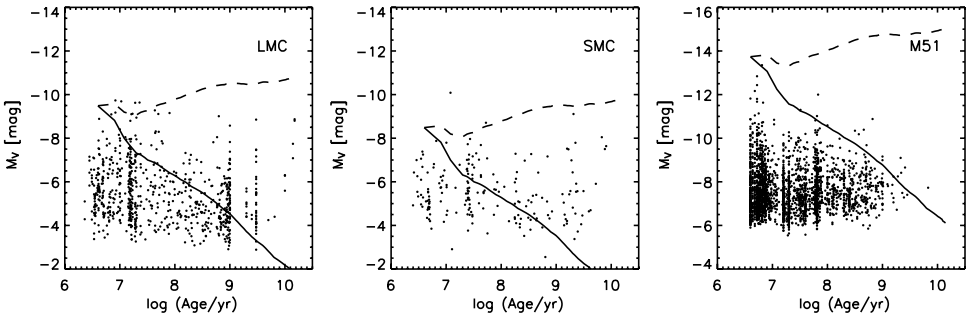

Figure 10.6: Cluster absolute magnitudes (M_V) for different ages for the LMC (**left**), the SMC (**middle**) and M51 (**right**). All samples are limited by a detection limit, which is why the lower parts of the diagrams are empty. The solid line shows the fading of a cluster in the V-band based on the `GALEV` models. The dashed line shows the expected luminosity of the maximum cluster mass as a function of time based on the size-of-sample effect and an exponents of the initial cluster mass function $\alpha' = 2$.

starting magnitude to the brightest clusters at log(age/yr) = 6.5. The dashed lines now represent the luminosity of the most massive cluster as a function of log(age/yr) based on the size-of-sample effect and $\alpha' = 2.0$. From the `GALEV` simple stellar population we took the evolution of the magnitudes in time for a single mass cluster with some reference mass ($M_{\rm ref}$), which is the maximum mass in the age range log(age/yr) < 7. We then add extra mass to $M_{\rm ref}$ as a function of log(age/yr), following Eq. 10.1. The magnitude then depends on the age and the exponent of the CIMF as

$$M_V(t) \propto M_V(M_{\rm ref}, t) - 2.5\ \log(t^{1/(\alpha'-1)}) \qquad (10.3)$$

where $M_{\rm ref}$ is a reference mass based on the observed maximum mass at young ages, $M_V(t)$ is the maximum magnitude as a function of age, t is the cluster age and α' is the exponent of the CIMF. The dashed lines represent the maximum luminosity based on the size-of-sample effect and Eq. 10.3, for $\alpha' = 2$. The lower luminosity increases with log(age/yr) for M51. This is since the clusters of M51 had to be detected in the F439W band in order to make the observed sample. Since clusters fade more rapidly in the filters bluer than the V band, we miss some clusters at older ages and faint magnitudes. Since we are here only interested in the maximum luminosity, this will not affect our results. When the colours are used for cluster identification, these colour differences have to be taken in to account.

The maximum luminosities of clusters in the LMC and SMC follow the dashed lines better than the fading line of the single mass cluster. The most luminous clusters in M51 seem to follow the fading of the single mass $M_{\rm ref}$ better then the dashed lines which are based on the size-of-sample prediction, which suggests that the underlying maximum mass is truncated at that mass.

Interestingly, Zhang & Fall (1999) made a similar plot for the luminosities of clusters in the "Antennae" galaxies (their Fig. 2). They also over-plot the luminosity evolution of single mass clusters in time. Their maximum luminosities seem to follow the models very well, which suggests that the maximum luminosity and hence the maximum mass of clusters in the "Antennae" galaxies does not follow the predicted size-of-sample relation of H03. *All this suggests that the maximum mass of clusters in M51 and the "Antennae"galaxies are not determined by size-of-sample effects, but instead has a physical upper limit.* The most luminous cluster in these galaxies however, in general being a young clusters due to the rapid fading in time of star clusters, *is* determined by size-of-sample effects. This agrees with what was found by Whitmore (2003) and L02, who showed that the maximum cluster luminosity in a galaxy depends on the total number of clusters in the galaxy above a certain luminosity. We will continue with this subject in § 10.6.

10.4. The luminosity functions of five galaxies

In this section we will present the LFs of (young) clusters in the SMC, LMC, NGC 5236, NGC 6946 and M51. For each galaxy the number of clusters as a function of M_V was determined and a fit of the form $N\,\mathrm{d}M_V = A\,10^{\beta\,M_V}\,\mathrm{d}M_V$ was performed. The index β of the magnitude distribution relates to the exponent of the LF as

$$-\alpha = -2.5\,\beta - 1 \tag{10.4}$$

where α is the exponent of the LF ($N\,\mathrm{d}L \propto L^{-\alpha}\mathrm{d}L$). In the following subsection we will first present the LFs and fit a power-law function to all cluster samples. In § 10.4.2 we will fit alternative functions and compare them with the power-law fits to determine the best fit model to the LFs. All results are summarised in Table 10.1.

10.4.1. The observed luminosity functions

SMC and LMC

The LFs of the SMC and LMC are based on the data of H03. The LFs are presented in the top two panels of Fig. 10.7. H03 report lower limit magnitudes of $M_V = -3.5$ and -4.5 for the LMC and SMC, respectively. Since the sample starts to be incomplete a bit bright-ward of the cut-off magnitude, we used very conservative completeness limits which are 1.5 mag brighter ($M_V = -5$ for the LMC and $M_V = -6$ for the SMC). H03 only corrected for foreground reddening ($E(B-V) = 0.09$ and 0.13 for the SMC and LMC respectively) and we have no extinction estimates for the individual clusters available. The detection limit is shifted the same amount as the LF when correcting for foreground extinction.

NGC 5236

The cluster sample of NGC 5236 is presented in L02. From the completeness tests presented in that paper and a distance modulus of 27.9, we found a 90% completeness limit of $M_V = -5.5$. We corrected the measured magnitudes for galactic foreground extinction based on Schlegel et al. (1998). We used the sample which had spurious sources removed after visual inspection. A foreground extinction correction of 0.218 mag was applied (Schlegel et al. 1998). The sharp cut-off at high luminosities is because some of the bright sources were saturated.

NGC 6946

The LF of clusters in NGC 6946 was presented in L02. We here use the sample of clusters where spurious sources have been removed after visual inspection. The 90% completeness limit, following L02, is $V = 22.0$ and a distance modulus of 28.9 mag was used. The magnitudes were corrected for 1.133 mag foreground extinction based on Schlegel et al. (1998). The final LF can be seen in Fig. 10.7 (second from bottom). The LF contains more bright clusters than the previous ones. In addition the slope is slightly steeper. The fact that LFs with brighter clusters are better fitted with steeper power-laws was already noted by L02. In § 10.4.2 we will compare this fit with a double power-law fit and a Schechter function.

M51

For the LF of M51 the data from Bastian et al. (2005b) is used. We refer to this paper for detailed explanation on data reduction and source detection. Ideally, we select clusters for the LF independent of the applied age fitting routine. The best criterion for this would be to select on extended objects brighter than the 90% completeness limit in F555W. Since we only found reliable radius estimates for 305 objects, we selected the observed clusters that passed our fitting criteria from Bastian et al. (2005b), e.g. the sources that were well fit by a cluster model. Since one of our source selection criteria is that the object has to be above the 90% completeness limit in at least four bands, it is of importance which band we use. Comparing the SEDs for different ages of the `GALEV` models to the 90% completeness limits in all filters, we found that all clusters are always above our 90% completeness limit in F555W, F675W and F814W once they are detected in the F439W filter. If we apply the F555W 90% cut to the sample, our four-filter criterion will cut the sample sometimes because the source has to be visible in F439W as well, depending on the age. To be sure that for all ages our sample is limited by a cut in the F555W band only, we add the maximum colour difference F439W – F555W from the `GALEV` models for clusters between 4×10^6 and 10^9 years to our F555W 90% completeness limit. This makes the cut in this filter 0.6 mag brighter than the 90% completeness limit of 22.7 mag. A distance modulus of M51 for 29.62 mag was used (Feldmeier et al. 1997) and a foreground extinction correction of 0.117 mag was applied (Schlegel et al. 1998). The LF for all clusters brighter than 22.0 mag in F555W is shown in the bottom panel of

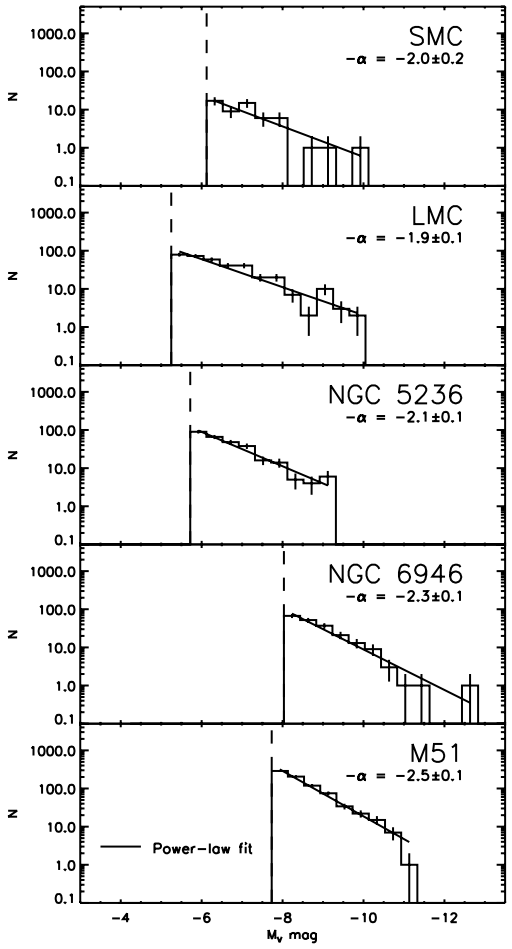

Figure 10.7: The (foreground extinction corrected) LFs for the five galaxies in our sample. In all graphs the dashed line represent the 90% completeness limit. The solid lines are fits to the data above the 90% completeness limit over the full range of the form $N\mathrm{d}M_V = A\,10^{\beta\,M_V}\mathrm{d}M_V$. From this the slope of the LF can be found using Eq. 10.4.

Fig. 10.7. As was the case for the LF of NGC 6946, we also fit a power-law which is steeper than the power-law CIMF index −2 of Zhang & Fall (1999). We will consider different functions in § 10.4.2.

10.4.2. Fitting other functions to the luminosity functions

The brighter LFs of NGC 6946 and M51 are fitted with power-law functions with steeper slopes ($-\alpha \simeq -2.4$) than the fainter ones ($-\alpha \simeq -2$). When a single power-law function is fitted to faint sides of the LFs of NGC 6946 and M51, we find similar values as for the SMC, LMC and NGC 5236. This suggests that the LFs turn over at the bright side, something what was found for the "Antennae" galaxies by W99 as

well. In order to quantify the deviation from a single power-law, we fitted *all* LFs of § 10.4.1 with a double power-law function with variable break point and a Schechter function. The Schechter function is generally used for the LF of galaxies. It has a power-law nature on the faint end and a exponential drop at the bright side. In terms of magnitudes the Schechter function can be expressed as

$$N(M_\lambda)\mathrm{d}M_\lambda = 0.4\,\ln(10)\,N_*\,10^{0.4\,(-\alpha+1)\,(M_*-M_\lambda)}\times \exp\left[-10^{0.4\,(M_*-M_\lambda)}\right]\,\mathrm{d}M_\lambda, \quad (10.5)$$

where M_λ is the magnitude in a band with central wavelength λ, N_* is a normalisation number, α is the exponent of the power-law part of the LF and M_* is the characteristic point of the function. M_* is the equivalent of L_* when using the Schechter function to fit the LF of galaxies.

To compare the different function fits for all five galaxies, we compare the reduced χ^2 values of the different fits. The ratio of $\chi^2_{\nu,\,\mathrm{single\,power-law}}/\chi^2_{\nu,\,\mathrm{double\,power-law}}$ is shown in the top panel of Fig. 10.8 for the five LFs. In the bottom panel we show the ratio of $\chi^2_{\nu,\,\mathrm{single\,power-law}}/\chi^2_{\nu,\,\mathrm{Schechter}}$. The χ^2_ν comparison shows that the LFs of NGC 6946 and M51 are better fitted with a function that drops at the bright end, although from the values in Table 10.1 and the χ^2_ν comparison mentioned, a single power-law distribution can not be excluded with a high significance level.

In Fig. 10.9 we show the best fits to the LFs for all five galaxies, based on their χ^2_ν results. The number of clusters is normalised to the observed area for fair comparison. We extrapolated the faint side of the LFs of NGC 6946 and M51 with a dashed line, this to show that these galaxies on the faint side have similar slopes as the other three cluster LFs. Another interesting fact is that NGC 6946 and M51 are on top, due to a high CFR. Therefore, they are also the only galaxies with cluster brighter than $M_V = -10$ mag.

A closer look at NGC 6946 and M51

To get a realistic idea of the location of the breakpoint, which we can compare with other galaxies, we need to take into account possible reddening. L02 did not determine reddening for the individual objects, but only mentions the Galactic foreground reddening. For the direction of NGC 6946 this is $A_V = 1.13$ and we corrected the V magnitudes of each cluster for this amount. The breakpoint was determined by fitting double power-laws with a variable breakpoint, exponents and normalisation constant. We found the break to be at $M_V = -8.9 \pm 0.4$, with an exponent faint-ward of the break of $-\alpha_1 = -1.7 \pm 0.5$ and $-\alpha_2 = -2.4 \pm 0.1$ bright-ward of the break. The (foreground) extinction corrected LF with the double power-law fit can be seen in the top left panel of Fig. 10.10. W99 observe similar behaviour for the LF of the "Antennae" galaxies. When they fit two power-laws, they find the breakpoint around $M_V = -10.3$, depending on the different samples they selected.

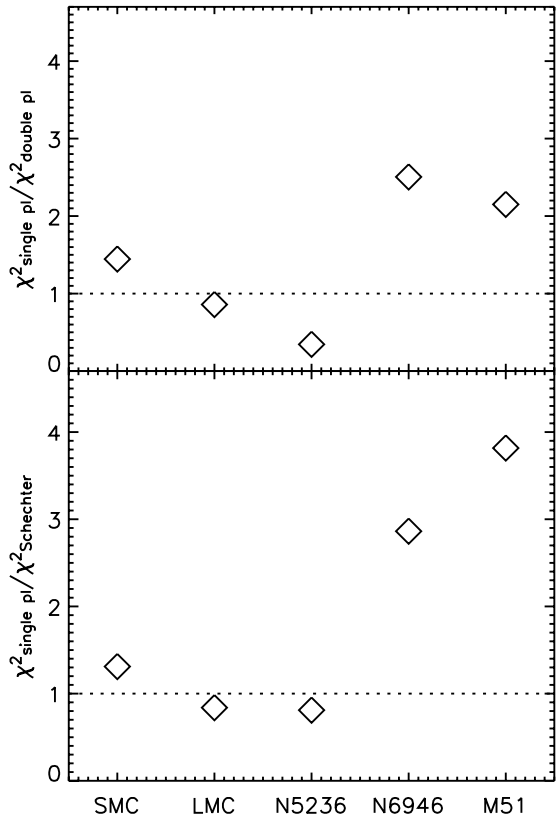

Figure 10.8: Comparison between the χ^2_ν results of the different functions that were fitted to all LFs. **Top:** Ratio of $\chi^2_{\nu,\,\rm single\,power-law}$ over $\chi^2_{\nu,\,\rm double\,power-law}$ for the five galaxies of which we have LFs. **Bottom:** Ratio of $\chi^2_{\nu,\,\rm single\,power-law}$ over $\chi^2_{\nu,\,\rm Schechter}$. The LFs of NGC 6946 and M51 are better fitted by a double power-law distribution or a Schechter function, as compared to a single power-law distribution.

We also fitted a Schechter function (Schechter 1976), which has a more gradual bend and it is usually used to fit the LF of galaxies. This was also done for the clusters in the "Antennae" galaxies by W99.

The top right panel of Fig. 10.10 shows the result of the Schechter function fit to the (foreground) extinction corrected LF of NGC 6946. The bend in the Schechter function occurs at $M_* = -10.2 \pm 0.6$, which is 1.2 mag fainter than the M_* of the "Antennae" galaxies ($M_* = -11.4 \pm 0.4$). The break point in the double power-law distribution occurs 1.2 mag fainter as compared to the "Antennae".

For M51, we corrected all magnitudes for the extinction values we acquired from the age fitting (see Bastian et al. (2005b) for details). This is important, since extinction effects might also affect the shape of the LFs. Bastian et al. (2005b) found that young clusters have on average higher extinction values than the older ones. L02 looked at the effect of differential extinction on the LF. He found that it makes the LF

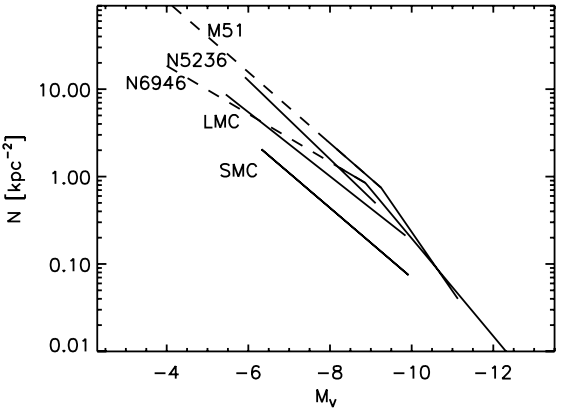

Figure 10.9: The best fit result to all five LFs. The number of clusters is normalised to the observed area of the galaxies in kpc^2. The full line is the region where data points were available from observations. The dashed lines are extrapolations. The two galaxies which are better fitted by a double power-law (NGC 6946 and M51), are on top and the only galaxies with cluster brighter than $M_V = -10$ mag.

steeper, but only when there is already a cut-off in the mass distribution on the high mass end. If the mass function is not truncated, differential extinction does not affect the shape of the LF, since then still power-laws with the same index would be added, resulting in a power-law with that index. In case there is a relation between the luminosity and extinction, for example because we can see more intrinsically bright clusters, the bright part of the LF will be extinct ed more and this could result in a drop. To check this, we plotted the available extinction and luminosities from Bastian et al. (2005b) in Fig. 10.11. We averaged the extinction for different luminosity bins, and there is no relation between the two parameters. So the fits to the LF of M51 will have a higher reliability than the ones of NGC 6946, since there individual source extinction is not known.

When we fit a double power-law distribution, the location of the bend is at $M_V = -9.3 \pm 0.4$. The exponents on the faint and bright side of the breakpoint are $-\alpha_1 = -2.0 \pm 0.1$ and $-\alpha_2 = -2.7 \pm 0.3$ respectively (bottom left panel of Fig. 10.10). These values are very similar to those found for NGC 6946. The bottom right panel of Fig. 10.10 shows the result of a Schechter function fit to the M51 clusters. The exponent is $-\alpha = -1.9$ and the bend is at $M_* = -10.3 \pm 0.5$.

The results of all fits to the LFs are summarised in Table 10.1. We added the values found by W99 for the "Antennae" galaxies as a comparison. The two exponents of the double power-law fits are very similar between NGC 6946, M51 and the "Antennae". The breakpoint in the case of the double power-law fit, however, occurs about 1.2 mag

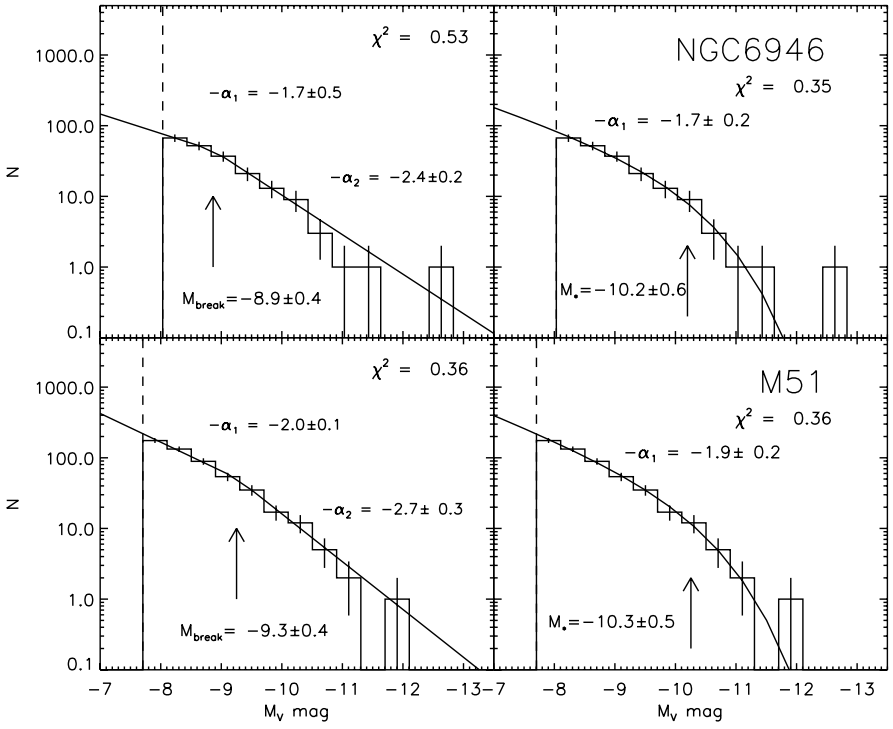

Figure 10.10: The extinction corrected LFs for NGC 6964 (**top**) and M51 (**bottom**). Results for a double power-law fit (**left**) and a Schechter function (**right**) to the same data are shown.

brighter in the "Antennae" galaxies. The value for M_* is also about 1 mag brighter compared to NGC 6946 and M51.

In the next section we will attempt to explain the shape of the LFs, in particular the bend observed for NGC 6946, M51 and the "Antennae" galaxies.

10.5. A cluster population model

Our goal is to understand why we observe a bend in the luminosity function of NGC 6946, M51 and the "Antennae" galaxies and not in the other galaxies in the sample. The luminosity function (LF) of a star cluster population is a combination of multi-age cluster initial mass functions, which all have age dependent mass to light ratios. Clusters will lose mass in time due to stellar evolution and tidal effects, which will also affect the luminosity as a function of age. When there are no ages and masses of the individual clusters available, an alternative way to look at how the LF is built

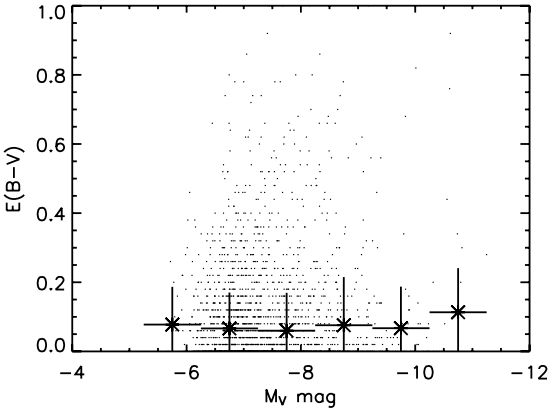

Figure 10.11: $E(B-V)$ *vs.* luminosity for all clusters of M51, taken from Bastian et al. (2005b). The average values at different magnitudes are indicated.

Table 10.1: Properties of the observed LFs.

Galaxy	$-\alpha_1$	$-\alpha_2$	Break (mag)	M_* (mag)	A_V (mag)
SMC	-2.0 ± 0.2	-	-	-	0.09
LMC	-1.9 ± 0.1	-	-	-	0.13
NGC 5236	-2.1 ± 0.1	-	-	-	0.218
NGC 6946	-1.7 ± 0.5	-2.4 ± 0.1	-8.9 ± 0.4	-10.2 ± 0.6	1.133
M51[1]	-2.0 ± 0.1	-2.7 ± 0.3	-9.3 ± 0.4	-10.3 ± 0.5	-
"Antennae"[2]	-1.9 ± 0.1	-2.8 ± 0.4	-10.3 ± 0.4	-11.4 ± 0.4	-

[1] Corrected for individual cluster extinction.
[2] Values from W99 for their sample of extended sources.

up is to model the LF based on various physical input parameters. In this section we will analytically generate the LF of a star cluster population.

10.5.1. Creating a synthetic cluster population

Set-up

The synthetic cluster population is based on an analytical model presented in Gieles et al. (2005). In that work it was used to predict ages and masses of the cluster population of M51. The LF follows directly from these predictions since the

combination of age and mass can be converted to luminosity using simple stellar population models.

The model creates a series of cells equally spaced in $\log(t)$ and $\log(M)$. Then a CIMF and formation rate are chosen. Based on these choices each cell is assigned a weight ($w(t, M_i)$). To acquire a CIMF with exponent $-\alpha'$ and a constant formation rate, $w(t, M_i)$ can be written as

$$w(t, M_i) = (t/t_{\min}) \times (\alpha' - 1) \times (M_i/M_{\max})^{1-\alpha'} \tag{10.6}$$

where $w(t, M_i)$ is the weight assigned to a cell with age t and mass M_i, $M_{\max}$ is the mass of the most massive cell in the simulation, $t_{\min}$ is the age of the youngest cell in the simulation and α' is the exponent of the mass function. The weight is now a function of age and initial mass, where the most massive cell in the youngest bin has a weight of one, and corresponds to 1 cluster per $\log(t)$–$\log(M)$ bin. This value is arbitrary and can change since later we will scale the total population to a different number. When $-\alpha' = -2$ is chosen, the weight depends on age and mass simply as: $w(t, M_i) \propto t/M_i$. When the cells are then binned in age, mass or luminosity, the weights of each cell are counted and the bin values now represent number of clusters. The main advantage of using these weight assigned cells spread equally in $\log(t)$ and $\log(M)$, is that it would otherwise be very time consuming to generate cluster populations with a well sampled mass function; the amount of clusters needed for that is too high. Also, the number of points per bin is now constant and it is straight-forward to create a variety of populations with different formation rates, disruption time scales etc. in a short time. The model from Gieles et al. (2005) is extended in this work to create LFs. To this end the age and mass dependent magnitudes of clusters are taken from the `GALEV` SSP models based on a Salpeter IMF. When generating a LF, the total weight of the cluster population is scaled to a realistic number of clusters. Then only bins with weights greater or equal to one are kept. In this way the predicted maximum luminosity follows directly from the model, depending on the number of clusters (=total weight) and the input variables.

Include stellar evolution and cluster disruption

In a recent study (Lamers et al. 2005a) it was shown that there is a simple analytical description of the evolution of the mass of a single cluster as a function of time (see Eq. 10.2, § 10.3.1). It takes into account the effect of mass loss due to stellar evolution, based on the mass loss predicted by the `GALEV` models and it includes mass loss due to tidal evaporation based on the N-body results of Baumgardt & Makino (2003). The mass as a function of time according to these analytical formula agrees very well with the predictions from N-body simulations (Lamers et al. 2005a). We assume stars of all type are lost due to disruption. In reality more low mass stars will leave the cluster. This might slightly affect the magnitudes as a function of time.

10.5.2. The luminosity function of a multi-age population

In the first step to understand the LF we generate an analytic cluster population with $\log(t)$ ranging from 7 to 9. Cells are spread equally in $\log(t)$ and $\log(M)$ space and weights are assigned to correct for the logarithmic binning in age and to create a mass function with $-\alpha' = -2.0$. Cluster masses were assigned between $10^3 M_\odot$ and $10^{12} M_\odot$. The upper mass was chosen unrealistic high, representing the lack of a physical upper limit to the most massive cluster in the mass function. The total weight is then scaled to 1000 clusters. In principle this step is not necessary, it tells us what the most luminous cluster in the sample is, since we will only use bins with values greater than one. (Note that due to the weights we use and the final scaling there are cells with weights much smaller than one.) Every cell is assigned a magnitude based on the `GALEV` models. The exponent of the resulting LF for this multi-age population is always $-\alpha = -2.0$. Although clusters with $\log(t) = 9$ have faded considerably, the final LF is still an addition of power-laws with exponents of -2, with no limit to the maximum mass and hence the maximum luminosity. For this reason, changes in the formation rate as well as bursts will have no effect on the slope. Mass dependent disruption will slightly change the slope (§ 10.5.5).

10.5.3. The luminosity function without a maximum mass

When the CIMF is not truncated, the mass of the most massive cluster observed will increase with increasing log(age/yr) due to the size-of-sample effect (§ 10.3; H03). The most massive cluster will depend on age as $\log(M_{\rm max}) \propto \log(t)$, when $-\alpha' = -2$. The dotted line in Fig. 10.12 takes this increase of the mass *and* the fading of the most massive cluster as a function of log(age/yr) into account. In two dex in age the maximum mass will also increase with two dex if the slope of the mass function is -2. This means that the most massive cluster at 10^9 years will be a factor of 100 more massive and hence 5 mag brighter than the one at 10^7 years. Since clusters fade about 4 mag between 10^7 and 10^9 years, these two effects almost cancel out. Not only the mass of the most massive cell will increase, but also the second most massive etc. Therefore, the LFs at different ages will all have clusters sampled between the detection limit and more or less the same maximum luminosity. So, the slope of the integrated luminosity function will be close to the slope of the CIMF for almost all luminosities, which we found already in § 10.5.2. This effect can be seen in Fig. 10.6 for the LMC and the SMC clusters. At all ages we find clusters between the detection limit and more or less the same maximum luminosity. Integration over all ages will yield a LF which has about the same slope as the mass function. This has always been assumed to be logic, but here we show that this is only the case when there is no maximum mass.

10.5.4. Truncation of the mass function

L02 has already shown that when generating a multi-age population with a truncation at the high mass side, the LF gets steeper. This can be understood as follows:

when the underlying mass function is truncated at some upper mass, the brightest cluster will be the most massive cluster in the youngest age bin. This holds when the MF is sampled up to the truncation limit in the youngest age bin. The older clusters have faded due to stellar evolution. Hence at the brightest end of the LF only the youngest clusters will contribute. Going to fainter magnitudes, more and more ages will contribute to the LF. At the luminosity of the most massive cluster in the oldest age bin and fainter, all ages will contribute, and therefore the slope faint-ward of that brightness will be the slope of the CIMF, similar to what we found in § 10.5.2. This is illustrated in Fig. 10.12. The decreasing line in the right hand panel represents the luminosity of a $10^6 M_\odot$ cluster between 10^7 and 10^9 years. The dark shaded region is where all clusters of all ages contribute to the same part of the LF. The light shaded region represent the clusters contributing to the bright end of the LF.

When there is a physical mechanism that does not allow clusters more massive than $M_{\rm max}$ to be formed, there should be an observable bend at $M_\lambda = M_\lambda(M_{\rm max}, t_{\rm max})$. With our model we now generate a cluster population with ages between 10^7 and 3×10^9 yr and masses between 10^2 and 10^6 and apply a detection limit at $M_V = -7$. The age range is based on the observed age range in M51. We excluded the clusters younger than log(age/yr)=7, since a large fraction of these clusters will not survive the first 10 Myr (e.g. Lada & Lada 2003; Bastian et al. 2005b). We apply no disruption or extinction. The total weight of this simulation is scaled to 1000 clusters. The brightest cluster now is the first bin at the bright side with a weight larger than 1. The resulting LF is shown in Fig. 10.13. The faint part has an exponent of $-\alpha = -2.0$, which is expected, since the underlying mass function has an exponent of $-\alpha' = -2$. On the bright side the slope is steeper (-2.5) and the break between the two power-laws is at $M_V = -9.3$ mag, which is close to the magnitude of a $10^6 M_\odot$ cluster with an age of 3×10^9 yr ($M_V(t = 3 \times 10^9 \text{ yr}; M = 10^6 M_\odot) = -9.1$ mag) . For NGC 6946 and M51 the observed break occurs at $M_V = -8.9 \pm 0.4$ mag and $M_V = -9.3 \pm 0.4$ mag respectively implies a maximum cluster mass of $6.9 \times 10^5 M_\odot$ and $1.0 \times 10^6 M_\odot$. For comparison, the bend in the LF of the "Antennae" galaxies at $M_V = -10.3$ corresponds to a maximum mass of $\sim 2.5 \times 10^6 M_\odot$, assuming the oldest cluster in the sample is also 3 Gyr. We also fit a Schechter function (Eq. 10.5) to the model as was done for the clusters in NGC 6946, M51 and the "Antennae" galaxies. When we fit this function to our model with α, N_* and M_* as variables we get a very good fit (see right panel of Fig. 10.13). As was the case with the Schechter fit to the observed LF of NGC 6946 and M51, the bend now occurs brighter than when breaking the LF into two power-law distributions. When comparing the bend points from the Schechter functions to the model, we find maximum cluster masses of $4.4 \times 10^5 M_\odot$, $4.8 \times 10^5 M_\odot$ and $1.3 \times 10^6 M_\odot$ for NGC 6946, M51 and the "Antennae" respectively. We note that the errors in the fitted break points and Schechter bends are large (~ 0.5 mag), which corresponds to a factor 1.5 in mass. It is therefore hard to place a hard limit on the upper mass of the CIMF.

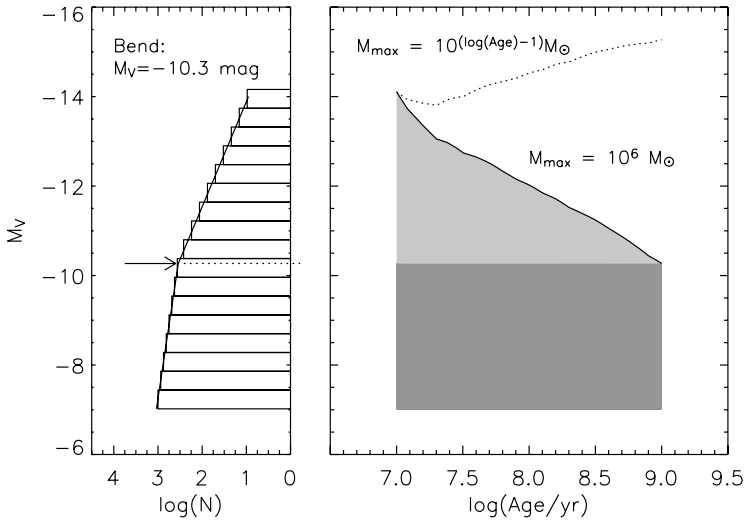

Figure 10.12: **Right**: Schematic picture of the two regions (dark and light grey) contributing to the LF when the underlying CIMF is truncated. The dark shaded region contributes to the faint end of the LF and the light shaded region to the bright end. The line indicates the brightness of a $10^6 M_\odot$ cluster. The dotted line indicates the brightness of the most massive cluster taking size of sampling effects into account. **Left**: Resulting LF.

10.5.5. Impact of different initial conditions

Our assumed initial conditions of § 10.5.4 might affect our results and in particularly the location of a break in the LF. We therefore created several cluster populations, with different initial conditions.

Varying cluster formation rate

For simplicity we have taken the cluster formation rate (CFR) to be constant over 3 Gyr in § 10.5.4. Especially when comparing with M51 and the "Antennae" galaxies this might be an over simplification. We generated models with bursts in the CFR, as is probably more realistic for M51 (Gieles et al. 2005). Bursts with increased CFRs of factors of 2-3 do not affect the location of the bend. For comparison with the LF of the "Antennae", we increased the CFR the last 160 Myr, based on the results of Wilson et al. (2003). For a CFR which was 3/5/10 times higher the last 160 Myr as before, the bend occurs 0.3/1.5/1.8 mag brighter. This would make our observed maximum masses 1.3/4/5 times lower. As was shown in § 10.3.1, the assumption of a constant CFR will always make it hard to directly compare the model with the data.

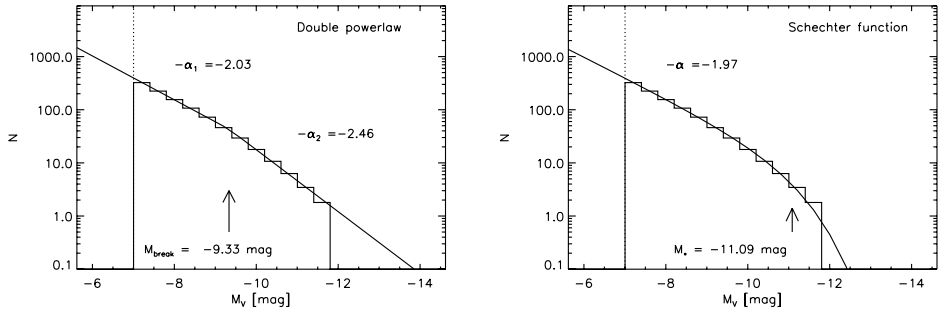

Figure 10.13: LF of a synthetic cluster population with a CIMF with exponent -2, a mass function truncation at $M_{\rm max} = 10^6 M_\odot$ and a detection limit at $M_V = -7$. The left panel shows a double power-law fit, where the slope bright-ward of the bend is steeper than the underlying mass function. The right panel shows a fit with a Schechter function.

The stellar IMF

Our SSP models assume a Salpeter IMF. When a Kroupa was assumed, the corresponding mass derived from a bend in the modelled LF will be about a factor of 2 lower. To explain the bend location in M51, NGC 6946 and the "Antennae" galaxies, our derived maximum masses will also be a factor of 2 lower.

The age range

We assumed clusters in the age range of $10^7 <$ age $< 3 \times 10^9$ years, based on the observed cluster ages in M51. When we would take 10^9 years as the maximum age range, the location of the bend would be 0.8 mag brighter. The maximum masses of our observations would be a factor of 2 lower in that case. If we would change the youngest cluster in our model from 10^7 years to 4×10^6 years, the modelled location of the bend does not change. However, when we assume that only 20% of the youngest clusters (e.g. age $< 10^7$ years) survive the gas removal phase (e.g. Fall 2004; Bastian et al. 2005b), it would place the bend 0.4 mag fainter. That would make our maximum masses derived from observations a factor of 1.5 more massive. In addition, clusters will probably loose 50-80% of their stars in this phase (Kroupa & Boily 2002), which will make *all* our derived *initial* maximum masses a factor 2-5 more massive.

The effect of disruption

Applying cluster disruption according to Eq. 10.2 affects only the LF at the faint end. The low mass clusters are disrupted faster and that will result in a shallower mass and hence LF at higher ages. Since the young clusters also contribute at these brightnesses, it is hard to quantify this affect. When applying the short cluster

disruption time of M51 ($t_4 = 10^8$ years), we find an exponent of the LF on the faint side of $\alpha = 1.7$ and the location of the bend does not change. It could explain why in the "Antennae" galaxies slopes significantly shallower than -2 are reported (W99) after various steps to removes stellar contamination. Also this value is close to the observed faint slope of the LF of NGC 6946 and it could explain why the slopes of the LF of the SMC and LMC are shallower than -2.

10.5.6. Testing the bend scenario in different filters

If the location of the bend in the LF is related to the most massive cluster in the oldest age bin (§ 10.5.4), it should appear at brighter luminosities in the red filters because old clusters have red colours. With this knowledge, we can test our theory on the cluster sample of M51, for which we have multiple filters available. With our model we can now predict the LF and a possible bend in all filters. We used a constant formation rate and a disruption time of clusters of $t_4 = 10^8$ years, as was found by Gieles et al. (2005). The CIMF was truncated at the high mass side. The clusters were generated and evolved according to method described in § 10.5.1. The bend will occur at different magnitudes for the different filters because the magnitude of the maximum cluster will be different in the different filters. The result is shown in Fig. 10.14. The top and bottom panel show the data in the F336W, F439W, F555W and F675W filters, roughly equal to U, B, V and R. In the top panel we plot the data and over plotted double power-law fits to the model. The break point between the two power-laws was based on the magnitudes of $M_{\rm max}$ in these filters at 10^9 years according to the `GALEV` SSP models. The predicted bend is indicated in each band in the top panel.

The break moves to brighter luminosities for redder filters as predicted, this is because clusters of 3×10^9 year are in general redder than younger clusters. For example, the $B-V$ colour at 10^9 year is 0.7 mag, so the bend in the V-band occurs 0.7 mag brighter than in the B-band. In the observed LF also the bend seems to move to brighter luminosities when going to redder filters. In the U-band, the bend is predicted 0.8 mag brighter than the detection limit. We thus only see the steep part of the LF. The observed LF of the U-band seems also to be a single power-law, although a slight bend is visible just bright-ward of the detection limit. The steep part is much shallower in the F336W band than in the other filters due to the rapid fading in that filter. The data and the model agree very well on this. The bottom panel of Fig. 10.14 shows the same data, but now the models were fitted with Schechter functions (Eq. 10.5). The fit to the model ends at the bright side at the last bin which had a value of 1 or higher. This means that this is the luminosity of the brightest cluster in the simulation. The brightest cluster in the model agrees well with the brightest cluster in the data.

The bend in the "Antennae" occurs ~ 5 mag brighter in the Ks-band (Mengel et al. 2005) as in the V-band (W99). The $V-K$ model colour of a cluster of 3 Gyr is around 3.2 mag. The V-band observations of W99 are not corrected for extinction,

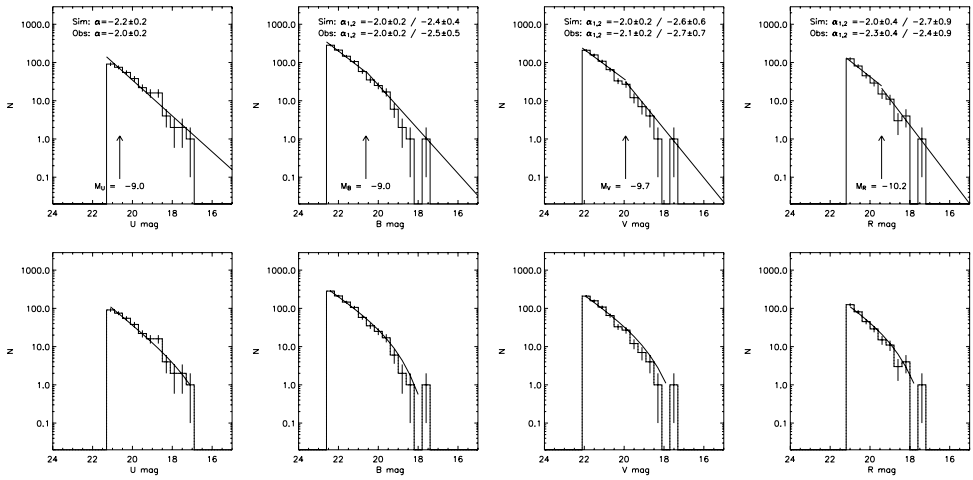

Figure 10.14: The LF of 705 clusters with ages between 10^7 and 10^9 year in M51 in the F336W, F439W, F555W and F675W bands. Over plotted with solid lines are fits to modelled luminosity function, based on a clusters IMF with exponent -2.1, equal number of clusters and a truncation of the mass function at $M_{\rm max} = 10^{5.9}$. **Top:** Fits to the model are two power-laws, with the break at $M_\lambda = M_\lambda(M_{\rm max}, t_{\rm max})$. The bend occurs to brighter magnitudes going to redder filters, since a cluster of age 10^9 years is brighter in the redder filters. **Bottom:** Same data, but now the fits to the model are Schechter functions.

making the bend in V fainter and most probably the observations by Mengel et al. (2005) are hampered by blends, making the bend brighter in Ks.

10.5.7. Effect of a bend in the mass function

The observed bend in the LF of the "Antennae" galaxies has been interpreted as a bend in the mass function (W99; Fritze-v. Alvensleben 1999). With our model we can predict how a bend in the CIMF would affect the LF. We generate a cluster sample between 10^7 and 10^9 years with a constant formation rate. We put a bend in the CIMF at $M = 10^4 M_\odot$, where the exponent is $-\alpha' = -1$ below the bend and $-\alpha' = -2$ on the high mass end. The resulting LF is shown in Fig. 10.15. On the very faint side the LF has the same slope as the underlying MF below $10^4 M_\odot$. Note that a slope of the LF of $-\alpha = -1$ shows up as a flat part in the magnitude distribution due to the conversion between the slope of the magnitude distribution and the slope of the LF (Eq. 10.4). On the bright side the LF has the same slope as the MF above $10^4 M_\odot$ ($-\alpha = -2$). The transition region is caused by the fading of a $10^4 M_\odot$ cluster between 10^7 and 10^9 years. When we would fit two power-laws over the whole LF, the break would be somewhere at $M_V = -6$ mag, i.e. much to faint to observe a bend in the MF at $10^4 M_\odot$.

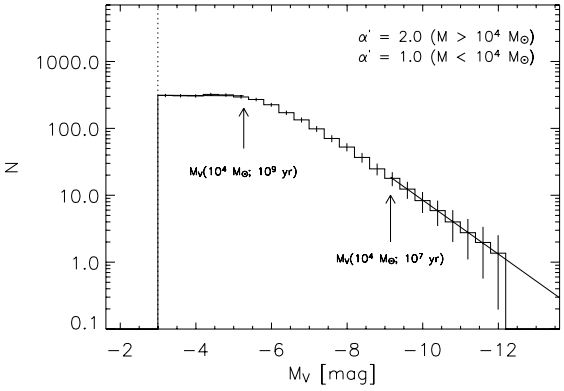

Figure 10.15: Simulated LF of clusters which are formed with a constant formation rate between 10^7 and 10^9 years and a bend in the CIMF. Below $10^4 M_\odot$ the mass function has an exponent of $-\alpha' = -1$ and above $10^4 M_\odot$ the exponent is $-\alpha' = -2$. The mass function has no truncation at high masses. At the bright side the LF has the a slope of $\alpha = 2$ and on the very faint side the slope is $\alpha = 1$.

10.5.8. Bend *vs.* no bend

So if the bend in the LF (§ 10.5.4) can be explained with a truncated mass function, why do the other galaxies in our sample (SMC, LMC, and NGC 5236, § 10.4.1-10.4.1) not show this bend? The answer is sampling statistics. If the bend is a physical feature occurring at a given mass, then it should always occur at a predictable luminosity (assuming the age distribution is known). Of the galaxies studied here, NGC 6946 and M51 (and the "Antennae") are the only ones where the LF is sampled above $M_V = -10$. In the SMC, LMC and NGC 5236 we do not sample the LF up to such bright magnitudes, so if the truncation occurs at the same mass as in N6946/M51 we would not be able to see it.

10.6. The maximum cluster luminosity

Now that we have shown that there are arguments to believe that the CIMF is truncated, it is interesting to compare how this might affect the maximum cluster luminosity in a galaxy. Whitmore (2003) plotted the maximum cluster luminosity in a set of galaxies is a function of the number of clusters above $M_V = -9$ mag. A fit to the data is close to the expected relation based on the size-of-sample effect and an exponent of the luminosity function of $\alpha = 2$. L02 has proposed a relation between the maximum cluster luminosity and the product of the observed area (A) and the area-normalised SFR ($\Sigma_{\rm SFR}$) of the galaxy, assuming that the cluster formation rate

is proportional to the SFR. The increase of the maximum cluster luminosity with the product $A{*}$SFR is consistent with the observed increase.

In the top panel of Fig. 10.16 we show the luminosity brightest cluster as a function of $\log(N(M_V < -8.5))$ from the sample of Larsen & Richtler (2000) with filled circles and Whitmore (2003) with open circles. The sample of Whitmore (2003) has been shifted to the right with 0.2 dex, which is the expected number of clusters missed between $M_V = -8.5$ and $M_V = -9.0$ based on a luminosity function with exponent $\alpha = 2$. The $\Delta \log(N)$ in a certain magnitude interval relates to the slope of the LF as

$$\Delta \log[N(\Delta M)] \;=\; 0.4\,(\alpha - 1)\,\Delta M, \tag{10.7}$$

where ΔM is the magnitude interval and α is the slope of the LF. We have updated the data for NGC 1569, based on the data of Hunter et al. (2000). This was an outlying point in Whitmore (2003), but we found more clusters in Hunter et al. (2000).

We have over-plotted the expected increase in maximum cluster luminosity with $\log(N)$ assuming the luminosity function is a single power-law distribution and based on a range of exponent ($1.7 < \alpha < 2.7$), which is the observed range of slopes in this work. The fit to the closed circles is shown with the solid line, which falls nicely within the predicted area and corresponds to a exponent of the LF of $\alpha = 2.45 \pm 0.30$. Note that although this value is slightly higher than found in § 10.4.2, it is still within the 1σ error. Also we here use an indirect method to determine the slope of the LF, based on a small number of data points.

L02 has quantified the expected scatter in the maximum cluster luminosity. The 1σ deviation is 1.04 mag from the mean and is independent of the number. We over-plotted the 3σ deviations. To show the effect of the expected scatter, we show a simulated set of maximum cluster luminosities as a function of $\log(N)$ in the middle and bottom panels of Fig. 10.16. The input exponent of the simulated LF was the value found from the fit to the observations (2.45). The same number of simulated maximum cluster luminosities as was observed is shown in the middle panel and a larger number in the bottom panel. The simulated luminosities show that luminosities close to the 3σ error line are expected even with the low number of galaxies. The 3σ scatter is a little bit higher on the bright side of the fit, which is because of the power-law nature of the LF function.

For the galaxies studied here, we find that the luminosity of the brightest cluster can be accounted for by sampling statistics. This is in contrast with the most massive cluster. This can be understood by looking at Fig. 10.2 and Fig. 10.6. There we can see that the most luminous cluster in each galaxy is always a young cluster ($\log(\mathrm{age/yr}) \simeq 7$). The most massive cluster, however, is usually in the older bins, since these cover a larger time in which it is more likely to form a more massive clusters. The physical upper limits we have derived in this work are not reached when sampling a CIMF during 10^7 years.

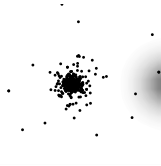

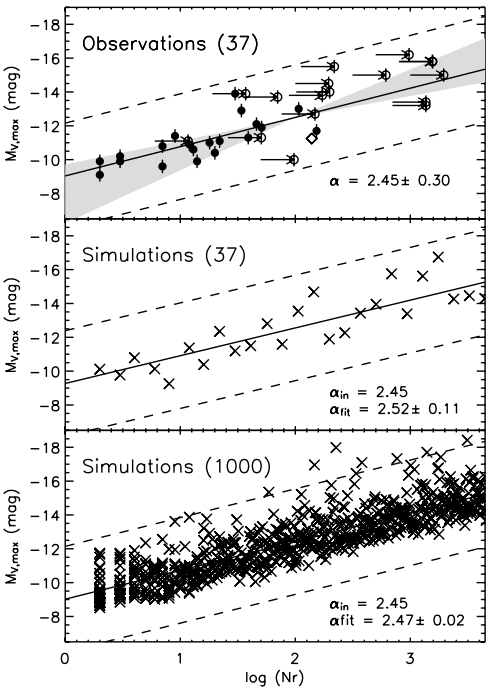

Figure 10.16: The maximum cluster luminosity in a galaxy *vs.* the number of clusters above a certain magnitude limit. **Top:** Observed maximum luminosities for 37 galaxies, compiled from a sample by Whitmore (2003) with open circles and Larsen & Richtler (2000) shown in full circles. The open circles are shifted 0.2 dex, since that sample is for clusters with $M_V < -9$ mag, while the sample of Larsen & Richtler (2000) is for clusters with $M_V < -8.5$. The grey area represents the expected range based on the size-of-sample effect and the observed range of α in this study ($-2.8 < -\alpha < -1.8$). The full line is a fit to the data. Some special cases are indicated as: M51 ($\diamond$), NGC 1569 ($\triangle$). The **middle** and **bottom** panel show simulated maximum cluster luminosities for similar number of galaxies as the observations and a large number respectively. The simulations were based on $-\alpha = -2.45$. In all three plots the 3σ deviation predicted by L02 is overplotted with a dashed line.

10.7. Discussion

A truncation of the cluster mass function raises the question what physical mechanism could be responsible for this cut-off. An answer might be present in the mass spectrum of giant molecular clouds (GMCs). Williams & McKee (1997) have shown that there is a distinct cut-off at the high mass end of the mass function of GMCs in the Milky Way. There are no clouds observed above $6 \times 10^6 M_\odot$, while there are $\sim$100 GMCs expected above that cut-off, based on statistical arguments. This might be caused by shear effects which do not allow clouds to grow larger than a certain size. The size and the mass of clouds are directly related by the virial theorem. Assuming that star clusters are formed with a star formation efficiency of $\epsilon = 0.01 - 0.1$ and that one single GMC produces one cluster, this implies it is not possible at this moment to form clusters more massive than $0.6 - 6.0 \times 10^5 M_\odot$ in the Milky Way. The Milky Way has formed a few massive clusters in the last few Myr, like Westerlund 1 with a mass of $\sim 10^5 M_\odot$ (Clark et al. 2005) and the Arches and Quintuplet clusters in the Galactic centre with masses of around $10^4 M_\odot$ (Figer et al. 1999).

A rough estimate can show that we would have expected more massive objects. Westerlund 1 is the most massive young cluster in the Milky Way disc. Of course we have to look at the size-of-sample that was used to discover it. Westerlund 1 is about 4.5 kpc away from the sun (Clark et al. 2005). Based on the most recent catalogue of open clusters by Kharchenko et al. (2005), Lamers et al. (2005a) estimated the masses of clusters in the solar neighbourhood. Within 600 pc from the sun, the catalogue is complete until 200 $M_\odot$, where about 100 clusters are found above that mass. The initial mass of the most massive cluster observed is estimated to be $3 \times 10^4 M_\odot$. The size of sample predicts $M_{\rm max} = N\, M_{\rm min} = 100 * 200 M_\odot = 2 \times 10^4 M_\odot$. So within the solar neighbourhood the mass of most massive cluster is determined by the size-of-sample effect. Assuming that the number density of clusters is constant until Westerlund 1, we can predict the expected maximum mass, based on statistical grounds. Based on the distance of 4.5 kpc, the expected number of clusters above 200 $M_\odot$ is about $(4500^2/600^2 = 56)$ times larger. This implies we would expect a maximum mass of $M_{\rm max} = 1.5 \times 10^6 M_\odot$. Although Westerlund 1 is a very massive cluster with $10^5\, M_\odot$, we would have expected at least one cluster above $10^6\, M_\odot$. Given that Westerlund 1 is highly obscured, it is unlikely that a 10 times more massive object would not have been found yet within a distance on 4.5 kpc from the sun. In fact, the mass of Westerlund 1 might be a reasonable upper limit, given that the most massive GMC is $6 \times 10^6\, M_\odot$ (Williams & McKee 1997) and a reasonable star formation efficiency of a few percent.

It is not clear what causes the cut-off of the cloud mass function. The maximum cluster mass seems to be environment dependent, since in the "Antennae" galaxies clusters of a few times $10^6 M_\odot$ are being formed. This could be because the maximum GMC mass is higher (Wilson et al. 2003), or because the star formation efficiency is much higher. The star formation efficiency is expected to be higher in high pressure environments (Elmegreen & Efremov 1997), which is the case in shock induced star formation environments like galaxy mergers (Schweizer 2005). The super massive cluster W3 in NGC 7252, with a dynamical mass of $10^8 M_\odot$ (Maraston et al. 2004), exceeds the limits we observe by almost two orders of magnitude. It was probably formed in the merger process of two gas-rich spirals and seems to be the tip of a continues power-law distribution (Miller et al. 1997).

As a comparison, the "Antennae" galaxies have not merged their nuclei yet. Simulations of the merging of two gas-rich spirals (Barnes & Hernquist 1991) have shown that in the third encounter the gas discs merge with relative velocities of more than 500 $\mathrm{km\,s^{-1}}$. Perhaps more massive clusters can be formed in these merging stages, due to the merging of clusters. Clusters also seem to form in complexes of multiple clusters and stars, with similar properties of their progenitor GMCs (Bastian et al. 2005a). Fellhauer & Kroupa (2005) have shown by numerical simulations that these complexes can collapse and form a single, diffuse, ultra-massive object, which might be the way W3 and other very massive clusters can be formed. During the merger shear-free regions exist, like in the *overlap-region* in the "Antennae"galaxies, where GMCs can grow bigger and more massive than in the galaxies we have studied here.

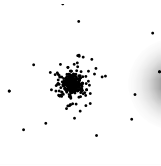

10.8. Conclusion

We have compared observed star cluster luminosity function in five galaxies with analytical cluster population models. Our main results can be summarised as follows:

- there are no clusters in M51 more massive than $M \simeq 1 \times 10^6 M_\odot$, although they are predicted by the size-of-sample effect. When comparing the maximum cluster mass in increasing log(age/yr) bins, the LMC and SMC cluster population show an increase consistent with the size-of-sample of effect. The cluster population of M51, however, shows a much shallower increase. This suggests a physical upper limit to the masses of clusters M51, although the shallow increase can also be reproduced by a combined effect of cluster disruption, infant mortality and an increasing cluster formation rate.

- when comparing the χ^2_ν results of different function fits to the five galaxies in our sample, we find that the LF of the SMC, the LMC and NGC 5236 can be well approximated by a power-law ($N\,\mathrm{d}L \propto L^{-\alpha}\,\mathrm{d}L$), with $1.9 < \alpha < 2.1$, while the LF of NGC 6946 and M51 are slightly better approximated with a double power-law or Schechter function.

- when fitting a double power-law function to the LF of NGC 6946 we find a break point at $M_V = -8.9 \pm 0.4$ mag. Faint-ward of the bend a power-law with exponent -1.7 ± 0.5 can be fitted. Bright-ward of the bend an exponent of -2.4 ± 0.1 is found. The LF can also be well fitted by fit a Schechter function with a bend at $M_V = -10.3 \pm 0.5$ mag.

- the LF of M51 shows a break at $M_V = -9.3 \pm 0.4$ mag. Faint-ward of the bend a power-law with exponent -2.0 ± 0.1 can be fitted. Bright-ward of the bend an exponent of -2.7 ± 0.3 is found. The LF of M51 is also well fitted by a Schechter function with a bend at $M_V = -10.3 \pm 0.5$ mag.

- the cluster LFs can be reproduced with a synthetic cluster population model. The bend in the LF of NGC 6946, M51 and "Antennae" galaxies can be explained with a truncation of the cluster mass function at $M_{\rm max} = 0.5{-}1{\times}10^6 M_\odot$ (M51/NGC 6946) and $1.3 - 2.5 \times 10^6 M_\odot$ ("Antennae").

In a follow-up study (Gieles et al. 2006c) we present an improved LF of star clusters in M51 based on *HST/ACS* data, taken as part of the Hubble Heritage project.

acknowledgements We are very grateful to Deidre Hunter who kindly provided the data of the SMC and LMC clusters. We like to thank Carsten Weidner and Pavel Kroupa for useful discussion. We acknowledge research support from and hospitality at the International Space Science Institute (ISSI) in Berne (Switzerland), as part of an International Team programme. Finally, we thank an anonymous referee for very constructive comments on the manuscript, which have improved the paper.

CHAPTER 11

Observational evidence for a truncation of the star cluster initial mass function at the high mass end

M. Gieles, S.S. Larsen, R.A. Scheepmaker, N. Bastian, M.R. Haas and H.J.G.L.M. Lamers

Astronomy and Astrophysics, v.446, p.L9–L12 (2006)

Abstract We present the luminosity function (LF) of star clusters in M51 based on *HST/ACS* observations taken as part of the Hubble Heritage project. The clusters are selected based on their size and with the resulting 5 990 clusters we present one of the largest cluster samples of a single galaxy. We find that the LF can be approximated with a double power-law distribution with a break around $M_V = -8.9$. On the bright side the index of the power-law distribution is steeper ($\alpha = 2.75$) than on the faint-side ($\alpha = 1.93$), similar to what was found earlier for the "Antennae" galaxies. The location of the bend, however, occurs about 1.6 mag fainter in M51. We confront the observed LF with the model for the evolution of integrated properties of cluster populations of Gieles et al. (2006b), which predicts that a truncated cluster initial mass function would result in a bend in, and a double power-law behaviour of, the integrated LF. The combination of the large field-of view and the high star cluster formation rate of M51 make it possible to detect such a bend in the LF. Hence, we conclude that there exists a fundamental upper limit to the mass of star clusters in M51. Assuming a power-law cluster initial mass function with exponential cut-off of the form $N\,\mathrm{d}M \propto M^{-\beta}\exp(-M/M_C)\,\mathrm{d}M$, we find that $M_C = 10^5\,M_\odot$. A direct comparison with the LF of the "Antennae" suggests that there $M_C = 4\times10^5\,M_\odot$.

11.1. Introduction

There is a relation between the luminosity of the brightest star cluster in a galaxy and the total number of clusters (Whitmore 2003; Larsen 2002), suggesting that sampling statistics is determining the luminosity of the most luminous cluster. Since the luminosity of clusters is heavily dependent on the age, a straightforward translation from most luminous to most massive is not possible. Recently, Hunter et al. (2003) showed that the maximum cluster mass increases with log(age/yr) in the LMC and SMC, which can be interpreted as a size-of-sample effect. Also Weidner et al. (2004) suggest that the maximum cluster mass in a galaxy depends on the star formation rate in the galaxy, hence the total number of clusters. This suggests that it would be *physically* possible to form a super massive cluster such as W3 in NGC 7252 with a mass of $8 \times 10^7\,M_\odot$ (Maraston et al. 2004) in our Milky Way, but the chance is just very small. This issue is still heavily under debate and is subject of this study.

The cluster luminosity function (LF) is a powerful tool for the study of star cluster populations. In a wide variety of environments the LF can often be well approximated by a power-law distribution: $N\,\mathrm{d}L \propto L^{-\alpha}\mathrm{d}L$, where the index α is between 1.8 and 2.4 (e.g. Larsen 2002; de Grijs et al. 2003a). The shape of the LF is related to, but not necessarily identical to the cluster initial mass function (CIMF). It is important to note that it is hard to relate the observed LF directly to the underlying CIMF, since the LF contains clusters of different ages. A star cluster fades about 5 magnitudes in 1 Gyr in the V-band, which makes it hard to estimate the mass without knowing the age.

The LF of clusters in the "Antennae" galaxies (Whitmore et al. 1999b), however, is much better approximated by a *double* power-law distribution. The bright side ($M_V > -10$) has a steeper slope (~ -2.7) than the faint side (~ -2). The latter is close to the value found for other galaxies. This double power-law nature with a *bend*, was interpreted by the authors as a turn-over in the *mass* function.

In Gieles et al. (2006b) we compared a cluster population model with various observed luminosity functions from the literature. We investigated various possible ways of detecting a truncated cluster initial mass function and the possible biases caused by extinction, disruption, variations in the cluster formation rate, etc. We concluded that a truncated CIMF will be observed as a bend in the integrated cluster luminosity function. We showed that tentative hints for a truncation are present in NGC 6946 (from Larsen 2002) and M51 (from Bastian et al. 2005b) and are clearly not present in the SMC and the LMC (from Hunter et al. 2003).

In this work we present a greatly improved LF of clusters in M51, based on recently released deep *HST* observations with the *Advanced Camera of Surveys (ACS)* covering the entire disc of M51. The great resolution of the *ACS* camera is exploited by selecting clusters based on their size. With this we are able to accurately select clusters, even when they are as faint as individual bright high mass stars. The improved resolution and larger field-of-view make it possible to confirm the suggestion of Gieles et al. (2006b) that the LF of M51 is of a double power-law nature.

We show that the bend in the LF is not necessarily related to a corresponding

turn-over in the MF, but results naturally if the CIMF is a power-law distribution truncated at the high-mass end.

In § 11.2 we describe the data, source selection and photometry. In § 11.3 we present the LF in the three available *ACS* filters of all extended objects in M51. A comparison with the model is done in § 11.4 and a discussion and the conclusions are presented in § 11.5.

11.2. Source selection and photometry

11.2.1. Data

We used the new *HST/ACS* (Hubble Heritage) data of M51 (NGC 5194) and its companion NGC 5195 in F435W (2720 sec.), F555W (1360 sec.), F658N (2720 sec.) and F814W (1360 sec.). Six pointings, corresponding to $430 \times 610''$ (=17.5×24.8 kpc), cover the entire disc of M51 plus the region with NGC 5195. For details on reduction we refer to Mutchler et al. (2005) and the M51 mosaic website (http://archive.stsci.edu/prepds/m51/).

11.2.2. Source selection

Source selection was done with the SExtractor package (Bertin & Arnouts 1996; version 2.3.2). A background map was made, by computing a mean and standard deviation of every section of the image with a user defined size. Deviating pixels were iteratively discarded until every pixel value of the background was within $\pm 3\sigma$ of the mean value. Every area of at least three adjacent pixels that exceeded the background by at least 5σ was called a source. For the details of the background estimation and source selection we refer to Bertin & Arnouts (1996). The F435W, F555W and F814W coordinates of the sources were cross-correlated and only sources within a two pixel uncertainty were kept. This resulted in a list of 75436 sources.

11.2.3. Photometry

Aperture photometry was performed on the sources in the list, using the package `IRAF/DAOphot` using a 5 pixel aperture radius and a background annulus with an inner radius of 10 pixels and a width of 3 pixels. Aperture correction from a 5 pixel aperture to 10 pixels (=0.5") were measured on artificial sources, generated by the `BAOlab` package (Larsen 1999; Larsen 2004). A Moffat profile (Moffat 1969) with power-law index of -1.5 and an effective radius ($r_{\rm eff}$), which is the radius containing half the cluster light in projection, of 3 pc was convolved with the filter dependent point spread function (PSF) of the *ACS* camera and the aperture correction was measured. The PSF we used was observationally determined from a crowded star field on a drizzled image of the Galactic globular cluster 47 Tuc. For each filter a separate PSF was determined. The resulting aperture corrections in F435W, F555W and F814W were $-0.16, -0.16$ and -0.17 mag, respectively. These values would be

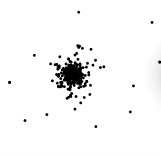

0.04 lower/higher for sources which are 1 pc bigger/smaller. The aperture corrections between 0.5" and infinity were taken from Table 5 of Sirianni et al. (2005). Finally, a correction for Galactic foreground extinction of $E(B-V) = 0.038$ was applied according to Appendix B of Schlegel et al. (1998). We did completeness tests by adding the same artificial clusters as used for determining the aperture correction to the image. A high background part of the image was used and the resulting 90% completeness limits in F435W, F555W and F814W were 23.3, 23.3 and 23.0 mag respectively.

11.2.4. Radius measurements

To distinguish between stars and clusters, we exploit the resolution of the *ACS* camera (1 pixel = 0.05") to measure the radii of all sources detected in F435W, F555W and F814W using the *ISHAPE* routine within the `BAOlab` package. In summary, analytic profiles with variable effective radii are convolved with the PSF, and are then fitted to each source in the data. The best-fit $r_{\rm eff}$ was determined by minimising the χ^2. We choose a Moffat profile with a power-law index of -1.5. Comparing the χ^2_ν of a point source (= PSF) fit to an extended profile fit, indicated whether a source is resolved. *ISHAPE* is able to pick up sources with a FWHM of 0.2 pixels, which corresponds to a $r_{\rm eff}$= 0.5 pc at the distance of M51 (distance modulus = 29.62, Feldmeier et al. 1997) The source detection and radius fits are used to define a source to be a cluster when

1. the source is detected in F435W, F555W and F814W,
2. the source magnitude is above the 90% completeness limit,
3. the sources is extended, defined as $r_{\rm eff} > 0.5$ pc,
4. the χ^2_ν of the extended profile fit is lower than that of the pure PSF fit.

These criteria resulted in 5 990 clusters brighter than $V = 23.3$ ($M_V = -6.32$).

11.3. The luminosity function

Following the source selection as described in § 11.2, we generate the LF of all clusters in the three available filters (left part of Fig. 11.1). The three columns on the left correspond with the F435W, F555W and F814W filters. In the top panels we fit a double power-law distribution, with a variable location of the break and indices and in the bottom panels we fit a Schechter function with variable M_* and index. The results of the different fits are summarised in Table 11.1. Note that the slopes on the faint sides correspond to the typical value of -2, found in other galaxies. The slopes on the bright side (α_2) are much steeper. The break appears at higher luminosities in the F814W filter. The double power-law break shifts about 0.5 mag to the red, going from F555W to F814W. The M_* values from the Schechter fit are about 0.2 mag brighter in F814W as compared to F435W and F555W.

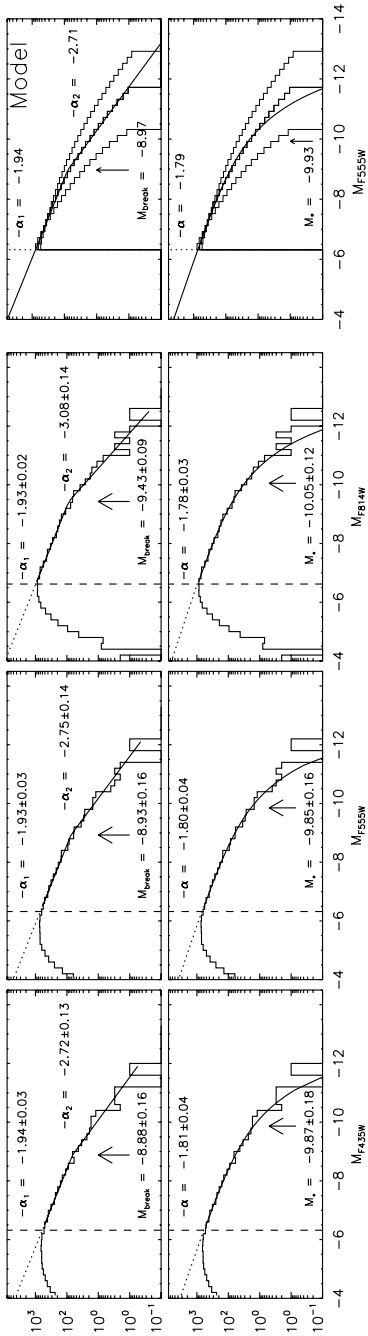

Figure 11.1: Luminosity function of all extended sources in M51 in F435W, F555W and F814W (**left three panels**) . The solid lines are the double power-law fits (top) and Schechter fits (bottom). The typical bend is indicated as M_* for the Schechter fits and $M_{\rm break}$ for the double power-laws. Also the slopes are indicated. The dotted line is the extrapolated distribution of the faint end. **Right:** LF of a synthetic cluster population with a CIMF with exponent -2, a mass function truncation at $M_C = 10^5 M_\odot$ and the same detection limit as the data. The top panel shows a double power-law fit, where the slope bright-ward of the bend is steeper than the underlying mass function. The bottom panel shows a fit with a Schechter (Schechter 1976) function. The thin lines are similar models, but with truncations at $10^6\,M_\odot$ (higher curve) and $10^4\,M_\odot$ (lower curve).

Table 11.1: Results of the different function fits to the observed LFs of Fig. 11.1 and the simulated LFs of § 11.4 .

	Double power-law			Schechter	
Filter	α_1	α_2	Break	α	M_*
		Observations			
F435W	1.94	2.72	-8.88	1.81	-9.87
F555W	1.93	2.75	-8.93	1.80	-9.85
F814W	1.93	3.08	-9.43	1.78	-10.05
	Models with $M_C = 10^5\,M_\odot$				
F439W	2.01	2.76	-8.99	1.85	-9.89
F555W	1.93	2.71	-8.94	1.79	-9.94
F814W	1.90	2.70	-9.60	1.76	-10.57

In Gieles et al. (2006b) we constructed the LF of M51 clusters based on the data of Bastian et al. (2005b). The data was based on two *WFPC2* pointings, and the LF showed that a double power-law function was better fit than a single power-law by a factor of two, when comparing χ^2_ν values. In this case, we obtain $\chi^2_\nu = 0.78$ for the double power-law fit in the F555W band, whereas the single power-law fit results in $\chi^2_\nu = 203$. This shows that the increase of the field-of-view and depth of the current data set contributes considerably to the significance of the result.

The downturn at bright magnitudes and the slopes of the double power-law distribution are very similar to what Whitmore et al. (1999b) found for the LF of the "Antennae" galaxies. The bend and M_*, however, occur about 1.6 mag brighter in the "Antennae" LF. We will explain this behaviour of the LF and the difference between the "Antennae" and M51 in § 11.4.

11.4. Comparison with a cluster population model

We have developed an analytical model which can reproduce the observable properties of a cluster population. The model was introduced in Gieles et al. (2005) for comparison with the age and mass distribution of M51 and used in Gieles et al. (2006b) to compare with LFs in different galaxies. The model generates cells which are equally spaced in log(age/yr) and log(mass/$M_\odot$). Weights are assigned to each cell, such that the integrated weights as a function of mass correspond to a chosen CIMF and formation rate and in that way correspond to number of clusters. Working with weights is preferred over generating the actual number of clusters, since this can be a very high number. Then cells are evolved as if they were clusters, where mass loss due to stellar evolution and disruption are taken into account by analytical functions derived by Lamers et al. (2005a).

In Gieles et al. (2006b) we showed that a physical limit to the maximum cluster mass will cause a bend in the LF. For details we refer to that paper. We generated sev-

eral populations with different maximum masses. A constant cluster formation rate between 6×10^6 yr and 10 Gyr is assumed and a power-law CIMF with an exponential cut-off $N\,\mathrm{d}M \propto M^{-\beta}\,\exp(-M/M_C)\,\mathrm{d}M$, with $\beta = 2$, similar to what has been proposed for the CIMF of globular clusters (Burkert & Smith 2000). The disruption parameters from Gieles et al. (2005) are adopted (i.e. $t_{\rm dis} = 10^8\,(M_i/10^4\,M_\odot)^{0.62}$ yr). We note that with these disruption parameters all cluster older than 2 Gyr are removed from the sample. We applied an extinction of $A_V = 0.25$ mag to all clusters, which is close to the average extinction measured by Bastian et al. (2005b). All masses are converted to *ACS* filter magnitudes, depending on their age, using the `GALEV` simple stellar population models (Anders & Fritze-v. Alvensleben 2003; Schulz et al. 2002). We fit the same functions to the artificial LFs as we did to the data. In the right panel of Fig. 11.1 we show the result for the F555W filter for $M_C = 10^5\,M_\odot$. The predicted LF parameters for all filters are summarised in the bottom part of Table 11.1. The bright side shows a steeper slope than the faint part, as is the case in the data. This is because the clusters with the maximum mass fade and therefore have an age-dependent contribution to the LF. The brightest cluster will be the youngest and going faint-wards, more older clusters will contribute to the LF. Faint-ward of $M_V \simeq -9$, clusters of all ages contribute. The fact that we find shallower slopes on the faint side than the input MF slope is due to the mass dependent disruption. The fact that the bend occurs at a higher luminosity in the F814W filter, in both the model and the data, is an important confirmation of our idea that the bend is caused by a truncated MF.

When we make a direct comparison with the "Antennae" galaxies, the MF is truncated at a higher mass ($M_C = 4 \times 10^5\,M_\odot$), since the bend there occurs 1.6 mag brighter (Whitmore et al. 1999b).

11.5. Discussion and conclusions

Does the fact that other galaxies have a single power-law LF imply that there is no upper limit to the cluster mass there? Probably not. The CIMF has to be sampled well enough to reach the critical $M_{\rm max}$, only then a bend will show up in the total cluster LF. M51 and the "Antennae" are forming enough clusters such that the CIMF is sampled until $M_{\rm max}$, and a bend in the LF is observable. The difference between $M_{\rm max}$ in M51 and the "Antennae" galaxies suggest that $M_{\rm max}$ is environment dependent.

These environmental differences might be caused by variations in the giant molecular cloud (GMC) mass distribution. Wilson et al. (2003) shows that the cloud mass function of the "Antennae" galaxies is truncated at higher masses than that of M51, which in turn is at much higher masses than in the Milky Way (Williams & McKee 1997). Other galaxies also seem to have GMC mass distributions which are truncated at the high mass end (Rosolowsky 2005). A truncated GMC mass function might impose a physical limit to the maximum star cluster mass, which will be observable in galaxies with a high star/cluster formation rates.

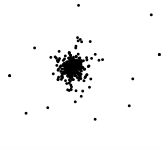

acknowledgements We thank Marcelo Mora at ESO/Garching for kindly providing us with the empirical *ACS* PSFs.

HOOFDSTUK 12

Samenvatting in het Nederlands

12.1. Sterrenhopen: algemene introductie

Een sterrenhoop is een verzameling sterren die door de onderlinge zwaartekracht bijelkaar gehouden wordt. Deze verzameling kan uit enkele tot vele miljoenen sterren bestaan die in een gebied van enkele lichtjaren in chaotische banen om elkaar en om het massa middelpunt van de sterrenhoop draaien. De verklaring voor dit groepsgedrag van sterren zit hem in het vormingsproces. Volgens de meest populaire theorieën over stervorming worden alle sterren in groepen gevormd die compact genoeg zijn om door de zwaartekracht bij elkaar gehouden te worden. Het is ook daarom dat alle sterren in een sterrenhoop (min of meer) dezelfde leeftijd hebben. Toch bevindt zich maar een klein percentage van alle sterren die we zien zich in een sterrenhoop. Ze hebben dus niet het oneindige leven. Er zijn interne en externe dynamische effecten die verantwoordelijk zijn voor het verlies van sterren uit een sterrenhoop. Dit proces, ook wel *verdampen* genoemd, lijdt uiteindelijk tot de volledige desintegratie. Het begrijpen van de levensloop van sterrenhopen vormt een belangrijk thema in dit Proefschrift. Waarom leven sterrenhopen in sommige melkwegstelsels maar enkele honderden miljoenen jaren, terwijl anderen die vlak na de Oerknal gevormd zijn er nog steeds zijn? Wat zijn de overlevingsstrategieën van sterrenhopen, en hoe hangen deze af van de hun eigenschappen?

Sterrenhopen zijn belangrijke studie objecten in de sterrenkunde. Alle sterren zijn ongeveer van dezelfde leeftijd, maar hebben niet allemaal dezelfde massa. Het is daarom mogelijk om te bestuderen hoe de evolutie van de individuele sterren afhangt van hun massa. Sterrenhopen stonden aan de basis van de huidige, zeer gedetailleerde modellen voor sterevolutie, die nu zeer nauwkeurig voorspellen wat, bijvoorbeeld,

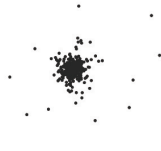

Figuur 12.1: Links: de open sterrenhoop *de Pleiaden* in het sterrenbeeld Taurus (stier). Rechts: bolvormige sterrenhoop M80 (NGC 6093).

Figuur 12.1: Izquierda: el cúmulo abierto las *Pléyades* en la constelacíon de Tauro. Derecha: cúmulo globular M80 (NGC 6093).

de helderheden van een sterrenhoop in verschillende golflengtes/kleuren is voor verschillende leeftijden. Dit heeft belangrijke consequenties: als de leeftijd bepaald kan worden met behulp van de kleuren en als de helderheid als functie van leeftijd bekend is, kan met behulp van een lichtkrachtmeting en een leeftijdsbepaling de afstand tot de sterrenhoop worden bepaald. Astandsbepalingen zijn cruciaal in de sterrenkunde, aangezien we alles *in projectie* zien, dat wil zeggen, twee-dimensionaal. Nauwkeurige afstandsbepalingen zorgen dus voor *ruimtelijk inzicht*, letterlijk een extra dimensie.

De sterrenhopen die we in onze Melkweg (het sterrenstelsel waar de zon zich in bevindt) kunnen waarnemen, worden in twee categorieën verdeeld: *de open sterrenhopen* en de *bolvormige sterrenhopen*. De open sterrenhopen zijn over het algemeen veel jonger en minder zwaar dan de bolvormige sterrenhopen. Met jong bedoelen we minder dan een miljard, wat vergeleken met de leeftijd van het heelal (ongeveer 13 miljard jaar), slechts in de orde van 10% is. De bolvormige sterrenhopen hebben leeftijden in de orde van de leeftijd van het heelal. Dit betekent dat ze vlak na de Oerknal en min of meer tegelijkertijd met het ontstaan van ons Melkwegstelsel gevormd zijn. Over het algemeen zijn de bolvormige sterrenhopen ook veel zwaarder (gemiddeld 100 000 keer zo zwaar als de zon). Een typische open sterrenhoop, is slechts 1000 keer zo zwaar als de zon. Figuur 12.1 laat links de open sterrenhoop de “Pleiaden” in het sterrenbeeld Stier zien. Deze wordt ook wel de Zeven Zusters genoemd en is op een heldere zomeravond met het blote oog te zien. Recht in Figuur 12.1 is de bolvormige sterrenhoop M80, of NGC 6093, te zien. Uit de plaatjes is direct het verschil te zien.

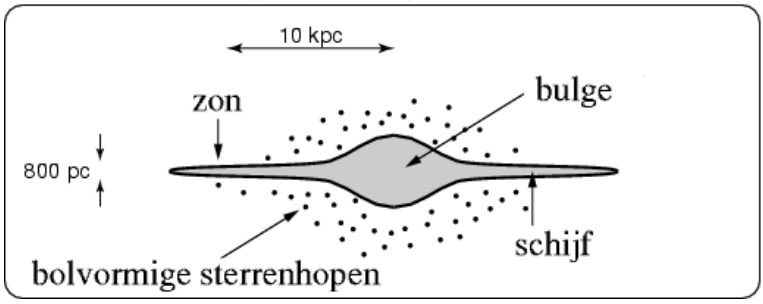

Figuur 12.2: Schematische weergave van de Melkweg (zijaanzicht). De Melkweg bestaat uit: *i)* een schijf, waarin zich voornamelijk jonge sterren en open sterrenhopen van allerlei leeftijden bevinden; *ii)* een halo met daarin de bolvormige sterrenhopen. De afstandseenheid pc staat voor parsec, wat ongeveer overeenkomt met 3 lichtjaar. Een lichtjaar is ongeveer 10^{16} meter.

Figuur 12.2: Esquema de la Vía Láctea (vista lateral). La Vía Láctea consiste en: *i)* un disco, en cual están sobre todo estrellas jovenes y cúmulos abiertos; *ii)* un halo con los cúmulos globulares dentro. La unidad de distancia es "parsec", que es aproximadamente tres años luz. Un año luz es más o menos 10^{16} metros.

In dit Proefschrift vinden we ook sterrenhopen in andere melkwegstelsels waar niet zo'n duidelijk onderscheid te maken is in twee typen. Jonge sterrenhopen met massa's vergelijkbaar met de bolvormige sterrenhopen.

De minder aansprekende naam M80 is omdat deze niet met het blote oog te zien is. Hij is ontdekt door de Franse astronoom Messier, die aan het einde van de 19^{e} eeuw alle nevels die hij met zijn telescoop waarnaam in een calatogus heeft opgenomen. De M in M80 is dus van Messier. Het was pas in de jaren 30 van de vorige eeuw dat Edwin Hubble ontdekte dat sommige van die nevels andere melkwegstelsels waren. Door hun afstand hebben ze echter min of meer dezelfde afmeting als de sterrenhopen in ons Melkwegstel. Een ander probleem veroorzaakt door projectie.

Het was in de jaren dertig dat de Britse astronoom Shapley, met behulp van de afstandsbepaling van enkele tientallen bolvormige sterrenhopen in onze Melkweg, het eerste (min of meer) correcte model van de Melkweg ontwikkelde. Bolvormige sterrenhopen draaien in ruime banen om het centrum van onze Melkweg (zie Figuur 12.2). Omdat Shapley de afstanden tot deze objecten wist, kon hij ook het middelpunt bepalen. Hij vond dat het middelpunt niet in de buurt van de zon ligt. Nadat een aantal eeuwen daarvoor al bleek dat de aarde niet in het middelpunt van ons zonnenstelsel stond bleek de zon nu ook ineens geen speciale positie te hebben. Ergens in de buitenwijken van een schijfvormig melkwegstelsel.

Dit Proefschrift richt zich op drie onderwerpen in het onderzoek naar sterrenhopen. In de Secties 12.2.1-12.2.3 wordt per deel van het Proefschrift een samenvatting gegeven. Het eerste gedeelte (Sectie 12.2.1) richt zich op waarnemingen van sterren-

hopen, vooral in andere melkwegstelsels. We hebben gekeken naar de vorming van sterrenhopen en vooral naar de leeftijdsverdeling van sterrenhopen. Hieruit kan namelijk de typische leeftijd of disruptietijd worden afgeleid. In Sectie 12.2.2 proberen we de waargenomen leeftijdsverdelingen in verschillende melkwegstelsels te verklaren met behulp van computersimulaties. Sectie 12.2.3 gaat over de maximale massa van sterrenhopen.

12.2. Samenvatting van dit Proefschrift

12.2.1. Deel I: Waarnemingen van de vorming en disruptie van sterrenhopen

In het eerste gedeelte van dit Proefschrift gebruiken we waarnemingen van de Hubble ruimtetelescoop om de sterrenhopen in M51 te bestuderen. M51 is een melkwegstelsel dat veel op het onze lijkt. Het staat ongeveer 24 lichtjaar bij ons vandaan en de schijf maakt een hoek van bijna 90° met de gezichtslijn. We kunnen daarom het hele melkwegvlak mooi zien (zie Figuur 1.3 in Hoofdstuk 1). Er is een kleiner melkwegstelsel te zien in de rechter bovenhoek van dit figuur. Dit kleinere stelsel, NGC 5195, is in interactie met de schijf van M51 en men denkt dat deze interactie de stervorming in M51 verhoogt. Het meeste licht in de spiraalarmen is afkomstig van *gloeiend* gas dat wordt aangestraald door jonge, zeer hete ($T > 20\,000°$), sterren. De duizend allerhelderste stipjes in dit plaatje blijken sterrenhopen te zijn. Deze sterrenhopen zien er van dichtbij waarschijnlijk net zo uit als M80 in Figuur 12.1 (rechts). Door de afstand van M51 zien we slechts kleine lichtpuntjes.

In **Hoofdstuk 2** laten we zien dat deze sterrenhopen ook weer gegroepeerd zijn in *complexen*. Deze complexen hebben afmetingen vergelijkbaar met die van de allergrootste molecuulwolken. Hier worden ook alle sterren uit gevormd worden. Echter, de massa's van de complexen zijn een factor twee tot drie lager. Op deze manier konden we afleiden dat 33%-50% van het moleculaire gas word omgezet in sterren.

In **Hoofdstuk 3** kijken we in M51 naar de eigenschappen van de verschillende sterrenhopen. Door de lichtkracht van de sterrenhopen te vergelijken met modellen (zie § 12.1) konden we de leeftijden en massa's bepalen van ongeveer duizend sterrenhopen. Ze zijn over het algemeen veel zwaarder dan de open clusters. Dit is omdat de kans een zware te vinden toeneemt als het totale aantal groter is. Vergelijk dit met de lengte van mensen: als je willekeurig duizend mensen van de straat selecteert is de kans om iemand die langer dan twee meter is te vinden groter dan wanneer je er maar 10 kiest. Ook laten we zien dat slechts een klein percentage ($\pm 30\%$) van de jonge sterrenhopen de eerste 10 miljoen jaar overleeft. Dit omdat in die tijd het gas wat niet gebruikt is voor de stervorming wordt weggeblazen door de sterrenwinden. Alle sterren, ook de zon, stoten gedurende hun leven materie uit, vergelijkbaar met wind. Het gas dat niet omgezet in sterren dient als een soort "zwaartekrachtslijn" om de sterren bij elkaar te houden. Als deze wordt verwijderd door sterwinden, gaan alle sterren hun eigen weg.

In **Hoofdstuk 4** bestuderen we de tijdschaal van disruptie van sterrenhopen in M51. We kijken dan naar diegene die deze eerste 10 miljoen jaar overleefd hebben en dan daarna sterren verliezen door allerlei interne en externe effecten. Door het aantal sterrenhopen per leeftijd te bekijken konden we afleiden wat de gemiddelde levensverwachting is. We vonden een zeer korte waarde, ongeveer 100 miljoen jaar. Ook bleek deze tijdschaal sterk af te hangen van de massa, hoe zwaarder hoe groter de overlevingskans.

Hoofdstuk 5 gebruikt de resultaten van Hoofdstuk 4 om een vergelijking te maken met resultaten in andere melkwegstelsels. Het blijkt dat de massa afhankelijkheid die we vonden ook in drie andere melkwegstelsels werd gevonden. Echter, de sterrenhopen in M51 leven het kortst van allemaal. Theoretische berekeningen voorspellen een levensverwachting die ongeveer 10 keer hoger is dan wat wij hebben waargenomen. Dit proberen we te verklaren in Deel II van dit Proefschrift.

12.2.2. Deel II: N-body berekeningen aan de disruptie van sterrenhopen

De korte disruptie tijden, zoals we die vonden uit waarnemingen in de voorgaande hoofstukken, konden niet verklaard worden met bestaande berekeningen van sterrenhopen die in een melkwegstelsel evalueren en sterren verliezen aan dat melkwegstelsel. In dit deel van het Proefschrift kijken we naar extra verstoringen die gedurende het leven van een sterrenhoop op zijn pad komen, zoals zware molecuulwolken en de spiraalarmen van het melkwegstelsel.

In **Hoofdstuk 6** geef ik een inleidende achtergrond over de bestaande theorieën. Als een zwaar object voorbij een sterrenhoop beweegt, geeft dit getijde krachten. Door de maan zijn er ook getijde krachten op de aarde, hierdoor hebben we twee vloedgolven in de oceanen. Er bestaan al theorieën die voorspellen wat deze krachten doen met sterrenhopen.

Deze theorie wordt vergeleken met zogenaamde "N-body" simulaties in **Hoofdstuk 7 en 8**. In een N-body simulatie worden alle krachten tussen alle sterren in een sterrenhoop nauwkeurig uitgerekend en de sterren worden aan de hand van de grootte en richting van de kracht verplaatst. Omdat deze berekeningen voor een variable aantal (N) lichamen (sterren, planeten, etc.) gedaan kan worden, wordt deze techniek "N-body berekening" genoemd. Het bekendste voorbeeld is het twee-body probleem (N=2, denk aan de aarde en de maan of de aarde en de zon die om elkaar heen draaien), wat al door Newton lang geleden opgelost is. Als N groter is dan twee, kan er gaan vergelijking voor de beweging meer worden opgesteld en kan de oplossing alleen gevonden worden door met hele kleine tijdstapjes alle sterren steeds een beetje te verplaatsen. Omdat deze krachten *van* alle sterren *op* alle sterren berekend moeten worden, duurt een berekening vier keer zo lang voor twee keer zoveel sterren. Daarom hebben we speciale super-computers in Marseille en Amsterdam gebruikt die gespecialiseerd zijn zwaartekrachts berekeningen. Ze worden *GRAPE*, een afkorting van *GRAvity PipE*, genoemd en kunnen 100 Tera ($= 10^{12}$) berekeningen per seconde maken.

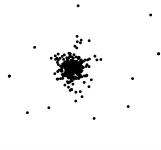

Met behulp van de *GRAPE* hebben we simulaties gedaan van sterrenhopen die door de spiraalarmen van een melkwegstelsel gaan en van botsingen met zware molecuulwolken. De spiraalarmen dragen maar een klein beetje bij aan het massa verlies van sterrenhopen, maar de botsingen met molecuulwolken daarentegen zijn verantwoordelijk voor een groot gedeelte van het massa verlies van sterrenhopen.

In **Hoofdstuk 9** combineren we de resultaten van Hoofdstuk 7 en 8 met andere resultaten voor het massa verlies door verdamping in het melkwegstels en massaverlies door evolutie van sterren in de zonsomgeving. Deze vier afzonderlijk contributies zouden dan het total massaverlies en daarmee de maximale leeftijd van sterrenhopen moeten verklaren. We hebben dit vergelijken de sterrenhopen in de omgeving van de zon en vonden zeer goede overeenkomst in de voorspelde leeftijdsverdeling en de waarnemingen.

12.2.3. Deel III: Een maximum massa voor reguliere sterrenhopen

Het derde en laatste gedeelte gaat over de maximum massa van sterrenhopen. Bij het bestuderen van de massa's en leeftijden van sterhopen in Hoofdstuk 3, vonden we, min of meer bij toeval, dat er een maximale massa blijkt te zijn voor de sterhopen in M51.

In **Hoofdstuk 10** introduceren we een methode om te zoeken naar een maximale massa. Het principe is heel simpel. Zoals al vermeld in § 12.2.1 neemt de kans om een zware sterrenhoop te vinden toe met het aantal sterrenhopen dat is waargenomen. Omdat de verdeling van het aantal sterrenhopen met een zekere massa bekend is, kan ook *voorspeld* worden wat de massa van de zwaarste sterrenhoop moet zijn gebaseerd op het waargenomen aantal. Vergelijk dit (wederom) met de lengteverdeling van mensen: uit een populatie studie kun je afleiden hoeveel procent van de mensen meer dan twee meter lang is. Stel dit is 1%, dat betekent dat als je honderd mensen van de straat plukt, dan verwacht je dat er één boven de twee meter zal zijn. Gebaseerd op deze stastische argumenten laten we zien dat in een aantal melkwegstelsels de massa van de zwaarste sterrenhoop volgens de verwachtingen afhangt van het totale aantal. In twee andere blijkt dit niet zo te zijn: *de zwaarste sterrenhoop is te licht voor het aantal dat is waargenomen.*. Tevens introduceren we een methode om naar deze maximale massa te zoeken zonder direct de massa's van de sterrenhopen te bepalen.

In **Hoofdstuk 11** gebruiken we de methode uit Hoofdstuk 10 om in M51 de maximale massa voor sterrenhopen te bevestigen. In een nieuwe dataset van M51 waarin een de gehele schijf gevangen is (Figuur 1.3) vonden we bijna vijf keer zoveel sterrenhopen dan voorheen. Dit betekent dat de verwachte massa van de zwaarste sterrenhoop nog hoger zou moeten zijn. Dit is echter niet het geval. Nu blijkt het dat er in andere melkwegstelsels sterrenhopen gevonden zijn die nog zwaarder zijn. Echter, andere onderzoekers hebben vastgesteld dat deze op kleine punten van sterrenhopen zoals we die kennen in de Melkweg. Vandaar dat we concluderen dat er een maximale bestaat voor de massa van *reguliere* sterrenhopen.

CAPÍTULO 13

Resumen en Castellano

13.1. Cúmulos de estrellas: Introducción general

Un cúmulo de estrellas es una colección de éstas, sostenidas por la gravitación mutua. Ésta colección puede contener desde pocas decenas de estrellas hasta millones de ellas, las cuales viajan dentro de un volumen de algunos años luz de radio en orbitas caóticas unas alrededor de otras y del centro de la masa del cúmulo. La explicación para éste comportamiento de las estrellas puede ser encontrada en el proceso de la formación. De acuerdo a la teoría referida a la formación de estrellas más popular, casi todas éstas se forman en grupos suficientemente densos para mantenerse ligados por su propia gravitación. Es por esta razón que todas las estrellas de un cúmulo tienen (más o menos) la misma edad. Pero hay solamente un porcentaje pequeño de todas las estrellas que vemos en un cúmulo, implicando que no tienen vida infinita. Existen efectos dinámicos internos y externos que son responsables de la pérdida de estrellas de un cúmulo. Esto lleva eventualmente a la desintegración completa del cúmulo, y se llama *evaporación*. Entender el curso de la vida de cúmulos forma una parte importante en esta Tesis. ¿Porqué los cúmulos viven solamente algunos centenares de años en algunas galaxias, mientras que otras se han formado poco tiempo después del "Big Bang" y aun están? ¿Cuál es la estrategia de los cúmulos para sobrevivir y cómo dependen éstos de sus características?

Los cúmulos son objetos de estudio importantes en astronomía. Todas las estrellas en su interior tienen aproximadamente la misma edad, pero no tienen todas la misma masa. Por esta razón es posible estudiar la evolución de las estrellas en función de sus masas. Los cúmulos sirvieron de base para los modelos detallados de evolución estelar, los cuales de hecho pueden predecir muy bien, por ejemplo, las luminosidades

de cúmulos de varias edades en varios colores.Esto tiene consecuencias importantes: Si la luminosidad es conocida en función de la edad es posible con una medicion de brillo, y una determinación de la edad, se puede obtener la distancia al cúmulo. Saber distancias es vital en astronomía, porque vemos todo proyectado. Determinaciones de distancias proveen *una noción de espacio*, literalemante, una dimensión extra.

Los cúmulos que podemos observar en la Vía Láctea (la galaxia donde está el sol), los podemos dividir en dos categorías: *los cúmulos abiertos* y los *cúmulos globulares*. Los cúmulos abiertos son generalmente mucho más jóvenes y menos masivos que los cúmulos globulares. Cuando decimos jóven, significa menos de mil millones de años, lo cual, comparado con la edad del universo (aproximadamente 13 mil millones de años), seria sólo del orden de 10 %. Los cúmulos globulares tienen edades del orden de la edad del universo. Ésto significa que están formados poco después del Big Bang y más o menos al mismo tiempo del nacimiento de la Vía Láctea. Generalmente los cúmulos globulares son masivos (en promedio 100 000 veces más pesados que el sol en cambio un cúmulo típico abierto es solamente 1000 veces mas pesado que el sol). A la izquierda, en la Figura 12.1 hay un cúmulo abierto, las *Pléyades* en la constelación de Tauro. Éste también es conocido como las Siete Hermanas y se puede ver con el ojo desnudo en una tarde clara del verano. A la derecha, en la Figura 12.1 se muestra el cúmulo globular M80, o NGC 6093. Éste cúmulo no es visible con el ojo desnudo y fue descubierto por el astrónomo francés Messier al final de la siglo 19. Él hizo un catálogo de todas las nebulosas que pudo ver con su telescopio. El M en M80 es por el nombre Messier. Fué justo en los años 30 del siglo pasado que Edwin Hubble descubrió que algunas de esas nebulosas eran otras galaxias. Por su distancia tienen, sin embargo, más o menos la misma dimensión que un cúmulo. Éste es otro problema causado por la proyección.

Era en los años treinta del siglo pasado cuando el astrónomo británico Shapley elaboró el primer modelo (más o menos) correcto de la Vía Láctea con la ayuda de determinaciones de distancias de algunas decenas de cúmulos globulares en nuestra galaxia. Cúmulos globulares viajan en orbitas amplias alrededor del centro de nuestra galaxia (véase Figura 12.2). Debido a que Shapley sabía las distancias a estos objetos, el pudo estimar también el centro de la galaxia. Él encontró que el centro de nuestro galaxia es muy distante del sol, al contrario de la idea general en esos tiempos. Varios siglos antes se descubrió que la tierra no estaba en el centro de nuestro sistema solar y ahora además que el sol tampoco está en un posición especial, sino en alguna parte en los suburbios de una galaxia en forma de disco.

Esta Tesis apunta hacia tres áreas en el estudio de cúmulos de estrellas. En las secciones 13.2.1 - 13.2.3 hay resumenes de las tres partes. La primera parte (seccion 13.2.1) es sobre las observaciones de los cúmulos, especialmente en otras galaxias. Hemos observado la formación de los cúmulos y especialmente la distribución por edad de éstos. De esto es posible deducir su tiempo de vida típico, que es el tiempo de destrucción del cúmulo. En la seccion 13.2.2 explicamos la observación de distribución de edades de cúmulos en varias galaxias por medio de las simulaciones por computador. Seccion 13.2.3 es sobre la masa máxima de los cúmulos.

13.2. Resumen de esta Tesis

13.2.1. Parte I: Observaciones de la formación y destrución de cúmulos

En la primera parte de esta Tesis utilizamos observaciones del telescopio espacial Hubble para estudiar los cúmulos en M51. M51 es una galaxia muy similar a la nuestra. Se encuentra aproximadamente a 24 años luz separada de nosotros y su disco hace un angulo de casi 90° con la línea de visión. Por esta razón podemos ver la galaxia completamente (véase Figura 1.3 en Capítulo 1). Hay una galaxia más pequeña en la esquina de arriba a la derecha. Esta galaxia, NGC 5195, interactua con el disco de M51 y se piensa que esta interacción incrementa la formación de estrellas en M51. La luz brillante es originada por gas irradiado que brilla intensamente a causa de estrellas jóvenes muy callientes ($T > 20\,000°$). Los puntos más brillantes son cúmulos. Desde una distancia pequeña estos cúmulos probablemente se ven como M80 en Figura 12.1 (derecha). Por la distancia de M51 vemos solamente puntos pequeños.

En el **Capítulo 2** demostramos que estos cúmulos están agrupados también. Llamamos a estos grupos *complejos*. Estos complejos tienen dimensiones similares a las de las nubes moleculares más grandes, de las cuales también se forman todas las estrellas. Sin embargo, las masas de los complejos son un factor de dos hasta tres veces más bajos de las masas de las nubes. De esta manera podríamos deducir que 33 %-50 % del gas molecular se convierte en estrellas.

En el **Capítulo 3** vemos en M51 las características de diversos cúmulos. Comparando la luminosidad del cúmulo con los modelos de evolución de éstos (véase § 12.1) nos es posible estimar las edades y las masas de aproximadamente mil cúmulos. Éstos son generalmente mucho más masivos que los cúmulos abiertos. Ésto es porque la probabilidad de encontrar un cúmulo masivo es más grande si el número total de cúmulos es más grande. Comparemos esto con la altura de la gente: si se eligen mil personas, al azar, de la calle, la probabilidad de encontrar una persona mas alta que dos metros es más grande que si se eligen solamente diez personas. También demostramos que un pequeño porcentaje ($\pm 30\,\%$) de los cúmulos jóvenes sobrevive sus primeros diez millones de años. Esto es por que en ese período el gas que no se ha transformado en estrellas es expulsado por los vientos de las estrellas jóvenes. Todas las estrellas, también el sol, expelen materia durante sus vidas, similar a un viento. El gas que no se ha convertido en estrellas funciona como *pegamento gravitacional*. Cuando es expulsado, todas las estrellas siguen su propia trayectoria.

En el **Capítulo 4** investigamos la escala típica de tiempo de destrución de cúmulos en M51. Consideramos aquellos que han sobrevivido a los primeros diez milliones de años y que después pierden estrellas por varias influencias internas y externas. Observando la cantidad de cúmulos pudimos deducir su expectativa de vida. Descubrimos que es muy breve, más o menos cien millones de años. También resultó que depende de la masa: mientras más masivo es un cúmulo, más alta la probabilidad de sobrevivir.

En el **Capítulo 5** usamos los resultados del Capítulo 4 para comparar con otras

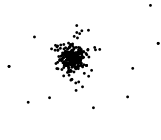

galaxias. Resultó que la dependencia de la masa es muy similar en otras tres galaxias, pero en M51 los cúmulos viven menos que en las otras. Cálculos teóricos predicen una expectativa de vida que es diez veces mayor que nuestras observaciones, esa diferencia se explica en la Parte II.

13.2.2. Parte II: Simulaciones de N-cuerpos de la destrución de cúmulos

Las cortas vidas de los cúmulos que observamos en los capítulos anteriores no pudieron ser explicados por los modelos existentes que calculan como pierden los cúmulos sus estrellas en una galaxia. En esta parte de la Tesis, investigamos trastornos adicionales en la vida de un cúmulo, como por ejemplo, colisiones con nubes moleculares y brazos de espirales.

En el **Capítulo 6**muestro una introducción sobre las teorías existentes. Cuando un objecto masivo pasa cerca de un cúmulo, éste ejerce fuerzas de marea en el cúmulo. De la misma manera que existen fuerzas de marea de la Luna hacia la Tierra, que causan la baja y alta de los mares. Existen teorías que predicen que pasa con un cúmulo por esas fuerzas.

En los **Capítols 7 y 8** comparamos las teorías con simulaciones de N-cuerpos. En una simulación de N-cuerpos todas las fuerzas, entre las estrellas, estan computadas y las estrellas estan en movimiento dependiendo de la dimensión y la dirección de las fuerzas. Debido a que éstas simulaciones se pueden hacer para un número de cuerpos variable N (estrellas, planetas, etc.), se llaman simulaciones de N-cuerpos. El ejemplo más famoso es el problema de dos-cuerpo (N=2, pensar en el sistema de la Tierra y la Luna o la Tierra y el Sol), que está solucionado por Newton hace muchos años. Cuando N es mas grande que dos, no existe una formula para los movimientos de los cuerpos y solamente se puede buscar el movimiento de las estrellas con pasitos pequeños y seguir el sistema en el tiempo, porque necesitamos computar las fuerzas de todas las estrellas hacia todas las estrellas, un cálculo cuesta cuatro veces más cuando hay el doble numero de estrellas. Por eso hemos hecho todos los cálculos en super-computadores especiales, en Marsella y Amsterdam. Estos computadores son especializados en cálculos de gravitación y se llaman *GRAPE*, desde *GRAvity PipE*, y pueden hacer 100 Tera ($= 10^{14}$) cálculos por segundo.

Con el *GRAPE* hicimos cálculos de cúmulos pasando a través de un brazo espiral de una galaxia y colisiones entre un cúmulo y nubes moleculares masivas. Los brazos espirales contribuyen levemente a la pérdida de estrellas del cúmulo, pero no así con las nubes moleculares. Son muy importantes en la destrución de cúmulos.

En el **Capítulo 9** combinamos los resultados de los Capítulos 7 y 8 con los resultados de la pérdida de masa por evaporación en una galaxia y por la evolución de las estrellas individuales en los cúmulos abiertos. Considerando estos cuatro procesos se puedecalcular la pérdida total de masa y se puede predecir la edad máxima de los cúmulos abiertos. Hemos comparado nuestro modelo con las observaciónes y existe mucho parecido.

13.2.3. Parte III: Un máximo para la masa de cúmulos regulares

La tercera Parte es sobre la masa máxima de cúmulos. Durante el estudio de las edades y las masa de cúmulos en M51 (Capítulo 3) encontramos, por suerte, que hay un máximo para la masa de un cúmulo.

En el **Capítulo 10** introducimos un método para buscar un máximo. El principio es muy fácil. Ya explicamos que en § 13.2.1 la oportunidad de buscar un cúmulo masivo se incrementa con el número de cúmulos observados, porque sabemos que al dividir el número de cúmulos por una masa particular, podemos *predecir* la masa del cúmulo más masivo basado en el número total. Comparando otra vez con las alturas de personas, asumir que 1 % de la gente mide más que dos metros. Esto significa que en cien personas, en promedio tiene que haberuna persona más alta que dos metros. Basado en estos argumentos demostramos en un número de galaxias que esto es aplicable. Pero, en dos galaxias resulta que *el cúmulo más masivo es demasiado ligero*. También introducimos un método para buscar un máximo en una galaxia sin deducir las masas de todos los cúmulos directamte.

Usamos este método en **Capítulo 11** para deducir el máximo para cúmulos en M51. En nuevos datos, en los cuales el disco entero de M51 esta visible (Figura 1.3) encontramos casi cinco veces más cúmulos que en el Capítulo 3, esto significa que la masa esperada es aun más pesada, pero no la encontramos. Hay cúmulos arriba de este límite que descubrimos en otras galaxias. Pero, otros investigadores han buscado que éstos tienen características fundamentales un poco diferentes que los cúmulos en la Vía Láctea. Por eso, concluimos que existe un máximo para las masas de cúmulos regulares.

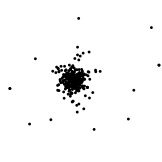

List of publications

Published in refereed journals

1. Gieles, Portegies Zwart, Baumgardt, Athanassoula, Lamers, Sipior & Leenaarts 2006, MNRAS, 371, 793 *Star cluster disruption by giant molecular clouds*

2. Lamers & Gieles 2006, A&A, 455, L17 *Star clusters in the solar neighbourhood: how are they destroyed?*

3. Anders, Gieles & de Grijs 2006, A&A, 451, 375 *Accurate photometry of extended spherically symmetric sources*

4. Gieles, Larsen, Bastian & Stein 2006, A&A, 450, 129 *The luminosity function of young star clusters: implications for the maximum mass and luminosity of clusters*

5. Gieles, Larsen, Scheepmaker, Bastian, Haas & Lamers 2006, A&A, 446, L9 *Observational evidence for a truncation of the star cluster initial mass function at the high mass end*

6. Bastian, Gieles, Efremov & Lamers 2006, A&A, 443, 79 *Hierarchical star formation in M51: Star cluster complexes*

7. Gieles, Bastian, Lamers & Mout 2005, A&A, 441, 949 *The Star Cluster Population of M51: III. Cluster disruption and formation history*

8. Lamers, Gieles, Bastian, Baumgardt, Kharchenko & Portegies Zwart 2005, A&A, 441, 117 *An analytical description of the disruption of star clusters in tidal fields with an application to Galactic open clusters*

9. Bastian, Gieles, Lamers, Scheempmaker & de Grijs 2006, A&A, 431, 905 *The Star Clusters Population of M51: II. Age distribution and relation between structural parameters*

10. Lamers, Gieles & Portegies Zwart 2005, A&A, 429, 173 *Disruption time scales of star clusters in different galaxies*

Submitted to refereed journals

1. Gieles, Athanassoula & Portegies Zwart 2006, MNRAS *The effect of spiral arm passages on the evolution of stellar clusters*

Published in conference proceedings

1. Gieles 2006, Workshop held in honour of H.J.G.L.M. Lamers, ed. A. de Koter, L. Smith & R. Waters, `astro-ph/0609103` *The role of tidal forces in star cluster disruption*

2. Haas, Gieles, Scheepmaker, Larsen, Lamers & Bastian 2006, Workshop held in honour of H.J.G.L.M. Lamers, ed. A. de Koter, L. Smith & R. Waters, `astro-ph/060918` *Variation of the cluster luminosity function across the disk of M51*

3. Gieles, Larsen, Haas, Scheepmaker & Bastian 2006, Globular clusters: Guides to Galaxies, ed. T. Richtler & S.S. Larsen, `astro-ph/0604578` *The maximum mass of star clusters*

4. Gieles, Portegies Zwart & Athanassoula 2006, Globular clusters: Guides to Galaxies, ed. T. Richtler & S.S. Larsen, `astro-ph/0605023` *The effect of giant molecular clouds on star clusters*

5. Scheepmaker, Gieles, Haas, Bastian, Larsen & Lamers 2006, Globular clusters: Guides to Galaxies, ed. T. Richtler & S.S. Larsen, `astro-ph/0605022` *The radii of thousands of star clusters in M51 with HST/ACS*

6. Anders, Gieles, de Grijs, & Fritze-v. Alvensleben 2005, ASSL Vol. 329: Starbursts: From 30 Doradus to Lyman Break Galaxies, 3P *Measuring sizes and compactnesses of young star clusters*

7. Bastian & Gieles 2003, in ASP Conf. Ser. 322: The Formation and Evolution of Massive Young Clusters, ed. H.J.G.L.M. Lamers, L.J. Smith & A. Nota, 205 *The star cluster populations of M51*

8. Gieles, Bastian & Lamers 2003, in ASP Conf. Ser. 322: The Formation and Evolution of Massive Young Clusters, ed. H.J.G.L.M. Lamers, L.J. Smith & A. Nota, 479 *The star cluster populations of M51*

9. Gieles, Baumgardt, Bastian & Lamers 2003, in ASP Conf. Ser. 322: The Formation and Evolution of Massive Young Clusters, ed. H.J.G.L.M. Lamers, L.J. Smith & A. Nota, 481 *Theoretical and observational agreement on mass dependence of cluster life time*

10. Lamers, Bastian & Gieles 2003, in ASP Conf. Ser. 322: The Formation and Evolution of Massive Young Clusters, ed. H.J.G.L.M. Lamers, L.J. Smith & A. Nota, 409 *The disruption time scales of clusters in different galaxies*

Dankwoord

Het is een groot plezier om allereerst mijn promotor Henny hier te bedanken. Ik herinner me het moment dat we voor het eerst over dit project spraken. Na afloop van mijn afstudeerpraatje zaten we in jouw kantoor en je vertelde ontzettend enthousiast over alle ideeën die er bestonden voor dit project en wat ik daar allemaal aan zou kunnen bijdragen. Nou, dat heb ik allemaal *niet* gedaan, maar we hebben wel met hetzelfde enthousiasme vier jaar lang samengewerkt in andere projecten die tot dit boekje hebben geleid! Die vrijheid die je mij hebt gegeven in mijn onderzoek heb ik als zeer waardevol beschouwd en je optimistische kijk op het onderzoek heeft mij veel plezier verschaft in het werk. Ik kijk er naar uit om met onze geplande ideeën, of totaal iets anders, in de toekomst te gaan werken. Daarnaast ben ik ook mijn copromotor Simon zeer veel dank verschuldigd. Je hebt mij met je aanstekelijke *drive* voor N-body simulaties besmet en ik ben zowaar bijna tot een theoreet bekeerd. Naast de astrophysica heb ik veel van je geleerd op het gebied van *wetenschapssociologie*.

Next to my official supervisors I was also helped a great deal by Lia Athanassoula, who I visited for four months in Marseille. I did *my first simulation* on a GRAPE over there and learned a lot about simulations and modeling. Also I am very grateful to Søren, with whom I worked on the last chapters in this thesis. I learned a lot from working on these projects with you and I hope we will get a change to figure some more things out together! Nate, many thanks to you for sharing your passion for research, the Family Guy, South Park and some of your funky opinions on life! I enjoyed many fun moments on summer schools, at conferences, in bars and other (drinking) locations around the world! (Also again thanks to Henny for bringing us to these places.....)

I am also grateful to many other collaborators for their contributions to this thesis and/or nice discussions, in particular: Holger Baumgardt, Yuri Efremov, Mike Sip-

ior, Peter Anders, Douglas Heggie, Bruce Elmegreen, Albert Bosma, Pavel Kroupa, Remco Scheepmaker and many others.

In the course of the years I have had several office mates in several offices. Thanks for your company, in order of appearance (in my office): Amina, Michaela, Leonardo SANDOVAL, Giuseppe, Jorrit, Alessia, Evghenni and Peter. Ook wil ik graag de afstudeerstudenten uit onze groep bedanken voor een hun scherpe vragen en leuke discussies: Jacqueline, Ilaan, Johan, Marcel, Diederik en Remco, bedankt!

Alfred, Cees, Marc en Arend-Jan, dank voor alle LaTeXnische hulp in het maken van dit boek (vooral de laatste weken). Alfred, dank voor *alle* IDL hulp in de afgelopen jaren en het last-minute gedoe om het filmpje in mijn proefschrift te krijgen!

In het eerste jaar van dit onderzoek heb ik nog (te)veel van mijn avonden langs de kant van het Merwedekanaal gesleten tijdens het coachen van Licht 2003. Alle roeiers, Jord, Maartje, Reinier en Paultje bedankt voor een supermooi jaar! Frank en Rutger bedankt voor het waarmaken van de ambitie! Het Orcahuis bedankt voor veel woonplezier en de traditionele (bah!) kerstdiners elk jaar in januari! Ook ben ik Orca's wielren cluppie dankbaar voor vele competatieve uurtjes op de weg op dinsdag-en vrijdagavond. Wegkapitein Reinder bedankt voor de organisatie en een vermakelijke zondag tijdens het Rondje Utrecht 2006. Uiteraard ook heel veel dank voor het ontwerpen van de (geniale) kaft van dit proefschrift! (Een fles rosé en photoshop bleken de ingrediënten voor een leuke avond en een grappig resultaat.)

Mijn goede vrienden, paranimf en ceremoniemeester Daniel en Joost, dank voor mooie tijden en goede herinneringen. Bassie en Kees, bedankt voor al het whiskey proeven en dieren braden! Selma en Guido bedankt voor jullie optimistische en humoristische kijk op dingen. Mijn vrienden uit het Orca bestuur 2000 bedankt voor veel leuke etentjes. Peter Jonker bedankt voor veel wijze raad en je gastvrijheid in Cambridge en Boston. Leonardo, Jorge Villa, Luzma y Jorge, gracias por "mejorar" la vida en Marsella. Axel y Cata, gracias por muchas noches divertidas! Cata "cuñada", gracias por ayudarme con el resumen en Castellano!

Mijn ouders, zusjes en andere familie ben ik dankbaar voor hun steun en interesse in mijn onderzoek! Het zal allemaal toch maar vaag geklonken moeten hebben als ik vertelde wat ik aan het doen was. Vaak was de locatie van de conferentie toch een leuker gespreksonderwerp dan het onderwerp van de conferentie zelf :-) Jullie interesse en waardering hebben mij wel heel erg geholpen en daar ben ik jullie heel dankbaar voor!

Mi amor Costy, gracias por aparecer en mi vida durante este tiempo. ¡Vamos a tu país ahora!

References

Aarseth, S. J. 1999, PASP, 111, 1333
Aguilar, L. A. & White, S. D. M. 1985, ApJ, 295, 374
Anders, P., Bissantz, N., Fritze-v. Alvensleben, U., & de Grijs, R. 2004, MNRAS, 347, 196
Anders, P. & Fritze-v. Alvensleben, U. 2003, A&A, 401, 1063
Ashman, K. M. & Zepf, S. E. 2001, AJ, 122, 1888
Athanassoula, E. 1984, Phys. Rep., 114, 321
Athanassoula, E. 1992, MNRAS, 259, 345
Athanassoula, E., Bosma, A., & Papaioannou, S. 1987, A&A, 179, 23
Barnes, J. E. & Hernquist, L. E. 1991, ApJ, 370, L65
Bastian, N., Emsellem, E., Kissler-Patig, M., & Maraston, C. 2006, A&A, 445, 471
Bastian, N. & Gieles, M. 2004, in ASP Conf. Ser. 322: The Formation and Evolution of Massive Young Star Clusters, ed. H. J. G. L. M. Lamers, L. J. Smith, & A. Nota, 205
Bastian, N., Gieles, M., Efremov, Y. N., & Lamers, H. J. G. L. M. 2005a, A&A, 443, 79 (**Chapter 2**)
Bastian, N., Gieles, M., Lamers, H. J. G. L. M., Scheepmaker, R. A., & de Grijs, R. 2005b, A&A, 431, 905 (**Chapter 3**)
Bastian, N. & Lamers, H. J. G. L. M. 2003, in Extragalactic Globular Cluster Systems, ed. M. Kissler-Patig, 28
Battinelli, P., Brandimarti, A., & Capuzzo-Dolcetta, R. 1994, A&AS, 104, 379
Battinelli, P. & Capuzzo-Dolcetta, R. 1991, MNRAS, 249, 76
Baumgardt, H. 2001, MNRAS, 325, 1323
Baumgardt, H., Hut, P., & Heggie, D. C. 2002, MNRAS, 336, 1069
Baumgardt, H. & Makino, J. 2003, MNRAS, 340, 227
Bergvall, N., Laurikainen, E., & Aalto, S. 2003, A&A, 405, 31
Bertelli, G., Bressan, A., Chiosi, C., Fagotto, F., & Nasi, E. 1994, A&AS, 106, 275
Bertin, E. & Arnouts, S. 1996, A&AS, 117, 393
Bessell, M. S., Castelli, F., & Plez, B. 1998, A&A, 333, 231
Bianchi, L., Thilker, D. A., Burgarella, D., et al. 2005, ApJ, 619, L71
Bica, E., Claria, J. J., Dottori, H., Santos, Jr., J. F. C., & Piatti, A. E. 1996, ApJS, 102, 57

Bik, A., Lamers, H. J. G. L. M., Bastian, N., Panagia, N., & Romaniello, M. 2003, A&A, 397, 473
Binney, J. & Tremaine, S. 1987, Galactic dynamics (Princeton, NJ, Princeton University Press, 1987)
Bissantz, N., Englmaier, P., & Gerhard, O. 2003, MNRAS, 340, 949
Boily, C. M. & Kroupa, P. 2003, MNRAS, 338, 673
Bok, B. J. 1934, Harvard College Observatory Circular, 384, 1
Böker, T., van der Marel, R. P., Mazzuca, L., et al. 2001, AJ, 121, 1473
Boselli, A., Lequeux, J., & Gavazzi, G. 2002, Ap&SS, 281, 127
Boutloukos, S. G. & Lamers, H. J. G. L. M. 2003, MNRAS, 338, 717
Brodie, J. P., Schroder, L. L., Huchra, J. P., et al. 1998, AJ, 116, 691
Burkert, A. & Smith, G. H. 2000, ApJ, 542, L95
Caldwell, J. A. R. & Laney, C. D. 1991, in IAU Symp. 148: The Magellanic Clouds, ed. R. Haynes & D. Milne, 249–+
Castor, J., McCray, R., & Weaver, R. 1975, ApJ, 200, L107
Cayatte, V., Kotanyi, C., Balkowski, C., & van Gorkom, J. H. 1994, AJ, 107, 1003
Chandar, R., Bianchi, L., & Ford, H. C. 2001, A&A, 366, 498
Chandar, R., Bianchi, L., Ford, H. C., & Sarajedini, A. 2002, ApJ, 564, 712
Chandrasekhar, S. 1942, Physical Sciences Data
Chernoff, D. F. & Weinberg, M. D. 1990, ApJ, 351, 121
Clark, J. S. & Negueruela, I. 2004, A&A, 413, L15
Clark, J. S., Negueruela, I., Crowther, P. A., & Goodwin, S. P. 2005, A&A, 434, 949
Dame, T. M., Ungerechts, H., Cohen, R. S., et al. 1987, ApJ, 322, 706
de Grijs, R. & Anders, P. 2006, MNRAS, 366, 295
de Grijs, R., Anders, P., Bastian, N., et al. 2003a, MNRAS, 343, 1285
de Grijs, R., Anders, P., Lamers, H. J. G. L. M., et al. 2005, MNRAS, 359, 874
de Grijs, R., Bastian, N., & Lamers, H. J. G. L. M. 2003b, MNRAS, 340, 197
de Grijs, R., Fritze-v. Alvensleben, U., Anders, P., et al. 2003c, MNRAS, 342, 259
de Grijs, R. & van der Kruit, P. C. 1996, A&AS, 117, 19
Dehnen, W. 2000, AJ, 119, 800
Dehnen, W. 2002, in ASP Conf. Ser. 275: Disks of Galaxies: Kinematics, Dynamics and Peturbations, ed. E. Athanassoula, A. Bosma, & R. Mujica, 105–116
Dias, W. S. & Lépine, J. R. D. 2005, ApJ, 629, 825
Dolphin, A. E. 2000, PASP, 112, 1383
Dolphin, A. E. & Kennicutt, Jr., R. C. 2002, AJ, 124, 158
Drimmel, R. 2000, A&A, 358, L13
Drimmel, R. & Spergel, D. N. 2001, ApJ, 556, 181
Efremov, Y. N. 1995, AJ, 110, 2757
Efremov, Y. N. 2004, [astro-ph/0410702]
Efremov, Y. N. & Elmegreen, B. G. 1998, MNRAS, 299, 588
Eggleton, P. P., Tout, C. A., & Fitchett, M. J. 1989, ApJ, 347, 998
Egusa, F., Sofue, Y., & Nakanishi, H. 2004, PASJ, 56, L45
Elmegreen, B. G. 1994, ApJ, 433, 39
Elmegreen, B. G. & Efremov, Y. N. 1997, ApJ, 480, 235
Elmegreen, B. G., Efremov, Y. N., & Larsen, S. 2000, ApJ, 535, 748
Elmegreen, B. G. & Elmegreen, D. M. 1983, MNRAS, 203, 31
Elmegreen, B. G. & Falgarone, E. 1996, ApJ, 471, 816
Elmegreen, B. G., Seiden, P. E., & Elmegreen, D. M. 1989, ApJ, 343, 602

Elmegreen, D. M., Elmegreen, B. G., Kaufman, M., et al. 2006, ApJ, 642, 158
Elmegreen, D. M., Kaufman, M., Elmegreen, B. G., et al. 2001, AJ, 121, 182
Elson, R. A. & Fall, S. M. 1988, AJ, 96, 1383
Elson, R. A. W. & Fall, S. M. 1985, ApJ, 299, 211
Elson, R. A. W., Fall, S. M., & Freeman, K. C. 1987, ApJ, 323, 54
Elson, R. A. W., Fall, S. M., & Freeman, K. C. 1989, ApJ, 336, 734
Fall, S. M. 2004, in ASP Conf. Ser. 322: The Formation and Evolution of Massive Young Star Clusters, 399
Fall, S. M., Chandar, R., & Whitmore, B. C. 2005, ApJ, 631, L133
Fall, S. M. & Zhang, Q. 2001, ApJ, 561, 751
Feldmeier, J. J., Ciardullo, R., & Jacoby, G. H. 1997, ApJ, 479, 231
Fellhauer, M. & Kroupa, P. 2002, AJ, 124, 2006
Fellhauer, M. & Kroupa, P. 2005, MNRAS, 359, 223
Figer, D. F., Kim, S. S., Morris, M., et al. 1999, ApJ, 525, 750
Fritze-v. Alvensleben, U. 1999, A&A, 342, L25
Fukushige, T. & Heggie, D. C. 2000, MNRAS, 318, 753
Fux, R. 2001, A&A, 373, 511
Garcia-Burillo, S., Guelin, M., & Cernicharo, J. 1993, A&A, 274, 123
Georgelin, Y. M. & Georgelin, Y. P. 1976, A&A, 49, 57
Geyer, M. P. & Burkert, A. 2001, MNRAS, 323, 988
Gieles, M., Athanassoula, E., & Portegies Zwart, S. F. 2006a, MNRAS, submitted (**Chapter 7**)
Gieles, M., Bastian, N., Lamers, H. J. G. L. M., & Mout, J. N. 2005, A&A, 441, 949 (**Chapter 4**)
Gieles, M., Baumgardt, H., Bastian, N., & Lamers, H. J. G. L. M. 2004, in ASP Conf. Ser. 322: The Formation and Evolution of Massive Young Star Clusters, ed. H. J. G. L. M. Lamers, L. J. Smith, & A. Nota, 481
Gieles, M., Larsen, S. S., Bastian, N., & Stein, I. T. 2006b, A&A, 450, 129 (**Chapter 10**)
Gieles, M., Larsen, S. S., Scheepmaker, R. A., et al. 2006c, A&A, 446, L9 (**Chapter 11**)
Gieles, M., Portegies Zwart, S. F., Baumgardt, H., et al. 2006d, MNRAS, 371, 793 (**Chapter 8**)
Giersz, M. & Heggie, D. C. 1996, MNRAS, 279, 1037
Girardi, L., Bressan, A., Bertelli, G., & Chiosi, C. 2000, A&AS, 141, 371
Gnedin, O. Y., Lee, H. M., & Ostriker, J. P. 1999, ApJ, 522, 935
Gnedin, O. Y. & Ostriker, J. P. 1997, ApJ, 474, 223
Gnedin, O. Y. & Ostriker, J. P. 1999, ApJ, 513, 626
Gonzalez, R. A. & Graham, J. R. 1996, ApJ, 460, 651
Goodwin, S. P. 1997, MNRAS, 286, 669
Grimm, H.-J., Gilfanov, M., & Sunyaev, R. 2003, MNRAS, 339, 793
Habing, H. J. & Israel, F. P. 1979, ARA&A, 17, 345
Harris, W. E. 1996a, AJ, 112, 1487
Harris, W. E. 1996b, VizieR Online Data Catalog, 7195, 0
Harris, W. E. & Pudritz, R. E. 1994, ApJ, 429, 177
Heggie, D. C., Giersz, M., Spurzem, R., & Takahashi, K. 1998, Highlights of Astronomy, 11, 591
Heggie, D. C. & Mathieu, R. D. 1986, LNP Vol. 267: The Use of Supercomputers in Stellar Dynamics, 267, 233
Heggie, D. C. & Ramamani, N. 1995, MNRAS, 272, 317

Helfer, T. T., Thornley, M. D., Regan, M. W., et al. 2003, ApJS, 145, 259
Henry, A. L., Quillen, A. C., & Gutermuth, R. 2003, AJ, 126, 2831
Hill, J. K., Waller, W. H., Cornett, R. H., et al. 1997, ApJ, 477, 673
Hodge, P. 1987, PASP, 99, 724
Hodge, P. 1988, PASP, 100, 576
Holmberg, J. & Flynn, C. 2000, MNRAS, 313, 209
Holtzman, J. A., Faber, S. M., Shaya, E. J., et al. 1992, AJ, 103, 691
Humphreys, R. M. & Davidson, K. 1979, ApJ, 232, 409
Hunter, D. A., Elmegreen, B. G., Dupuy, T. J., & Mortonson, M. 2003, AJ, 126, 1836
Hunter, D. A., O'Connell, R. W., Gallagher, J. S., & Smecker-Hane, T. A. 2000, AJ, 120, 2383
Kennicutt, R. C. 1998a, ApJ, 498, 541
Kennicutt, Jr., R. C. 1998b, ARA&A, 36, 189
Kennicutt, Jr., R. C., Edgar, B. K., & Hodge, P. W. 1989, ApJ, 337, 761
Kennicutt, Jr., R. C., Lee, J. C., Funes, J. G., Sakai, S., & Akiyama, S. 2005, in ASSL Vol. 329: Starbursts: From 30 Doradus to Lyman Break Galaxies, ed. R. de Grijs & R. M. González Delgado, 187
Kharchenko, N. V., Piskunov, A. E., Röser, S., Schilbach, E., & Scholz, R.-D. 2005, A&A, 438, 1163
King, I. 1958, AJ, 63, 465
King, I. 1962, AJ, 67, 471
King, I. R. 1966, AJ, 71, 64
Kranz, T., Slyz, A., & Rix, H.-W. 2001, ApJ, 562, 164
Krist, J. 1995, in ASP Conf. Ser. 77: Astronomical Data Analysis Software and Systems IV, ed. R. A. Shaw, H. E. Payne, & J. J. E. Hayes, 349
Kroupa, P. 1998, MNRAS, 300, 200
Kroupa, P. 2001, MNRAS, 322, 231
Kroupa, P. 2005, in ESA SP-576: The Three-Dimensional Universe with Gaia, ed. C. Turon, K. S. O'Flaherty, & M. A. C. Perryman, 629
Kroupa, P. & Boily, C. M. 2002, MNRAS, 336, 1188
Kundic, T. & Ostriker, J. P. 1995, ApJ, 438, 702
Kuno, N., Nakai, N., Handa, T., & Sofue, Y. 1995, PASJ, 47, 745
Lada, C. J. & Lada, E. A. 1991, in ASP Conf. Ser. 13: The Formation and Evolution of Star Clusters, ed. K. Janes, 3–22
Lada, C. J. & Lada, E. A. 2003, ARA&A, 41, 57
Lamers, H. J. G. L. M. & Gieles, M. 2006, A&A, 455, L17 (**Chapter 9**)
Lamers, H. J. G. L. M., Gieles, M., Bastian, N., et al. 2005a, A&A, 441, 117
Lamers, H. J. G. L. M., Gieles, M., & Portegies Zwart, S. F. 2005b, A&A, 429, 173 (**Chapter 5**)
Lamers, H. J. G. L. M., Panagia, N., Scuderi, S., et al. 2002, ApJ, 566, 818
Lançon, A. & Mouhcine, M. 2000, in ASP Conf. Ser. 211: Massive Stellar Clusters, ed. A. Lançon & C. M. Boily, 34
Larsen, S. S. 1999, A&AS, 139, 393
Larsen, S. S. 2000, MNRAS, 319, 893
Larsen, S. S. 2002, AJ, 124, 1393
Larsen, S. S. 2004, A&A, 416, 537
Larsen, S. S., Brodie, J. P., Elmegreen, B. G., et al. 2001, ApJ, 556, 801
Larsen, S. S. & Richtler, T. 1999, A&A, 345, 59

Larsen, S. S. & Richtler, T. 2000, A&A, 354, 836
Larson, R. B. 1981, MNRAS, 194, 809
Leitherer, C., Schaerer, D., Goldader, J. D., et al. 1999, ApJS, 123, 3
Lejeune, T. & Schaerer, D. 2001, A&A, 366, 538
Levine, E. S., Blitz, L., & Heiles, C. 2006, Science, 312, 1773
Maíz-Apellániz, J. 2001, ApJ, 563, 151
Makino, J., Fukushige, T., Koga, M., & Namura, K. 2003, PASJ, 55, 1163
Maraston, C., Bastian, N., Saglia, R. P., et al. 2004, A&A, 416, 467
Martos, M., Hernandez, X., Yáñez, M., Moreno, E., & Pichardo, B. 2004, MNRAS, 350, L47
Massey, P. 2002, ApJS, 141, 81
Massey, P., Lang, C. C., Degioia-Eastwood, K., & Garmany, C. D. 1995, ApJ, 438, 188
Mathewson, D. S. & Ford, V. L. 1984, in IAU Symp. 108: Structure and Evolution of the Magellanic Clouds, ed. S. van den Bergh & K. S. D. Boer, 125–136
McCrady, N., Gilbert, A. M., & Graham, J. R. 2003, ApJ, 596, 240
McMillan, S. L. W. & Hut, P. 1996, ApJ, 467, 348
Meatheringham, S. J. 1991, in IAU Symp. 148: The Magellanic Clouds, ed. R. Haynes & D. Milne, 89
Mengel, S., Lehnert, M. D., Thatte, N., & Genzel, R. 2002, A&A, 383, 137
Mengel, S., Lehnert, M. D., Thatte, N., & Genzel, R. 2005, A&A, 443, 41
Meurer, G. R., Heckman, T. M., Leitherer, C., et al. 1995, AJ, 110, 2665
Miller, B. W., Whitmore, B. C., Schweizer, F., & Fall, S. M. 1997, AJ, 114, 2381
Mobasher, B. 2002, HST Data Handbook: Introduction to Reducing HST Data, Volume 1, Version 4.0 (User's Guide, Hubble Space Telescope, January 2002. Edited by Bahram Mobasher. Baltimore: Space Telescope Science Institute)
Moffat, A. F. J. 1969, A&A, 3, 455
Murali, C. & Weinberg, M. D. 1997, MNRAS, 291, 717
Murray, N., Quataert, E., & Thompson, T. A. 2005, ApJ, 618, 569
Mutchler, M., Beckwith, S. V. W., Bond, H., et al. 2005, American Astronomical Society Meeting Abstracts, 206, 37
Nakai, N., Kuno, N., Handa, T., & Sofue, Y. 1994, PASJ, 46, 527
Nieten, C., Neininger, N., Guélin, M., et al. 2006, A&A, 453, 459
Oort, J. H. 1958, Ricerche Astronomiche, 5, 507
Ostriker, J. P., Spitzer, L. J., & Chevalier, R. A. 1972, ApJ, 176, L51+
Parmentier, G., de Grijs, R., & Gilmore, G. 2003, MNRAS, 342, 208
Piskunov, A. E., Kharchenko, N. V., Röser, S., Schilbach, E., & Scholz, R.-D. 2006, A&A, 445, 545
Plummer, H. C. 1911, MNRAS, 71, 460
Pols, O. R., Schroder, K.-P., Hurley, J. R., Tout, C. A., & Eggleton, P. P. 1998, MNRAS, 298, 525
Portegies Zwart, S. F., Hut, P., Makino, J., & McMillan, S. 1998, A&A, 337, 363
Portegies Zwart, S. F., Makino, J., McMillan, S. L. W., & Hut, P. 2001a, ApJ, 546, L101
Portegies Zwart, S. F., Makino, J., McMillan, S. L. W., & Hut, P. 2002, ApJ, 565, 265
Portegies Zwart, S. F., McMillan, S. L. W., Hut, P., & Makino, J. 2001b, MNRAS, 321, 199
Rand, R. J. 1993, ApJ, 410, 68
Rand, R. J. & Kulkarni, S. R. 1990, ApJ, 349, L43
Rix, H.-W. & Rieke, M. J. 1993, ApJ, 418, 123
Roberts, W. W. 1969, ApJ, 158, 123
Romaniello, M., Panagia, N., Scuderi, S., & Kirshner, R. P. 2002, AJ, 123, 915

Rosolowsky, E. 2005, PASP, 117, 1403
Rots, A. H., Bosma, A., van der Hulst, J. M., Athanassoula, E., & Crane, P. C. 1990, AJ, 100, 387
Salo, H. & Laurikainen, E. 2000, MNRAS, 319, 377
Salpeter, E. E. 1955, ApJ, 121, 161
Savage, B. D. & Mathis, J. S. 1979, ARA&A, 17, 73
Scalo, J. M. 1986, Fundamentals of Cosmic Physics, 11, 1
Schechter, P. 1976, ApJ, 203, 297
Schlegel, D. J., Finkbeiner, D. P., & Davis, M. 1998, ApJ, 500, 525
Schmidt, M. 1959, ApJ, 129, 243
Schulz, J., Fritze-v. Alvensleben, U., Möller, C. S., & Fricke, K. J. 2002, A&A, 392, 1
Schweizer, F. 1976, ApJS, 31, 313
Schweizer, F. 2005, in ASSL Vol. 329: Starbursts: From 30 Doradus to Lyman Break Galaxies, 143
Scoville, N. Z., Polletta, M., Ewald, S., et al. 2001, AJ, 122, 3017
Seigar, M. S. & James, P. A. 1998, MNRAS, 299, 685
Sirianni, M., Jee, M. J., Benítez, N., et al. 2005, PASP, 117, 1049
Smith, L. J. & Gallagher, J. S. 2001, MNRAS, 326, 1027
Solomon, P. M., Rivolo, A. R., Barrett, J., & Yahil, A. 1987, ApJ, 319, 730
Spinnato, P. F., Fellhauer, M., & Portegies Zwart, S. F. 2003, MNRAS, 344, 22
Spitzer, L. 1987, Dynamical evolution of globular clusters (Princeton, NJ, Princeton University Press, 1987, 191 p.)
Spitzer, L. J. 1940, MNRAS, 100, 396
Spitzer, L. J. 1958, ApJ, 127, 17
Spitzer, L. J. & Chevalier, R. A. 1973, ApJ, 183, 565
Stark, A. A. 1984, ApJ, 281, 624
Stark, A. A. & Brand, J. 1989, ApJ, 339, 763
Stetson, P. B. 1987, PASP, 99, 191
Strong, A. W. & Mattox, J. R. 1996, A&A, 308, L21
Sygnet, J. F., Tagger, M., Athanassoula, E., & Pellat, R. 1988, MNRAS, 232, 733
Tagger, M., Sygnet, J. F., Athanassoula, E., & Pellat, R. 1987, ApJ, 318, L43
Takahashi, K. & Portegies Zwart, S. F. 2000, ApJ, 535, 759
Terlevich, E. 1987, MNRAS, 224, 193
Theuns, T. 1991, Memorie della Societa Astronomica Italiana, 62, 909
Toomre, A. & Toomre, J. 1972, ApJ, 178, 623
Tremonti, C. A., Calzetti, D., Leitherer, C., & Heckman, T. M. 2001, ApJ, 555, 322
Vallée, J. P. 2005, AJ, 130, 569
van den Bergh, S. 1969, ApJS, 19, 145
van den Bergh, S., Morbey, C., & Pazder, J. 1991, ApJ, 375, 594
van der Kruit, P. C. 1988, A&A, 192, 117
van der Kruit, P. C. 2002, in ASP Conf. Ser. 273: The Dynamics, Structure History of Galaxies: A Workshop in Honour of Professor Ken Freeman, ed. G. Da Costa & H. Jerjen, 7
van der Kruit, P. C. & Searle, L. 1981a, A&A, 95, 105
van der Kruit, P. C. & Searle, L. 1981b, A&A, 95, 116
van der Kruit, P. C. & Searle, L. 1982a, A&A, 110, 61
van der Kruit, P. C. & Searle, L. 1982b, A&A, 110, 79
van Dokkum, P. G. 2001, PASP, 113, 1420

Vesperini, E. 1998, MNRAS, 299, 1019
Vesperini, E. & Zepf, S. E. 2003, ApJ, 587, L97
Weidner, C., Kroupa, P., & Larsen, S. S. 2004, MNRAS, 350, 1503
Weinberg, M. D. 1994a, AJ, 108, 1398
Weinberg, M. D. 1994b, AJ, 108, 1403
Weinberg, M. D. 1994c, AJ, 108, 1414
Westerlund, B. E. 1997, The Magellanic Clouds (Book,)
Whitmore, B., Heyer, I., & Casertano, S. 1999a, PASP, 111, 1559
Whitmore, B., Schweizer, F., Leitherer, C., Borne, K., & Robert, C. 1993, AJ, 106, 1354
Whitmore, B. C. 2003, in A Decade of Hubble Space Telescope Science, 153–178
Whitmore, B. C. 2004, in ASP Conf. Ser. 322: The Formation and Evolution of Massive Young Star Clusters, ed. H. Lamers, L. J. Smith, & A. Nota, 419
Whitmore, B. C. & Schweizer, F. 1995, AJ, 109, 960
Whitmore, B. C., Schweizer, F., Kundu, A., & Miller, B. W. 2002, AJ, 124, 147
Whitmore, B. C. & Zhang, Q. 2002, AJ, 124, 1418
Whitmore, B. C., Zhang, Q., Leitherer, C., et al. 1999b, AJ, 118, 1551
Wielen, R. 1971, A&A, 13, 309
Wielen, R. 1985, in IAU Symp. 113: Dynamics of Star Clusters, ed. J. Goodman & P. Hut, 449–460
Wielen, R. 1988, in IAU Symp. 126: The Harlow-Shapley Symposium on Globular Cluster Systems in Galaxies, ed. J. E. Grindlay & A. G. D. Philip, 393–406
Williams, J. P., Blitz, L., & Stark, A. A. 1995, ApJ, 451, 252
Williams, J. P. & McKee, C. F. 1997, ApJ, 476, 166
Wilson, C. D., Scoville, N., Madden, S. C., & Charmandaris, V. 2003, ApJ, 599, 1049
Zepf, S. E., Ashman, K. M., English, J., Freeman, K. C., & Sharples, R. M. 1999, AJ, 118, 752
Zhang, Q. & Fall, S. M. 1999, ApJ, 527, L81
Zhang, Q., Fall, S. M., & Whitmore, B. C. 2001, ApJ, 561, 727
Zimmer, P., Rand, R. J., & McGraw, J. T. 2004, ApJ, 607, 285
Zwicky, F. 1955, PASP, 67, 232